Entangled states of light and atomic spin oscillators for quantum noise reduction in Gravitational Wave Detectors

PhD thesis

Author: **Valeriy Novikov**

Danish Center for Quantum Optics
Niels Bohr Institute
Faculty of Science
University of Copenhagen
Denmark

This thesis has been submitted to the PhD School of Science at the University of Copenhagen.

Academic supervisor: Professor Eugene Simon Polzik

External referee №1: Associate Professor Dr. Stefan Danilishin

External referee №2: Professor Dr. Lukas Novotny

Chair of the committee: Professor Thomas Heimburg

Thesis submission: November 2, 2023

Thesis defense: December 6, 2023

Abstract

This thesis is dedicated to the methods of quantum noise reduction in composite quantum systems. The quantum noise is a major limitation for the sensitivity of future generations of laser interferometric Gravitational Wave Detectors (GWDs), whose mirrors can be regarded as free test masses. One of the most promising directions in quantum noise suppression for such GWDs is the application of non-classical states of light. In order to boost the sensitivity of GWD in broadband spectral range, it has been proposed to use frequency dependent single-mode squeezed states or conditional two-mode squeezed states. Theoretically, the performance of these protocols will be only restricted by the quality of the non-classical states of light. However, the practical implementation of such schemes involves the utilization of so-called filter optical cavities. An external resonator with extremely narrow bandwidth can be used to set the desired dependence of squeezing angle on the Fourier frequency for the single-mode squeezing. If two-mode squeezed states are exploited, the GWD itself can play a role of the filtering cavity. In turn, it imposes strict requirements on tuning the multiple interlinked parameters of the optical interferometer. Both approaches are complicated by experimental challenges related to the control of filtering resonators and/or changes in the established configuration of GWDs.

The main focus of this thesis is the investigation of the alternative strategy, where quantum noise reduction will be achieved by using an auxiliary harmonic oscillator that is the ensemble of spin polarized cesium atoms. Analogous to GWD, the spin oscillator is also exposed to quantum noise. However, the total noise in the hybrid system, composed of an atomic ensemble and a GWD, can be partially or completely eliminated. It has been previously demonstrated that the reference spin oscillator facilitates mitigation of the quantum noise in a dielectric membrane in MHz spectral range. At the same time, the atomic oscillator is highly tunable and can in principle be adjusted to match the GWD, making a joint measurement of two disparate systems feasible. From an experimental point of view, the spin oscillator might be added to the GWD as an external module without necessity to substantially modify the current design of the detection schemes. On the other hand, the spin ensembles compare favorably with filtering cavities in terms of complexity of control.

The dynamics of a spin oscillator, suitable for broadband sensitivity enhancement of GWDs in the spectral range of interest, should be predominantly driven by quantum noise at acoustic spectral frequencies. Moreover, in order to set the link between the GWD and the atomic ensemble, an Einstein–Podolsky–Rosen (EPR)-entangled state of light resilient to low-frequency technical noise is needed. In this thesis we report the preparation and characterization of each subsystem, performed separately. First, we present the entanglement source of two optical modes, having the wavelengths of 852 nm and 1064 nm that match the frequencies of lasers used to probe the atomic spin ensemble and GWD, respectively. We observe EPR correlations spanning down to audioband ($\Omega \gtrsim 10$ kHz). The entanglement is verified by EPR-steering and Duan criteria. The recorded level of two mode squeezing (-7.1 dB) is one of the highest (to our knowledge) to date for such large wavelength separation. Secondly, we prove the strong contribution of quantum back action (QBA) noise to the dynamics of the spin oscillator, using ponderomotive squeezing as a benchmark. In particular, we measure -3 dB and -0.7 dB of light noise reduction below shot noise level caused by interaction with the atomic ensemble, whose resonance frequency is set to 20 kHz and 6 kHz, respectively. The factors compromising the spin oscillator in quantum regime at near-DC spectral frequencies are explored and discussed. It has also been shown that QBA-dominated motion can be obtained for the atomic ensemble initialized in a state with an effective negative mass, which is a key feature for quantum noise cancellation in the joint measurement. The dissertation is complemented by theoretical analysis of the scheme under realistic experimental conditions.

The achieved performance of two quantum systems makes them ready for proof-of-principle experiment addressing the upper part of audio frequency range. In a long term prospective, presented results can serve as

a foundation for quantum noise reduction in sensitivity band of contemporary state-of-the-art interferometric GWDs. The comprehensive mathematical model of the experiment accounts for various imperfections and yields the set of parameters to optimize the efficiency of the protocol.

Resumé

Denne afhandling omhandler metoder til reduktion af kvantestøj i målinger udført på sammensatte kvantesystemer. Kvantestøj forventes at blive en større begrænsning for følsomheden af fremtidige generationer af laserinterferometriske gravitationsbølgedetektorer (GWD'er), hvis testspejle kan betragtes som frie masser. En af de mest lovende retninger inden for kvantestøjsreduktion for sådanne GWD'er er anvendelsen af ikke-klassiske lystilstande. For at forbedre GWD'ens sensitivitet i et bredt spektrum er det blevet foreslået at bruge frekvensafhængige enkelt-mode-klemte tilstande eller betingede to-mode-klemte tilstande. Teoretisk vil disse protokollers ydeevne kun være begrænset af kvaliteten af de ikke-klassiske lystilstande. Implementeringen af sådanne protokoller vil i praksis indebære brugen af såkaldte optiske filterkaviteter. En ekstern resonator med ekstremt smal båndbredde kan bevirke den ønskede afhængighed af klemningsvinkel på Fourier-frekvensen for en enkelt-mode-klemt tilstand. Hvis to-mode-klemte tilstande benyttes, kan GWD selv spille rollen som filterkavitet. Dette indebærer strenge krav til indstillingen af de mange sammenkoblede parametre for det optiske interferometer. Begge tilgange bliver besværliggjort af eksperimentelle udfordringer relateret til kontrol af filterresonatorer og/eller ændringer i GWD'ernes etablerede konfiguration.

Hovedfokus i denne afhandling er undersøgelsen af en alternativ strategi, hvor kvantestøjsreduktion opnås ved brug af en harmonisk referenceoscillator, der består af et ensemble af spinpolariserede cæsiumatomer. Analogt med GWD er denne spinoscillator også udsat for kvantestøj. Dog kan den samlede støj i det hybride system, der er sammensat af et atomart ensemble og en GWD, delvist eller fuldstændigt elimineres. Det er blevet eksperimentelt vist, at referencespinoscillatoren faciliterer reduktionen af kvantestøj i en dielektrisk membran i MHz-området. Samtidig er den atomare oscillator meget justerbar og kan i princippet tilpasses til at matche GWDen, hvilket gør en fælles måling af to forskelligartede systemer mulig. Fra et eksperimentelt synspunkt kan spinoscillatoren kombineres med GWDen som et eksternt modul, hvorved markante ændringer af det nuværende design af detekteringsprotokoller kan undgås. Derudover er spinensemblerne, sammenlignet med filterkaviteter, lovende systemer med hensyn til kompleksiteten af styringen.

Responset for en spin-oscillator som er kompatibelt med følsomhedsforøgelse af GWD over et bredt bånd i det spektrale interesseområde, bør være domineret af kvantestøj ved akustiske frekvenser. Desuden er der behov for en stærk Einstein–Podolsky–Rosen (EPR)-sammenfiltret tilstand af lys, der er robust over for lavfrekvent teknisk støj, for at etablere forbindelsen mellem GWD og atomensemblet. I denne afhandling rapporterer vi forberedelsen og karakteriseringen af hvert delsystem, udført separat. Først præsenterer vi kilden til sammenfiltring af to optiske tilstande med bølgelængderne 852 nm og 1064 nm, der matcher frekvenserne af lasere til at måle på atomspinensemblet og GWD, henholdsvis. Vi observerer EPR-korrelationer, der spænder ned til akustiske frekvenser ($\Omega \gtrsim$ 10 kHz), og sammenfiltringen verificeres ved hjælp af EPR-styring og Duan-kriterierne. Det registrerede niveau af to-mode-klemning ($-7,1$ dB) er et af de højeste hidtil (efter vores vidende) for så stor en bølgelængdeseparation. For det andet påviser vi det stærke bidrag af kvantetilbagevirkningsstøj (QBA) til dynamikken i spin-oscillatoren, ved hjælp af ponderomotiv klemning som benchmark. Vi måler specifikt -3 dB og $-0,7$ dB lysstøjsreduktion under haglstøjsniveauet, forårsaget af interaktion med atomensemblet, hvis resonansfrekvens er sat til 20 kHz og 6 kHz, henholdsvis. Faktorer, der kompromitterer spin-oscillatoren i kvanteregimet tæt på DC-frekvensområdet, udforskes og diskuteres. Det er også blevet påvist, at QBA-domineret dynamik kan opnås når atomensemblet initieret i en tilstand med en effektiv negativ masse, hvilket er en central egenskab ved kvantestøjannullering i en fælles måling af de to systemer. Afhandlingen suppleres med teoretisk analyse af protokollen under realistiske eksperimentelle betingelser.

Den opnåede ydeevne for de to kvantesystemer gør dem klar til et proof-of-principle-eksperiment, der adresserer den øvre del af lydfrekvensområdet. På lang sigt kan de præsenterede resultater udgøre fundamentet for reduktion

af kvantestøj i frekvensbåndet af relevans for nutidige state-of-the-art interferometriske GWD'er. Den omfattende matematiske model for eksperimentet tager højde for forskellige mangler og giver et sæt parametre for at optimere effektiviteten af protokollen.

Thesis structure

The manuscript contains five chapters. The structure is as follows:

Chapter 1: This chapter gives the introduction to the detection of gravitational waves by means of laser interferometers. We discuss the most essential features of such GWDs, define the problem of quantum noise and analyze its spectral properties. Next, we give an overview of methods that can potentially lead to the sensitivity improvement beyond the limit set by the quantum noise. The emphasis is made on techniques manipulating the vacuum state of light entering the GWD interferometers through the dark port.

Chapter 2: The purpose of this chapter is to familiarize the reader with the concept of quantum noise reduction, which takes the center stage of presented work. The idea of quantum back action (QBA) evasion for an arbitrary optomechanical object in the reference frame of a second oscillator with an effective negative mass is presented and applied to the specific case of the GWD. The atomic spin ensemble is used as a platform to construct the auxiliary oscillator. We investigate the parallel scheme where the atomic system and GWD are measured simultaneously, being connected by means of entangled state of light. The *virtual rigidity* method is proposed and analyzed to resolve the difficulties, when matching the spectral responses of the spin oscillator and the GWD. The limitations of this technique along with the detrimental impact of optical losses and the finite degree of correlations between entangled optical modes are covered.

Chapter 3: This part reports the first achievement of the thesis, giving an overview of the experiment, in which the source of EPR-entanglement was built and characterized. First, the criteria of the entanglement are detailed. Then we explore the equations of motion for an optical cavity with a non-linear medium inside and arrive at a mathematical expression that predicts the level of interbeam correlations in the presence of optical losses and phase noise. Next, we give the description of the experimental setup and explain the motivation behind the choice of the optical parametric oscillator (OPO) design and the detection scheme used in the protocol. Calibrations of pump threshold power and escape efficiency are demonstrated. We then discuss the low-frequency homodyne detection setup. The special attention is paid to the phase locking scheme for the two-mode entangled state of light, which is more sophisticated compared to the control of a single-mode squeezing. Finally, the two-mode squeezing in amplitude and phase light quadratures is measured. It is used to verify EPR-steering and Duan criteria and confirm the entanglement. We also outline the upgrade of the phase locking scheme and stabilization of the cavity length using optical fields detuned from fundamental frequencies of the OPO. After having the new scheme implemented and applied to the OPO, we envision the extension of EPR correlation further down into the acoustic frequency range.

Chapter 4: This chapter describes the second main experimental result of this thesis that is the preparation of the spin oscillator. We review the mathematical model and start with the spin polarized ensemble of atoms in an external magnetic field, followed by the interplay with a probe optical field in a reference framework of Faraday interaction. The impact of alignment spin operators due to the tensor interaction is also addressed. Next, we perform the experimental characterization. In particular, we focus on coherently induced Faraday rotation (CIFAR) and magneto-optical resonance spectroscopy (MORS) techniques to estimate the atomic readout rate and the quality of the coherent spin state, respectively. The mitigation and characterization of broadband noise was carried out as well. Thus, we address each source of noise contributing to the total noise budget. We proceed to explore the spin noise spectra, scanning the atomic resonance frequency from MHz range towards audioband. We witness a significant impact of the quantum back action noise on the atomic response across the whole spectral range. However, when acoustic frequencies are approached, quantum noise contributions cease to be dominant, as manifested in the decline of the probe light squeezing induced by the spin oscillator. This is attributed to the technical noise or/and the dynamics of the spin alignment operators. Finally, the downshift of the effective spin

resonance frequency arising from the *virtual rigidity* phenomenon is experimentally demonstrated.

Chapter 5: We continue discussing the performance of the hybrid system consisting of the atomic spin ensemble coupled to the EPR-entangled state of light from the theoretical point of view. In particular, we envision that the experimental setup presented in this thesis is suitable for the reduction of quantum noise of light in the kHz range. Instead of calculating the sensitivity improvement of a 'fictitious' GWD interferometer combined with spin oscillator as done in chapter 2, we now consider the conditional two-mode squeezed state of light, where the phase of one quadrature is rotated due to the interaction with the atomic ensemble. Such a language allows for building an analogy with the frequency-dependent single-(two-) mode squeezing generated by means of a filtering cavity, presented in chapter 1.

List of publications

Peer-reviewed articles:

- Tulio Brito Brasil, Valeriy Novikov, Hugo Kerdoncuff, Mikael Lassen and Eugene S. Polzik. Two-colour high-purity Einstein-Podolsky-Rosen photonic state. *Nature Communications.* **13**, 4815 (2022).
- Jun Jia, Valeriy Novikov, Tulio Brito Brasil, Emil Zeuthen, Jörg Helge Müller, Eugene S. Polzik. Acoustic frequency atomic spin oscillator in the quantum regime. *Nature Communications.* **14**, 6396 (2023).

Conference posters:

- Valeriy Novikov, Tulio Brito Brasil, Hugo Kerdoncuff, Mikael Lassen, and Eugene S. Polzik, "Two-color high-purity entanglement," in Conference on Lasers and Electro-Optics, Technical Digest Series (Optica Publishing Group, 2022), paper JW3B.131

Contents

Chapter 1

Detection of gravitational waves using laser interferometry

1.1 Introduction. Operating principles of contemporary GWDs

General relativity predicts that energy-mass density fluctuations generate gravitational radiation. This phenomenon manifests as a perturbation of the space-time itself [1]. Consequently, the gauging of such space modulation provides an opportunity to detect gravitational waves. The amplitudes of gravitational waves arising due to the most powerful astrophysical events when reaching the vicinity of our solar system are expected to be extremely small [2]. Direct detection of gravitational waves requires measurements with unprecedented precision, implying complex scientific and engineering challenges.

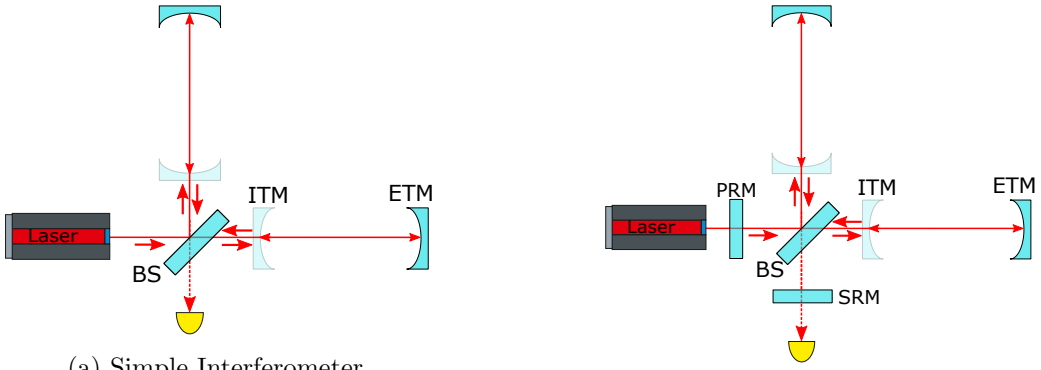

(a) Simple Interferometer.

(b) Advanced LIGO (simplified).

Figure 1.1: Simplified schematics of GWDs in laser Michelson interferometer configuration. **(a)**: The end test mass (ETM) mirror together with the input test mass (ITM) mirror form a Fabri-Perot cavity in each arm of the interferometer. **(b)**: Dual-recycled Fabry-Perot Michelson Inteferometer used in Advanced LIGO [3]. Inclusion of the power recycling mirror (PRM) allows for increasing the intensity of circulating laser radiation. The bandwidth of the interferometer is controlled by the signal recycling mirror (SRM).

Ground-based Gravitational Wave Detectors (GWDs) in laser Michelson interferometer configuration were shown to be one of the most promising candidates for that task [4]. This type of GWDs has significant advantages over other types: their scalability allows for an increase in signal-to-noise ratio, and they have wide operational bandwidth in comparison to Weber bar detector type that relies upon resonant detection [5]. When passing some localized area, gravitational waves modulate the relative motion of free falling bodies. The underlying idea of interferometric GWDs is to record the impact of such perturbation onto interference pattern change that can be directly measured. The laser radiation serves as a probing instrument for test mirrors that play the role of free mass objects. The approximation of free mass motion is valid since the mechanical resonance frequency of suspended mirrors $\Omega_M \approx 1$ Hz and their decay rate γ_M are significantly smaller than the lower edge of the spectral range of interest [6].

The simplified scheme of an interferometric GWD is presented in Figure 1.1(a). Upon entering the interferometer, a strong laser light is spatially split on a symmetric beamsplitter (BS). The two parts travel in orthogonal directions and reflect from two end test mass (ETM) mirrors. The interferometer is adjusted in such a way that the reflected fields interfere destructively at the output port (referred to as 'dark port'). The arrival of gravitational waves creates a space strain, leading to the relative change of arm lengths. Therefore, the condition for the destructive interference on the dark port is not fulfilled anymore, which allows the detection of gravitational waves.

Here we briefly summarize the basic operational principles of interferometric GWDs. First, we specify that setting the 'dark fringe' configuration is a crucial point of the scheme because the signal-to-(shot) noise ratio is maximized when the phase difference between the two arms is π [7]. In addition, the destructive interference at the output port allows to remove the classical noise from the laser. Next, the large length of the arms enhances the gravitational wave tidal force acting on the ETM mirrors. The inclusion of the input test mass (ITM) mirrors, as displayed in Figure 1.1(a), forms a Fabry-Perot cavity in each arm. It leads to an increased storage time of light in the arms and enables the accumulation of a higher signal phase shift. Figure 1.1(b) shows an 'advanced' interferometer design [3]. The circulating optical power is boosted by adding a power recycling mirror (PRM) into the input interferometer port. Signal recycling mirror (SRM) in combination with ITM forms a signal recycling cavity (SRC) and improves the extraction of the gravitational wave signal.

Advances in developments of the Michelson type laser GWD design resulted in the emergence of detectors whose peak strain sensitivity exceeds $10^{-23}\sqrt{\mathsf{Hz}}$ [8, 9]. Such progress has made it possible to directly detect gravitational waves due to the merging of a pair of black holes [10], and the collision of two neutron stars [11]. However, the sensitivity must be enhanced even further in order to get access to a wider range of cosmic events. It implies that various sources of noise must be eliminated. Within the last decades, significant progress has been made toward the reduction of thermal noise, Newton noise, and seismic noise. On the other hand, further development in this direction brings us to the level where the quantum noise is becoming a bottleneck in the next generations of GWDs. Quantum noise in the Michelson laser interferometer configuration of GWDs is the main subject of this chapter and this thesis in general.

1.2 Quantum noise in GWDs

We investigate the Fabry-Perot Michelson (FPM) configuration of interferometers, where the ITM mirrors together with the ETM mirrors constitute cavities with bandwidth γ_L. Since interferometric GWDs operate in the dark fringe configuration, the quantum noise originates from the quantum vacuum penetrating through the dark port [7, 12]. The following system of quantum Langevin equations describes the interaction[1] between the intracavity optical mode $\{\hat{x}_L, \hat{p}_L\}$ and the differential mechanical mode of the test mass mirrors $\{\hat{x}_M, \hat{p}_M\}$ [13]

$$\frac{d}{dt}\hat{x}_L = -\frac{\gamma_L}{2}\hat{x}_L + \sqrt{\gamma_L}\hat{x}_{L,in}, \tag{1.1a}$$

$$\frac{d}{dt}\hat{p}_L = -\frac{\gamma_L}{2}\hat{p}_L + \sqrt{\gamma_L}\hat{p}_{L,in} - \mu\hat{x}_M, \tag{1.1b}$$

$$\frac{d}{dt}\hat{x}_M = -\gamma_M\hat{x}_M + \Omega_M\hat{p}_M + \sqrt{\gamma_M}\hat{x}_{M,in}, \tag{1.1c}$$

$$\frac{d}{dt}\hat{p}_M = -\gamma_M\hat{p}_M - \Omega_M\hat{x}_M + \sqrt{\gamma_M}\hat{p}_{M,in} - \mu\hat{x}_L - k\frac{d^2h}{dt^2}, \tag{1.1d}$$

where $\mu = (\alpha_0/L)\sqrt{\omega_0/(2M\Omega_M)}$ determines an opto-mechanical interaction strength, $\alpha_0 = \sqrt{I}$ and ω_0 is the (coherent state) amplitude and the frequency of the optical field circulating in the interferometer, I is the intensity, L is the length of arms cavities, M is the mass of ETM mirrors. The set $\{\hat{x}_{L,in}, \hat{p}_{L,in}\}$ describes the optical mode on the input of the interferometer, whereas $\{\hat{x}_{M,in}, \hat{p}_{M,in}\}$ correspond to the intrinsic thermal noise attributed to the mechanical mode. The last term on the right-hand side of eq.(1.1d) represents the acceleration of the mirror

[1] Operators $\hat{x}_M$ and $\hat{p}_M$ correspond to $X_M\sqrt{(2\hbar)/(M\Omega_M)}$ and $P_M/\sqrt{1/(2\hbar M\Omega_M)}$, where X_M and P_M are position and momentum of the mirror. Observables $\hat{x}_L$ and $\hat{p}_L$ represent the quadratures of the optical field defined according to two-photon formalism (see section 1.3.1). Indices 'L' and 'M' denote 'light' and 'mechanics' (test mass mirror) respectively.

produced by the transient gravitational wave, where h is the fractional change of the interferometer arms. The gravitational 'tidal' force thus couples to the mechanical motion via the coefficient $k = L\sqrt{M/(2\hbar\Omega_M)}$. The solution of eqs.(1.1c),(1.1d) in the Fourier domain can be written in the form

$$\hat{x}_M = \chi_M(\Omega)\left(-\mu\hat{x}_L + \Omega^2 k h(\Omega) + \sqrt{\gamma_M}\left(\frac{i\Omega+\gamma_M}{\Omega_M}\hat{x}_{M,in} + \hat{p}_{M,in}\right)\right). \tag{1.2}$$

The Fourier frequency Ω and the susceptibility function

$$\chi_M(\Omega) = \frac{\Omega_M}{\Omega_M^2 - \Omega^2 - i\gamma_M\Omega + (\gamma_M/2)^2} \tag{1.3}$$

were introduced in eq.(1.2). Later, we will be using the approximation $\chi_M(\Omega) \approx -\Omega_M/\Omega^2$, which works well in the limit $\Omega \gg \Omega_M, \gamma_M$. We will also neglect the intrinsic thermal fluctuations (terms $\propto \hat{x}_{M,in}, \hat{p}_{M,in}$) in the mechanical mode in eq.(1.2) for simplicity since they can be reduced to such extent that they become negligible in comparison to the contribution from other terms[2]. Substituting eq.(1.2) into eq.(1.1b), one obtains the following expression for the optical mode $\hat{p}_{L,out} = \hat{p}_{L,in} - \sqrt{\gamma_L}\hat{p}_L$ exiting the interferometer

$$\hat{p}_{L,out} = \frac{\gamma_L + i\Omega}{\gamma_L - i\Omega}\hat{p}_{L,in} + \frac{\mu^2\chi_M}{(\gamma_L - i\Omega)^2}\hat{x}_{L,in} + \frac{k\mu\Omega^2\chi_M}{\gamma_L - i\Omega}h(\Omega). \tag{1.4}$$

As can be seen from eq.(1.4), $\hat{p}_{L,out}$ consists of three terms. The first term $\propto \hat{p}_{L,in}$ describes fundamental phase fluctuations shot noise (SN - also referred to as imprecision noise) translated from the out-of-phase quadrature of the incoming vacuum state of light. The second term $\propto \hat{x}_{L,in}$ is the source of quantum radiation pressure noise (QRPN), also known as Quantum Back Action Noise (QBAN), arising due to the opto-mechanical interaction. The last term $\propto h(\Omega)$ is the modulation caused by gravitational waves and is considered as the signal of interest. The input-output relations eq.(1.4) can be rewritten in a more convenient form (more familiar for the GWD community) [7]

$$\hat{p}_{L,out} = e^{2i\beta_{ph}}\left(\hat{p}_{L,in} - K_{FPM}\hat{x}_{L,in}\right) + e^{i\beta_{ph}}\sqrt{2K_{FPM}}\frac{h(\Omega)}{h_{SQL}}, \tag{1.5}$$

where $\beta_{ph} = \arctan(\Omega/\gamma_L)$ is the phase acquired by the component of light at the sideband frequency Ω relative to the carrier. The optomechanical coupling factor K_{FPM} and the expression h_{SQL} are defined as

$$h_{SQL} = \sqrt{\frac{8\hbar}{ML^2}}\frac{1}{\Omega}; \quad K_{FPM} = K_I\frac{2\gamma_L}{\Omega^2\left(\Omega^2+\gamma_L^2\right)} = \frac{K_I}{\Omega^2}K_{0I}, \quad K_{0I} = \frac{2\gamma_L}{\Omega^2+\gamma_L^2}, \quad K_I = \frac{4I_0\Omega_0}{M\gamma_L L^2}, \tag{1.6}$$

where the index 'FPM' signifies that we study the case of the Fabry-Perot Michelson interferometer. Both frequency independent (K_I) and frequency dependent parts of the coupling factor may vary for different configurations of GWDs [7, 9]. However, the term $1/\Omega^2$ in K_{FPM} is always present, referring to the approximation of free mass motion, which is valid under the conditions Ω_M,$\gamma_M \ll \Omega$. For the Fourier frequencies well within the cavity linewidth $\Omega \ll \gamma_L$ we obtain $K_{0I} \to 2/\gamma_L = \text{const}$, and the coupling factor $K_{FPM} \propto 1/\Omega^2$ looks similar to the coupling factor in the case of a simple Michelson interferometer. Normalizing quantum noise eq.(1.5) by the signal, we introduce the strain equivalent noise operator $\hat{h}$ for the phase quadrature

$$\hat{h}_n(\Omega) \equiv \hat{h}_n|_{\hat{p}_{L,out}} = \frac{h_{SQL}}{\sqrt{2K_{FPM}}}\left(\hat{p}_{L,in} - K_{FPM}\hat{x}_{L,in}\right) \tag{1.7}$$

and calculate[3] its power spectral density (PSD) using $S_h = \langle in|\,\hat{h}_n^\dagger\hat{h}_n\,|in\rangle$. The quantum state at the dark port is the vacuum $|in\rangle = |0\rangle$, therefore

$$S_h|_{\hat{p}_{L,out}} = \frac{h_{SQL}^2}{2}\cdot\left(\frac{1}{K_{FPM}} + K_{FPM}\right). \tag{1.8}$$

The result obtained above is valid when the measurement is performed on the phase quadrature of the output light $\hat{p}_{L,out}$.

[2] It is the relevant assumption for "quantum noise limited GWD interferometers"

[3] Here and further in the thesis the expressions for the PSD of the strain sensitivity are obtained after implementing the symmetrization of the operator expectations [7].

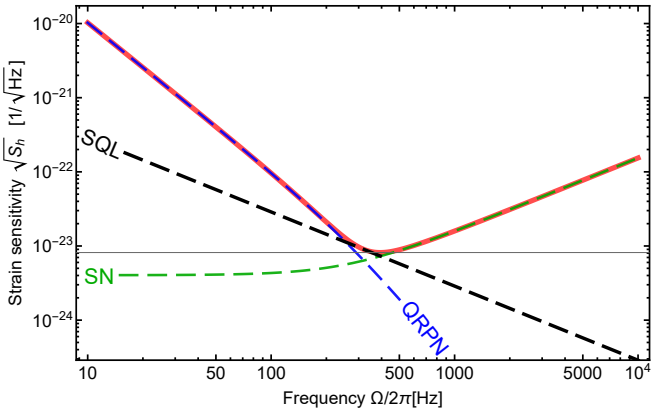

(a) The red solid curve represents the strain sensitivity for the following set of parameters: $M = 40$ kG, $L = 4$ km, $I = 5$ kW, $\gamma_L = 220$ Hz [9]. The individual contributions from shot noise (SN, dashed green line) and quantum radiation pressure noise (QRPN, dashed blue line) are also shown.

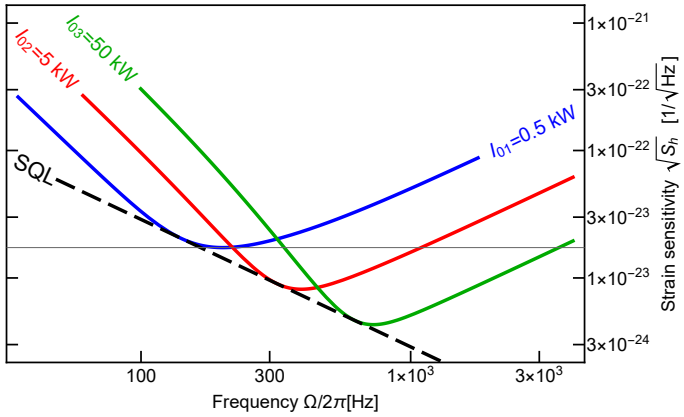

(b) Effect of varying circulating power I is demonstrated. In particular, the SQL is achieved at different Fourier frequencies, representing "displacement" along the SQL curve.

Figure 1.2: The spectra of strain sensitivity $\sqrt{S_h|_{\hat{p}_{L,out}}}$ for the GWD (Fabry-Perot Michelson interferometer). The standard quantum limit (SQL) is shown as a black curve.

The total strain-equivalent quantum noise spectrum is presented in Figure 1.2(a). We now consider the behavior of QRPN and SN as a function of Fourier frequency. While shot noise itself is flat, the amplitude of the signal degrades beyond the operational bandwidth γ_L of the arm cavities as follows from the term K_{OI} in the optomechanical coupling factor K_{FPM}. Hence, $S_h|_{\hat{p}_{L,out}}$ rolls up at high frequencies Ω. In contrast, QRPN dominates at low frequencies, being driven by the dependence of K_{FPM} on the frequency.

Eq.(1.7) indicates the limit of maximum achievable sensitivity arising from the Heisenberg uncertainty principle. This limit, also known as the Standard Quantum Limit (SQL), is expressed by the term h_{SQL} in eq.(1.6). The sensitivity reaches the SQL at a certain Fourier frequency, which yields $K_{FPM} = 1$, corresponding to equal contributions from SN and QRPN. Thus, the optimal Fourier frequency for the reduction of the total quantum noise is determined by the selected set of the parameters of a GWD (for example, the effect of variation of an injected optical power is shown in Figure 1.2(b)). Ultimately, the reduction of SN inevitably enhances the contribution from QRPN and vice versa. Therefore, for a given interferometer geometry and magnitude of test masses, the SQL can not be surpassed by simply adjusting the laser power.

1.3 Overcoming quantum noise

There exist several strategies that can reduce the quantum noise in the detection of gravitational waves below the SQL. One class of such strategies relies on amplitude-phase correlations introduced between the quadratures of light before or after the interforometer. Another approach is to modify the susceptibility function (frequency response) of interferometer. These techniques will be reviewed in the next subsections.

1.3.1 Non-classical states of light

Non-classical squeezed states of light play an important role in the schemes of sensitivity improvement of interferometric GWDs. We describe this type of quantum states using two-photon formalism [14]. We define the quadrature operators $\hat{x}_L$, $\hat{p}_L$ of an optical mode (they were used in eq.(1.1) to describe an optomechanical interaction) by means of the creation/annihilation operators of photons $\hat{a}_{L,+}$ and $\hat{a}_{L,-}$ on a sideband frequencies Ω with respect to the carrier frequency ω_0:

$$\hat{x}_L = \frac{\hat{a}_{L,+} + \hat{a}^\dagger_{L,-}}{\sqrt{2}}, \quad \hat{p}_L = \frac{\hat{a}_{L,+} - \hat{a}^\dagger_{L,-}}{\sqrt{2}i}, \tag{1.9}$$

where $\hat{a}_{L,\pm}$ are introduced as

$$\hat{a}_{L,+} = \sqrt{\frac{\omega_0 + \Omega}{\omega_0}}\hat{a}_{L,\omega_0+\Omega}, \quad \hat{a}_{L,-} = \sqrt{\frac{\omega_0 - \Omega}{\omega_0}}\hat{a}_{L,\omega_0-\Omega}. \tag{1.10}$$

An arbitrary quadrature in the phase space is now determined as $\hat{q}_L(\zeta) = \cos(\zeta)\hat{p}_L + \sin(\zeta)\hat{x}_L$. The input-output relations for an interferometer may be obtained in a form eq.(1.5) using quadratures defined according to eq.(1.9) (see, for example, [7]).

Single mode squeezed states of light

The parametric interaction $\omega_P = 2\omega_0 \leftrightarrow \omega_0 + \omega_0$, which corresponds to creation of photon pair at frequency ω_0 while pump photon is absorbed and vice versa, is described by Hamiltonian:

$$\hat{H}_{int} \propto i\hbar g \left(\hat{a}_{L,P}\hat{a}^\dagger_{L,+}\hat{a}^\dagger_{L,-} - \hat{a}^\dagger_{L,P}\hat{a}_{L,+}\hat{a}_{L,-}\right), \tag{1.11}$$

where $\hat{a}_{L,P}$ is the annihilation operator of the field at the pump frequency ω_P and $\hat{a}_{L,\pm}$ are defined in eq.(1.10). Assuming that the drive field is in a strong coherent state that is not getting depleted, one can use the approximation, where the operator $\hat{a}_{L,P}$ is substituted with it's coherent amplitude $\alpha_{L,P}$. Such parametric interaction transforms the fields $\hat{a}_{L,+,in}$, $\hat{a}_{L,-,in}$ according to:

$$\hat{a}_{L,+} = \cosh(r)\hat{a}_{L,+,in} + \sinh(r)\hat{a}^\dagger_{L,-,in}, \tag{1.12a}$$
$$\hat{a}_{L,-} = \cosh(r)\hat{a}_{L,-,in} + \sinh(r)\hat{a}^\dagger_{L,+,in}, \tag{1.12b}$$

leading to the reduction of noise in amplitude quadrature $\hat{x}_L$ and the enhancement of the noise in the orthogonal quadrature $\hat{p}_L$:

$$\hat{x}_L = e^{-r}\hat{x}_{L,in} \tag{1.13a}$$
$$\hat{p}_L = e^{+r}\hat{p}_{L,in} \tag{1.13b}$$

A squeezed state of vacuum can be described as as an initial vacuum state transformed by the (single mode) squeezing operator $\hat{S}(r,\phi)$:

$$|sq\rangle = \hat{S}(r,\phi)|0\rangle \tag{1.14}$$

where $\hat{S}(r,\phi)$ is given by

$$\hat{S}(r,\phi) = \exp\left[r(\hat{a}_{L,+}\hat{a}_{L,-}e^{-2i\phi} - \hat{a}^\dagger_{L,+}\hat{a}^\dagger_{L,-}e^{2i\phi})\right], \tag{1.15}$$

where $r > 0$ and ϕ are the amplitude and the phase of squeezing. The case $\phi = 0$ corresponds to amplitude squeezed vacuum with squeezed canonical position $\hat{x}_L$ and excessive noise in the canonical momentum as considered in eq.(1.13). If $\phi = \pi/2$, then the phase quadrature $\hat{p}_L$ becomes maximally squeezed such that $\hat{p}_L = e^{-r}\hat{p}_{L,in}$, $\hat{x}_L = e^r\hat{x}_{L,in}$.

Two-mode squeezed vacuum

We next consider the parametric interaction in the form of eq.(1.11), but created/annihilated pairs of photons have now different frequencies. In particular, the pump photon $\omega_P = 2\omega_0 + \Delta$ is split onto 'signal' ($\omega_s = \omega_0$) and 'idler' ($\omega_i = \omega_0 + \Delta$) photons[4], fulfilling the condition of energy conservation $\omega_P = \omega_s + \omega_i$. The interaction Hamiltonian is given by

$$\hat{H}_{int} \propto i\hbar g \left[\left(\alpha_{L,P}\hat{a}^\dagger_{L,s+}\hat{a}^\dagger_{L,i-} - \alpha^*_{L,P}\hat{a}_{L,s+}\hat{a}_{L,i-}\right) + \left(\alpha_{L,P}\hat{a}^\dagger_{L,s-}\hat{a}^\dagger_{L,i+} - \alpha^*_{L,P}\hat{a}_{L,s-}\hat{a}_{L,i+}\right)\right], \tag{1.16}$$

[4]signal and idler optical modes will be later interacting with test mass mirror 'M' and atomic spin system 'S' respectively

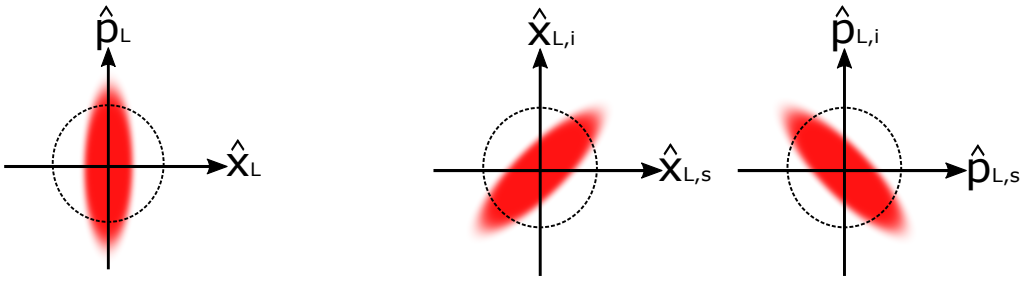

(a) A single-mode squeezed vacuum (example of amplitude squeezing).

(b) A two-mode squeezed state of vacuum.

Figure 1.3: Squeezed states of light in the phase space.

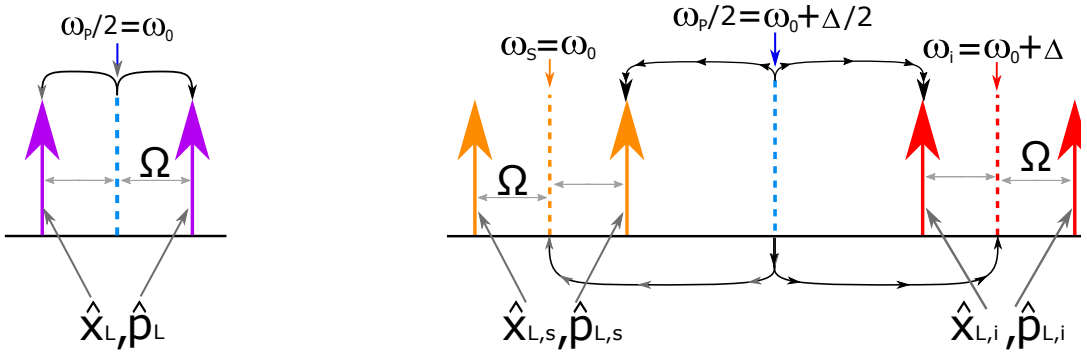

Figure 1.4: Single-mode and two-mode squeezed states (left and right parts, respectively) are viewed as entanglement between sidebands in two-photon formalism.

where, according to eq.(1.9), $\hat{a}_{L,s\pm} \propto \hat{a}_{L,\omega_0\pm\Omega}$ and $\hat{a}_{L,i\pm} \propto \hat{a}_{L,\omega_0+\Delta\pm\Omega}$ respectively. Thus, we introduced four sidebands around $\pm\Omega$ both for signal and idler central frequencies. Following the same procedure outlined in the previous section for single mode squeezed states, we define $\hat{a}_{L,s\pm,in}$ and $\hat{a}_{L,i\pm,in}$ that are associated with signal/idler modes before parametric interaction. The evolution driven by the Hamiltonian eq(1.16) leads to the transformation:

$$\hat{a}_{L,s+} = \cosh(r)\hat{a}_{L,s+,in} + \sinh(r)\hat{a}^{\dagger}_{L,i-,in}, \tag{1.17a}$$

$$\hat{a}_{L,s-} = \cosh(r)\hat{a}_{L,s-,in} + \sinh(r)\hat{a}^{\dagger}_{L,i+,in}, \tag{1.17b}$$

$$\hat{a}_{L,i+} = \cosh(r)\hat{a}_{L,i+,in} + \sinh(r)\hat{a}^{\dagger}_{L,s-,in}, \tag{1.17c}$$

$$\hat{a}_{L,i-} = \cosh(r)\hat{a}_{L,i-,in} + \sinh(r)\hat{a}^{\dagger}_{L,s+,in}. \tag{1.17d}$$

In a result, the lower sideband of the signal field at the frequency $\omega_s - \Omega$ is now correlated with higher sideband of the idler field at the frequency $\omega_i + \Omega$ and vice versa. In general, it applies to any pair of frequencies symmetric relative to $\omega_P/2 = \omega_0 + \Delta/2$. Next, we introduce the canonical position and momentum operators for signal/idler modes before/after parametric interaction $\hat{x}_{L,s(i)}$, $\hat{p}_{L,s(i)}$, $\hat{x}_{L,s(i),in}$ and $\hat{p}_{L,s(i),in}$ as it was done in eq.(1.9). One can see that while input optical fields are completely independent, the amplitude quadratures $\hat{x}_{L,s}$, $\hat{x}_{L,i}$ become correlated, whereas the phase quadratures $\hat{p}_{L,s}$, $\hat{p}_{L,i}$ are anticorrelated:

$$\hat{x}_{L,s} \mp \hat{x}_{L,i} = e^{\mp r}\left(\hat{x}_{L,s,in} \mp \hat{x}_{L,i,in}\right), \tag{1.18a}$$

$$\hat{p}_{L,s} \pm \hat{p}_{L,i} = e^{\mp r}\left(\hat{p}_{L,s,in} \pm \hat{p}_{L,i,in}\right). \tag{1.18b}$$

In terms of PSD this might be written as:

$$S_{\frac{1}{\sqrt{2}}(\hat{x}_{L,s,in}\mp\hat{x}_{L,i,in}),\frac{1}{\sqrt{2}}(\hat{x}_{L,s,in}\mp\hat{x}_{L,i,in})}=1, \qquad S_{\frac{1}{\sqrt{2}}(\hat{x}_{L,s}\mp\hat{x}_{L,i}),\frac{1}{\sqrt{2}}(\hat{x}_{L,s}\mp\hat{x}_{L,i})}=e^{\mp 2r}, \tag{1.19a}$$

$$S_{\frac{1}{\sqrt{2}}(\hat{p}_{L,s,in}\pm\hat{p}_{L,i,in}),\frac{1}{\sqrt{2}}(\hat{p}_{L,s,in}\pm\hat{p}_{L,i,in})}=1, \qquad S_{\frac{1}{\sqrt{2}}(\hat{p}_{L,s}\pm\hat{p}_{L,i}),\frac{1}{\sqrt{2}}(\hat{p}_{L,s}\pm\hat{p}_{L,i})}=e^{\mp 2r}, \tag{1.19b}$$

where, for example, $S_{\hat{x}_{L,s}\hat{x}_{L,s}} =< \Delta\left(\hat{x}_{L,s}\right)^2 >$. Measuring the difference of the amplitude quadratures and the sum of the phase quadratures, we would observe the reduction of the fluctuations in comparison to independent vacuum fields, at the cost of increased noise in sum of amplitude/difference of phase quadratures due to the Heizenberg uncertainty principle. This feature can be seen if one compares the wave functions of two mode vacuum state in position and momentum representations:

$$\psi_{00}(x_{L,s},x_{L,i})=\frac{1}{\sqrt{\pi}}\exp\left[\frac{-x_{L,s}^2}{2}\right]\exp\left[\frac{-x_{L,i}^2}{2}\right]=\frac{1}{\sqrt{\pi}}\exp\left[\frac{-\left(x_{L,s}-x_{L,i}\right)^2}{4}\right]\exp\left[\frac{-\left(x_{L,s}+x_{L,i}\right)^2}{4}\right], \tag{1.20a}$$

$$\tilde{\psi}_{00}(p_{L,s},p_{L,i})=\frac{1}{\sqrt{\pi}}\exp\left[\frac{-p_{L,s}^2}{2}\right]\exp\left[\frac{-p_{L,i}^2}{2}\right]=\frac{1}{\sqrt{\pi}}\exp\left[\frac{-\left(p_{L,s}-p_{L,i}\right)^2}{4}\right]\exp\left[\frac{-\left(p_{L,s}+p_{L,i}\right)^2}{4}\right] \tag{1.20b}$$

with the wave functions of two mode squeezed state

$$\psi_R(x_{L,s},x_{L,i})=\frac{1}{\sqrt{\pi}}\exp\left[-\left(\frac{e^{2r}}{4}\right)\left(x_{L,s}-x_{L,i}\right)^2\right]\exp\left[-\left(\frac{e^{-2r}}{4}\right)\left(x_{L,s}+x_{L,i}\right)^2\right], \tag{1.21a}$$

$$\tilde{\psi}_R(p_{L,s},p_{L,i})=\frac{1}{\sqrt{\pi}}\exp\left[-\left(\frac{e^{2r}}{4}\right)\left(p_{L,s}+p_{L,i}\right)^2\right]\exp\left[-\left(\frac{e^{-2r}}{4}\right)\left(p_{L,s}-p_{L,i}\right)^2\right]. \tag{1.21b}$$

Such states are named as two mode squeezed vacuum (TMSV) or the twin-beam state [15]. Any observable of single mode of TMSV has the variance

$$S_{\hat{x}_{L,s},\hat{x}_{L,s}}=S_{\hat{x}_{L,i},\hat{x}_{L,i}}=S_{\hat{p}_{L,s},\hat{p}_{L,s}}=S_{\hat{p}_{L,i},\hat{p}_{L,i}}=\frac{1+e^{4r}}{2e^{2r}}>1, \tag{1.22}$$

corresponding to the thermal state where the noise exceeds the vacuum noise and grows up with increase of r. The Wigner function of TMSV is given by the expression:

$$\begin{aligned}W(x_{L,s},x_{L,i},p_{L,s},p_{L,i})=\frac{1}{\pi}\exp\left[-\left(\frac{e^{2r}}{4}\right)\left(x_{L,s}-x_{L,i}\right)^2+\left(p_{L,s}+p_{L,i}\right)^2\right)\Big]+\\ \times\exp\left[-\left(\frac{e^{-2r}}{4}\right)\left(\left(x_{L,s}+x_{L,i}\right)^2+\left(p_{L,s}-p_{L,i}\right)^2\right)\right].\end{aligned} \tag{1.23a}$$

By analogy with eq.(1.14) and eq.(1.15) one can define a two-mode squeezing operator

$$\hat{S}_{TMSV}(r,\phi)=\exp\left[\left(r^*\hat{a}_{L,s+}\hat{a}_{L,i-}-r\hat{a}_{L,s+}^{\dagger}\hat{a}_{L,i-}^{\dagger}\right)\right] \tag{1.24}$$

that converts a two-mode vacuum state into squeezed:

$$\left|TMSV\right\rangle_{si}=\hat{S}_{TMSV}(r,\phi)\left|00\right\rangle_{si}. \tag{1.25}$$

Since the noise is partially cancelled in the observables $\hat{x}_{L,s}-\hat{x}_{L,i}$ and $\hat{p}_{L,s}+\hat{p}_{L,i}$, we introduce the linear combination $\hat{q}_L^g$ of the quadratures $\hat{q}_{L,s(i)}(\zeta)=\cos\left(\zeta_{s(i)}\right)\hat{p}_{L,s(i)}+\sin\left(\zeta_{s(i)}\right)\hat{x}_{L,s(i)}$:

$$\hat{q}_L^g(\zeta)=\hat{q}_{L,s}(\zeta)+g\hat{q}_{L,i}(-\zeta)=\left(\hat{p}_{L,s}+g\hat{p}_{L,i}\right)\cos\left(\zeta\right)+\left(\hat{x}_{L,s}-g\hat{x}_{L,i}\right)\sin\left(\zeta\right). \tag{1.26}$$

Considering the correlations between output fields according to eq.(1.17) we get a new equation for $\hat{q}^g(\zeta)$:

$$\hat{q}^g_L(\zeta) = (\cosh(r) - g\sinh(r))\,\hat{q}_{L,s,in}(\zeta) + (\sinh(r) - g\cosh(r))\,\hat{q}_{L,i,in}(\zeta). \tag{1.27}$$

We take into account that $S_{\hat{q}_{L,i,in}(\zeta),\hat{q}_{L,i,in}(\zeta)} = S_{\hat{q}_{L,s,in}(\zeta),\hat{q}_{L,s,in}(\zeta)} = 1$, $S_{\hat{q}_{L,s,in}(\zeta),\hat{q}_{L,i,in}(\zeta)} = 0$, obtain the PSD for $\hat{q}^g_L(\zeta)$:

$$S_{\hat{q}^g_L(\zeta)\hat{q}^g_L(\zeta)} = (\cosh(r) - g\sinh(r))^2 + (\sinh(r) - g\cosh(r))^2 \tag{1.28}$$

and perform the optimization of the relative weight g:

$$g_{opt} = \tanh(2r), \quad S_{\hat{q}^g_L(\zeta)\hat{q}^g_L(\zeta)}|_{g=g_{opt}} = \frac{1}{\cosh(2r)}. \tag{1.29}$$

Thus, the optimal relative weight depends on the amplitude of the squeezing (the strength of parametric interaction). In contrast, one can explore the following combination:

$$\hat{q}^{g,N}_L(\zeta) = N\left[\hat{q}_{L,s}(\zeta) + g\hat{q}_{L,i}(-\zeta)\right], \quad N = \left(1+g^2\right)^{-0.5}, \quad S_{\hat{q}^{g,N}_L(\zeta)\hat{q}^{g,N}_L(\zeta)} = \frac{S_{\hat{q}^g_L(\zeta)\hat{q}^g_L(\zeta)}}{1+g^2}. \tag{1.30}$$

In such a case the optimal value for relative weight g is always equal to 1 that yields:

$$S_{\hat{q}^{g,N}_L(\zeta)\hat{q}^{g,N}_L(\zeta)}|_{(g_{opt}=1)} = e^{-2r}, \tag{1.31}$$

which is a direct consequence of eq.(1.19).

1.3.2 Variational readout

We consider the situation when the arbitrary light quadrature $\hat{q}_{L,out}(\zeta)$ is recorded in order to measure the modulation caused by the passage of gravitational waves. The strain equivalent noise operator of GWD is now given by:

$$\hat{h}_n|_{\hat{q}_{L,out}(\zeta)} = \frac{h_{SQL}}{\sqrt{2K_{FPM}}}\left(\hat{p}_{L,in} - \left[K_{FPM} - \cot(\zeta)\right]\hat{x}_{L,in}\right). \tag{1.32}$$

The PSD of the strain sensitivity eq.(1.32) is now a generalized case of eq.(1.8), being written as

$$S_h|_{\hat{q}_{L,out}(\zeta)} = \frac{h^2_{SQL}}{2K_{FPM}} \cdot \left(1 + \left[K_{FPM} - \cot(\zeta)\right]^2\right). \tag{1.33}$$

Figure 1.5 demonstrates that the measurement of the output light quadrature other than $\hat{p}_{L,out}(\zeta)$ can lead to the suppression of quantum noise below the SQL in a narrow band of the frequency spectrum. Moreover, it is possible to totally cancel QRPN by setting $K_{FPM} \equiv K_{FPM}(\Omega) = \cot(\zeta)$ at any Fourier frequency. However, this would require implementing in some way a frequency-dependent detection angle ζ.

This approach can be understood better by invoking the concept of pondermotive squeezing [16]. The initial vacuum state (with no correlations between its quadratures) after interaction with a mechanical oscillator takes the form

$$|out\rangle = \hat{R}(\theta_{1,pond})\hat{S}(r_{pond}, 0)\hat{R}(\theta_{2,pond})\,|in\rangle\,, \tag{1.34}$$

where $\hat{R}(\theta)$ determines the rotation in the phase space and $\hat{S}(r,\phi)$ is defined in eq.(1.15). Therefore, one can see that the initial vacuum state becomes squeezed and experiences a rotation in the phase space. The squeezing factor r_{pond} and angles $\theta_{1(2),pond}$ depend on the optomechanical coupling factor $K_{FPM}(\Omega)$:

$$r_{pond} = \ln\left[\frac{K_{FPM}(\Omega)}{2} + \sqrt{1 + \left(\frac{K_{FPM}(\Omega)}{2}\right)^2}\right], \quad \theta_{1,pond} = -\frac{1}{2}\arctan\left[\frac{K_{FPM}(\Omega)}{2}\right] + \frac{\pi}{4}, \quad \theta_{2,pond} = \theta_{1,pond} - \frac{\pi}{2} \tag{1.35}$$

Fulfilling the requirement $K_{FPM}(\Omega) = \cot(\zeta)$ results in the projection of the observed optical output field onto the axis that corresponds to the maximally squeezed quadrature. Thus, the amplitude-phase correlations $\propto \langle \hat{x}_L \hat{p}_L^+ \rangle$ caused by the pondermotive squeezing are utilized to completely cancel QRPN term, leaving only shot noise (as displayed on Figure 1.5). However, apart from the challenge of implement the required frequency dependence of the homodyne detection angle $\zeta(\Omega)$, such a strategy entails losing the part of the signal $h(\Omega)$ that carries the information about gravitational waves. This happens because the modulation caused by the arrival of gravitational waves is always stored in $\hat{p}_{L,out}$, while the projection onto the axes with minimal quantum noise does not correspond to the detection of the phase optical quadrature. Nevertheless, since a QBAN-free measurement can be accomplished, the signal-to-noise ratio can be improved by increase of the circulating optical power in the interferometer.

The strategy of such *variational readout* was initially conceived in [17] and explored in [16], where a post filtering of the signal was proposed by means of external cavities positioned at the output of the interferometer. In order to practically achieve a reasonable cancellation of QRPN, the homodyne phase angle needs to be controlled with a high precision, meaning stringent requirements for the optoelectronic control of the filter cavities [16].

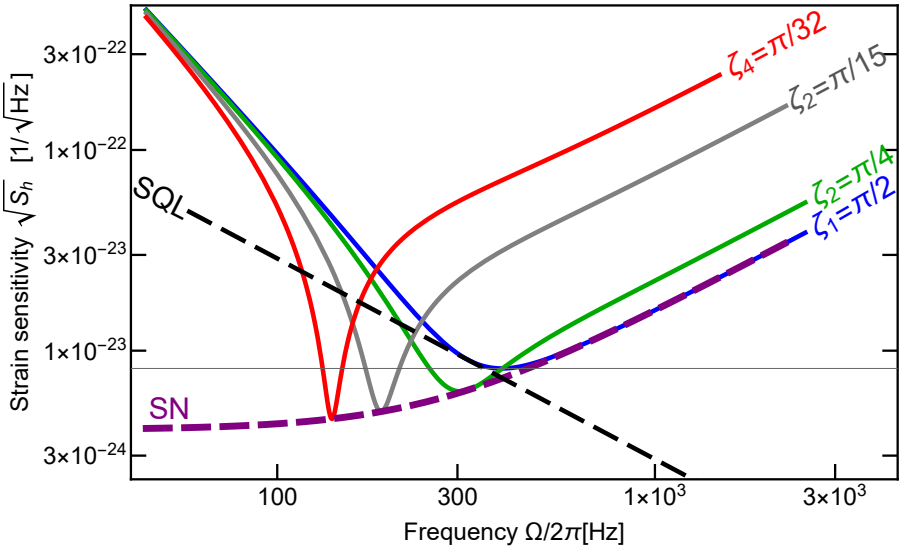

Figure 1.5: Quantum noise spectra at different homodyne detection angle ζ. Once a frequency-dependent homodyne detection angle $\zeta(\Omega)$ =arccot$[K_{FPM}(\Omega)]$ is set, QBAN-free measurement (purple dashed line) is possible.

1.3.3 Injection of frequency-independent squeezing

Instead of changing the quantum state of light, which exits the interferometer (section1.3.2), one can modify it before it enters the GWD. In particular, a vacuum state of light, entering from the dark port of the interferometer, is replaced by a squeezed state. The PSD of of the quantum noise is calculated using expression

$$S_{h_{sq(R,\xi)}}|_{\hat{q}_{L,out}(\zeta)} = \langle in| \, h_n^+ h_n \, |in\rangle \tag{1.36}$$

where $|in\rangle = \hat{S}(R,\xi)\,|0\rangle$ is squeezed state, see eq.(1.14), eq.(1.15). Therefore, the spectrum of $S_{h_{sq(R,\xi)}}|_{\hat{q}_{L,out}}$ is given by:

$$S_{h_{sq(R,\xi)}} = \frac{h_{SQL}^2 \left(e^{-2R} + (1 - \cos\left[2(\xi + \Phi)\right] \sinh\left(2R\right)\right)}{2K_{FPM} \sin^2\left(\Phi\right)}, \tag{1.37}$$

where

$$\cot\left(\Phi\right) = K_{FPM} - \cot\zeta. \tag{1.38}$$

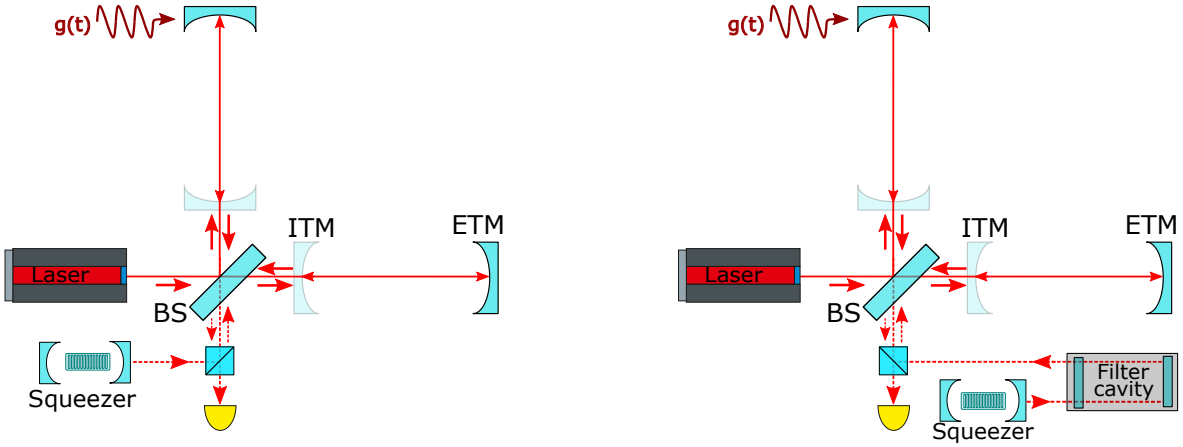

(a) Injection of a squeezed state with the fixed phase.

(b) A squeezing source in combination with a filter cavity producing frequency dependent squeezed state.

Figure 1.6: Configurations of GWDs enhanced by squeezed states of light.

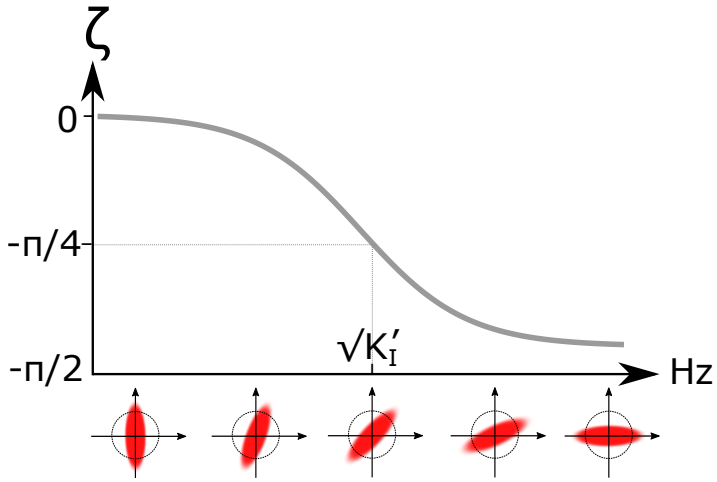

Figure 1.7: The rotation of the quadrature of a single-mode squeezed vacuum state as a function of the frequency Ω required to achieve the broadband quantum noise reduction in GWDs.

Measuring phase quadrature ($\zeta = 0$) and injecting phase squeezed vacuum state $\xi = \pi/2$ gives a particular case of formula eq.(1.37):

$$S_{h_{sq(R,\pi/2)}}|_{\hat{p}_{L,out}} = \frac{h_{SQL}^2}{2} \cdot \left(\frac{1}{K_{FPM} e^{2R}} + K_{FPM} e^{2R} \right). \tag{1.39}$$

Since optomechanical factor K_{FPM} is proportional to the circulating power, the injection of squeezing changes effective value $K'_{FPM} = K_{FPM} e^{2R}$ and hence, effective intensity $I' = I e^{2R}$. In the case of phase squeezed vacuum, the effective intensity increases. This can be used to minimize the negative influence of SN without boosting the actual optical power. However, the reduction of the shot noise is accompanied by an amplification of QRPN contribution at the same time, as can be also seen from eq.(1.39). Opposite effect is observed when amplitude squeezed vacuum enters the dark port of the interferometer. QRPN term is decreased at the price of amplified SN. Ultimately, in both cases the SQL can be only reached, but can not be surpassed, as demonstrated in Figure 1.8. However, sending a squeezed state of light with squeezed quadrature set by the phase $\xi = \pi/4$ allows to beat the SQL in a narrrow frequency range, paying the price of the deteriorated sensitivity beyond this range. Such effect appears due to inducing of amplitude-phase cross-correlations.

To the best of knowledge of the author, the QRPN is not yet the main limitation for the sensitivity of

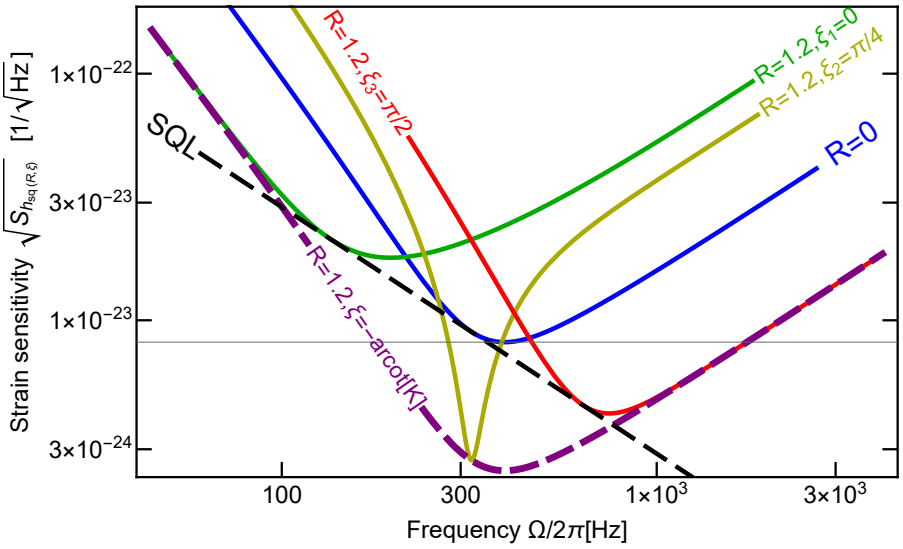

Figure 1.8: Comparison of quantum noise spectra without and with injected squeezed vacuum with different squeezing angles, when the phase quadrature $\hat{p}_{L,out}$ is detected. While the injection of pure phase-(amplitude-) squeezed vacuum leads to effective increase (reduction) of power, the squeezing with $\xi = \pi/4$ allows for beating of the SQL within a narrow spectral range at the cost of a sensitivity reduction in the high and low frequency limits. The sensitivity performance when using the squeezing with the optimal frequency-dependent angle is shown by the dashed purple line.

contemporary GWDs, since the ubiquitous technical noise dominates in low spectral range. The calibration of QRPN was reported in [18], where (frequency independent) squeezed vacuum state has been injected. The reduction of SN by means of squeezed light was performed in [19], [20] and [21]. Micromechanical resonators were utilized to measure [22] and manipulate QRPN in MHz [23] and audio-frequency range [24].

1.3.4 Injection of frequency-dependent squeezing

Unlike the squeezed light with fixed squeezing quadrature, the injection of frequency dependent squeezed states of vacuum can help to reach the broadband sensitivity improvement beyond the SQL. If the the phase of squeezing $\xi_{rot} = \xi_{rot}(\Omega)$ is a function of Fourier frequency such that $\cot[\xi_{rot}(\Omega)] = -K_{FPM}(\Omega)$ is fulfilled, the expression eq.(1.37) for the strain referenced sensitivity takes the form

$$S_{h_{sq(R,\xi_{rot})}}|_{\hat{p}_{L,out}} = \frac{h_{SQL}^2}{2} \cdot \left(\frac{1}{K_{FPM}} + K_{FPM} \right) e^{-2R}. \tag{1.40}$$

As a result, both SN and QRPN are suppressed simultaneously, and the quantum noise reduction is constrained only by factor of squeezing R, as shown in Figure 1.8.

One proposal to impart the frequency dependent rotation in phase space relies on the interaction of squeezed state with a filter cavity prior to injecting it into the interferometer [16]. As shown in [6], the reflection from a detuned resonator changes quadrature phase angle ζ_f of the optical field according to

$$\xi_f(\Omega) = \text{Arccot}\left[\frac{2\delta_f \gamma_f}{\gamma_f^2 - \delta_f^2 + \Omega^2} \right], \tag{1.41}$$

where γ_f is the bandwidth of filter cavity and δ_f is the detuning of the optical carrier frequency from the cavity resonance. If the detuning $\delta_f = \gamma_f$ is selected, the dependences of ξ_f and coupling factor K_{FPM} (given by eq.(1.6)) in the limit $\Omega \ll \gamma_L$ on the frequency Ω match each other. The role of the filter cavity is to produce such a rotation of squeezing that cancels the effect of pondermotive squeezing caused by an optomechanical interaction with the test mass mirror. Post-filtering resonators in sec.1.3.2 operate on a similar principle. In general case, a cascade

of N cavities is required to set the dependence of quadrature phase angle ζ_f on the Fourier frequency, where the highest power of Ω in numerator and denominator is $2N$ [6]. Therefore, to rigorously counterbalance the effect of the pondermotive squeezing for FPM configuration, at least two resonators will be needed.

The experimental demonstration of a frequency dependent rotation of the squeezing angle in the frequency range $\Omega \approx 1$ kHz using a 2-meter rigid filtering resonator was reported in [25]. The exploitation of a 300-m suspended filter cavity allowed to generate the frequency dependent squeezing suitable for a broadband quantum noise reduction below 100 Hz in KAGRA, advanced LIGO and advanced VIRGO [26]. Experimental challenges for implementation of the frequency dependent squeezing injection are similar to the complications related to *variational readout* proposal [27], mainly caused by necessity to operate a long baseline optical resonator with extremely low losses in order to provide a narrow linewidth. The performance of frequency dependent squeezing in [26, 25] is also limited by phase noise and mode mismatching.

1.3.5 Conditional squeezing using EPR entanglement

The strategy reviewed in this subsection is an alternative interpretation of the previous approach. Namely, the frequency dependent phase rotation of the probe optical field due to quantum back action is now compensated without involving an external cavity. The interferometer itself serves as such a pre-filtering resonator, and injected single mode squeezing is replaced by the Enstein-Podolsky-Rosen (EPR) entangled state of light, which amounts to a *conditional* squeezing. In the proposed scheme [28] two entangled optical modes (that are frequency non-degenerated) are sent onto the dark port of the interferometer. The signal mode is resonant with arm cavities and with a signal recycling cavity, coinciding with the frequency mode of the interferometer pumped by the probe laser. Hence, the modulation caused by the passage of GWs as well as back action due to the interaction with the mirror are imprinted onto the signal quadrature. At the same time, the idler field is detuned from arm cavities and doesn't read out the signal produced by GWs together with QRPN. However, the appropriate selection of the detuning from SRC can lead to the frequency dependent quadrature rotation of reflected idler field. As shown in [28], this rotation in the phase space might completely counterbalance the undesired accumulation of back action in the signal mode without affecting signal term (modulation of mirror due to GWs). This could be achieved by proper tuning of the idler frequency and a delicate adjustment of SRC. The protocol is completed by independent homodyne detections of both signal and idler modes. The noise cancellation occurs as two photocurrents from each homodyne detector are appropriately combined.

We introduce the signal $\{\hat{x}_{L,s,in}, \hat{p}_{L,s,in}\}$ and the idler $\{\hat{x}_{L,i,in}, \hat{p}_{L,i,in}\}$ optical modes, assuming their correlations according to eq.(1.18), eq.(1.19). The signal phase quadrature $\hat{p}_{L,s}$ passes interferometer, records the modulation $h(\Omega)$ induced by the arrival of GWs and accumulates QRPN as described in eq.(1.5). One can treat the latter fact as the rotation in the phase space and write the noise part of phase signal quadrature $\hat{p}_{L,s,out}$ after exiting the interferometer in the form:

$$\hat{p}_{L,s,out} = \hat{x}_{L,s,in} \cos(\Phi_s) - \hat{p}_{L,s,in} \sin(\Phi_s), \quad \Phi_s(\Omega) = \frac{\pi}{2} + \arccos\left(\frac{K_{FPM}}{\sqrt{1+K_{FPM}^2}}\right). \tag{1.42}$$

If idler phase quadrature $\hat{p}_{L,i}$ after interaction with SRC experiences the effective rotation in phase space that is opposite to the rotation of signal quadrature

$$\hat{p}_{L,i,out} = \hat{x}_{L,i,in} \cos(\Phi_i) - \hat{p}_{L,i,in} \sin(\Phi_i), \quad \Phi_i(\Omega) = -\Phi_s(\Omega), \tag{1.43}$$

then the noise suppression associated with the observable $\hat{p}^g_{L,out} = \hat{p}_{L,s,out} - g\hat{p}_{L,i,out}$ is achieved as dictated by eq.(1.29): $g = \tanh 2r$, $S_{\hat{b}_2^g \hat{b}_2^g} = 1/\cosh(2r)$. The expression for the strain equivalent noise is given by:

$$S_{h_{cond.sq.}} = \frac{h_{SQL}^2}{2K_{FPM}\cosh(2r)}\left(1+K_{FPM}^2\right). \tag{1.44}$$

This limit for the sensitivity is higher than the limit of the protocol using the injection of light with frequency-dependent squeezing (see eq.(1.40)). The reason is that the idler mode adds extra quantum noise to the measurement error. Compared to the injection of single-mode squeezing, the EPR-entanglement-based strategy performs

worse by factor of $e^{2r}/\cosh(2r) \sim 2$ in the limit of big r, when the most beneficial choice is to measure the signal and the idler modes with equal weights.

In the experimental demonstrations [29, 30] both optical modes were sent onto a ∼1-meter filter resonator. Such cavities had adjustable detuning for both signal and idler wavelengths. Hence, quadrature rotation could be imprinted onto both frequency modes. Thus, accumulation of QRPN and, subsequently, pondermotive squeezing was simulated for the signal optical mode. As a result, conditional squeezing with the desired frequency dependence imposed onto signal, being compensated by idler afterwards, was successfully shown with the quantum noise reduction 2-3 dB relative to SN, addressing sub-MHz spectral range.

1.3.6 Quantum speed-meter

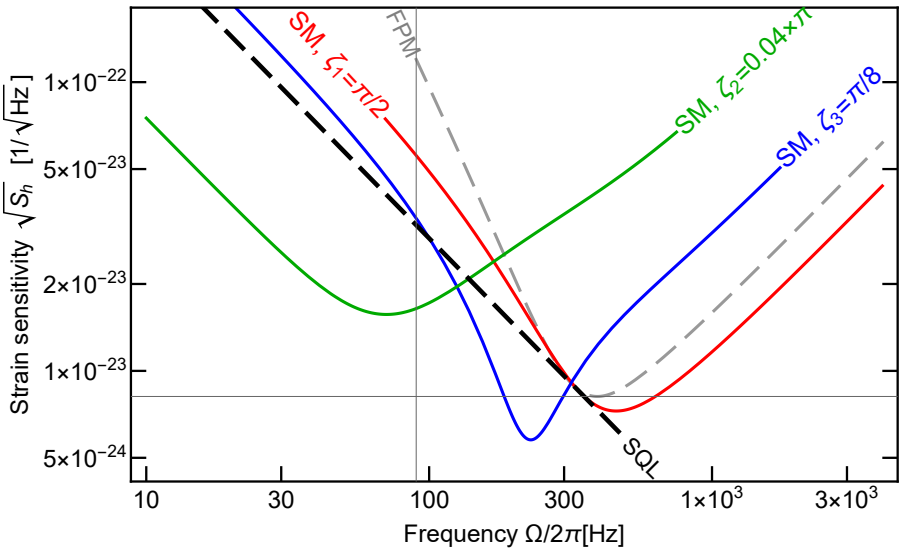

Figure 1.9: Spectra of quantum noise for GWD in *speed-meter* (SM) configuration (using Sagnac interferometer), no squeezing is injected to the dark port. As a reference, an ordinary 'position-like' measurement noise spectrum is shown with the gray line. In order to produce sensitivity curves demonstrated above, eqs.(459-460) from [6] were used.

Approaches of pre-filtering (frequency-dependent squeezing injection) and post-filtering (variational readout) have one common feature which might be attributed to 'position-like' measurement. Namely, the detrimental effect of the frequency dependence of the optomechanical coupling is counteracted using a specially tailored modification to the quantum state either entering or exiting the dark port of the interferometer. As mentioned above, the reduction of the total quantum noise can be established by inducing correlations between QRPN and SN.

One of the possible alternative strategies that has been suggested is the concept of *speed meter*, when the momentum of a mechanical object is effectively measured. In order to implement the speed meter (GWD) interferometer, one will need to arrange a scheme such that the probe light interacts with test mass mirror twice. A properly chosen phase shift of the light quadrature between the first and the second measurements allows to acquire the information about the speed of the mirror. As a result, the effective response function of a mechanical system itself changes, comparing favorably [6] to K_{FPM} for an 'ordinary' GWD interferometer (given by eq.(1.6)).

The speed measurement of test mass mirror might be implemented by establishing the coupling between GWD interferometer and another optomechanical system called a *sloshing cavity*. In this scheme, the optical quadrature after reading out the mechanical motion and exiting interferometer interacts with a external cavity. The transfer function of the sloshing cavity is adjusted in such a way, that reflected quadrature re-enters dark port of the interferometer with accrued π-phase shift in the spectral range within the bandwidth of the sloshing cavity. After the second reflection from the free-mass mirror, the momentum of mechanical object is eventually imprinted onto optical quadrature.

The need for an external sloshing cavity for GWD might be obviated according to proposal [31]. The light quadrature after the first interaction undergoes the rotation of polarization inside interferometer by 90°, being redirected to test mass mirror. The perpendicular polarization is effectively decoupled from the mechanical motion. Therefore, during the second interaction the light quadrature doesn't record the modulation induced by GW signal, while cancellation of noise associated with position measurement does occurs. In that case, an orthogonal polarization mode of Michelson arms replaces the sloshing cavity. The approach implies utilization of polarization optics that can rotate the polarization and provide required phase delay [7].

An alternative way to exclude the sloshing cavity [6] is to convert the interferometer to Sagnac configuration [32], in which the light travels sequentially through the two Michelson arms. Specifically, Sagnac interferometer with ring-shaped Fabry-Perot cavities has optomechanical coupling factor

$$K_{SM}(\Omega) \propto 1/\left(\left(\Omega^2 - \Omega_{SM}^2\right)^2 + \delta_{SM}^2\Omega^2\right), \tag{1.45}$$

where Ω_{SM} is sloshing rate and δ_{SM} is extraction rate [33]. In contrast to eq.(1.6), the coupling factor is roughly constant for spectral frequencies approaching 0. It opens up the opportunity to cancel QRPN in a broad spectral range of interest by adjusting the homodyne detection phase ζ [6], as shown in Figure 1.9. Similarly, frequency-independent squeezing with optimal squeezing angle leads to sensitivity enhancement (this case is not explored on Figure 1.9).

Chapter 2

Proposal for quantum noise evasion in GWDs using an auxiliary spin ensemble

2.1 Concept of quantum back action free measurement

Eq.(1.1) for a single mechanical oscillator reveals that the readout of $\hat{x}_M$ happens together with recording of light noise onto the orthogonal quadrature $\hat{p}_M$ (see eq.(1.1b) and eq.(1.1d), respectively). This implies that improving the measurement precision of the position of an object, an observer is losing information about its momentum. More generally, the measurement of any quadrature for a quantum system perturbs the canonically conjugate variable due to the *quantum back action* effect.

These remarks assume the situation where the measurement is performed much faster than a coherent evolution of the quantum system characterized by time $t_{coh} = 2\pi/\Omega_M$ where Ω_M is the oscillation frequency. Turning to a different scenario, we now consider that the measurement time is comparable or exceeds t_{coh}. The motion of a quantum mechanical oscillator in the phase space can be expressed by the following set of equations

$$\hat{x}_M(t) = \quad \cos(\Omega_M t)\hat{x}_M(0) + \sin(\Omega_M t)\hat{p}_M(0), \tag{2.1a}$$
$$\hat{p}_M(t) = -\sin(\Omega_M t)\hat{x}_M(0) + \cos(\Omega_M t)\hat{p}_M(0), \tag{2.1b}$$

in which the harmonic evolution is made explicit. Reading $\hat{x}_M(t)$ entails the accumulation of quantum back action noise (QBAN) in $\hat{p}_M(t)$. As a result, the continuous measurement contaminates the trajectory of the oscillator since the uncertainty in the momentum causes the disturbance of the position at later times as the evolution of the system is described by eqs.(2.1).

Here we start to investigate a 'trick' that allows to counteract the effect of quantum back action. The approach described below relies on the concepts of trajectories without quantum uncertainties [34] and quantum mechanics free subsystems [35]. We consider the measurement performed on a mechanical object that acts as a quantum harmonic oscillator with Hamiltonian $\hat{H}_M$ encoded in variables $\{\hat{x}_M, \hat{p}_M\}$. Instead of directly probing this object (as shown, for example, in eq.(1.1)), we now measure its motion relative to another *reference quantum oscillator* $\{\hat{x}_S, \hat{p}_S\}$. Hamiltonians of two systems have the same structure given by:

$$\hat{H}_i = \frac{\Omega_i}{2}\left(\hat{x}_i^2 + \hat{p}_i^2\right) + \sqrt{\Gamma_i}\hat{x}_i\hat{x}_L, \quad i = M, S. \tag{2.2}$$

The first term of Hamiltonian describes the harmonic motion while the second term determines the interaction between the oscillators and the probe light $\{\hat{x}_L, \hat{p}_L\}$ characterized by readout rate Γ_i. Using eq.(2.2), we write down the equation describing the evolution of each oscillator (for simplicity we neglect the damping and intrinsic noise associated with the objects):

$$\dot{\hat{x}}_i = \Omega_i\hat{p}_i, \tag{2.3a}$$
$$\dot{\hat{p}}_i = -\Omega_i\hat{x}_i + \sqrt{\Gamma_i}\hat{x}_{L,in}. \tag{2.3b}$$

Eqs.(2.3) describe a rotation in the phase space disturbed by quantum back action $\propto \hat{x}_{L,in}$. The velocity of rotation is determined by the resonance frequency Ω_i, and the direction of the rotation can be either counter-clockwise (if $\Omega_i > 0$) or clockwise (if $\Omega_i < 0$). We now suppose that the frequency of reference oscillator Ω_S is *negative* and opposite to frequency of the first oscillator: $\Omega_M = -\Omega_S = \Omega_R > 0$. The next assumption is that the two systems have the same readout rates $\Gamma_M = \Gamma_S = \Gamma$ and are probed with the same input light $\hat{x}_{L,in}$. The system consisting of two oscillators is described by

$$\frac{d\left(\hat{x}_M + \hat{x}_S\right)}{dt} = \Omega_R \left(\hat{p}_M - \hat{p}_S\right), \tag{2.4a}$$

$$\frac{d\left(\hat{p}_M - \hat{p}_S\right)}{dt} = (-\Omega_R)\left(\hat{x}_M + \hat{x}_S\right), \tag{2.4b}$$

which can be considered as a motion of a single oscillator encoded in $\hat{x}_+, \hat{p}_-$ where $\hat{x}_\pm \equiv \left(\hat{x}_1 \pm \hat{x}_2\right)/\sqrt{2}$, $\hat{p}_\pm \equiv \left(\hat{p}_1 \pm \hat{p}_2\right)/\sqrt{2}$. Solving eqs.(2.3) in the frequency domain for each of oscillator, we arrive at:

$$\hat{x}_i(\Omega) = \frac{\Omega_i}{\Omega_i^2 - \Omega^2}\sqrt{\Gamma_i}\hat{x}_{L,in}, \quad \hat{p}_i(\Omega) = \frac{i\Omega}{\Omega_i^2 - \Omega^2}\sqrt{\Gamma_i}\hat{x}_{L,in}. \tag{2.5}$$

As follows from eq.(2.5), the term $\propto \hat{x}_{L,in}$ vanishes completely from the variables $\{\hat{x}_+, \hat{p}_-\}$ if $\Gamma_M = \Gamma_S$ and $\Omega_M = -\Omega_S$. It is tantamount to the total cancellation of quantum back action due to the destructive interference of QBAN from each oscillator. Thus, eq.(2.4) describes the dynamics of the composite system, whose trajectory in the phase space is quantum back action free. Imperfect matching of probed and reference systems leads to partial cancellation of QBAN in EPR variables $\{\hat{x}_+, \hat{p}_-\}$ and, in particular, renders two oscillators entangled [36] provided fulfilled condition [37]:

$$\overline{\Delta\left(\frac{\hat{x}_M + \hat{x}_S}{\sqrt{2}}\right)^2} + \overline{\Delta\left(\frac{\hat{p}_M - \hat{p}_S}{\sqrt{2}}\right)^2} < 2. \tag{2.6}$$

The *negative mass*[1] of the of reference oscillator is the crucial condition that makes establishing quantum correlations between two subsystems possible - otherwise, coupling of EPR variables $\hat{x}_+$ and $\hat{p}_-$ is not set. If $\Omega_M = \Omega_S$, the relative position $\hat{x}_-$ is coupled to relative momentum $\hat{p}_-$ (as well as $\hat{x}_+$ couples to $\hat{p}_+$), but in those variables the cancellation of QBAN is not feasible.

As stated in section 1.2, a free mass mirror in a GWD interferometer is in principle the extreme case of a harmonic oscillator with the resonance frequency[2] $\Omega_M \to 0$, whose motion is disturbed by QBAN. The evasion of this noise by measurement in a frame of another reference oscillator is the subject matter for this thesis. The multi-atoms spin ensemble (caesium vapour) [38] in external magnetic field turned out to be a promising candidate [34] for joint measurement with GWD interferometer. The main advantages of caesium atomic system are tunability of resonance frequency, low intrinsic losses, high efficiency of interaction with light and the feature to mimic the dynamics of an oscillator with negative frequency. The suppression of the QBAN using a cesium atomic spin ensemble was experimentally demonstrated in [39] for a dielectric membrane nanomechanical oscillator. The hybrid entanglement between two oscillators was shown in [40]. In both works degree of matching between disparate systems was a limitation factor.

2.2 Joint measurement on GWD interferometer and atomic oscillator. Cascade and parallel approaches. Ideal case

In this section, we begin presenting the general theory of joint measurements on atomic ensembles and GWDs. The reference spin oscillator with effective negative mass is described by interaction Hamiltonian eq.(2.2). Unlike the idealized case outlined by eq.(2.5), this oscillator is now driven not only by quantum noise of probe light, but also by the thermal stochastic force $\hat{f}_{Th}$:

[1] Since negative resonance frequency is equivalent to negative mass in terms of the motion in the phase space [34], we will use the term *negative mass oscillator* when referring to the object with $\Omega_S < 0$.

[2] Practically, Ω_M has a small, but finite value so that the definitions of $\hat{x}_M$ and $\hat{p}_M$ used in eq.(1.1) further are still valid.

$$\hat{x}_S(\Omega) = \chi_S(\Omega)\left(\sqrt{\Gamma_S}\hat{x}_{L,in} + \sqrt{\gamma_S}\hat{f}_{Th}\right), \tag{2.7}$$

where the susceptibility function for the atomic ensemble

$$\chi_S(\Omega) = \frac{\Omega_S}{\Omega_S^2 - \Omega^2 - i\gamma_S\Omega + (\gamma_S/2)^2} \tag{2.8}$$

was used (in accordance with eq.(1.3), which is the particular case for GWDs). The factor γ_S represents the decay rate of the atomic oscillator (which was assumed to be 0 earlier for simplicity). The readout of the spin system is described by [39]

$$\hat{x}_{L,out} = \hat{x}_{L,in} \tag{2.9a}$$

$$\hat{p}_{L,out} = \hat{p}_{L,in} + \sqrt{\Gamma_S}\hat{x}_S. \tag{2.9b}$$

One can see from eq.(2.9a) that the amplitude quadrature $\hat{x}_L$ remains isolated from other variables, whereas $\hat{p}_L$ contains information about spin motion encoded in $\hat{x}_S$. We finally obtain the input-output relations for the atomic system:

$$\hat{x}_{L,out} = \hat{x}_{L,in} \tag{2.10a}$$

$$\hat{p}_{L,out} = \hat{p}_{L,in} + \Gamma_S\chi_S\hat{x}_{L,in} + \sqrt{\gamma_S\Gamma_S}\chi_S\hat{f}_{Th}. \tag{2.10b}$$

The second oscillator is a test mass mirror, it's interaction with optical field is enhanced by optical cavities and described by eq.(1.1). First, we introduce the cascade scheme [41], where the light $\{\hat{x}_L, \hat{p}_L\}$ sequentially interacts with the atomic spin ensemble $\{\hat{x}_S, \hat{p}_S\}$ and then with the mirror of GWD (being defined by $\{\hat{x}_M, \hat{p}_M\}$ in the phase space). Using input-output relations eq.(1.5), eq.(2.10) for both systems, we obtain for the optical readout quadrature $\hat{p}_{L,out}$ after probing two systems[3]:

$$\hat{p}_{L,out} = \hat{p}_{L,in} + (\Gamma_S\chi_S(\Omega) - K_{FPM})\cdot\hat{x}_{L,in} + \left[\sqrt{K_{FPM}}\frac{h}{h_{SQL}} + \sqrt{\Gamma_S\gamma_S}\chi_S(\Omega)\hat{f}_{Th}\right]. \tag{2.11}$$

Then the strain sensitivity operator is introduced by normalizing quantum noise on h, analogous to eq.(1.7). It's spectrum is given by:

$$S_{h_{cas}} = \frac{h_{SQL}^2}{2K_{FPM}}\left(1 + (\chi_S\Gamma_S - K_{FPM})^2 + \Gamma_S\gamma_S\chi_S^2\sigma_{Th}\right) \tag{2.12}$$

where σ_{Th} is the spectral density of the thermal force $\hat{f}_{Th}$. The second term on the right-hand side of eq.(2.11) and eq.(2.12) represents the total QBAN. It can be completely cancelled by making the adjustment of the parameters attributed to the oscillators that ensures:

$$K_{FPM} = \Gamma_S\chi_S(\Omega). \tag{2.13}$$

We re-write eq.(2.13) in a form of two equations, emphasizing the terms that depend and don't depend on Fourier frequency. Assuming Ω to be well within the bandwidth of the interferometer $\Omega \ll \gamma_L$, we obtain:

$$\frac{1}{\Omega^2} = \frac{-1}{\Omega_S^2 - \Omega^2 - i\gamma_S\Omega + (\gamma_S/2)^2}, \tag{2.14a}$$

$$K_S = K_I', \tag{2.14b}$$

[3]We denote the optical mode entering the atomic spin ensemble as $\{\hat{x}_{L,in}, \hat{p}_{L,in}\}$. The output filed in eq.(2.10) is the input mode in eq.(1.5) and the field $\{\hat{x}_{L,out}, \hat{p}_{L,out}\}$ is the output in eq.(1.5)

where we have introduced the *coupling rate* Ω_{qS} for atomic ensemble and defined frequency independent part K'_I of coupling factor for GWD:

$$\Omega_{qS}^2 \equiv K_S = \Gamma_S|\Omega_S| \tag{2.15a}$$

$$K'_I = K_I K_{OI}|_{\Omega\to 0} = \frac{2K_I}{\gamma_L} \tag{2.15b}$$

The condition eq.(2.14a) may be approximately satisfied in the limit γ_S, $\Omega_S \to 0$ (implying γ_S, $|\Omega_S| \ll \Omega$), meaning that spin ensemble should also approach the limit of free mass motion. Note that the sign on the right part of eq.(2.14a) signifies that we have chosen the negative resonance frequency for atomic oscillator. At the same time, eq.(2.14b) demands the adjustment of the rates of interaction with the light for each system. This condition can be fulfilled, for example, by tuning the optical readout rate of spin oscillator. Removing QBAN, we add the thermal noise of the atomic ensemble into the hybrid system. However, the impact of the thermal force might be reduced to the level well below QBAN. The similarity is seen between the approach described here and the injection of frequency dependent squeezing. In the latter scheme the initial squeezed light interacts with filter cavity in order to acquire the necessary frequency dependence on squeezing angle. In the approach presented in this section the role of the filter cavity is played by the spin oscillator. However, the injection of frequency dependent squeezing results in the suppression of both SN and QBAN. In contrast, the measurement in a frame of reference oscillator leads to quantum back action free motion. The shot noise might be further reduced by enhancing the circulating power or injecting (phase) squeezed state instead of vacuum (see section 1.3.3). Alternatively, the order of two oscillators might be changed. The light can pass the GWD first and then interact with the atomic ensemble. In such a case the protocol will be analogous to variational readout proposal (presented in section 1.3.2), where the filter cavity is placed at the output of GWD interferometer.

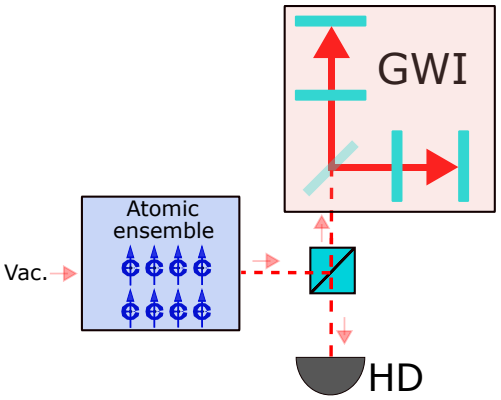

(a) Sequential scheme.

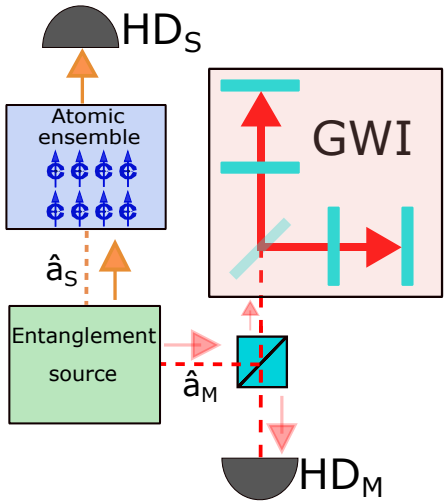

(b) Parallel scheme.

Figure 2.1: Measurement performed on the GWD, using the atomic spin ensemble as a reference frame.

In order to implement the scheme outlined above, it is necessary that both the GWD and the reference oscillator are probed by the same optical mode. However, the atomic spin ensembles reported in [38] are operated at the wavelength 852 nm, which is approximately 200 nm less than the typical wavelength used in contemporary GWD interferometers. The issue of wavelength mismatching can be solved if the cascade probing is replaced by a *parallel measurement* [42, 41]. We introduce two optical modes: the first mode $\{\hat{x}_{L,s}, \hat{p}_{L,s}\}$ is sent to the interferometer while the second mode $\{\hat{x}_{L,i}, \hat{p}_{L,i}\}$ interacts with the atomic spin oscillator. These optical modes, denoted as 'signal' and 'idler' respectively, have different carrier frequencies suitable for each system. We now assume that probe beams are prepared in a perfect *entangled state*:

$$\hat{x}_{L,s,in} = \hat{x}_{L,i,in}, \quad \hat{p}_{L,s,in} = -\hat{p}_{L,i,in}. \tag{2.16}$$

Both systems are probed simultaneously by mixing entangled modes with respective coherent fields, and the results of the measurement on each system are combined. From eq.(2.10) and eq.(1.5) we obtain input-output relations for the parallel scheme:

$$\hat{p}_{L,par.,out} \equiv \hat{p}_{L,s,out}+\hat{p}_{L,i,out} = (\hat{p}_{L,s,in} + \hat{p}_{L,i,in})+(\chi_S\Gamma_S\hat{x}_{L,i,in} - K_{FPM}\hat{x}_{L,s,in})+\left(\sqrt{K_{FPM}}\frac{\hat{h}}{h_{SQL}} + \chi_S\sqrt{\Gamma_S\gamma_s}\hat{f}_{Th}\right). \tag{2.17}$$

Having the condition eq.(2.14) satisfied, we can see that the parallel measurement simultaneously cancels SN and QBAN. Indeed, the first term on the right hand side of eq.(2.17) is zeroed as the phase quadratures of perfect EPR-entangled modes are anticorrelated (eq.(2.16), right part). In turn, the second term on the right hand side of eq.(2.17) disappears if the amplitude quadratures are perfectly correlated (eq.(2.16), left part) and the negative mass of the spin oscillator is set. Consequently, the total quantum noise is suppressed, in contrast to the sequential scheme. The same result is achieved in the strategy of conditional squeezing using EPR entanglement (section 1.3.4). In fact, these two approaches are based on the same principle: while the signal mode record the modulation imposed by GW, the idler compensates the QBAN, accrued by the signal optical field. The rotation of the idler quadrature in the phase space is caused by impact from the atomic spin oscillator in one case and by the signal recycling cavity in another case.

2.3 Non-perfect matching. Virtual rigidity

Here we explore the feasibility of performing a proper matching of the GWD and the spin ensemble in the experiment. In order to do that, we return to the conditions given by eqs.(2.14), which remain valid for both the cascade and the parallel schemes. The term K_I' defines the strain sensitivity of GWDs, depending on such crucial parameters as circulating power, the mass of suspended mirrors and the length of interferometer's arms. Contemporary configurations of GWDs are operated at such experimental conditions that correspond to the range $50 - 100$ Hz for $\sqrt{K_I'}$. Therefore, having the condition on the spin resonance frequency $\Omega_S \to 0$ from eq.(2.14a) fulfilled, we must select high values of the atomic readout rate $\Gamma_S = K_S/|\Omega_S| \gg \sqrt{K_I'}$ in order to satisfy eq.(2.14b). However, this inevitably counteracts another part of condition eq.(2.14a) since the linewidth γ_S of the atomic ensemble grows with an increase of the readout rate. Namely, γ_S is decomposed into two parts. The first part $\gamma_{S,in}$ represents the intrinsic losses, which do not with Γ_S. In contrast, the second part scales linearly with the readout rate, the constant of proportionality is mainly defined by the atomic density. The latter is interlinked to the atomic *cooperativity*[4] C_s in the paper [43], leading to the expression for the total spin decay rate:

$$\gamma_S = \gamma_{S,in} + \frac{\Gamma_S}{C_s}, \tag{2.18}$$

where the second term on the right hand side will also be denoted as $\gamma_{S,pb}$. In principle, realizing a large value C_s together with small natural linewidth $\gamma_{S,in}$ would bring γ_S close to 0. However, the maximum value of cooperativity for such system reported to date [44] doesn't exceed 10. It is, generally speaking, not enough to counterbalance the impact of the readout rate on the atomic linewidth. Moreover, to comply with the condition $\Omega_S \approx 0$ is an experimental challenge in itself for any physical platform, since low spectral frequencies are strongly contaminated by various sources of classical noise that compromise quantum features of the system.

The approach of *virtual rigidity* outlined in [43] allows to circumvent the complications introduced above and thus offers a more realistic way towards combining atomic oscillators with GWDs. The key idea is to effectively modify the susceptibility of the spin ensemble and emulate the shift of its resonance frequency. To implement such a transformation of the atomic response, one needs to induce correlations between SN and QBAN [6] by varying the phase of homodyne detection ζ_S. Discarding the contribution of the thermal force in the input-output relations given by eq.(2.10), we obtain the following expression for arbitrary detection quadrature $\hat{q}_{L,i}(\zeta_S) = \hat{p}_{L,i}\cos(\zeta_S) + \hat{x}_{L,i}\sin(\zeta_S)$:

[4]Note that the spin cooperativity is defined differently in Chapter 4, eq.(4.62), where C_q represents the ratio between QBAN and thermal noise.

$$\hat{q}_{L,i,out}(\zeta_S) = \hat{q}_{L,i,in}(\zeta_S) + \chi_S \Gamma_S \cos(\zeta_S)\hat{x}_{L,i,in}, \tag{2.19}$$

which is then re-written in the new basis $[\hat{q}_{L,i}(\zeta_S), \hat{q}_{L,i}(\zeta_{S\perp})]^T = \boldsymbol{R}(\zeta_S)[\hat{x}_{L,i}, \hat{p}_{L,i}]^T$ (where $\boldsymbol{R}(\zeta_S)$ is the rotation matrix):

$$\hat{q}_{L,i,out}(\zeta_S) = [1 + \chi_S \Gamma_S \cos(\zeta_S)\sin(\zeta_S)]\,\hat{q}_{L,i,in}(\zeta_S) + \chi_S \Gamma_S \cos^2(\zeta_S)\hat{q}_{L,i,in}(\zeta_{S\perp}). \tag{2.20}$$

The terms $\propto \hat{q}_{L,i,in}(\zeta_{S\perp})$ and $\propto \hat{q}_{L,i,in}(\zeta_S)$ represent *effective* quantum back-action noise and imprecision noise, respectively. The redefined SN engulfed part of the original QBAN, the two effective sources of quantum light noise arise from orthogonal light quadratures and remain uncorrelated. We take the ratio of amplitudes of the back-action noise term and imprecision noise contribution from eq.(2.20):

$$\frac{\mathrm{Amp}_{\mathrm{QBAN,eff.}}}{\mathrm{Amp}_{\mathrm{imp.,eff.}}} = \frac{\chi_S \Gamma_S \cos^2(\zeta_S)}{1 + \chi_S \Gamma_S \cos(\zeta_S)\sin(\zeta_S)} = \frac{\Gamma_S \Omega_S \cos^2(\zeta_S)}{\Gamma_S \Omega_S \sin(\zeta_S)\cos(\zeta_S) + \Omega_S^2 - \Omega^2 - i\gamma_S\Omega + (\gamma_S/2)^2} \tag{2.21}$$

and compare it with $K_{FPM}(\Omega) = K_I'/\Omega^2$ as it defines the ratio between QBAN and imprecision noise for GWDs. One can interpret eq.(2.21) as change of effective Larmor frequency

$$\Omega_{S,eff}^2 = \Omega_S^2 + \Gamma_S \Omega_S \sin(\zeta_S)\cos(\zeta_S). \tag{2.22}$$

Depending on homodyne detection phase ζ_S (as well as the sign of Ω_S) the resonance frequency is either increased or reduced. In particular, $\Omega_{S,eff}^2$ can be shifted down to 0, if readout rate is significant enough $\Gamma_S \gtrsim |\Omega_S|$. In such a case we emulate a free mass motion[5] for the spin oscillator. At the same time, we need to match the numerator in eq.(2.21) to K_I'. The choice of the values for the initial Larmor frequency Ω_S and the atomic readout rate Γ_S according to [43]:

$$\Omega_S = -\sqrt{K_I' \tan(\zeta_S)} \tag{2.23a}$$

$$\Gamma_S = \sqrt{\frac{K_I'}{\sin(\zeta_S)\cos^3(\zeta_S)}} \tag{2.23b}$$

for given K_I' straightforwardly yields $\Gamma_S|\Omega_S|\cos^2(\zeta_S) = K_I'$ and $\Omega_{S,\mathrm{eff.}}^2 = 0$. Altogether it means that both condition eq.(2.14a) (for Larmor frequency only) and condition eq.(2.14b) are fulfilled[6] without need to prepare the spin oscillator with $\Omega_S \to 0$ and high read-out rate Γ_S. It significantly mitigates tough requirements on the cooperativity C_s. Technical problems related to control of atomic ensemble in the regime of free mass motion are also evaded.

Eqs.(2.23a)-(2.23b) provide a freedom in selection of parameters Γ_S, Ω_S. In particular, the initial Larmor frequency is permitted to be as big as experimentalists desire as soon as ζ_S approaches $\pi/2$. However, one can reveal the limited performance of the 'virtual rigidity': the amendment term to the atomic resonance frequency Ω_S is real, therefore the imaginary part of the susceptibility function comprising atomic linewidth γ_S can not be compensated. We notice that minimization of the readout rate as function of homodyne phase ζ_S

$$\Gamma_S(\zeta_S) \xrightarrow[\zeta_S \to \pi/6]{} \min = \frac{4\sqrt{K_I'}}{3^{3/4}}. \tag{2.24}$$

minimizes the decoherence rate in accordance to eq.(2.18). However, it comes with the disadvantage of strict requirement on thr Larmor frequency: $\Omega_S = \sqrt{\sqrt{3}K_I'}$.

One may want to keep the detection phase for the spin system fixed $\zeta_S = 0$, thus measuring the optical phase quadrature, and at the same time implement the shift of atomic resonance frequency by means of 'virtual

[5] disregarding γ_S for now

[6] one can define the *effective* atomic coupling rate $\Omega_{qS,eff} = \Omega_{qS}\cos(\zeta_S)$ and hence $K_{S,eff} = K_S \cos^2(\zeta_S)$. The condition eq.(2.14b) is then written as $K_{S,eff.} \equiv K_I'$.

rigidity'. The strategy outlined in [43] proposes to exploit carrier phase angle ϕ_S instead. This angle can be defined as the relative phase between probe field and part of two mode squeezed vacuum sent to atomic ensemble and was assumed to be set at 0 in all considerations above. But the variation of ϕ_S has exactly the same effect as tuning homodyne detection phase [43]: in fact, in all expressions eq.(2.22)-(2.23) we should make a substitution $\zeta_S \leftrightarrow \phi_S - \zeta_S$. For example, the choice $\zeta_S = 0$ and $\phi_S = \pi/6$ corresponds to optimal configuration that reduces the unwanted contribution from imaginary part of susceptibility function as in eq.(2.24).

As another remark, the 'virtual rigidity' can be also applied to the GWD for the opposite purpose: to convert the initial free-mass object to the effective harmonic oscillator. The respective homodyne phase angle ζ_M and carrier phase ϕ_M must be tuned, and the logic outlined in eq.(2.19)-(2.23) is in principle valid for the test mass mirror interacting with probe optical field. However, we will stick to the conventional settings $\zeta_M = 0$, $\phi_M = 0$ for GWDs throughout this chapter.

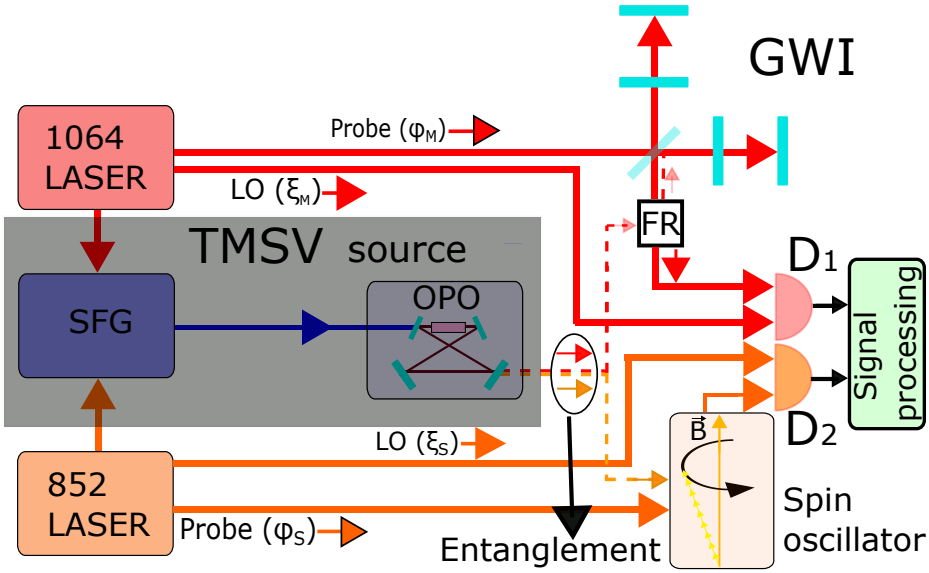

Figure 2.2: The scheme of a parallel measurement, performed on the GWD and the atomic ensemble. The entangled modes, upon exiting the source of two-mode squeezed vacuum (TMSV), are injected to the GWD interferometer and the spin oscillator. Adjusting the phase of the coherent probe field ϕ_S or homodyne detection phase ζ_S, one can tune the effective resonance frequency of the atomic oscillator by means of the virtual rigidity in order to match the spectral responses of two systems. The idea of the protocol is described in the text, for more details see [43]. The main part of TMSV source is the optical parametric oscillator (OPO), which is pumped by the field obtained as a result of the sum frequency generation (SFG) process.

2.4 Sensitivity improvement: imperfections included

Having described the idealized case in section 2.2, we now estimate the quantum noise reduction for the parallel scheme, gradually introducing imperfections of the spin ensemble and the entanglement source. First, we replace infinite two-mode squeezing eq.(2.16) by realistic quantum state of light. Studying the impact of atomic decay rate, we will show that imaginary part of χ_S may be partially counterbalanced by adjusting atomic central frequency Ω_S or/and readout rate Γ_S without use of virtual rigidity. Next, we explore the importance of high cooperativity C_S and appropriate choice $\phi_S = \pi/6$ of carrier phase angle when virtual rigidity is applied. Finally, we investigate the effect of optical losses.

To begin, we define the strain equivalent noise operator for the measurement of the signal force in the parallel scheme as

$$\hat{h}_{n,atoms} = \frac{h_{SQL}}{\sqrt{2K_{FPM}}}\left(\hat{p}_{L,s,in} - K_{FPM}\hat{x}_{L,s,in} + g(\hat{p}_{L,i,in} + \Gamma_S\chi_S\hat{x}_{L,i,in} + \sqrt{\Gamma_S\gamma_S}\chi_S\hat{f}_{Th})\right). \tag{2.25}$$

Here $\hat{p}_{L,par.,out.} \equiv \hat{p}_{L,s,out} + g\hat{p}_{L,i,out}$ is measured in contrast to the case of equal weights ($g = 1$) in eq.(2.17) when combining the measurement outcomes from the GWD and the spin oscillator.

2.4.1 Finite entanglement

We now account for the finite degree of interbeam correlations. Instead of using eq.(2.16), we assume a two-mode squeezed state by eq.(1.18), where the coefficient r defines the strength of entanglement. Using the features eq.(1.19) of entangled beams $\hat{x}(\hat{p})_{L,s}$ and $\hat{x}(\hat{p})_{L,i}$, we write the expression for PSD of strain sensitivity given by eq.(2.25):

$$S_{h_{atoms}} = \frac{h_{SQL}^2}{2K_{FPM}} \left(\sigma_M(\omega) - 2g\sigma_{IS}(\omega) + g^2\sigma_S\right), \tag{2.26}$$

where the terms σ_M and σ_S are spectral densities of interferometer and spin ensemble strain sensitivities respectively, while σ_{IS} is their cross-spectral density:

$$\sigma_I = \left(1 + K_{FPM}^2\right)\cosh(2r), \tag{2.27a}$$

$$\sigma_S = \left(1 + (\chi_S\Gamma_S)^2\right)\cosh(2r) + \Gamma_S\gamma_S\chi_S^2\sigma_T, \tag{2.27b}$$

$$\sigma_{IS} = (1 + \chi_S\Gamma_S K_{FPM})\sinh(2r), \tag{2.27c}$$

where σ_T is the spectrum of $\hat{f}_{Th}$. The optimal choice g_{opt} that minimizes $S_{h_{atoms}}$ changes eq.(2.26) to:

$$S_{h_{atoms}}|_{g_{opt.}} = \frac{h_{SQL}^2}{2K_{FPM}\sigma_S}\left(\sigma_S\sigma_I - |\sigma_{IS}|^2\right). \tag{2.28}$$

Assume for now that condition eq.(2.13) is fulfilled perfectly. Together with approximation of sufficiently small contribution from spin thermal noise $\Gamma_S\gamma_S\chi_S^2\sigma_T \ll \sigma_S$ we finally obtain for PSD of strain sensitivity eq.(2.28):

$$S_{h_{atoms}}|_{g_{opt.}} = \frac{h_{SQL}^2}{2K_{FPM}\cosh(2r)}\left(1 + K_{FPM}^2\right), \quad g_{opt} = \tanh(2r). \tag{2.29}$$

The total quantum noise is homogeneously reduced in the whole spectral range by factor of $\cosh(2r)$. The result obtained in eq.(2.29) coincides with eq.(1.44), which corresponds to the scheme utilizing an EPR-entanglement, whose second mode is reflected from the signal recycling cavity, being detuned from it (the first mode probes the motion of ETM mirrors).

2.4.2 Effect of mismatching in susceptibilities

Above we assumed that the spectral responses of the atomic ensemble and the GWD to quantum back action are precisely matched, particularly meaning $\Omega_S = 0$ and the absence of the imaginary part of χ_S. The latter is in principle feasible if, for example, a large cooperativity C_S is achieved (see section 2.3). Now we select a realistic range of values for C_S (the case $C_S = 5$ is investigated in Figure 2.3) and firstly study the performance of the protocol without applying the virtual rigidity, while fulfilling the condition eq.(2.14b) on the coupling rates. Eq.(2.18) shows that the atomic linewidth $\gamma_{S,pb}$ grows $\propto K_S/(\Omega_S C_S)$ with reduction of the Larmor frequency, deteriorating the noise suppression. Figure 2.3(b) displays that the finite and relatively large (compared to the assumed GWD coupling rate $\sqrt{K_I'}$) Larmor frequency $\Omega_{S,opt}$ allows to perform the optimization of the *sensitivity gain*, predominantly addressing the drop in lower spectral range. Values of Ω_S below $\Omega_{S,opt}$ lead to the broadband reduction of the sensitivity due to the stronger impact of imaginary part of $\chi_S(\Omega)$. In contrast, the substantial mismatch of resonance frequencies causes impaired performance of the protocol, when increasing $\Omega_S > \Omega_{S,opt}$. The value $\Omega_{S,opt.}$ is determined by the parameters of the atomic system, mainly, the cooperativity. In order to fix the product $\Gamma_S \times \Omega_S$, one should adjust the readout rate while scanning the Larmor frequency, as also demonstrated on Figure 2.3(b).

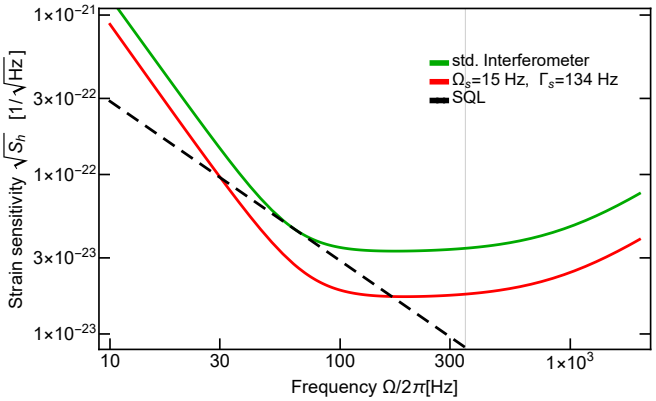

(a) The strain sensitivity of the GWD. The green curve shows the case of quantum noise limited interferometer described by eq.(1.8). The red curve demonstrates the GWD combined with the atomic spin ensemble in the parallel scheme, whose quatum noise is given by $S_{h,atoms}$ from eq.(2.26) with optimized relative weight g, the resonance frequency Ω_S and the readout rate Γ_S of the spin oscillator.

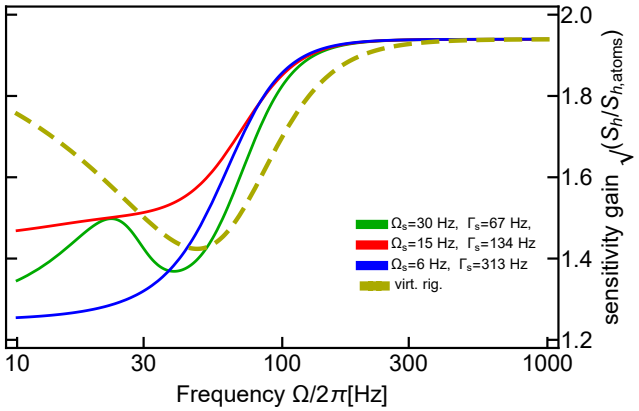

(b) The sensitivity gain relative to the SQL-limited interferometer. S_h and $S_{h,atoms}$ are given by eq.(1.8) and eq.(2.26), respectively. The green, red and blue curves demonstrate the sensitivity improvement for different parameters (readout rate Γ_S and Larmor frequency Ω_S) of the spin ensemble. The dashed yellow line corresponds to the case of implemented *virtual rigidity* with optimized parameters and is shown for reference (it is not described by eq.(2.26)).

Figure 2.3: The reduction of quantum noise in the GWD coupled to the atomic oscillator. The interferometer is operated using the circulating power $I = 1$ kW, the mass of ETM $M = 40$ kG and the arm lengths $L = 4$ km, giving the coupling rate $\sqrt{K_I'} = 63.1$ Hz and the cavity bandwidth $\gamma_L \approx 950$ Hz. The source of entangled light is characterized by the factor of two-mode squeezing $r = 1$. The spin ensemble has the cooperativity $C_S = 5$ and the intrinsic linewidth $\gamma_S = 0.5$ Hz. The spectrum of the thermal force σ_T is assumed to have its minimal value, corresponding to the atomic ground state.

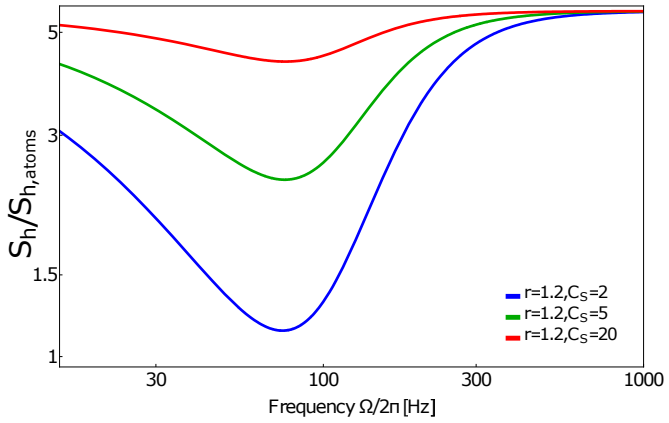

(a) The effect of different cooperativity C_S values is investigated when the virtual rigidity is applied ($\phi_S = \pi/6$, $\Omega_{S,eff} \approx 0$, $K_{S,eff} = K_I$).

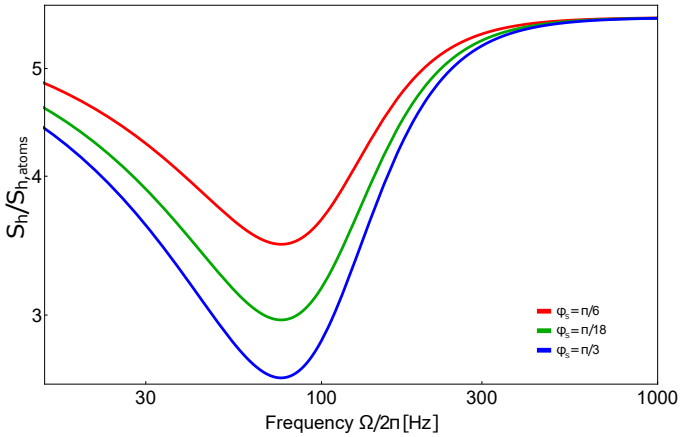

(b) The effect of different carrier phase angle ϕ_S values is shown when the virtual rigidity is applied and $C_S = 5$ is set.

Figure 2.4: Sensitivity gain relative to the quantum noise limited interferometer (the latter is defined by S_h in eq.(1.8)). The sensitivity of the GWD coupled to the atomic spin ensemble corresponds to $S_{h,atoms}$.

We move to the next step, where the virtual rigidity is exploited. Hence, the effective resonance frequencies and coupling rates of two systems are 'automatically' matched. At the same time, the uncompensated imaginary part of χ_S as well as boosted contribution of intrinsic thermal spin noise σ_T show up due to arising of γ_S and reveal themselves as a dip in the sensitivity gain centered at some spectral frequency below $\sqrt{K_I'}$. The different cooperativity C_S values are tested on Figure 2.4(a) while the rest parameters are fixed. As an example, at $r = 1.25$

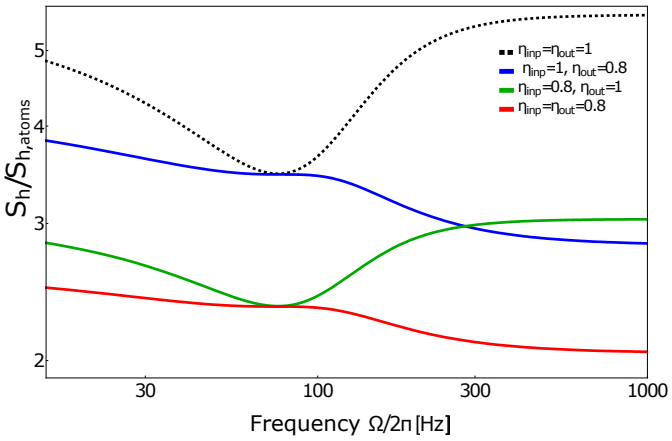

(a) Equal (symmetric) optical losses in spin and GWD channels.

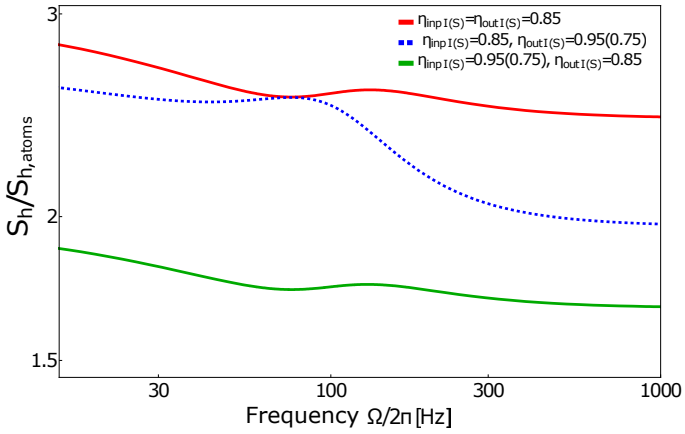

(b) Non-symmetric losses.

Figure 2.5: Effect of optical losses on the sensitivity gain relative to "standard" (SQL-limited) interferometer. Two mode squeezing factor $r = 1.2$ and cooperativity $C_s = 10$ are set, when virtual rigidity is applied ($\phi_S = \pi/6$).

and $K_I' = (100\text{Hz})^2$ a critical value $C_S \sim 10$ might be defined. When this value is exceeded, the dip is strongly reduced, providing rather flat sensitivity gain across the spectral range of interest. Figure 2.4(b) demonstrates another important feature of the virtual rigidity concept as stated by eq.(2.24). Namely, the choice of carrier phase angle for the atomic ensemble $\phi_{S,opt.} = \pi/6$ gives the lowest possible impact of uncompensated imaginary part of spins susceptibility function due to atomic decay rate (alternatively, the homodyne angle ζ_S is tuned, while ϕ_S is fixed). In contrast, varying ϕ_S as extra degree of freedom is accompanied by a sharp decline of sensitivity gain, which is explicitly pronounced around the dip.

2.4.3 Influence of optical losses

The optical losses in the hybrid system can be divided into two groups: losses induced before and after interaction with GWD/atomic systems, denoted as input ('in') and output ('out') losses, respectively. Both types are be taken into account using beam splitter model of absorption: optical mode (for example, the signal or idler mode of the entanglement) is mixed with vacuum, losses determine the transmissivity/reflectivity of the fictitious beam splitter. We define the coefficients $\eta_{S,in}$ and $\eta_{M,in}$ for each (spins/GWD) channel representing their efficiencies. Interbeam correlations eq.(1.19) are impaired due to the losses:

$$\langle \Delta\left(\hat{x}_{L,s,in} - \hat{x}_{L,i,in}\right)^2 \rangle = \frac{\eta_{M,in} + \eta_{S,in}}{2}\cosh(2r) + \frac{2 - (\eta_{M,in} + \eta_{S,in})}{2} + \sqrt{\eta_{M,in}\eta_{S,in}}\sinh(2r). \tag{2.30}$$

In case of symmetric losses $\eta_{M,in} = \eta_{S,in} = \eta_{in}$ the right hand side of eq.(2.30) equals $\eta_{in}e^{-2r} + (1 - \eta_{in})$. Thus, adding input losses can be seen as the reduction of the two-mode squeezing level r before light starts to interact with oscillators. The output losses $\{\eta_{M,out}, \eta_{S,out}\}$ decrease the homodyne detection efficiency, changing the input-output relations on example of atomic system eq.(2.10b) according to:

$$\hat{p}_{L,i,out} = \sqrt{\eta_{S,out}}\left[\hat{p}_{L,i,in} + \chi_S\Gamma_S\hat{x}_{Li,in} + \chi_S\sqrt{\Gamma_S\gamma_S}\hat{f}_T\right] + (1 - \sqrt{\eta_{s,out}})\hat{z}_i. \tag{2.31}$$

Here $\hat{z}_i$ is the vacuum field, which enters the signal quadrature through reflective port of emulated beam splitter. Eq.(2.28) can be used to calculate strain sensitivity in the presence of optical losses, but the expressions for σ_I, σ_S and σ_{IS} are now given by:

$$\sigma_I = \eta_{M,in}\left(1+K_{FPM}^2\right)\left(\cosh\left(2r\right)+\frac{1-\eta_{M,in}}{\eta_{M,in}}+\frac{\Omega^4}{\Omega^4+K_{I,FPM}^2}\cdot\frac{1-\eta_{M,in}}{\eta_{M,in}\eta_{M,out}}\right), \tag{2.32a}$$

$$\sigma_S = \eta_{S,in}\left(1+\left(\chi_S\Gamma_S\right)^2\right)\left(\cosh\left(2r\right)+\frac{1-\eta_{S,in}}{\eta_{S,in}}+\frac{|\chi_S^{-1}|^2}{|\chi_S^{-1}|^2+\Gamma_S^2}\cdot\frac{1-\eta_{S,in}}{\eta_{S,in}\eta_{S,out}}\right)+\Gamma_S\gamma_S\chi_S^2\sigma_T, \tag{2.32b}$$

$$\sigma_{IS} = \sqrt{\eta_{M,in}\eta_{S,in}}\left(1+\chi_S\Gamma_S K_{FPM}\right)\sinh\left(2r\right). \tag{2.32c}$$

The improvement of sensitivity with included optical symmetric losses ($\eta_{M,in(out)} = \eta_{S,in(out)}$) is presented on Figure 2.5(a). As can be seen, in the high frequency limit $\Omega > \sqrt{K_I'}$ the sensitivity is predominantly determined by total optical losses $\eta_{M(S),tot} = \eta_{M(S),in} + \eta_{M(S),out} = \eta_{tot}$. Indeed, the expression for sensitivity gain $G = (S_h|_{\hat{p}_{L,out}})/S_{h,atoms}$ with respect to the quantum noise limited interferometer (given by eq.(1.8)) can be written as:

$$G(\Omega > \sqrt{K_I'}) \approx \frac{\Lambda_M}{\frac{1}{\cosh\left(2r\right)}+\Lambda_M+\Lambda_S}, \quad \Lambda_j = \frac{\eta_{j,in}+\eta_{j,out}-\eta_{j,in}\eta_{j,out}}{\eta_{j,in}\eta_{j,out}}, \quad j = \overline{I,S}. \tag{2.33}$$

In the approximation of small losses eq.(2.33) converts to:

$$G(\Omega > \sqrt{K_{I,FPM}}) \approx \frac{\left(\frac{2\eta_{tot}-3}{\eta_{tot}-1}\right)}{\frac{1}{\cosh\left(2r\right)}+2\left(\frac{2\eta_{tot}-3}{\eta_{tot}-1}\right)}. \tag{2.34}$$

Therefore, the input and output losses are equally important. Another situation is for low frequency range $\Omega < \sqrt{K_I'}$. Increasing input losses is more detrimental in comparison to output losses:

$$G(\Omega < \sqrt{K_{I,FPM}}) \approx \frac{1+\epsilon_{I,in}}{\frac{1}{\cosh\left(2r\right)}+\epsilon_{I,in}+\epsilon_{S,in}+\epsilon_{S,Out}\tan\left(\phi_S\right)}, \quad \epsilon_{j,l} = \frac{1-\eta_{j,l}}{\eta_{j,l}}, \quad j = \overline{I,S}, \quad l = \overline{\text{in,out}}. \tag{2.35}$$

The case of non-symmetric losses is investigated on Figure 2.5(b). Remarkably, the sensitivity gain scales down rapidly with the growth of the imbalance between the input optical losses. The effect is pronounced less if the output losses are significantly different.

2.4.4 Optimization of squeezing factor

The presence of intrinsic spin thermal noise along with non-perfect matching of susceptibilities between two systems results in a complex dependence of the strain sensitivity $S_{h,atoms}$ on squeezing factor r and Fourier spectral frequency Ω. Consequently, increasing the strength of correlations r improves the broadband suppression of total quantum noise only until a certain value r_{min} is reached. The level r_{min} depends on cooperativity C_S, carrier phase angle ϕ_S and interferometer coupling rate K_I'. Exceeding such threshold will allow to gain the sensitivity at high/low frequencies at the cost of extra noise around $\Omega \sim \sqrt{K_I'}$, making a characteristic dip [7] bigger. One can optimize the squeezing factor r for a specific spectral frequency Ω, obtaining $r_{\text{opt.}}(\Omega)$ [43], as shown on Figure 2.6(a). It will result in the best possible sensitivity gain $S_{h,atoms}(r_{\text{opt.}}(\Omega),\Omega)$ (fig.2.6(b), black curve) in a whole spectrum range of interest. At any fixed value $r > r_{min}$ optimal sensitivity gain might be achieved only locally, around specific Ω. From the experimental point of view it would be beneficial to choose $r = r_{min}$ for the given setup since it will ensure the most uniform improvement in the sensitivity across the entire frequency range.

[7] Such a deep is clearly seen, for example, in Figure 2.4(a,b)

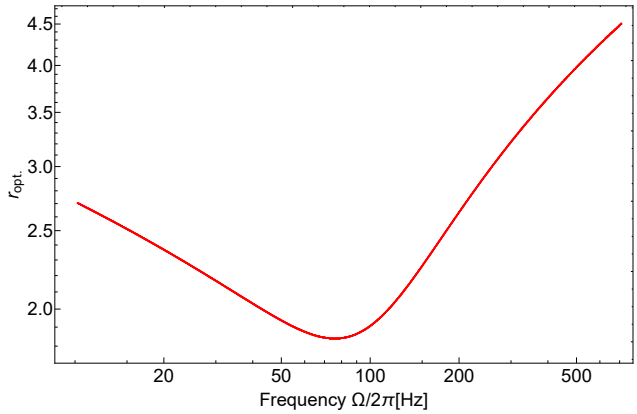

(a) Squeezing factor r optimized across the spectral range of interest.

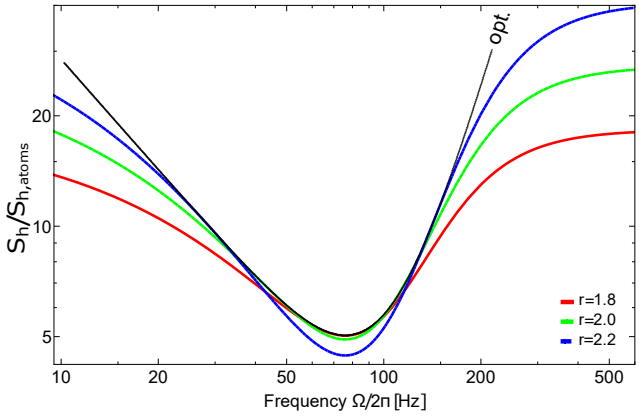

(b) Sensitivity gain relative to the SQL-limited GWD, when r is adjusted as function of Fourier frequency Ω, corresponding to the black curve. Red, green and blue curves demonstrate the sensitivity improvement, when coefficients r are fixed.

Figure 2.6: Optimization of squeezing factor $r = r(\Omega)$ is explored. $C_S = 10$, $K_I' = (100Hz)^2$, $\phi_S = \pi/6$ entail $r_{min} \approx 1.85$.

Chapter 3

Entanglement source

3.1 Introduction

Exploitation of quantum effects enabled completely new methods in computation and communications protocols. Quantum information processing (QIP) and quantum key distribution (QKD) can be given as examples. Among various physical platforms, light is a promising candidate for implementation of aforementioned quantum algorithms. Distinctive properties of photons make them an excellent carrier of information and can be utilized in quantum networks [45]. In quantum computation, light can serve as a primary platform [46], but also as a part of integrated schemes [47]. In particular, the electromagnetic field efficiently couples to systems that act like harmonic oscillators, such as optomechanical membranes and atomic ensembles extensively discussed in this thesis. It opens up the possibility to leverage the benefits of *continuous variables* (CV) in quantum enhanced protocols implemented in hybrid composite systems [48].

Entangled states of light play a key role in majority of quantum algorithms, being, for example, an essential part of quantum teleportation scheme [49],[50]. Remarkably, having distributed the entanglement between light modes with different wavelengths (colors), one can use the teleportation to link physically disparate quantum systems, which are suitable for solution of specific classes of tasks. A significant advantage of entanglement in continuous variables is the opportunity to perform the protocols, inclding teleportation, in unconditional manner [48],[51]. However, strong correlations between entangled modes are required in order to ensure the sufficient fidelity of operations. Therefore, the development of methods to generate high-quality entanglement sources is an important task in contemporary quantum engineering.

In this chapter we describe the preparation and characterization of the entanglement between optical modes separated by $\sim$ 200 nm and encoded in continuous variables. High level of interbeam correlations allows for demonstration of EPR-steering, the entanglement is also proved by means of Duan criterion. The quantum noise reduction -7.1 dB below the shot noise level is achieved down to middle-audioband frequencies. It thus represents an important intermediate result, considering the goal to create the entanglement source suitable for the scheme of sensitivity improvement for GWDs studied in this thesis. The specific choice of 852 nm and 1064 nm for the wavelengths of the entangled optical modes is made to enable interaction with the spin ensemble of Cs atoms and GWD interferometer respectively. However, exploiting the flexibility of the scheme presented in this chapter, it is feasible, for example, to implement the quantum interface between telecom fiber networks with quantum memory that might be seen as essential component of a quantum repeater [52, 53, 54]. In a broader prospective, one can envision an application of EPR-entangled states in the field of metrology [55].

The experiment was carried out by the author of this thesis and Tulio Brito Brazil. The author contributed to all parts of experiment, such as building the optical setup, setting and adjusting the electronic control schemes, collection and processing of final experimental data.

3.1.1 Review of criteria for entanglement

The concept of entangled states was introduced by Schrodinger [56] and played an essential role in the formulation of the EPR-paradox [57], which raised the concerns about the completeness of quantum mechanics theory developed by that time. The entanglement is defined through the violation of separability criterion, which for

particular case of 2 modes takes the form:

$$\hat{\rho} = \sum_{j}^{N} \mu_j \rho_j^A \otimes \rho_j^B, \tag{3.1a}$$

$$\hat{\rho} = \int \rho_\alpha^A \otimes \rho_\alpha^B P(\alpha)\, d\alpha. \tag{3.1b}$$

Here the expressions for both cases of discrete variables (DV) and continuous variables (CV) are presented in eq.(3.1a) and eq.(3.1b) respectively, $\sum_j^N \mu_j = 1$, $\int P(\alpha)\, d\alpha = 1$, index j (variable α) determines discrete (continuous) spectrum of density operator $\hat{\rho}_{A(B)}$. For the mode $m = \{A, B\}$ we define the observable $\hat{x}_l^m$ with eigen-(wave)-vectors $|x_l^m\rangle$ and eigenvalues x_l^m as a result of measurement in basis set by $l = \{\theta, \phi\}$, $\theta(\phi)$ is a choice for the mode $A(B)$. Using the (conditional) probability $P_{loc}(x_l^m|l, \alpha) = \langle x_l^m|\, \hat{\rho}_l\, |x_l^m\rangle$ to perform the measurement of localized quantum state in mode $A(B)$, we can re-write the separability condition eq.(3.1) in terms of hte joint probability $P(x_\theta^A, x_\phi^B)$:

$$P(x_\theta^A, x_\phi^B) = \int P_{loc}(x_\theta^A|\theta, \alpha) P_{loc}(x_\phi^B|\phi, \alpha) P(\alpha)\, d\alpha. \tag{3.2}$$

The EPR-paradox questioned the completeness of quantum mechanics, proposing the 'modification' of introduced theory, but assuming the validity of the *local realism*. The concept developed by Bell, however, allowed to reconsider the main conclusions of EPR-paper. In assumption of locality principle, Bell [58] and Clauser [59] deduced the expression of joint probability $P(x_\theta^A, x_\phi^B)$ in the manner of eq.(3.2):

$$P(x_\theta^A, x_\phi^B) = \int P(x_\theta^A|\theta, \alpha) P(x_\phi^B|\phi, \alpha) P(\alpha)\, d\alpha, \tag{3.3}$$

where α is now considered as the *local hidden variable*. The latter is the set of parameters distributed between modes A and B, which in some sense pre-determines the results of measurements in each mode while remaining (technically) inaccessible in the experiments. Eq.(3.3) forms the basis of Bell inequalities: postulates of the locality principle should be complied if inequality holds. Whereas violation of Bell inequality, as well as failure of eq.(3.3), is permissible by quantum mechanics theory but implies the failure of the theory of local hidden variables that might be treated as extrapolation of local realism concept in that case. Violation of Bell inequality was predicted to be possible in case of utilization of so called Bell states which will later turn out to be perfectly entangled state [60]. It has to be noted that eq.(3.3) does not necessarily assumes that the measurements on the local quantum states are performed since $\rho^{A(B)}$ is not introduced in contrast to eq.(3.2). From this perspective, the violation of Bell inequalities is more challenging compared to the violation of separability condition.

The EPR-paradox can be studied in terms of inferred variances. We consider the situation, where two observers, Alice and Bob, measure the canonical position of localized objects ($x^A \equiv x$ and x^B, respectively), and Alice tries to predict the result of her measurement using the information obtained from Bob measurement outcome. In order to do so, Alice calculates the expected value $x_{pre}(x^B)$. She then can estimate the discrepancy between obtained and predicted results, using the expression:

$$\Delta_{inf}(x)^2 = \int \left(x - x_{pre}(x^B)\right)^2 P(x, x^B)\, dx dx^B, \tag{3.4}$$

which will be referred to as the inferred variance. The right hand side of eq.(3.4) can be minimized if $x_{pre} = \langle x|x^B\rangle$ is selected for each possible x^B [61]:

$$\Delta_{inf}(x)^2 \to \mathsf{min} \equiv V_{A|B}^x \tag{3.5}$$

We follow the same procedure for determining $\Delta_{inf}^2(p)$ and $V_{A|B}^p$ for the canonical momentum p. The Heisenberg uncertainty principle dictates that [61] the requirement $\Delta_{inf}(x)^2 \Delta_{inf}(p)^2 \geq V_{A|B}^x V_{A|B}^p \geq 1$ should be satisfied for the localized quantum state in Alice mode. On the other hand, observing

$$\Delta_{inf}(x)^2\Delta_{inf}(p)^2 < 1 \tag{3.6}$$

brings to the precision level beyond the Heisenberg fundamental limit. Since fulfilling the condition eq.(3.6) manifests the incompatibility of local realism with quantum mechanics, it can be considered as EPR criterion leading to EPR-paradox as was formulated in [62].

The condition eq.(3.6) can not imply a direct exchange of the information between Alice and Bob. However, it might appear that Bob through his local measurement implements the control of the state in Alice mode. Hence, the criterion eq.(3.6) is linked to EPR-steering [61]. Apart from measuring the inferred variances, Reid also proposed alternative strategy to witness EPR-paradox. One can assume the particular case, where Alice makes a prediction $x_{pre} = gx^B$, based on result of Bob's measurement x^B. The selection $g = \Delta(xx^B)/\Delta(x^B)^2$ for Gaussian case leads to minimized inferred variance $\Delta^2_{inf}(x) = V^x_{A|B}$, see eq.(3.5). Therefore, such a reduction of the noise in the linear combinations of Alice's and Bob's canonical variables $\left\{\hat{x}^A - g\hat{x}^B, \hat{p}^A - g'\hat{p}^B\right\}$ that satisfies

$$\Delta\left(x^A - gx^B\right)^2 \Delta\left(p^A - g'p^B\right)^2 < 1 \tag{3.7}$$

is equal to the condition eq.(3.6) and proves the EPR-paradox[1]. The inequality (3.7) offers the convenient way to verify EPR-steering criterion in the experiments and will be extensively investigated further in this thesis.

We now study the case of two-mode Gaussian states characterized by homodyne measurements and examine the EPR-paradox by describing the results in terms of joint probability $P(x^A_\theta, x^B_\phi)$ (see eq.(3.3), eq.(3.2)). Failure of

$$P(x^A_\theta, x^B_\phi) = \int P_{loc}(x^A_\theta|\theta,\alpha)P(x^B_\phi|\phi,\alpha)P(\alpha)\,d\alpha \tag{3.8}$$

is equivalent to the demonstration of EPR paradox here [63]. Condition eq.(3.8) was written under the assumption of localized quantum state in Alice's mode, but not in Bob's mode, thus implying 'asymmetric' locality principle.

One can see that condition eq.(3.8) is not equal to requirements eq.(3.2) and eq.(3.3), although each of the three conditions can be violated if the distributed modes display quantum correlations. In particular, the violation of separability condition doesn't necessarily lead to the confirmation of the EPR-paradox. In fact, we will use the definition of EPR-entanglement as subtype of an entanglement strong enough to prove Reid criterion. In turn, demonstration of the EPR-paradox is in general not sufficient for violation of the Bell inequality. Although measuring canonical variables $\{\hat{x}, \hat{p}\}$ can not show the inconsistency between the theory of local hidden variables with predictions of quantum mechanics for two-mode Gaussian states in CV [61], in generalized case the certification of Bell nonlocality demands stronger correlations in comparison to the steering effect. At the same time, as was pinpointed earlier, demonstration of EPR-steering is more feasible from experimental point of view and in principle can serve as a quantitative measure of entanglement level for investigated state. Exploring the correlations between two modes, one can introduce the parameter ϵ_{EPR} as a product of variances in eq.(3.7):

$$\epsilon_{EPR} = \Delta\left(x^A - gx^B\right)^2 \Delta\left(p^A - g'p^B\right)^2 \tag{3.9}$$

obviously having in mind values $\epsilon_{EPR} < 1$. As an alternative to the EPR-steering metric, we can apply the measure of intermode correlation strength from Duan criterion[2] [37]:

$$\Delta_D = \Delta\left(\frac{x^A - x^B}{\sqrt{2}}\right)^2 + \Delta\left(\frac{p^A + p^B}{\sqrt{2}}\right)^2. \tag{3.10}$$

The Duan criterion is derived from the separability condition and the positive partial transpose (PPT) criterion [64]. Hence Duan sets the threshold $\Delta_D = 2$; reducing this value for specific two-mode states is enough to demonstrate an entanglement. As expected, the violation of the inequality in Reid criterion is more demanding than violation of the Duan inequality. We also notice that reducing noise down $\Delta_D = 1$ is sufficient condition to infer EPR-paradox verification.

We now consider two-mode squeezed state of light (eq.(1.21), eq.(1.23)) with correlations between modes characterized by parameter r. Taking into account eq.(1.18), eq.(1.19), we expect to obtain for inferred variances $\Delta_{inf}(x)^2$, $\Delta_{inf}(p)^2$ (eq.(3.5))

[1] We will refer to this as demonstration of EPR paradox in a manner proposed in original EPR paper

[2] this criterion was already introduced in eq.(2.6) to prove entanglement between two disparate mechanical systems

$$\Delta_{inf}(x)^2|_{\min} = \Delta_{inf}(p)^2|_{\min} = \frac{1}{\cosh(2r)} \tag{3.11}$$

as well as for linear combinations $x^A - gx^B$ and $p^A - g'p^B$ with $g_{opt} = -g'_{opt} = \tanh(2r)$, as predicted by eq.(1.29). As a result, the EPR steering is confirmed with ϵ_{EPR} equal to:

$$\epsilon_{EPR} = \left(\frac{1}{\cosh(2r)}\right)^2. \tag{3.12}$$

At the same time, the Duan criterion yields for TMSV state:

$$\Delta_D = 2e^{-2r}. \tag{3.13}$$

Along with level of two-mode squeezing r, EPR and Duan criteria are the main instruments for characterization of the entangled state of light reported in this thesis.

3.1.2 Experimental approaches

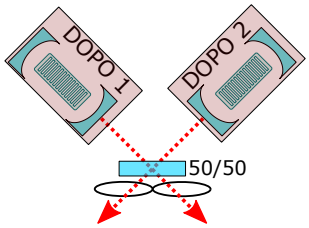

(a) Two monochromatic optical modes are overlapped onto symmetric beamsplitter, producing entanglement.

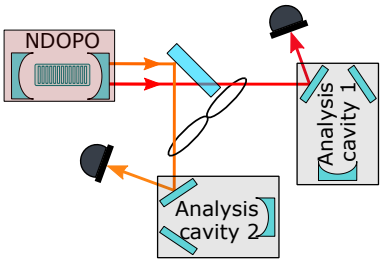

(b) Non-monochromatic entanglement is characterized without external local oscillators by means of 'self-homodyning'.

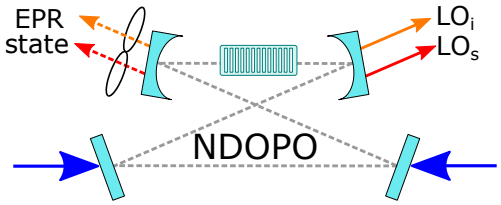

(c) Cavity is pumped from different directions, creating twin different-color twin beams and local oscillators for each wavelength.

Figure 3.1: Different approaches to generate EPR-entangled states of light.

$\chi^{(2)}$-nonlinear media enable efficiently generating two-mode squeezed states, which makes them central for many experimental techniques for demonstrating and exploiting continuous-variable entanglement. Inherently weak non-linear interaction can be enhanced by placing $\chi^{(2)}$-medium inside a resonator. The first observation of continuous-variable entanglement evidenced as a violation of the EPR criterion was made in [65]. Optical Parametric Oscillator was operated below threshold with type-II parametric down conversion process. Entanglement was obtained for frequency degenerate fields that had orthogonal polarizations. The quadratures in the phase space for each mode played a role of canonical position and momentum, optical modes were explored by means of homodyne detection. Calculation of inferred variances eq.(3.4) confirmed entanglement characterized by factor $\epsilon_{EPR} = 0.7 < 1$ eq.(3.9). Since then, many efforts were made to improve the strength of correlation and their stability. A substantial progress was achieved by using an interference of two single-mode squeezed states of light, each of them produced by type-I process in subthreshold OPO. Provided well-established techniques for the generation of high-quality single-mode squeezed states exist, this strategy led to the strongest (to date) level of entanglement with $\epsilon_{EPR} = 0.04$ measured in [66]. On the other hand, frequency tunability of entanglement sources has been also explored by operating OPO in non-degenerate configuration. In [67] the violation of EPR paradox was certified for the spectral modes that are separated by two free spectral ranges (FSR) symmetrically to degenerate mode, leading to ~ 1 GHz frequency difference. This experiment was designed in such a way, that only a frequency near-degenerate entangled state can be prepared and detected. Phase-matching conditions were confining the frequency difference for entangled modes, and at the same time preparation method of local oscillators (LOs) has limited them to be practically monochromatic.

In order to demonstrate the entanglement between beams of truly different colors (i.e. with a large wavelength separation), one can in principle utilize the non-linear interaction enhanced by a cavity. The adjustment of phase-matching conditions guarantees signal-idler entangled modes to be non-degenerate. However, homodyne detection

is typically not available due to absence of LOs. One way to circumvent this issue is to operate OPO above the threshold. In experiments [68], [69] bright entangled beams after exiting the OPO were sent onto auxiliary cavities and detected after reflection. The phase of the sidebands reflected from the cavity is rotated depending on the Fourier frequency. Thus, the 'self-homodyning' has been realised with the mean fields that served as a reference and replaced LOs. While this scheme allows for verification of entanglement criteria, the characterization of output state is still not equivalent to the proper homodyne measurement. A frequency dependent phase after the reflection from "auxiliary" cavities makes possible to detect squeezing in phase/amplitude quadratures only in specific frequency ranges. Furthermore, the imbalance between the amplitude and phase correlations was observed in experiments [68] [69]. The quantum noise suppression in the sum of phase quadratures was limited possibly due to excess phase noise of pump laser and could be observed for the values of the power of the injected pump close to the threshold.

OPA below threshold was predicted to enable EPR correlations between different colors [70]. In experimental realizations phase sensitive [71] and phase insensitive [72] regimes were explored. Proper characterization of obtained correlations was achieved by combining OPA regime with above threshold OPO to generate LOs, which were used to implement the homodyne detection. Such strategy allowed to unite the advantages of OPO and OPA. Symmetric noise suppression in both sum of phase quadratures and difference of amplitude quadratures was accomplished, in contrast to [68]. After optimization of detection efficiency, 6dB of two-mode squeezing [73] was demonstrated, meaning strong different-color entanglement. Unfortunately, performance of OPO above threshold limits phase-locking stability in this case and consequently reduces the level of signal-idler correlations, especially in low-frequency range. Moreover, both OPO and OPA share the same phase-matching conditions. As a result, the entangled beams are strictly linked to local oscillators, leading to lack in the flexibility of such experimental realization.

3.2 Theory of Optical Parametric Oscillators: equations of motion

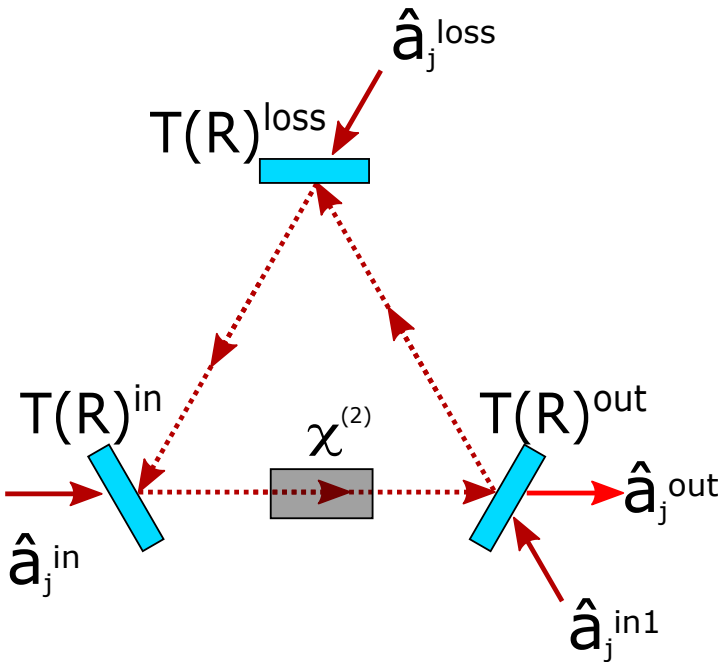

Figure 3.2: Simplified illustration of cavity with non-linear medium $\chi^{(2)}$ inside. Coefficients $T(R)^{in}$ and $T(R)^{out}$ represent the transmissivity (reflectivity) of input and output port, respectively. The coefficients $T(R)^{loss}$ correspond to the fictitious mirror to account for the intracavity losses. The optical fields $\hat{a}_j^{in}$ and $\hat{a}_j^{out}$ enter the cavity through input and output mirrors, whereas $\hat{a}_j^{loss}$ appears due to the intracavity losses. Index j refers to the signal, idler or pump field.

We study three wave mixing process inside an optical resonator with a $\chi^{(2)}$-nonlinear medium inside. Instead of eq.(1.16), we now write down the interaction Hamiltonian as:

$$\hat{H}_{int} \sim i\hbar g \left(\hat{a}_P \hat{a}_s^\dagger \hat{a}_i^\dagger - \hat{a}_P^\dagger \hat{a}_s \hat{a}_i \right), \tag{3.14}$$

where $\hat{a}_{s(i)}$ (the index 'L' is omitted) are the field operators for the signal (idler) carrier frequency. Signal, idler and pump fields (denoted as $\hat{a}_j$, where $j = \overline{s,i,P}$, respectively) interact inside an *optical parametric oscillator* (OPO), which consists of a cavity with 3 mirrors and $\chi^{(2)}$ medium inside, as presented in Figure 3.2. The first mirror (with T_j^{in}/R_j^{in} as coefficients of transmission/reflection) is the input port for drive fields $\hat{a}_j^{in}$. The second mirror will be referred to as the output port (T_j^{out}/R_j^{out}), the fields exiting OPO through this mirror $\hat{a}_j^{out}$ are sent to the detector. However, we also assume that external fields can enter OPO through the output port, and we denote them as $\hat{a}_j^{in1}$. The last mirror (T_j^{loss}/R_j^{loss}) is used to introduce intracavity losses (in the simplified model this mirror is only source of losses in the OPO). In that case the 'transmission' T_j^{loss} of the last mirror determines losses. This mirror also allows the another external field $\hat{a}_j^{loss}$ to enter cavity. Hence, we write down the Langevin equations for signal, idler and pump modes in the following form:

$$\frac{d}{dt}\hat{a}_s = i\Delta_s \hat{a}_s - \gamma_s \hat{a}_s + g\hat{a}_P \hat{a}_i^+ + \sqrt{2\gamma_s^{in}}\hat{a}_s^{in} + \sqrt{2\gamma_s^{out}}\hat{a}_s^{in1} + \sqrt{2\gamma_s^{loss}}\hat{a}_s^{loss}, \tag{3.15a}$$

$$\frac{d}{dt}\hat{a}_i = i\Delta_i \hat{a}_i - \gamma_i \hat{a}_i + g\hat{a}_P \hat{a}_s^+ + \sqrt{2\gamma_i^{in}}\hat{a}_i^{in} + \sqrt{2\gamma_i^{out}}\hat{a}_i^{in1} + \sqrt{2\gamma_i^{loss}}\hat{a}_i^{loss}, \tag{3.15b}$$

$$\frac{d}{dt}\hat{a}_P = i\Delta_P \hat{a}_P - \gamma_P \hat{a}_P + g\hat{a}_s \hat{a}_i + \sqrt{2\gamma_P^{in}}\hat{a}_P^{in} + \sqrt{2\gamma_P^{out}}\hat{a}_P^{in1} + \sqrt{2\gamma_P^{loss}}\hat{a}_P^{loss}, \tag{3.15c}$$

where for each line: the first term on the right hand side corresponds to the detuning Δ_j of the signal (idler/pump) frequency from the cavity resonance, the second term describes the damping of the fields inside the resonator with overall leakage (decay) rate $\gamma_{s(i)}$, the third term corresponds to parametric interaction on the nonlinear medium with interaction strength g, and the last three terms correspond to the couplings of the intracavity fields to the external fields $\hat{a}_j^{in}$, $\hat{a}_j^{in1}$ and $\hat{a}_j^{loss}$. The coupling with each external field injected to the OPO is characterized by it's own leakage rate γ_j^k:

$$\gamma_j^k = \frac{c}{L}\left(1 - \sqrt{1 - T_{k,j}}\right), \quad k = \overline{\mathsf{in,out,loss}}, \quad j = \overline{\mathsf{s,i,P}}, \tag{3.16}$$

where c is the speed of light, L is the cavity length, $(c/L)^{-1}$ is round trip time of photon in a resonator. Total leak rate combines all losses sources of OPO for each wavelength: γ_j: $\sum_k \gamma_j^k = \gamma_j$.

In order to study signal-idler correlations, we do several simplifications here: we suppose that the cavity is resonant with the signal ω_s ($\hat{a}_s$) and idler ω_i ($\hat{a}_i$) modes (that implies $\Delta_s = \Delta_i = 0$). We also consider the regime of strong and undepleted pump that is described by the classical coherent amplitude $\alpha_P = \tilde{\alpha}_P e^{i\theta_P}$, therefore we will discard the Langevin equation for the pump (α_P remains unchanged). Finally, for the signal/idler ports all external fields $\hat{a}_{s(i)}^k$, $k = \overline{in, in1, loss}$ are in vacuum state. We again introduce the amplitude $\hat{x}_{s(i)}$, phase $\hat{p}_{s(i)}$ and generalized quadratures $\hat{q}_{s(i)}(\zeta)$. Using eq.(3.15), one can obtain the dynamics of signal/idler quadrature operators:

$$\frac{d}{dt}\hat{q}_s(\psi_+) = \epsilon\sqrt{\gamma_s\gamma_i}\hat{q}_i(\psi_-) - \gamma_s\hat{q}_s(\psi_+) + \sqrt{2\gamma_s^{in}}\hat{q}_s^{in}(\psi_+) + \sqrt{2\gamma_s^{out}}\hat{q}_s^{in1}(\psi_+) + \sqrt{2\gamma_s^{loss}}\hat{q}_s^{loss}(\psi_+) \tag{3.17a}$$

$$\frac{d}{dt}\hat{q}_i(\psi_-) = \epsilon\sqrt{\gamma_s\gamma_i}\hat{q}_s(\psi_+) - \gamma_i\hat{q}_i(\psi_-) + \sqrt{2\gamma_i^{in}}\hat{q}_i^{in}(\psi_-) + \sqrt{2\gamma_i^{out}}\hat{q}_i^{in1}(\psi_-) + \sqrt{2\gamma_i^{loss}}\hat{q}_i^{loss}(\psi_-) \tag{3.17b}$$

where $\hat{q}_{s(i)}^k(\psi_\pm) = \cos(\psi_\pm)\hat{x}_{s(i)}^k + \sin(\psi_\pm)\hat{p}_{s(i)}^k$, $k = \overline{in, in1, loss}$; parameter $\epsilon = \tilde{\alpha}_P/\alpha_{P,th}$ determines the ratio between pump field amplitude $\tilde{\alpha}_P$ and threshold value $\alpha_{P,th} = \sqrt{\gamma_s\gamma_i}/g$. Eqs.(3.17) show that the parametric interaction happens only between signal $\hat{q}_s(\psi_+)$ and idler $\hat{q}_i(\psi_-)$ quadratures whose phases are anti-symmetric relative to the pump phase such that $\psi_\pm = \theta_P/2 \pm \theta$. Notably, the quadratures of incoming vacuum fields $\hat{q}_{s(i)}^j(\psi_\pm)$ do not depend on phase angle; hereinafter we omit their phases. Without a loss of generality we can set $\theta_P = 0$.

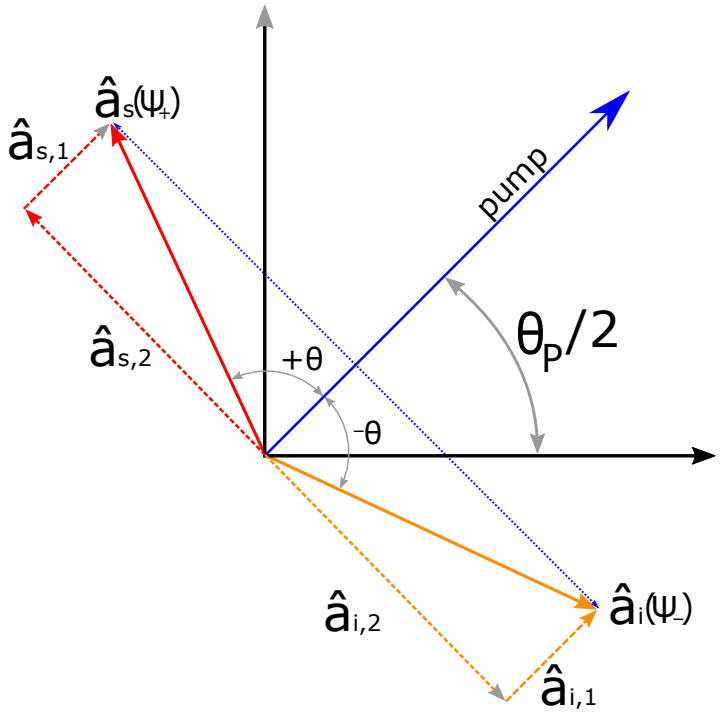

Figure 3.3: Phasor diagram of parametric down-conversion.

Then the expression $\hat{q}_s(\psi_+) - \hat{q}_i(\psi_-)$ converts to $\hat{x}_s - \hat{x}_i$ when $\theta = 0$ and $\hat{p}_s + \hat{p}_i$ at $\theta = \pi/2$ (see Figure 3.3), which can be recognized as EPR-variables.

We apply a Fourier transformation to the system3.17 and write down the equations in a matrix form:

$$\begin{bmatrix} \gamma_s - i\omega & \epsilon\sqrt{\gamma_s\gamma_i} \\ \epsilon\sqrt{\gamma_s\gamma_i} & \gamma_s - i\omega \end{bmatrix} \begin{bmatrix} \hat{q}_s(\psi_+) \\ \hat{q}_i(\psi_-) \end{bmatrix} = \tag{3.18}$$

$$= \begin{bmatrix} \sqrt{2\gamma_s^{in}} & 0 \\ 0 & \sqrt{2\gamma_i^{in}} \end{bmatrix} \begin{bmatrix} \hat{q}_s^{in} \\ \hat{q}_i^{in} \end{bmatrix} + \begin{bmatrix} \sqrt{2\gamma_s^{out}} & 0 \\ 0 & \sqrt{2\gamma_i^{out}} \end{bmatrix} \begin{bmatrix} \hat{q}_s^{in1} \\ \hat{q}_i^{in1} \end{bmatrix} + \begin{bmatrix} \sqrt{2\gamma_s^{loss}} & 0 \\ 0 & \sqrt{2\gamma_i^{loss}} \end{bmatrix} \begin{bmatrix} \hat{q}_s^{loss} \\ \hat{q}_i^{loss} \end{bmatrix}$$

The system eq.3.18 can be applied to get a solutions for intracavity fields $\{\hat{q}_s(\psi_+), \hat{q}_i(\psi_-)\}$. The next step is to obtain the expressions for output (transmitted) fields $\left\{\hat{q}_s^{out}(\psi_+), \hat{q}_i^{out}(\psi_-)\right\}$ using the input/output relations:

$$\hat{q}_{s(i)}^{out}(\psi_\pm) = \sqrt{2\gamma_{s(i)}^{out}}\hat{q}_{s(i)}(\psi_\pm) - \hat{q}_{s(i)}^{in1} \tag{3.19}$$

and to detect the linear combination of output fields $\hat{q}_s^{out}$, $\hat{q}_i^{out}$

$$\hat{A}_{tot}^{out}(\phi) = N(\phi)\left[\cos(\phi)\hat{q}_s^{out}(\psi_+) - \sin(\phi)\hat{q}_i^{out}(\psi_-)\right]. \tag{3.20}$$

Here $N(\phi)$ is the normalization factor which determines the reference which we want to compare with. If we measure any superposition of two modes ($\phi \neq (\pi/2)n$, n - any integer number), then $N = 2$ since our benchmark is two independent modes each SQL-limited. Otherwise we should compare with SQL in single mode, and in that case $N = 1$. Calculating the variance of the output field $\langle \Delta\left(\hat{A}_{tot}^{out}(\phi)\right)^2 \rangle \equiv S_{\hat{A}_{tot}^{out},\hat{A}_{tot}^{out}}$, we finally arrive to the following result [67]:

$$S_{\hat{A}_{tot}^{out},\hat{A}_{tot}^{out}} = N(\phi)\left[1 + 4\epsilon\eta_{esc}\frac{2\epsilon(\sigma\cos^2(\phi) + \sigma^{-1}\sin^2(\phi)) - \left(\Delta^2 + 1 + \epsilon^2\right)\sin(2\phi)}{(\Delta^2 + (E+\Lambda)^2)\cdot(\Delta^2 + (E-\Lambda)^2)}\right]. \tag{3.21}$$

Here $\eta_{esc.s(i)} = \gamma^{out}_{s(i)}/\gamma_{s(i)}$ is escape efficiency for signal(idler) wavelength, $\eta_{esc} = \sqrt{\eta_{esc.s}\eta_{esc.i}}$ is the generalized escape efficiency, $\Delta = \Omega/\sqrt{\gamma_s\gamma_i}$ is the normalized Fourier frequency, $\sigma = \sqrt{\eta_{esc.s}/\eta_{esc.s}}$ is escape efficiency asymmetry, $\Lambda = (\rho+\rho^{-1})/2$ represents the loss asymmetry with $\rho = \sqrt{\gamma_s/\gamma_i}$, $E = \sqrt{\epsilon^2 + \Lambda^2 - 1}$. In addition to intracavity losses, we introduce the losses attributed to the propagation way of signal/idler mode to the homodyne detection setup. It is done by replacing escape efficiency $\eta_{esc,j}$ by the total efficiency $\eta_j = \eta_{esc,j}\eta_{det,j}$ in eq.(3.21). The new term $\eta_{det,j}$ is the detection efficiency, which takes into account a non-ideal degree of overlapping with Local oscillators, the photodiode efficiency and the absorption on the optics between OPO and homodyne detectors. In case of symmetric losses ($\rho = \sigma = \Lambda = 1$ and $E = \epsilon$), the best quantum noise suppression relative to the two-mode vacuum noise is achieved at subtraction of signal from idler with equal weights [67] (setting $\phi = \pi/4$), as given by the following expression:

$$S_{\hat{A}^{out}_{tot},\hat{A}^{out}_{tot}}|_{\pi/4} = 2\left(1 - \eta\frac{4\epsilon}{\Delta^2 + (\epsilon+1)^2}\right) \tag{3.22}$$

that coincides with the result for the single-mode squeezing. Dependence of interbeam correlations on the pump power for different total losses is presented on Figure 3.4. We also notice that the choice $\phi = 3\pi/4$ leads to the detection of the sum of two quadratures and yields the maximal enhancement of quantum noise relative to vacuum noise since we would detect anticorrelated quadratures in this case (corresponding to antisqueezing if the analogy to in single mode squeezing is made). The noise in single (either signal or idler) mode is obtained from the eq.(3.21) by setting $\phi = 0$ or $\phi = \pi/2$ [67] and corresponds to the thermal state as in eq.(1.22).

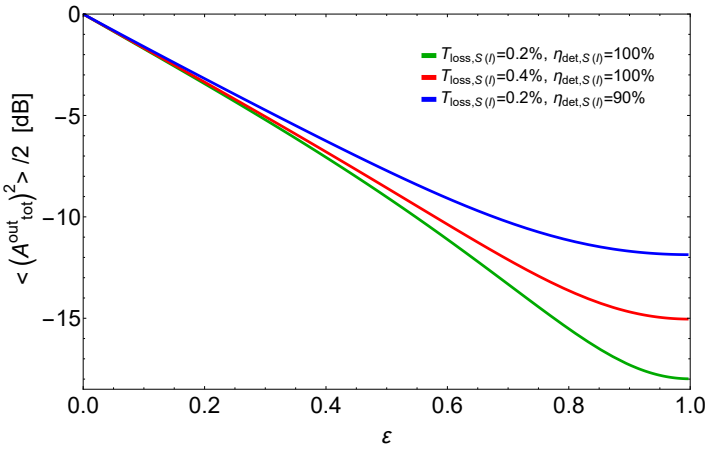

(a) The case of symmetric losses between signal and idler channels. The effect of changing of intracavity losses $T_{loss,s(i)}$ (leading to changing of escape efficiency) as well as varying detection efficiency $\eta_{det,s(i)}$ is shown.

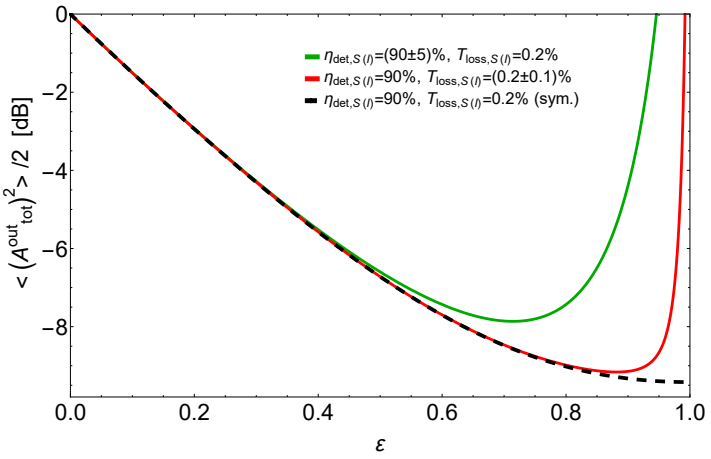

(b) The interbeam correlations at asymmetric intracavity losses or detection efficiencies are compared with the case of symmetric losses. The total escape efficiency and total detection efficiency are equal to $\eta_{esc} = \sqrt{\eta_{esc,s}\eta_{esc,i}}$=0.984 (corresponding to $T_{loss} = 0.2\%$) and $\eta_{det} = \sqrt{\eta_{det,s}\eta_{det,i}}$=0.9, respectively.

Figure 3.4: Interbeam correlations with equal weights $\phi = \pi/4$ is plotted as a function of pump power. Losses due input/output ports remain the same: $T_{out,s(i)} = 0.12$, $T_{out,s(i)} \gg T_{loss,s(i)} \gg T_{in,s(i)}$ (so $T_{in,s(i)} \approx 0$), $\Delta = 0$.

Non-equal losses for the signal and idler modes (due to different intracavity losses $T_{loss,s} \neq T_{loss,i}$ or detection efficiencies $\eta_{det,s} \neq \eta_{det,i}$) cause a sharp enhancement of quantum noise and contamination of signal-idler correlation (shown on Figure 3.4(b)) starting from some critical value of ϵ (which depends on concrete values of escape efficiencies) in comparison to symmetric case (displayed on Figure 3.4(a)). Asymmetric losses make the choice of equal weights for $\hat{q}_s$ and $\hat{q}_s$ non-optimal. Therefore, the deviation from $\phi = \pi/4$ can compensate the asymmetry and improve the strength of signal-idler correlation, see Figure 3.5(a). In particular, a fine alignment of the relative weight $g = g(\psi)$ allows to almost completely recover the interbeam correlations in comparison to the symmetric case.

The next step is the inclusion of the phase noise into the model. The detrimental effect of the phase noise can be understood as a jitter in ψ_+ and ψ_- angles, which determine the phase of signal and idler quadrature, respectively. As a result, instead of detecting $\hat{q}_s(\psi_+)$ for the signal quadrature, one measures $\hat{q}_s(\psi_{+,1}) = \cos(\theta_s)\hat{q}_s(\psi_+) +$

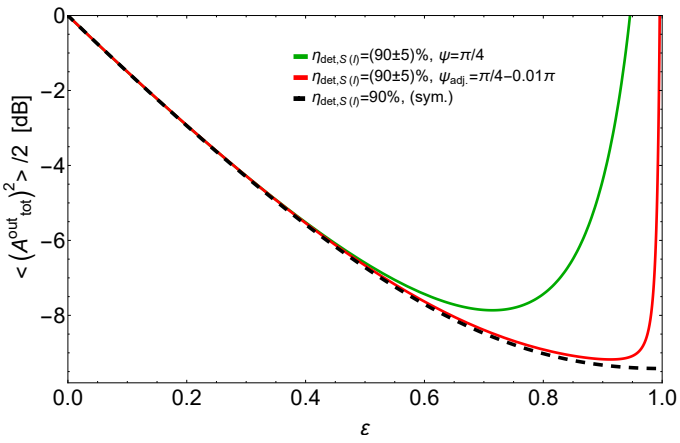

(a) The case of asymmetric detection efficiencies but equal total losses associated with OPO $\gamma_s = \gamma_s$ is demonstrated. Comparing $\langle\Delta\left(\hat{A}^{out}_{tot}(\phi=\pi/4)\right)^2\rangle$ and $\langle\Delta\left(\hat{A}^{out}_{tot}(\phi=\pi/4-0.01\pi)\right)^2\rangle$, one can see that the adjustment of the relative weight mitigates the sharp rise of quantum noise at pump power close to threshold $\epsilon \to 1$. Thus, the effect of non-equal losses is partially cancelled. The case with symmetric equal efficiencies $\eta_{det,s} = \eta_{det,i}$ is shown as reference.

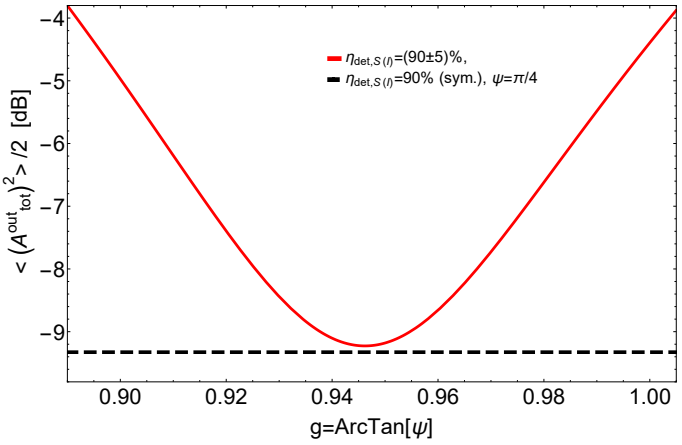

(b) The regime of strong pump $\epsilon = 0.9$ is explored for the case $\eta_{det} = \sqrt{\eta_{det,s}\eta_{det,i}} = 90\%$ and $\eta_{esc,s} = \eta_{esc,i} = 98.4\%$. The equal detection efficiencies $\eta_{det,s} = \eta_{det,i}$ entail $\langle\Delta\left(\hat{A}^{out}_{tot}(\epsilon=0.9,\phi=\pi/4)\right)^2\rangle = -9.33$dB. Introducing the unequal detection efficiencies $\eta_{det,s} = 95\%$, $\eta_{det,i} = 85\%$, we obtain only 4.4dB noise suppression relative to the shot noise, if we record equal superposition of signal and idler quadratures (setting $\phi = \pi/4$). The correlations $\langle\Delta\left(\hat{A}^{out}_{tot}(\epsilon=0.9,\phi)\right)^2\rangle$ at different relative weights are displayed, and the optimal value ϕ_{opt} might be found, giving in our case $\langle\Delta\left(\hat{A}^{out}_{tot}(\epsilon=0.9,\phi_{opt})\right)^2\rangle = -9.23$dB.

Figure 3.5: The possibility to compensate the unequal efficiencies of signal and idler channels by varying the relative weight in $\langle\Delta\left(\hat{A}^{out}_{tot}(\phi)\right)^2\rangle$ is explored.

$\sin(\theta_s)\hat{q}_s(\psi_+ + \pi/2)$, where $\theta_s = \psi_{+,1} - \psi_+$ represents the fluctuations of the signal phase. Similarly, the quadrature $\hat{q}_i(\psi_{-,1}) = \cos(\theta_i)\hat{q}_s(\psi_-) + \sin(\theta_i)\hat{q}_s(\psi_- + \pi/2)$ is detected for the idler mode. The spectrum of the noise associated with the observable $\hat{A}^{out}_{tot,1}(\phi) = \left[\cos(\phi)\hat{q}^{out}_s(\psi_{+,1}) - \sin(\phi)\hat{q}^{out}_i(\psi_{-,1})\right]$ is given by

$$S_{\hat{A}^{out}_{tot,1},\hat{A}^{out}_{tot,1}}|_{\phi=\pi/4} = \langle\Delta\left(\left\{\cos(\theta_s)\hat{q}_s(\psi_+) + \sin(\theta_s)\hat{q}_s(\psi_+ + \pi/2)\right\} - \left\{\cos(\theta_i)\hat{q}_i(\psi_-) + \sin(\theta_i)\hat{q}_i(\psi_- + \pi/2)\right\}\right)^2\rangle =$$
$$= \langle\Delta\left(\hat{q}_s(\psi_+)\right)^2\rangle + \langle\Delta\left(\hat{q}_i(\psi_-)\right)^2\rangle -$$
$$- 2\cos(\theta_s)\cos(\theta_i)\langle\Delta\left(\hat{q}_s(\psi_+)\hat{q}_i(\psi_-)\right)\rangle - 2\sin(\theta_s)\sin(\theta_i)\langle\Delta\left(\hat{q}_s(\psi_+ + \pi/2)\hat{q}_i(\psi_- + \pi/2)\right)\rangle \quad (3.23)$$

where the case of equal losses and, consequently, $\phi = \pi/4$ is chosen. The second line in eq.(3.23) corresponds to the noise in each of signal/idler modes seperately (which are in thermal states, and $\langle\Delta\left(\hat{q}_{s(i)}(\psi_\pm)\right)^2\rangle$ doesn't depend on phase angle $\psi_\pm$). The third line describes signal-idler correlations. As was shown earlier, $\{\hat{q}_s(\psi_+), \hat{q}_s(\psi_-)\}$ are always correlated, and as a direct consequence, $\{\hat{q}_s(\psi_+ + \pi/2), \hat{q}_s(\psi_- + \pi/2)\}$ are always anticorrelated, therefore:

$$\langle\Delta\left(\hat{q}_s(\psi_+)\hat{q}_i(\psi_-)\right)\rangle > 0$$
$$\langle\Delta\left(\hat{q}_s(\psi_+ + \pi/2)\hat{q}_i(\psi_- + \pi/2)\right)\rangle < 0 \quad (3.24)$$

whereas $|\langle\Delta\left(\hat{q}_s(\psi_+)\hat{q}_i(\psi_-)\right)\rangle| = |\langle\Delta\left(\hat{q}_s(\psi_+ + \pi/2)\hat{q}_i(\psi_- + \pi/2)\right)\rangle|$. We introduce root mean square (RMS) quadrature fluctuation in signal $\overline{\theta_s}$ and idler $\overline{\theta_i}$ modes ($\overline{\theta_j} = \sqrt{\int \theta_j^2 d\theta_j}$). Averaging over jittering of quadrature angles, we obtain the spectrum of interbeam correlations from eq.(3.23):

$$S_{\hat{A}^{out}_{tot,1},\hat{A}^{out}_{tot,1}}|_{\phi=\pi/4} = \langle\Delta\left(\hat{q}_s(\psi_+)\right)^2\rangle + \langle\Delta\left(\hat{q}_i(\psi_-)\right)^2\rangle - 2\langle\Delta\left(\hat{q}_s(\psi_+)\hat{q}_i(\psi_-)\right)\rangle\cos\left(\overline{\theta_s} + \overline{\theta_i}\right) \quad (3.25)$$

Phase noise hinders quantum noise reduction as represented in eq.(3.25), which corresponds to $S_{\hat{A}_{tot}^{out},\hat{A}_{tot}^{out}}|_{\phi=\pi/4}$ (given by eq.(3.22)) in the case $\overline{\theta_s} = \overline{\theta_i} = 0$. Eq.(3.25) can be also written in a form

$$S_{\hat{A}_{tot,1}^{out},\hat{A}_{tot,1}^{out}}|_{\phi=\pi/4} = \left[S_{\hat{A}_{tot}^{out},\hat{A}_{tot}^{out}}|_{\phi=\frac{\pi}{4}}\right]\cos^2\left(\frac{\overline{\theta_s}+\overline{\theta_i}}{2}\right) + \left[S_{\hat{A}_{tot}^{out},\hat{A}_{tot}^{out}}|_{\phi=\frac{\pi}{4}+\frac{\pi}{2}}\right]\sin^2\left(\frac{\overline{\theta_s}+\overline{\theta_i}}{2}\right) \tag{3.26}$$

where the term $S_{\hat{A}_{tot}^{out},\hat{A}_{tot}^{out}}|_{\phi=\frac{\pi}{4}+\frac{\pi}{2}}$ stands for the quantum noise of sum of correlated quadratures, being also equivalent to the difference of anticorrelated observables. The contribution of this component is increased with the growth of $\overline{\theta_s}$ and $\overline{\theta_i}$, thus compromising the suppression of quantum noise given by $S_{\hat{A}_{tot,1}^{out},\hat{A}_{tot,1}^{out}}|_{\phi=\pi/4}$.

The effect of the phase noise is demonstrated on Figure 3.6 for the 'symmetric' phase noise ($\overline{\theta_s} = \overline{\theta_i}$) for simplification. The instability of LO phase weakens the signal-idler correlations at $\epsilon \to 1$ similar to the effect of asymmetric losses. The effect of the phase noise can not be mitigated by changing the relative weight of detected quadratures.

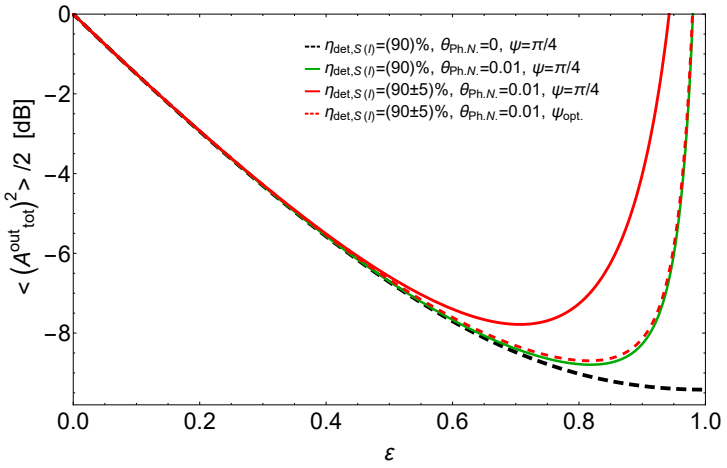

Figure 3.6: The phase noise effect is now taken into account, and it's detrimental impact on signal-idler correlations at $\epsilon \to 1$ is shown for the case of symmetric and asymmetric detection efficiencies (including the case when the relative weight is optimizated).

One can consider the interbeam correlations in the context of EPR steering criterion. If we want to minimize the quantum noise in comparison to the SQL of the signal quadrature only, the choice of equal weights ($\phi = \pi/4$ at $\eta_s = \eta_i$) is no longer optimal, as demonstrated on Figure 3.7. Instead, we should measure $\hat{A}_{tot}^{out}|_{steer.} = \hat{q}_s^{out} - g\hat{q}_i^{out}$. Optimization of g (for specific case $\Omega = 0$) leads to [9]:

$$g_{opt.}(\Omega = 0) = \frac{4\epsilon\eta 1(1+\epsilon^2)}{\epsilon^4 + 2\epsilon^2(4\eta - 1) + 1} \tag{3.27a}$$

$$S_{\hat{A}_{tot}^{out},\hat{A}_{tot}^{out}}(\Omega = 0)|_{\text{steer}} = 1 - \frac{8\epsilon^2\eta(2\eta - 1)}{\epsilon^4 + 2\epsilon^2(4\eta - 1) + 1} \tag{3.27b}$$

The difference between eq.(3.27) and eq.(3.22) is seen as the particular case of comparison between eq.(1.31) and eq.(1.29). For demonstration of EPR steering it is more beneficial to choose $g_{opt.}$ from eq.(3.27a) in the limit of low pump power $\epsilon \to 0$, whereas $g = 1$ would cause the excessive noise. At the same time, when ϵ approaches (limit of high level of two-mode squeezing) $g_{opt.} \to 1$ and $S_{\hat{A}_{tot}^{out},\hat{A}_{tot}^{out}}|_{\text{steer.}}$ (eq.(3.27b)) becomes equal to eq.(3.22).

3.3 Scheme to generate entanglement: introduction

In section 3.1.2 we discussed the problems of experimental detection of entangled states of light encoded in optical amplitude-phase quadratures. Here we address these challenges and propose the alternative strategy that leads to the high-quality, tunable and versatile two-colour source of the EPR state. The experimental setup for

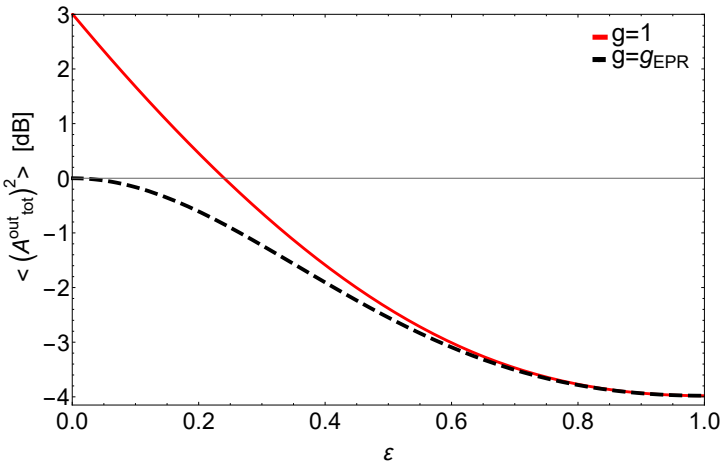

Figure 3.7: Signal-idler correlations in the OPO output as a function of ϵ when $g = g_{opt.}$ from eq.(3.27b) (the best choice for EPR-steering criterion violation) and $g = 1$ which is optimal for optimization relative to 2-mode SQL. $\Delta = 0$, $\eta_s = \eta_i$, phase noise is absent.

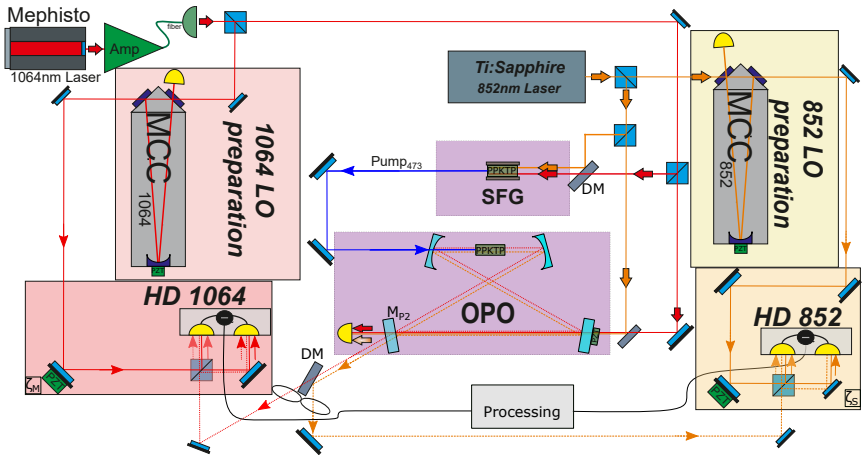

Figure 3.8: The experimental setup for the generation and the measurement of the entangled state of light required for establishing the link between the GWD and the atomic spin ensemble, as described in section 2.2. The entangled beams are produced by the optical parametric oscillator (OPO), which consists of the bow-tie optical cavity with the $\chi^{(2)}$ non-linear medium inside. The parametric down-conversion process implemented in the OPO requires the pump, which is obtained by overlapping two lasers (Mephisto and Ti:Sapphire, respectively) and realizing the sum frequency generation (SFG) process on another $\chi^{(2)}$ non-linear medium. The entanglement is verified by means of homodyne detection (HD) of each twin beam, where the local oscillators (LO) are prepared by taking the optical mode of respective laser. The quality of LOs modes and their low frequency stability is improved using mode cleaner cavities (MCCs). See text for details.

generation and characterization of different color entanglement is shown on Figure 3.8 and can be divided onto six parts: the optical parametric oscillator (OPO), the preparation of the pump for the OPO, the preparation of the local oscillator (LO) and the homodyne detection (HD) for each entangled mode. We start with two laser sources generating radiation at ω_s and ω_i frequencies, respectively. Coherent fields from these lasers are combined on $\chi^{(2)}$ non-linear medium, their interaction leads to the up-converted parametric field as a result of a Sum Frequency Generation (SFG) process: $\omega_s + \omega_i \to \omega_P$. Experimental details of control and characterization of the SFG will be given in section 3.6. The SFG field serves as a pump for the parametric down conversion (PDC) process inside the OPO ($\omega_P \to \omega_s + \omega_i$), which results in the generation of the entanglement between signal and idler modes. Since the PDC in the OPO and the up-conversion in the SFG are mutually reverse and operate under

the same phase-matching conditions, we use the same non-linear medium in both cases. The properties of this medium are explored in section 3.5. The geometry and the design of the OPO are discussed in section 3.7, while the stabilization of the OPO length in order to maintain the resonance conditions is studied in section 3.8. The characterization of the most essential features of the OPO that have a direct impact on the quality of the EPR-state is described in section 3.9. After exiting the OPO, the entangled beams are spatially separated by the Dichroic Mirror (DM), directed towards homodyne detectors (HD) and overlapped with respective LOs. The LO for the signal (idler) is made by taking a small portion of the radiation from the respective laser that is then properly stabilized and filtered. LOs should meet strict requirements for low frequency homodyne detection (LFHD), the procedure of their preparation is given in the section 3.10.1. The homodyne detection itself is detailed in section 3.10.2. The strategy and the implementation of the phase locking is a part of the homodyne detection setup, but is described separately (in section 3.10.3), being one of the most crucial parts for this experiment. The results of the characterization of the entangled state are outlined in section 3.11.

The scheme with two lasers presented here is beneficial in several aspects in comparison to previous approaches. Following proposed design, we combine stability of the OPO performance operated below threshold and advantage to exploit two local oscillators. Thus, we get the opportunity to perform careful and proper characterization by means of the homodyne detection. We also highlight the flexibility and the versatility of the setup in terms of characterization. Originating from initial lasers fields in essence, LOs are in principle completely independent from entangled modes which are determined by phase matching conditions of OPO, in contrast to [71]. Another circumstance should be taken into account: there is a possibility to operate the entangler in regime which is free of contamination by classical noise. It will be shown in section 3.8.2 that is devoted to 'advanced locking scheme'.

3.4 Laser sources

We use Innolight Mephisto Nd:YAG laser as source of light on signal frequency ω_s, corresponding to the wavelength 1064nm which is used to probe laser interferometer type GWD. Mephisto laser produces ≈ 600 mW of optical power; after magnification on Nufern fiber amplifier (PSFA-1064-50-10W-2-1) we finally obtain ≈ 10 W on 1064 nm. M-Squared Ti:Sapphire laser (SolsTiS PSX-R) provides up to 2 W on 852 nm wavelength (ω_i). The essential lasers features, relaxation oscillation performance for Ti:Sapph laser and mainly amplitude noise were extensively studied in [74].

3.5 Crystal

A non-linear medium exploited in this experiment is periodically poled potassium-titany1-phosphate (PPKTP) crystal. Such type of material is quite often used in squeezing experiments [75],[76] owing to high values of non-linear coupling strength, low losses caused by absorption and relatively high damage threshold level [77]. In both SFG and PDC processes we target at conversion 473 nm $\leftrightarrow$ 852 nm + 1064 nm and type-0 polarization matching. Required quasi phase matching for given poling period 6.12 μm is achieved at temperature $T_{ph.m} \approx 68°$. Reflection from OPO crystal surfaces is a crucial circumstance for this experiment, since it might facilitate pollution of entangled modes via back-scattering (will be detailed in section3.8.2) and also hampers compatibility with GWD interferometer [75]. We characterize the AR coating of the crystal and find less than 0.1% reflection from each surface. Influence of blue light induced infrared absorption (BLIIRA) [78] and grey tracking [79] phenomenon on OPO crystal were concluded to be insignificant (see section 3.9.1). Photothermal effects, such as thermal lensing and local heating of crystal, had a noticeable impact on SFG process, limiting it's efficiency and stability.

The size of crystal is 1x1x10mm. The length l_c sets the Boyd-Kleinman conditions [80] onto the size of waist for fundamental and pump modes ($w_{\lambda_{i(s)}}$ and w_{λ_P} respectively) inside the crystal, demanded for optimal conversion efficiency:

$$w_{opt.,\lambda_j} = \sqrt{\frac{l_c \lambda_j}{2\pi n_i \zeta_{B.-K.}}}, \quad j = \overline{s,i,P} \tag{3.28}$$

where $\zeta_{B.-K.}$ is Boyd-Kleiman optimal focusing parameters. For considered here crystal and non-linear conversion process we have:

$$w_{opt.,\lambda_s} \approx 19.7\mu\text{m}, \quad w_{opt.,\lambda_i} \approx 17.5\mu\text{m}, \quad w_{opt.,\lambda_p} \approx 13.2\mu\text{m} \tag{3.29}$$

3.6 Preparation of pump for OPO

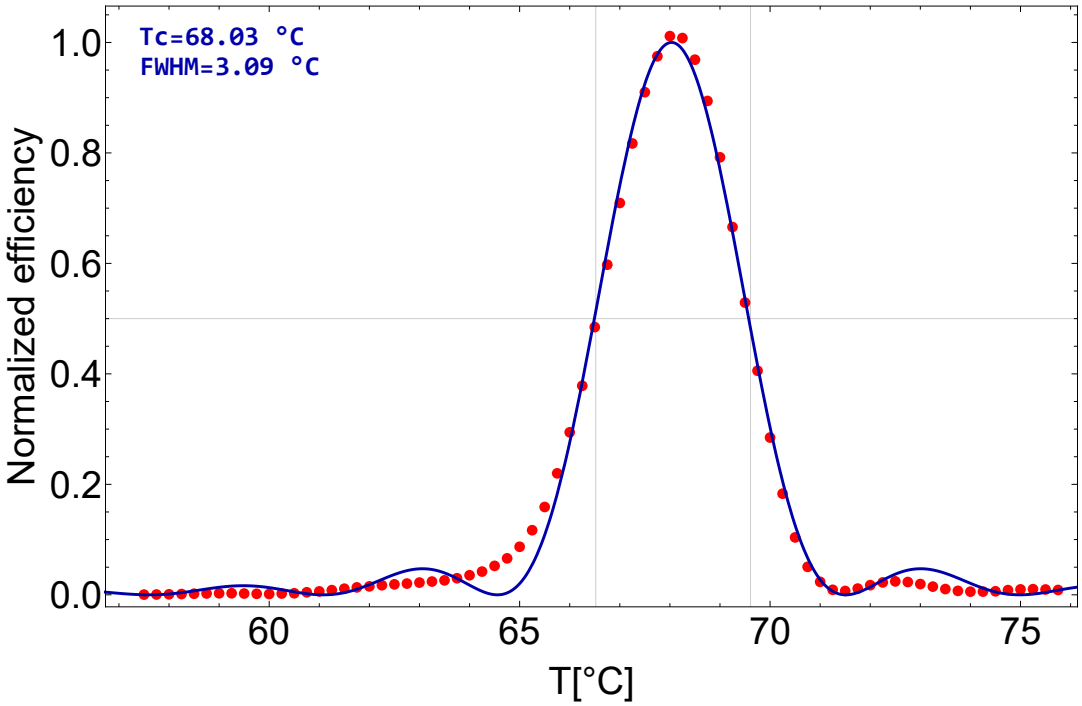

Figure 3.9: SFG efficiency as function of temperature of phase matching

To generate the pump radiation for OPO, we exploit parametric upconversion process. Two optical modes from Mephisto and Ti:Sapph lasers are combined on a dichroic mirror and then sent to non-linear medium (PPKTP crystal, described in sec.3.5). The beam waists of focused incoming optical modes were chosen to coincide with optimal values (3.29) determined by Boyd-Kleinman conditions (eq.3.28), also their polarizations are matched. As a result, the field on their sum frequency is produced whose power P_P might be estimated from the following expression [74]:

$$P_P = \alpha P_s P_i \tag{3.30}$$

where P_s, P_i are optical powers of impinging laser modes on the crystal (indices $i(s)$ denote 1064 nm and 852 nm lasers respectively) and α describes conversion efficiency of the parametric process. Having mode matching and phase matching conditions (see Fig.3.9) optimized, we measure $\alpha \approx 0.05$ [1/W] [74] that leads to $P_P \approx 1$W when all available power from both lasers $P_s|_{\text{max.}} \approx 10$ W and $P_i|_{\text{max.}} \approx 2$ W is sent to the crystal. Obtained SFG power already substantially exceeds OPO threshold reported in section3.9.2. Therefore, we decided to stick to single-pass configuration as we don't need to enhance upconversion efficiency by adding resonator[81]. When obtaining the main results of this chapter (section3.11) and also doing alignment procedures, we make sure to operate SFG crystal safely below the damage threshold [77].

3.7 OPO: design considerations, geometry and assembly

The first decision regarding the design of OPO to be made is the choice between standing wave or travelling wave configurations. Various aspects such as losses, mechanical robustness, astigmatism, tunability/flexibility must be taken into account. Decisive factor was, however, spatial separation of incoming and exiting modes in the OPO. Anticipating future application of this entanglement source in quantum noise suppression for GWD,

we choose to utilize the travelling wave cavity, since such design provides optical isolation of interferometer from back-scattered light [75],[76]. Compared to travelling wave, standing wave cavities open the access to higher bandwidth of entanglement due to reduction of optical path - but this is not the most critical circumstance for the experiment outlined here since our purpose is to demonstrate entanglement on the frequecy range approaching audio band.

Bow-tie and triangular structures are the most prominent among various types of ring cavities. Bow tie configurations is advantageous for outlined experiment since it ensures tight waist size of intracavity mode, which is necessary for efficient parametric down-conversion process. Additionally, increasing number of optical elements enables versatility in implementation of cavity locking schemes. We are also interested in compactness of cavity while having relatively big length of optical path as consequence of travelling wave structure. Having these considerations in mind, we choose the bow-tie configuration. The problem of astigmatism, which can entail difficulties of mode matching between signal modes and local oscillators, turns out to be not crucial for our protocol, as will be shown later.

Next, we must choose between the options to have double resonance (only for signal and idler modes) or triple resonance (also for pump) for the OPO. While benefits of triple resonance are straightforward, its feasibility is a challenging task. Bow-tie cavity geometry in principle allows[3] the OPO to resonate for signal, idler and pump modes, even despite the dispersion of non-linear crystal. However, setting up the triple resonance implies advanced requirements on the coating of optical elements, which would be difficult to fulfill. We also consider the challenge in implementation of such a locking scheme that maintains resonance conditions for 3 different wavelength. Refraining from the resonance for the pump, one has to increase the pump power on the input of OPO in order to maintain good nonlinear interaction efficiency. It is not an obstacle for us since SFG process yields amount of pump power exceeding OPO threshold. We finally stick to double-resonant configuration.

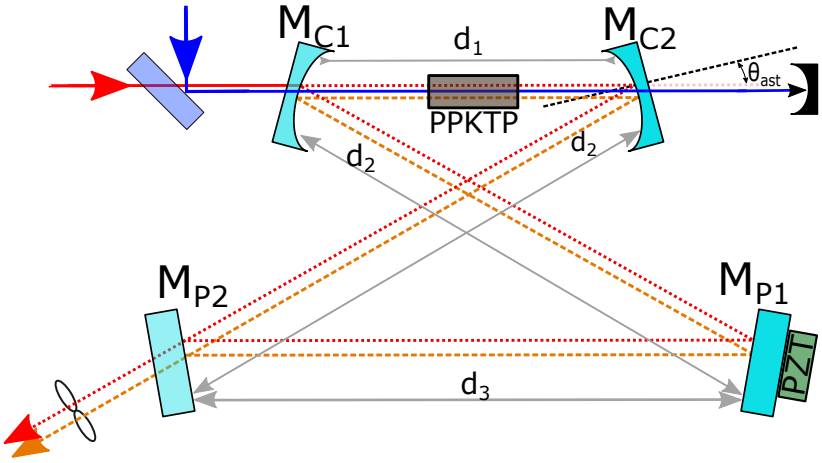

(a) Bow-tie configuration of OPO.

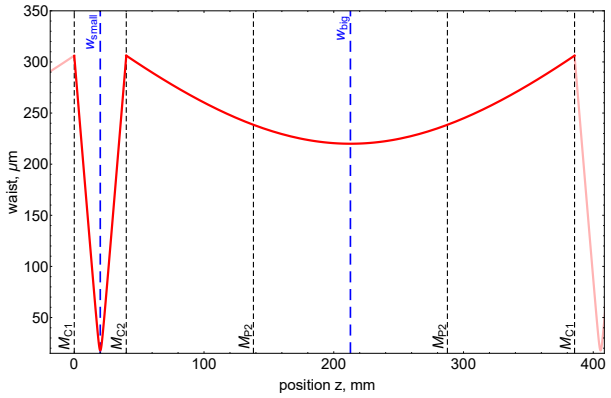

(b) The idler beam propagates through the cavity. Reflecting from each curved mirrors, the optical mode starts converging like it would be after going through lens. Therefore the beam profile has two waists

Figure 3.10: The design and geometry of OPO.

Layout of OPO is shown in Fig.3.10(a). Having symmetric bow-tie configuration, cavity consists of two planar (M_{P1}, M_{P2}) and two curved (M_{C1}, M_{C2}) mirrors. Pump enters through mirror M_{C1}, output port is mirror M_{P2}. All mirrors are provided by LaserOptik. The mirrors M_{C1}, M_{C2} have HR coating for signal-idler wavelengths and AR coating for pump, their diameter is 7mm, thickness is 6.35mm and radius of curvature is -38mm. Two planar mirrors have the same thickness, being half an inch in diameter. While M_{P1} is also HR on frequencies of twin beams, M_{P2} has reflectivity 88% on fundamental wavelengths, which was chosen to provide a desired balance between value of oscillation threshold for pump $P_{P,\text{th.}}$ and escape efficiency η_{esc}. Selected features of mirrors along with optimized intracavity losses (will be characterized in section3.9.1) resulted in measured finesse ≈ 52 and linewidth ≈ 15 MHz for signal and idler, given the round trip length of cavity ≈ 45 cm. The main

[3]The cavity geometry can provide the resonance for each (signal, idler,pump) wavelength with the waist size close to values set by Boyd-Kleimann conditions

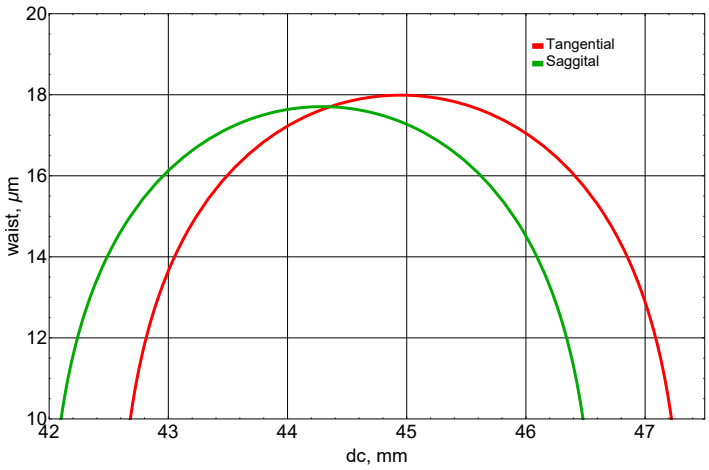

(a) Small minimal waist - between two curved mirrors.

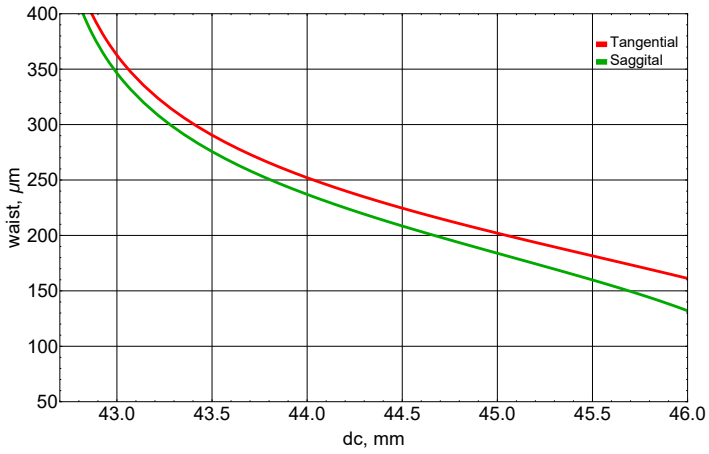

(b) Big minimal waist - between two planar mirrors.

Figure 3.11: Effect of astigmatizm is shown on the minimal waist size as function of distance between curved mirrors. As can be seen, the proper choice of curved mirror separation provides the equal size of tangential and saggital sizes of smaller waist (on the crystal), but not for the bigger waist. As a result, output signal modes will have elongated shapes that complicates their overlapping with Local oscillators.

parameters of OPO cavity are listed in table3.1. The OPO length is controlled by attached to $\mathrm{M_{P1}}$ PZT element that is standard ceramic stack from Piezomechanik. Temperature of the crystal oven is adjusted/maintained by actuation of Peltier element. The temperature readout is implemented by means of thermistor. Mechanical stability of cavity is ensured by its monolithic configuration [74].

Designing the geometrical structure of cavity, we aim to approach a perfect accomplishment of Boyd-Kleinmann conditions eq.(3.28) for the size of the signal and idler waists that should be located the center of the crystal. For the given crystal it leads to eq.(3.29) just as for the SFG process. Therefore we need the cavity to sustain the resonance for signal/idler modes determined by given waist sizes. We use ABCD-formalism (also known as Ray-matrix formalism) to describe the dynamics of intracavity modes expressed by q-parameter. The condition on self-producing mode

$$q = \frac{Aq + B}{Cq + D} \tag{3.31}$$

means that the q-parameter for some fixed position z_0 inside cavity should remain the same after one round trip. Coefficients A,B,C,D in this case form the M matrix for the beam that comes full circle and interacts with all optical elements. For example, if we choose z_0 to be in the middle between two curved mirrors M_{c1} and M_{c2}, then the ABCD-matrix for the round trip is written as

$$M_{\mathsf{OPO}} \equiv \begin{bmatrix} A & B \\ C & D \end{bmatrix} = \begin{bmatrix} 1 & \frac{d_c}{2} \\ 0 & 1 \end{bmatrix} \begin{bmatrix} 1 & 0 \\ -\frac{2}{R_c} & 1 \end{bmatrix} \begin{bmatrix} 1 & d_p \\ 0 & 1 \end{bmatrix} \begin{bmatrix} 1 & 0 \\ -\frac{2}{R_c} & 1 \end{bmatrix} \begin{bmatrix} 1 & \frac{d_c}{2} \\ 0 & 1 \end{bmatrix}, \tag{3.32}$$

where R_c is radius of curvature for mirrors M_{c1} and M_{c2}. Effective distance between curved mirrors d_c and the distance d_p are determined as

$$d_c = d_1 - l_c\left(1 - \frac{1}{n}\right), \quad d_p = d_{tot} - d_1, \quad d_{tot} = d_1 + d_3 + 2d_2. \tag{3.33}$$

Note that refractive index n depends on wavelength in formula for d_c. If z_0 is located in the middle between two planar mirrors M_{p1} and M_{p2}, the M-matrix can be written by replacement $d_c \leftrightarrow d_p$ in eq.(3.32). The solutions of eq.(3.31) for these two cases (reference point is either between M_{p1}-M_{p2} or M_{c1}-M_{c2}) give the following results of minimal waist sizes

$$w^2_{\lambda_j,\mathsf{p(c)}} = \frac{\lambda_j}{2\pi}\sqrt{\frac{R_c - d_{c(p)}}{R_c - d_{p(c)}}\,(R_c d_{tot} - d_c d_p)}. \tag{3.34}$$

Consequently, the optical mode, which is resonant for OPO in bow-tie cavity configuration, has two waists [82]. One (w_{c}) is placed in the middle between M_{c1} and M_{c2}, whereas the second (w_{p}) is located in the middle between M_{p1} and M_{p2}. It is natural to use the smaller waist w_{c} to fulfill Boyd-Kleimann conditions. Therefore, the crystal is placed in the middle between M_{c1} and M_{c2}. Adjusting cavity geometry (mainly the distance d_1), we approximately achieve requirements eq.(3.29) for signal and idler wavelengths. While the procedure of mode matching for auxiliary seed (on signal wavelength) and locking beams (both signal and idler wavelengths) for OPO is straightforward, the search of optimal pump configuration is experimentally challenging because of the absence of resonance for λ_p wavelengths and small size of w_P. We achieve mode matching for SFG field, maximizing the efficiency of parametric gain (described in the section 3.9.2).

The effect of astigmatism originates from non-perpendicular descent of impinging beam onto curve mirror. The reflection from $\mathrm{M_{c1}}$ and $\mathrm{M_{c2}}$ is determined by Ray matrix with effective radii of curvatures $R_c \cos(\theta_{\mathsf{ast.}})$ and $R_c/\cos(\theta_{\mathsf{ast.}})$ in horizontal and vertical directions, respectively. This leads to different beam profiles in tangential and saggital planes along the propagation inside OPO. The most important consequence for us is that horizontal and vertical beam waists don't coincide in general, as shown on Fig.3.11. We reduce the incidence angle until modes start to clip the mounts inside the cavity. As a result, $2\theta_{\mathsf{ast.}} \approx 7.2°$ was set. As can be seen in Fig.3.11(a), correct adjustment of distance between curve mirrors d_c completely compensates astigmatism for smaller beam waist w_c, but not for big waist w_p. Consequently, the output modes for entangled twin beams will be affected by astigmatism. This will prevent their perfect mode-matching to local oscillator fields to some extent.

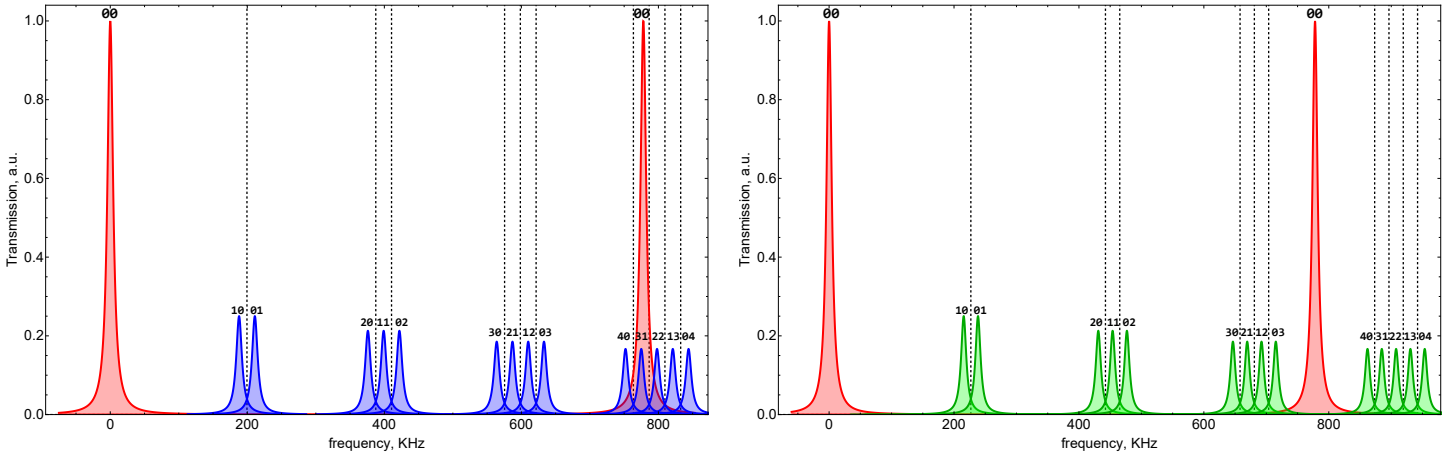

(a) In previous cavity configuration we had Gouy phases $\zeta_{\mathsf{Gouy,ox}} \approx 97°$, $\zeta_{\mathsf{Gouy,oy}} \approx 87°$. The family of 4th-order HG modes then overlapped with 00-peak, as can be confirmed by calculation of their spacing using eq.(3.35): $(\omega_{0,4}/\Delta_{\mathsf{FSR}}) < 1 < (\omega_{4,0}/\Delta_{\mathsf{FSR}})$.

(b) By changing d_1 we increased Gouy phases: $\zeta_{\mathsf{Gouy,ox}} \approx 110°$, $\zeta_{\mathsf{Gouy,oy}} \approx 99°$. It was enough to shift $m+n=4$ HG modes away from fundamental mode while keeping reasonable separation from 3-rd order modes.

Figure 3.12: Contribution of high-order modes to the OPO spectrum.

Non-perfect alignment of OPO for $\mathrm{TEM_{00}}$ resonant mode gives a rise to higher order Hermite-Gaussian (HG) modes also supported by cavity. The spacing of $\{m,n\}$ HG mode relative to fundamental 00-mode

$$\omega_{m,n} = \frac{m\zeta_{\mathsf{Gouy,ox}} + n\zeta_{\mathsf{Gouy,oy}}}{2\pi}\Delta_{\mathsf{FSR}} \tag{3.35}$$

is determined by Gouy phases [83] $\zeta_{\mathsf{Gouy,ox}}$ and $\zeta_{\mathsf{Gouy,oy}}$ in tangential and saggital planes respectively:

$$\zeta_{\mathsf{Gouy}} = \mathsf{sgn}(B)\arccos\left(\frac{A+D}{2}\right), \tag{3.36}$$

where elements A,B,D are taken from round-trip Ray matrix (eq.(3.32)). In our experiment, the initial geometry of OPO resulted in overlapping of fundamental $\mathrm{TEM_{00}}$ signal modes with family $m+n=4$ of higher-order HG modes, as demonstrated in Fig.3.12(a). This circumstance deteriorated the quality of beam profile of output entangled modes and limited the maximum possible degree of matching with respective LOs. The Gouy phase for

bow-tie cavity is strongly sensitive to the distance d_1 between M_{c1} and M_{c2} mirrors. Careful control of d_1 allowed us to change the Gouy phase and cancel contamination of fundamental mode (see Fig.3.12(b))

Cavity Parameter	Symbol	Value	Unit
Signal wavelength	λ_s	1064	nm
Idler wavelength	λ_i	852	nm
Pump wavelength	λ_p	473	nm
Output Coupler Signal/Idler Refl.	$R_{escs,i}$	0.88	-
Waist size in cr., Signal	ω_s	19.7	μm
Waist size in cr., Idler	ω_i	17.6	μm
Waist size in cr., Pump	ω_p	13.2	μm
Total length	d_{tot}	≈450	mm
Finesse Signal/Idler	$F_{s,i}$	≈ 52	-
Linewidth at Signal/Idler	$\delta\nu_{s,i}$	≈ 15	MHz
Curved Mirror Radius of Curvature	RoC	-38	mm

Table 3.1: Essential parameters of OPO cavity

3.8 OPO Locking

3.8.1 Current scheme: locking fields on fundamental frequencies

In order to keep OPO in double resonance, we exploit double-stage Pound-Drever-Hall locking [84] scheme. Specifically, OPO length stabilization relative to 1064nm laser is followed by locking of 852nm laser relative to the cavity. The first stage is implemented by sending feedback signal to piezoelectric transducer (PZT) attached to $\mathsf{M_{P1}}$ mirror, while another PZT element in 852 laser head module was controlled in the second stage. The auxiliary beams on fundamental wavelengths were initially phase modulated using electro optical modulators (EOM) with ≈ 8MHz sidebands. These optical fields were then injected into the OPO through $\mathsf{M_{P1}}$ mirror (shown in Fig.3.13(a)) and travelled along direction opposite to pump propagation. Exiting the OPO through $\mathsf{M_{P2}}$ mirror and being split onto dichroic mirror, auxiliary beams were detected and demodulated, as displayed on Fig.3.13(b). Obtained error signals (shown on Fig.3.13(c)) were sent onto PID-modules. See [74] for details.

3.8.2 Future: frequency shifted beams

In experiments [75],[7],[9] targeted to exploit single-mode squeezed states for quantum noise reduction in GWDs, resonance conditions in OPO were provided without injection of strong fields on fundamental frequency. Instead, cavity was stabilized for pump wavelength, and utilization of 'wedged' crystal allowed to achieve double resonance. Absence of locking beams on fundamental frequency facilitated remarkable performance of squeezed states in low(audio)-frequency band. In contrast, the strategy described in section3.8.1 implies presence of classical auxiliary fields on signal/idler wavelength inside OPO. As was outlined earlier, we inject locking beams in such a way that they initially counterpropagate relative to generated twin beams. However, travelling within cavity, auxiliary fields experience back reflection (mainly due to the crystal non-perfect AR-coating) and eventually enter fundamental modes, bringing the classical noise associated with lasers, Even tiny reflection (leading to several nW only) would be sufficient to contaminate signal/idler modes and cause degrading of measured correlations. One way to address this issue is to properly suppress the intensity noise of injected locking beams before they enter cavity. We explored the performance of the system in such regime and managed to certify entanglement on spectral range down to 10 KHz (characterization will be detailed in section3.11). However, on lower frequencies we suffered from the classical noise. In order to completely cancel this detrimental effect of auxiliary beams, we have to move them away from fundamental frequencies, but still keep the resonance conditions for OPO.

To accomplish this task, we follow the approach sketched on Fig.3.14(a). The small part of initial laser radiation on frequency ω_0 (corresponds to fundamental frequency of either signal or idler entangled beam) passes

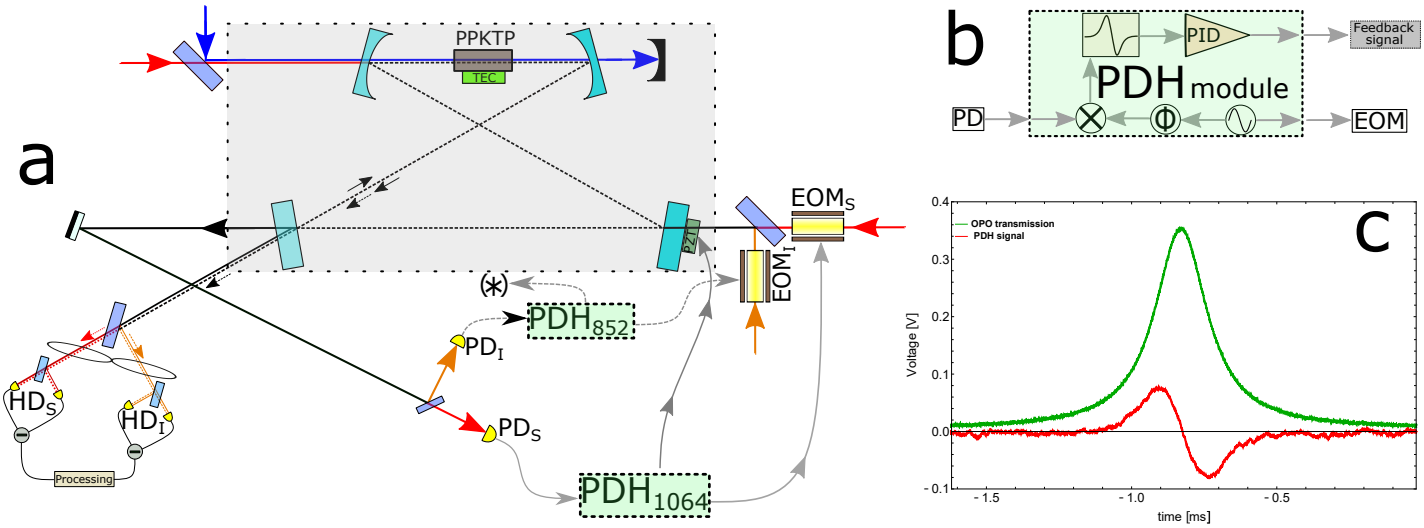

Figure 3.13: Implementation of OPO lock to achieve double resonance. Subplot **(a)**: the sketch of the setup, including optics and electronics. Symbol $(*)$ means electronic signal directed to the piezo actuator of Ti:Sapph laser. Subplot **(b)**: detailed configuration of PDH module. Subplot **(c)**: examples of OPO transmission signal and PDH error signal measured for signal mode (1064 nm) while the piezo attached to OPO cavity mirror was scanned.

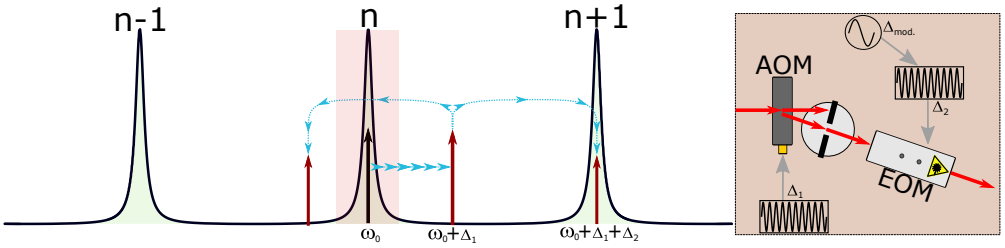

(a) The shift of a locking beam (for example, on signal wavelength) to the next free spectral range (FSR). Initially matching n-th frequency mode of the cavity, the injected beam propagates through AOM+EOM setup (shown on the subplot on the right side). As a result, the locking beam is moved to $(n+1)$-th frequency mode.

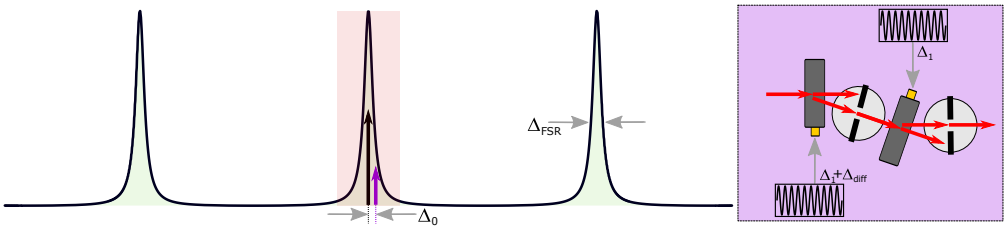

(b) The shift of the seed for implementation of the phase lock. Being initially tuned to the resonance of n-th frequency mode of the cavity, the seed is transmitted through the double AOM-setup (shown on the subplot on the right side). As a result, the seed is detuned from the resonance (while still being within n-th frequency mode). It allows to prevent the pollution of the lower (acoustic) sideband frequencies with respect to the fundamental frequency ω_0.

Figure 3.14: The idea of advanced OPO locking that will enable to avoid the injection of classical beams on fundamental frequencies. See text for details.

acousto optical modulator (AOM), driven by rf-frequency Δ_1. The scattered light into the first order now has frequency $\omega_1 = \omega_0 + \Delta_1$. Being spatially separated from fundamental field (ω_0), this scattered mode is directed on electro optical modulator (EOM) where phase modulation with frequency Δ_2 and depth β is induced. After

exiting EOM, the modulated light can be presented as

$$e^{i\omega_1 t} \rightarrow e^{i[\omega_1 t+\beta \sin(\Delta_2 t)]} \approx e^{i\omega_1 t} + \frac{\beta}{2} e^{i(\omega_1+\Delta_2)t} - \frac{\beta}{2} e^{i(\omega_1-\Delta_2)t} \tag{3.37}$$

We adjust Δ_1 and Δ_2 in such a way, that $\Delta_1 + \Delta_2$ matches Free Spectral Range Δ_{FSR} of OPO cavity. As a result, the second term ($\propto e^{i(\omega_1+\Delta_2)t}$) on the right side of eq.(3.37) is moved to the next resonance relative to fundamental wavelength and is used as the locking beam. At the same time, sharing the same spatial mode other components ($\propto e^{i(\omega_1-\Delta_2)t}$ and $\propto e^{i\omega_1 t}$) remain away from any OPO resonance and will be reflected from OPO, locked by $e^{i(\omega_1+\Delta_2)t}$. The sidebands needed for PDH error signal[84] are generated due to frequency modulation of electronic local oscillator, which drives EOM. If we assume modulation of Δ_2 with frequency Δ_{mod} and small depth β_{mod}, then the term $e^{i(\omega_0+\Delta_{\mathsf{FSR}})t}$ will convert into

$$e^{i(\omega_0+\Delta_{\mathsf{FSR}})t} \rightarrow e^{i\left[(\omega_0+\Delta_{\mathsf{FSR}})t+\beta_{mod.}\sin(\Delta_{mod.}t)\right]} \approx e^{i(\omega_0+\Delta_{\mathsf{FSR}})t} + \frac{\beta_{mod}}{2} e^{i[(\omega_0+\Delta_{\mathsf{FSR}})+\Delta_{mod}]t} - \frac{\beta_{mod}}{2} e^{i[(\omega_0+\Delta_{\mathsf{FSR}})-\Delta_{mod}]t} \tag{3.38}$$

The same sidebands ($\pm\Delta_{mod}$) will be imposed onto field $\sim e^{i(\omega_1-\Delta_2)t}$.

Both signal and idler locking beams enter OPO through $\mathsf{M_{P1}}$ mirror, counter-propagate inside the cavity with respect to pump and detected in transmission after $\mathsf{M_{P2}}$ mirror, thus replacing previous non-shifted auxiliary fields in the scheme shown in Fig.3.13(a). We choose Δ_1 to be $\approx$ 120MHz to implement the initial frequency shift by AOM and then adjust the frequency Δ_2 of the electronic signal driving EOM to match one of the sidebands to the next (which is defined as $(n+1)$-th, if we denote n-th resonance as the frequency mode where entangled beams are created) resonance of OPO, as shown in Fig.3.15(a). Since $\Delta_{FSR} \approx$ 780MHz, we end up with $\Delta_2 \approx$ 660MHz. Finally, modulating Δ_2 with $\Delta_{mod.} \approx$ 1MHz, we obtain PDH error signal, as presented on the Fig.3.15(b).

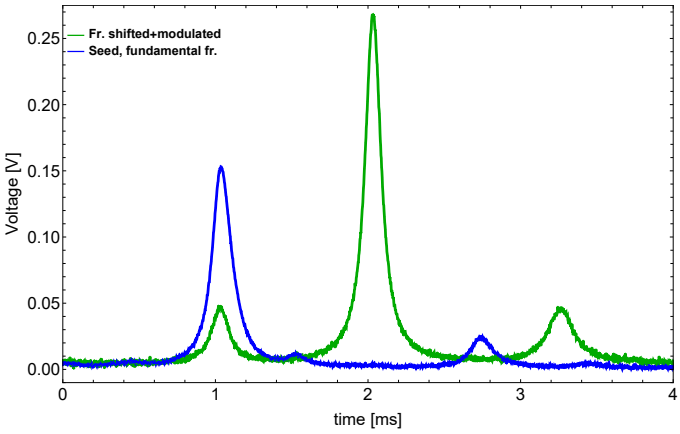

(a) The electronic signal recorded on the photodetector used to lock OPO.

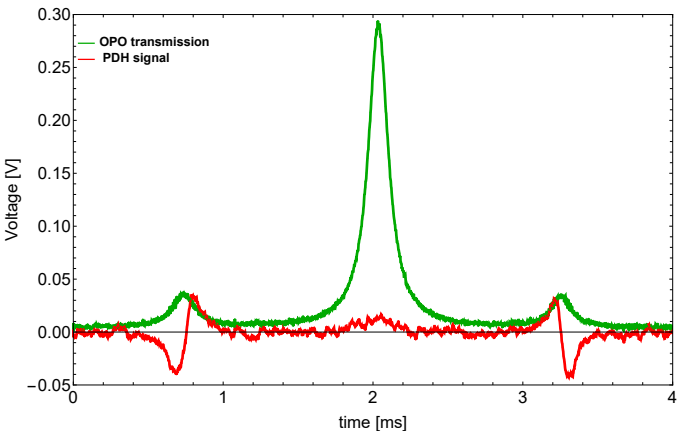

(b) The electronic signal recorded on the photodetector used to lock OPO together with PDH error signal.

Figure 3.15: The implementation of advanced locking of OPO, presented in section 3.8.2. **Left panel (subplot (a))**: Shift of locking beam to the next FSR. Green curve is the detected locking auxiliary signal field (on 1064nm) passed through AOM+EOM system when the cavity length is scanned. The range of scan is chosen in such a way that central big peak corresponds to $e^{i(\omega_0+\Delta_{FSR}+\Delta_1)t}$ (it corresponds to the first term on the right-hand side of eq.(3.37)). The smaller left peak is upper modulation sideband of $e^{i(\omega_0+\Delta_1)t}$ carrier and coincides with $n+1$ resonance ($\omega_0 + \Delta_{FSR}$), while the smaller right peak comes from lower modulation sideband of $e^{i(\omega_0+2\Delta_{FSR}+\Delta_1)t}$ carrier. Blue curve is the transmission of seed on signal fundamental wavelength (not used in main experiment): big peak corresponds to OPO $(n+1)$-resonance on frequency $\omega_0 + \Delta_{FSR}$ (entangled signal field is generated in n-resonance on frequency ω_0) matching sideband $e^{i(\omega_0+\Delta_1+\Delta_2)t}$ of locking field. The small peak appears due to non-ideal mode matching. **Right panel (subplot (b))**: Green curve is locking beam (in this case the left small peak corresponds to desired frequency $\omega_1 + \Delta_2$ to lock the OPO), The red curve is PDH error signal (generated for both $\omega_1 \pm \Delta_2$ components) as specified by eq.(3.38) .

3.9 OPO characterization

3.9.1 Intracavity losses

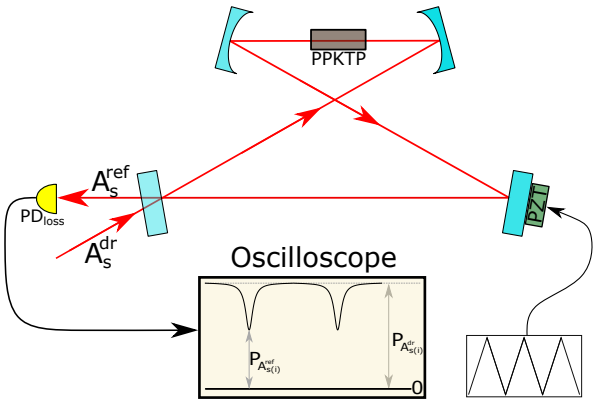

(a) Experimental setup to measure intracavity losses. OPO cavity is driven through the output port by strong coherent field either on signal or idler frequency. The pump is not shown on the sketch; however, it was also injected when effect of BLIIRA was investigated. Pump presence didn't run parametric processes since it's propagation direction was opposite to travelling through the OPO drive fields.

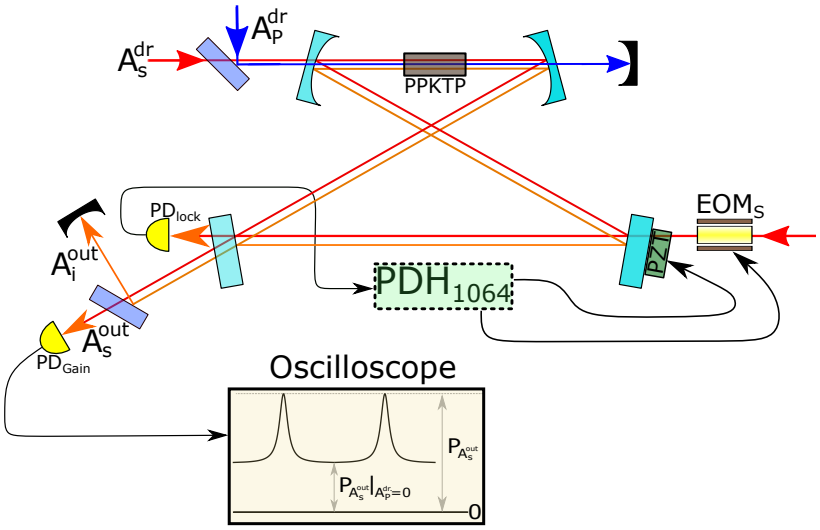

(b) Experimental setup to calibrate the pump power threshold.

Figure 3.16: Characterization of intracavity losses (left subplot) and parametric gain (right subplot) for the OPO.

In order to estimate intracavity losses, we measure the power of reflected field from the output port of the OPO ($\mathsf{M_{P2}}$ mirror). To understand the underlying idea, we use eqs.(3.15) and study the dynamics of signal mode (the same logic will be applied to idler field also) in the absence of pump that excludes parametric interaction and coupling between signal and idler. The OPO is now driven by strong coherent field that enters the output port only ($\hat{a}_j^{in1}$ is replaced by A_j^{dr}). Therefore we can write down the Langevin equation for the coherent amplitude of intracavity signal/idler field (instead of using field operators). Applying then input output relations, we obtain the following expression for the output field to be detected:

$$A_j^{out} = \frac{2\gamma_s^{out} - \gamma_j - i\Omega}{\gamma_j + i\Omega} A_j^{ref} = \frac{\gamma_j^{out} - \gamma_j^{loss} - i\Omega}{\gamma_j^{out} + \gamma_j^{loss} + i\Omega} A_j^{ref}, \quad j = \overline{s,i}. \tag{3.39}$$

In eq.(3.39) the approximation $\gamma_j^{out}, \gamma_j^{loss} >> \gamma_j^{in}$ was made. This assumption is valid for the OPO implemented in this thesis. The input port mirror $\mathsf{M_{C1}}$ is HR, while $\mathsf{M_{P2}}$ has a power reflection coefficient $R^{out} = 88\%$ (measured independently) and intracavity losses are envisioned to come mainly from crystal coating, being several order above losses on HR mirrors $\mathsf{M_{P1}}$, $\mathsf{M_{C2}}$. The drive field A_j^{dr} is completely reflected from the OPO being far detuned from resonance $\Omega >> \gamma_j$, whereas setting $\Omega = 0$ leads to characteristic dip in detected field. The size of the dip will be then determined by the ratio γ_j^{loss}/γ_j. Comparing the power of measured field being on and off resonance with the cavity, we obtain

$$\delta P \equiv \frac{P_{A_j^{out}}|_{on}}{P_{A_j^{out}}|_{off}} = \frac{A_j^{ref}\left(A_j^{ref}\right)^*|_{\Omega=0}}{A_j^{ref}\left(A_j^{ref}\right)^*|_{\Omega>>\gamma_j}} = \left(\frac{\gamma_j^{out} - \gamma_j^{loss}}{\gamma_j^{out} + \gamma_j^{loss}}\right)^2, \quad j = \overline{s,i}. \tag{3.40}$$

Using definition of leak rates in eq.(3.16), we obtain the expression for intracavity losses:

$$T_j^{loss} = 1 - \left[1 - \frac{T_j^{out}}{2}\left(\frac{1-\sqrt{\delta P}}{1+\sqrt{\delta P}}\right)\right]^2, \quad j = \overline{s,i}, \tag{3.41}$$

where approximation of small losses was used T_j^{loss},$T_j^{out} << 1$. Hence, escape efficiency is calculated as

$$\eta_{esc.,j} = \frac{T_j^{loss}}{T_j^{loss} + T_j^{loss}}, \quad j = \overline{s,i}, \tag{3.42}$$

just using the definition. Provided the precise knowledge of reflection/transmission of the output coupler, the measurement of the amplitude of reflected field yields a reasonable accuracy to estimate the intracavity loss, in comparison to the derivation through the finesse [75]. At the same time, the method presented above is more convenient than measuring transmissivity/refectivity/scattering of each optical element from the OPO separately. In our experiment, we take the coherent fields from respective lasers and send the drive signal/idler onto the output OPO port in such a way, that injected fields travel inside the cavity along the direction opposite to the propagation of the pump, as shown in Fig.3.16(a). During the measurement the piezo in OPO is scanned that allows us to see the characteristic dips in reflected power (Fig.3.17). We obtain the values of intracavity losses $T_s^{loss} = T_i^{loss} = 0.15\%$, which correspond to escape efficiencies $\eta_{esc.,s} = \eta_{esc.,i} = 99\%$ given $R_{s(i)}^{out} = 0.88$. The investigation of intracavity losses on the pump power was also performed. It was possible because pump actually didn't cause parametric processes being counter propagated with respect to injected bright fields on fundamental wavelengths. The increase of pump power up to operating point (approximately 1/2 of threshold level) didn't trigger noticeable enhancement of intracavity losses. Therefore, the detrimental effect of Blue Light Induced Infrared Absorption (BLIIRA) [78] on non-linear medium (PPKTP crystal) didn't have an impact on interbeanm correlations in the main experiment.

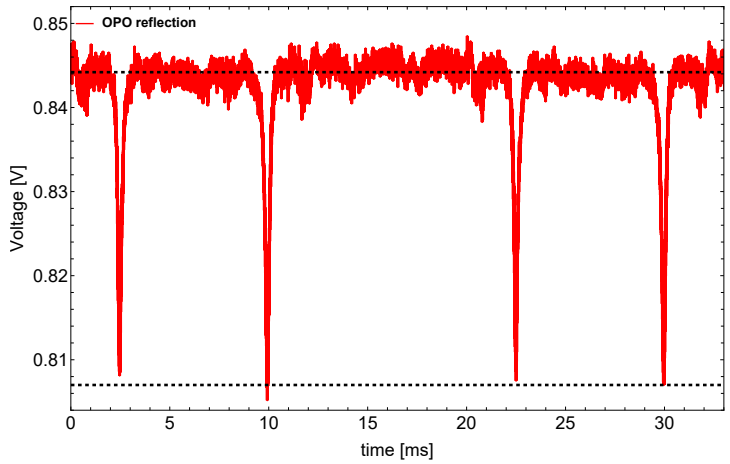

Figure 3.17: The result of calibration of intracavity OPO losses for signal wavelength (1064nm) was shown. The cavity lengths was scanned, and the ratio between reflected power on resonance and power of drive field entering output was estimated (the bottom of the dips and the DC-top level, respectively). The analogous procedure was performed for the idler wavelength (852nm).

3.9.2 Gain

We start with signal/idler/pump dynamics as done in system of eqs.(3.15), but now we assume the classical drive fields for the signal wavelength and for the pump ($\hat{a}_s^{in}$ and $\hat{a}_P^{in}$ are replaced by A_s^{dr} and A_P^{dr}, respectively) while the rest external fields $\hat{a}_i^{in}$ and $\hat{a}_j^k$, $k = \overline{\mathsf{in1,loss}}$, $j = \overline{s,i,P}$ are in vacuum states. In that case all intracavity fields $\hat{a}_j$ become classical (being described by α_j), and quantum fluctuation will be neglected further. Setting all

frequency detunings $\Delta_j = 0$, we rewrite eqs.(3.15) for classical fields:

$$\frac{d}{dt}\alpha_s = -\gamma_s\alpha_s + g\alpha_P\alpha_i^* + \sqrt{2\gamma_s^{in}}A_s^{dr}, \tag{3.43a}$$

$$\frac{d}{dt}\alpha_i = -\gamma_i\alpha_i + g\alpha_P\alpha_s^*(+0), \tag{3.43b}$$

$$\frac{d}{dt}\alpha_P = -\gamma_P\alpha_P - g\alpha_s\alpha_i + \sqrt{2\gamma_P^{in}}A_P^{dr}. \tag{3.43c}$$

Assuming $|A_s^{dr}| << |A_P^{dr}|$ and undepleted regime for pump, we immediately obtain the solution of eq.(3.43c) in a form of steady intracavity pump field: $\dot{\alpha}_P = 0$, $\alpha_P = \left(\sqrt{2\gamma_P^{in}}/\gamma_P\right)A_P^{dr}$. Next, we consider equal optical losses for signal and idler $\gamma_s = \gamma_i = \gamma$ and denote $G = g\alpha_P$. We also search for steady solutions for signal and idler ($\dot{\alpha}_s = \dot{\alpha}_i = 0$). Combining eq.(3.43a) and eq.(3.43b)and using input-output relationships $A_j^{out} = \sqrt{2\gamma_j^{out}}\alpha_j$, we obtain the following expression for output signal field A_s^{out} (corresponding to frequency which was driven by classical input light A_s^{dr}):

$$A_s^{out} = \frac{2\sqrt{\gamma^{in}\gamma^{out}}}{\gamma\left(1 - \frac{|G|^2}{\gamma^2}\right)}A_s^{dr}. \tag{3.44}$$

It follows from equation eq.(3.44) that drive field A_s^{dr} is amplified due to the parametric interaction with pump while transmitting the OPO. This amplification does not depend on pump phase since A_s^{out} is a function of $|G|^2$. We define a parametric gain as a ratio between powers of output signal field with and without injected pump and get the following result using eq.(3.44):

$$\mathsf{Gain} \equiv \frac{P_{A_s^{out}}}{P_{A_s^{out}}|_{A_P^{dr}=0}} = \frac{1}{\left(1 - \frac{g^2|\alpha_P|^2}{\gamma^2}\right)^2}. \tag{3.45}$$

We insert the definition of threshold pump power $\alpha_{P,th.} = \gamma/g$ into eq.(3.45) and arrive at

$$Gain = \frac{1}{\left(1 - \frac{P_P}{P_{P,th}}\right)^2}, \tag{3.46}$$

where $P_P = \alpha_P\alpha_P^*$ and $P_{P,th} = \alpha_{P,th}\alpha_{P,th}^*$

In experiment (see Fig.3.16(b)) seed on signal wavelengths infiltrates the OPO with pump through the input coupler. Output seed is spectrally filtered (using dichroic mirror) to remove DFG field on idler frequency and is sent to photodetector. The OPO is locked for signal wavelength only, and the piezo in TiSapph laser cavity is scanned. Hence, the result of parametric interaction of seed and pump is seen as peaks (parametrically amplified seed) on top of background (transmitted seed without amplification), yielding the parametric gain. We then vary the input pump power and measure the gain. Finally, eq.(3.46) is utilized to calibrate the threshold power of OPO. Described procedure gives us (Fig.3.18) the value of threshold $|A_P^{dr}|^2 = 320$ mW in terms of input power.

3.10 Detection

This section covers the preparation of local oscillators (LOs) and the homodyne detection. The description of the phase locking is also given here. The similar scheme was used for characterization of both signal and idler entangled twin beams (the example for 1064 nm mode is shown in Fig.3.19).

3.10.1 Preparation of Local Oscillators

The central part of LO preparation is the mode-cleaner cavity (MCC). It performs two functions: first, it obviates the effect of beam pointing which can result in reduction of common mode rejection ratio (CMRR) of homodyne detector due to inhomogeneity of photodiode [75]. Secondly, it provides spatial filtering of LO beam profile, facilitating the overlapping with measured optical mode. We employ typical triangular configuration of

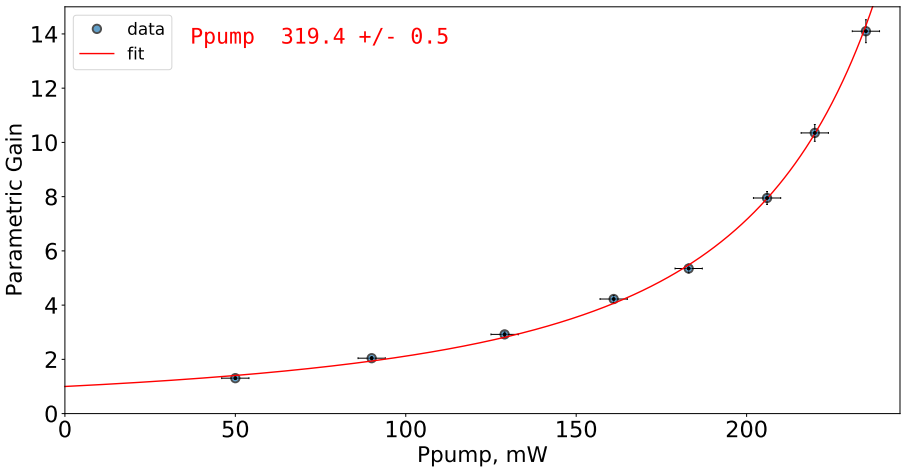

Figure 3.18: The characterization of the parametric gain of the OPO. Different values of the pump power are used, and eq.(3.46) is applied in order to extract the value of the pump threshold.

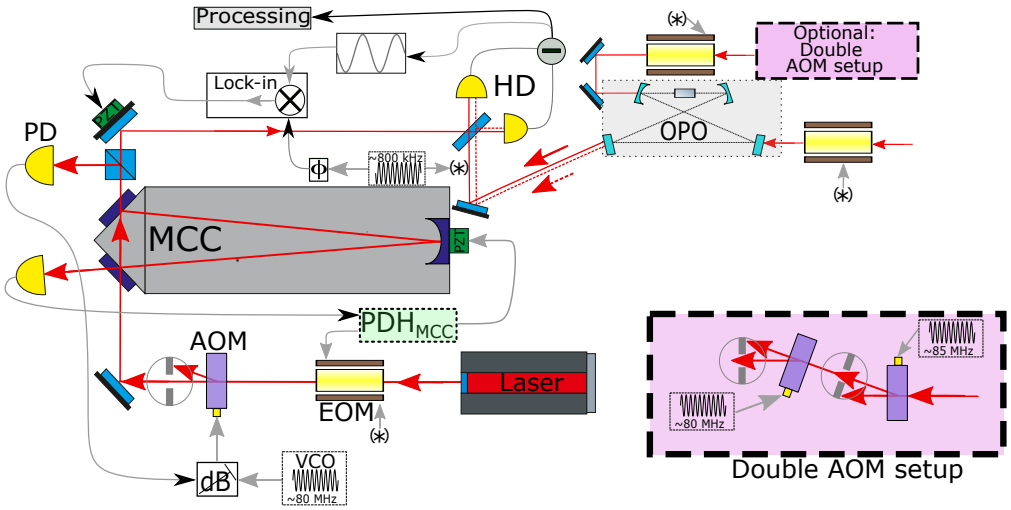

Figure 3.19: The sketch of the experimental setup used to prepare the local oscillator (LO) and perform the homodyne detection (HD). The optical mode of the laser is transmitted through the triangular mode cleaner cavity (MCC), which is locked using Pound-Drever-Hall (PDH) technique. The phase modulation was induced by means of the electro optical modulator (EOM), the feedback signal was sent to piezo electric transducer attached to the curved mirror in the MCC. The intensity stabilization of LO can be applied by controlling the efficiency of scattering on acousto-optic modulator (AOM). The phase lock is implemented by using the interferometric signal between the LO and the back-reflected beam used to lock the OPO (the latter will be replaced by the seed injected to the OPO and detuned from the resonance by using double AOM setup), see text for details. Other abbreviations used in the caption: photodetector (PD), voltage-controlled oscillator (VCO).

travelling-wave cavity for MCC. Cavity is formed by two planar and one curved HR mirros embedded in monolithic aluminium block. The cavity lengths are chosen to be ≈0.45m, yielding the bandwidth ≈4 MHz and finesse ≈ 200. Small part (∼1-5 mW) of initial laser (Ti:Sapph/Mephisto) radiation not used for SFG process is sent onto the input of MCC after having experienced ∼20-30 MHz phase modulation. MCC is locked by means of PDH technique using the light reflected from the input port mirror. Feedback signal controlling the length is applied to PZT element attached to the curved mirror. Filtered mode of LO propagates towards detectors after exiting opposite

mirror.

After transmission through MCC, the position and mode shape fluctuations are transformed into intensity instability, which is added to initial power fluctuations of lasers. In principle, classical noise associated with intensity fluctuations should not be major limitation of homodyne detector with strong CMRR [75]. However, we enhance the performance of LFHD setup by introducing the power stabilization scheme that suppresses the noise in the LO mode before overlapping with entangled mode. Intensity fluctuations are cancelled by adjusting the scattering efficiency of the acousto-optical modulator (AOM) [85], [86] inserted just before MCC. After MCC LO is split onto two parts, reflected field is sent to in-loop detector. Deviation of the voltage from the preset value on the in-loop detector is transformed into feedback signal, which controls the attenuation of RF signal driving AOM. Faraday isolator[4] just before overlapping LO with signal mode can be introduced with the purpose to mitigate the effect of parasitic interference. It prevents back reflected light to counter propagate in LO mode with subsequent possibility to be scattered forward and induce a modulation of LO power.

3.10.2 Homodyne measurement

This part of the experimental setup includes matching of prepared LOs with signal/idler modes and characterization of resulting quantum states. Our endeavor was to minimize the amount of optics on the path of entangled beams to exclude unnecessary sources of optical losses. Only indispensable optics was used, such as dichroic mirror to spatially separate signal twin mode from idler. Therefore, we added lenses only in LO optical path to perform mode matching. Having astigmatism due to the bow-tie configuration and not having it into MCC output, we managed to achieve visibilities $\eta_{1064} = 99.2\%$ and $\eta_{852} = 99.0\%$.

Signal (idler) mode overlaps with respective LO onto symmetric beam-splitter (BS), and outputs are directed onto corresponding homodyne detector (HD). HDs were built in 'current-subtraction' configuration. Utilizing low noise transimpedance amplifier, carefully choosing other electronic components and employing post-amplification of photocurrents, we obtain clearance up to 20 dB, and flatness of shot noise down to 1 KHz. We exploited InGaAs PIN FND-500 photodiodes for HD to measure signal (1064nm) and idler (852nm) entangled modes respectively with 12V applied bias voltage. We roughly estimated quantum efficiencies of photodiodes from the ratio between output voltage and incident optical power and found $\eta_{ph,1064} \approx \eta_{ph,852} \approx 90\%$. Common mode rejection ratio (CMRR) for each HD was measured by inducing amplitude modulation and comparing balanced output with amplitude noise. This yields 40dB CMRR for both photodetectors in spectral range $\Omega \gtrsim 100$KHz with tendency to drop to 25-30 dB for frequencies approaching 10 KHz. Both shot-noise flatness and CMRR were limited by non-ideally symmetric splitting ratio of BS and inhomogeneity of quantum photodiodes. This effect was partially compensated by adjusting the positions of beams on photodiodes. Sensitivity of transmission/reflection of BS to polarization was also utilized to optimize splitting ratio. However, we also have to keep polarization matching between LO and entangled modes. Polarization optics was added in LO paths, but not in signal modes. Therefore we weren't able to significantly deviate from fixed polarization of LO. Finally, scattering loss issue is another factor which reduces CMRR. To deal with this problem, clean environment of the experiment was established. The next step will be to properly isolate detection stage by external enclosure.

3.10.3 Phase lock

In order to verify entanglement by EPR-steering or by Duan criteria, both amplitude $\{\hat{x}_s, \hat{x}_i\}$ and phase $\{\hat{p}_s, \hat{p}_i\}$ quadratures have to be measured. If homodyne detection in each mode is used to characterize entangled state, the phases of of local oscillators $\{\Phi_{LO,s}, \Phi_{LO,i}\}$ should be set fixed relative to the pump phase $\theta_P/2$: $\Phi_{LO,s} = \Phi_{LO,i} = \theta_P/2$ ($\Phi_{LO,s} = \Phi_{LO,i} = \theta_P/2 + \pi/2$) when amplitude(phase) quadratures are measured (see Fig.3.20). However, we recall that according to eq.(3.17), eq.(3.22) measuring the difference (provided symmetric losses) of any quadratures that are anti-symmetric relative to the pump phase $\theta_P/2$ (denoted as $\hat{q}_s(\psi_+) - \hat{q}_i(\psi_-)$, $\psi_\pm = \theta_P/2 \pm \theta$ from section 3.2) should yield the quantum noise reduction. Noise cancellation also occurs in quantum observable $\hat{q}_s(\psi_+ + \pi/2) + \hat{q}_i(\psi_- + \pi/2)$. Therefore, one can change the basis of quadratures from $\left\{\hat{x}_{s(i)}, \hat{p}_{s(i)}\right\}$ to $\left\{\hat{q}_{s(i)}(\psi_\pm), \hat{q}_{s(i)}(\psi_\pm + \pi/2)\right\}$. Consequently, the phases for local oscillators have to be symmetric

[4] not shown in Fig.3.19

relative to the pump phase:

$$\left(\frac{\theta_P}{2} - \Phi_{LO,s}\right) = -\left(\frac{\theta_P}{2} - \Phi_{LO,i}\right), \tag{3.47}$$

if the difference of amplitude quadratures (in new basis) is explored. Similarly, in order to measure the sum of phase quadratures, one needs to comply with $(\theta_P/2 - \Phi_{LO,s}) + \pi/2 = -(\theta_P 2 - \Phi_{LO,i}) + \pi/2$. There is no requirement to keep $\Phi_{LO,s(i)}$ fixed relative to $\theta_P/2$ any longer.

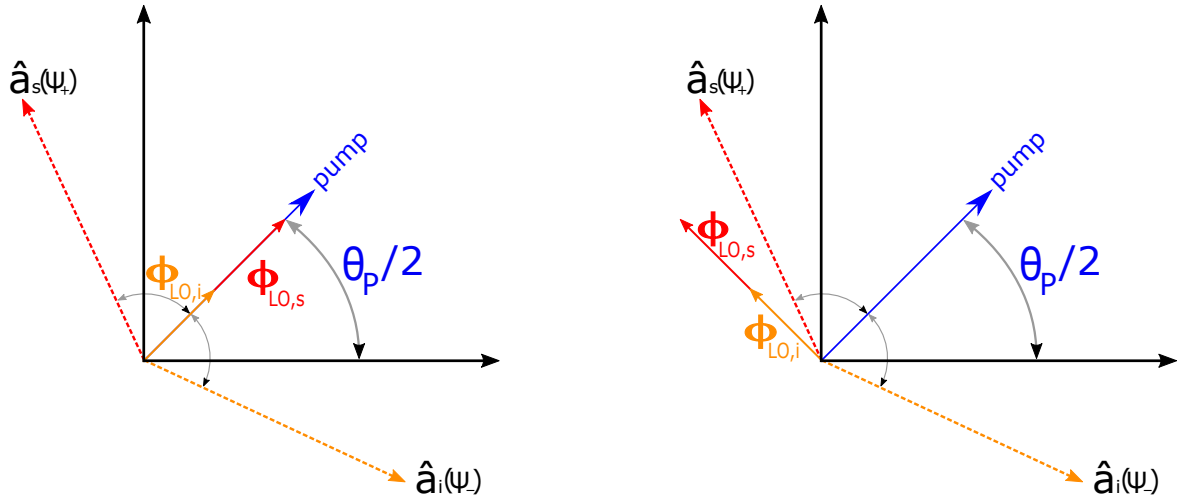

(a) Detection of amplitude quadratures

(b) Detection of phase quadratures

Figure 3.20: The idea of the phase lock on the phasor diagram. Ideally the phases of Local oscillators $\theta_{LO,s}$, $\theta_{LO,i}$ should be locked relative to the phase of pump field $\theta_P/2$: as demonstrated on the figure, setting $\theta_{LO,s} = \theta_{LO,i} = \theta_P/2$ ($\theta_P/2 + \pi/2$) allows for measuring of 'genuine' amplitude(phase) quadratures. In reality, we can only provide the assymmetry of LOs phases with respect to $\theta_P/2$ or $\theta_P/2 + \pi/2$, while each of phases $\theta_{LO,s}$, $\theta_{LO,i}$ (if treated separately) is still running free relative to pump phase . However, it was sufficient to verify entanglement (see text for details)

In order to implement phase locking for characterization of the entanglement source, we exploit the *coherent locking* strategy [87] developed for control of squeezed states of light and adapt it to the case of non-degenerate entanglement characterization. The underlying principle of coherent locking can be understood by studying eq.(3.15) of intracavity fields evolution. In the main experiment, apart from pump A_P^{dr}, OPO is driven through the input port by strong coherent field A_s^{dr} which in general case is detuned from resonance signal frequency ω_s by non-zero Δ_s. In the following we will refer to the $A_s^{dr} = |A_s^{dr}|e^{i\theta_{CLF}}$ as Coherent Sideband Field (CSF) on frequency ω_{CSF} with the optical phase θ_{CLF}. Inside the OPO the parametric interaction of two drive fields leads to parametric amplification of CSF (see eq.(3.44)) and creation of Generated Sideband Field (GSF) whose frequency should obey $\omega_{GSF} = \omega_P - \omega_{CSF}$ and have the offset $\Delta_i = -\Delta_s$ relative to idler resonance frequency. Again applying input-output relationships, we obtain the following expressions for the CSF and GSF transmitted through the output port of the OPO:

$$A_s^{out} = \frac{2(\gamma + i\Delta_i)\sqrt{\gamma^{in}\gamma^{out}}}{(\gamma + i\Delta_s)(\gamma + i\Delta_i) - |G|^2} A_s^{dr}, \tag{3.48a}$$

$$A_i^{out} = \frac{2(\gamma + i\Delta_i)\sqrt{\gamma^{in}\gamma^{out}}}{(\gamma + i\Delta_s)(\gamma + i\Delta_i) - |G|^2} \frac{g\sqrt{2\gamma_P^{in}}}{\gamma\gamma_P} (A_s^{dr})^* A_P^{dr}, \tag{3.48b}$$

where we define the output fields as $A_{s(i)}^{out} = |A_{s(i)}^{out}|e^{i\theta_{out,s(i)}}$. From eq.(3.48a) we can see that the phase $\theta_{out,s}$ of CSF on the OPO output is determined by θ_{CLF}, while the phase $\theta_{out,i}$ of GSF exiting the cavity is set by both pump and CSF phases $\theta_{GSF} = \theta_P - \theta_{CLF}$. Exiting the cavity, CSF and GSF propagate together with signal and idler entangled modes and reach the relative HDs. Observing beat notes between signal (idler) local oscillator and CSF (GSF) and demodulating the electronic signals with frequency $\Omega_{dem.} = |\Delta_s|$, we obtain the interference

fringes that are driven by the $\theta_{CSF} - \Phi_{LO,s}$ for the signal arm and $\theta_{GSF} - \Phi_{LO,i}$ for the idler arm, respectively. If we implement the phase lock in both arms and set

$$\theta_{out,s} - \Phi_{LO,s} \equiv \theta_{CSF} - \Phi_{LO,s} = \Phi_{lock,s} = 0, \tag{3.49a}$$

$$\theta_{out,i} - \Phi_{LO,i} \equiv (\theta_P - \theta_{CSF}) - \Phi_{LO,i} = \Phi_{lock,i} = 0, \tag{3.49b}$$

then the condition eq.(3.47) is automatically fulfilled that makes it possible to detect $\hat{q}_{s(i)}(\phi_\pm)$ and observe the noise suppression by subtracting one from another. From the other side, the choice $\Phi_{lock,s} = \Phi_{lock,i} = \pi/2$ enables to record $\hat{q}_{s(i)}(\phi_\pm + \pi/2)$ the measuring. Verification of noise reduction in $\hat{q}_s(\phi_+ + \pi/2) + \hat{q}_i(\phi_- + \pi/2)$ completes the certification of entanglement.

The approach presented above contains an inherent drawback since it doesn't provide the access to $\{\hat{x}_{s(i)}, \hat{p}_{s(i)}\}$ in the pump reference frame. While not preventing to verify Duan/EPR-steering criteria, it appears to become a problem, when setting the link between the entanglement and the atomic spin ensemble. In order to achieve the proper control over measured signal/idler quadratures, the phase θ_{CSF} of the CSF should be linked to the pump phase θ_P. It was implemented for a single-mode squeezer [75] and for an entanglement source where the signal and the idler were separated by single free spectral range [9]. However, this strategy can not be applied for the case of strongly non-degenerate (different colour) OPO.

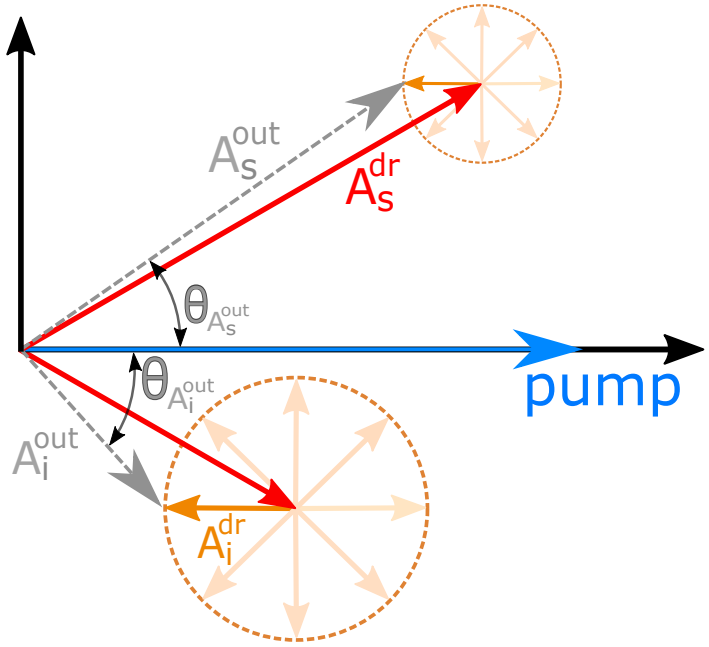

Figure 3.21: The effect of double seeding on the phasor diagram that breaks the symmetry between phases of A_s^{out} and A_i^{out} relative to the pump phase and thus causes sub-optimal quadrature detection. Specific case $\theta_P = 0$, ISR=0.25, $\theta_{CLF1} = \pi/6$ clearly reveals that $\theta_{A_s^{dr}} \neq -\theta_{A_i^{dr}}$ if θ_{CLF2} is π (as an illustrative example).

To obtain main results reported in this chapter, we didn't inject external CLF into the OPO. Instead, we exploited the locking beam on signal wavelength, which was already applied to using PDH technique (see section 3.8), but, as we show below, also served another purpose in our experiment. Entering cavity through the mirror M_{P1} and initially counter-propagating relative to pump, this seed experiences reflection due to non-ideal AR coating of OPO optical elements (mainly from the crystal). Due to that spurious back-reflection, the small part ($\sim 0.1\%$) of intracavity seed field travels inside the OPO along the direction of pump and undergoes parametric interaction on the crystal. As a result, back-reflected seed is parametrically amplified and GSF is generated. We notice that in eq.(3.48) $\Delta_s = \Delta_i \equiv 0$ now since the frequency of signal locking beam coincides with resonance frequency of OPO. However, we preserve the notation CLF and GSF for convenience. Both CLF and GSF exit OPO through output coupler M_{P2} in signal and idler entangled modes and after spatial separation on dichroic mirror reach the homodyne detectors. Here CLF/GSF meet respective LOs, whose phase was modulated by EOM on a frequency $\Omega_{ph.l.}$ above the spectral range of interest (typically $\Omega_{ph.l.}$ was chosen around $600 - 800$ KHz).

The electronic signal of each interference between CLF(GSF) and signal(idler) LO was amplified using low noise 30dB amplifiers and then was sent to SR-830 Lock-in Amplifier where demodulation on the frequency $\Omega_{ph.l.}$ was implemented. The demodulated electronic signal now could be used as an error signal containing the information about relative phase of CLF/GSF. The choice of demodulation phase between 0 and $\pi/2$ allowed us to lock either the phase $\Phi_{lock,s(i)} = 0$ or $\Phi_{lock,s(i)} = \pi/2$ relative to the LO phase in order to detect amplitude or phase quadrature, respectively. Finally, the error signal was sent to PID-controller, and the feedback signal controlled the PZT-element attached to the mirror in LO optical path after MCC. The schematics of introduced phase lock is shown on Fig.3.19. We also note, that in different configurations the modulation $\Omega_{ph.l.}$ could be applied not to LO, but to the locking beam itself.

Presented above strategy suffers from the following defect. Along with locking beam on signal wavelength (1064nm), the idler seed beam (852nm) enters OPO and experiences back reflection, thus being involved in parametric interaction between pump and reflected signal locking field. We consider the case when two coherent locking fields are injected, namely, CLF1 $A_s^{dr} = |A_s^{dr}|e^{i\theta_{CLF1}}$ as a field on signal wavelength and CLF2 $A_i^{dr} = |A_i^{dr}|e^{i\theta_{CLF2}}$ as a field on idler wavelength respectively. Solving eqs.(3.15), we obtain the expression for output fields:

$$A_s^{out} = \frac{2\sqrt{\gamma^{in}\gamma^{out}}}{\gamma\left(1-\frac{g^2(A_P)^2}{\gamma^2}\right)}\left[\frac{g}{\gamma}A_P(A_i^{dr})^* + A_s^{dr}\right] \sim \epsilon|A_i^{dr}|e^{i(\theta_P-\theta_{CLF2})} + |A_s^{dr}|e^{i\theta_{CLF1}}, \tag{3.50a}$$

$$A_i^{out} = \frac{2\sqrt{\gamma^{in}\gamma^{out}}}{\gamma\left(1-\frac{g^2(A_P)^2}{\gamma^2}\right)}\left[\frac{g}{\gamma}A_P(A_s^{dr})^* + A_i^{dr}\right] \sim \epsilon|A_s^{dr}|e^{i(\theta_P-\theta_{CLF1})} + |A_i^{dr}|e^{i\theta_{CLF2}}. \tag{3.50b}$$

Each CLF on the OPO output consists of two parts: parametrically amplified field on initial wavelengths and field arising due to difference frequency generation as a result of interaction between pump and opposite seed. Because of that, the phase of both classical fields A_s^{out} and A_i^{out} depend on phases of initial CLF1 and CLF2 as well as pump phase and the amplitudes of all 3 fields. It can be seen that now locking the phases according to eq.(3.49) does not fulfil the condition eq.(3.47) in general case if the phase θ_{CLF2} of CLF2 is not locked relative to phase θ_{CLF1} of CLF1 or to the pump phase θ_P.

The random drift of $\theta_{CLF,2}$, in essence, represents phase noise. Assuming equal losses in signal and idler modes, we select homodyne phases $\theta_{A_{s(i)}^{out}} - \Phi_{LO,s(i)} \equiv \Phi_{lock,s(i)} = 0$ and analyze the noise of observable $\hat{A}_{tot,2}^{out} = \left[\hat{q}_s^{out}(\theta_{A_s^{out}}) - \hat{q}_i^{out}(\theta_{A_i^{out}})\right]$. Similarly to eq.(3.25), one obtains

$$S_{\hat{A}_{tot,2}^{out},\hat{A}_{tot,2}^{out}} = \langle\Delta\left(\hat{q}_s\right)^2\rangle + \langle\Delta\left(\hat{q}_i\right)^2\rangle - 2\langle\Delta\left(\hat{q}_s(\psi_+)\hat{q}_i(\psi_-)\right)\rangle\cos\left(\overline{\Delta\theta_{CLF}}\right) \tag{3.51}$$

where $\overline{\Delta\theta_{CLF}}$ is root mean square of $\Delta\theta_{CLF} = \theta_{A_s^{out}} + \theta_{A_i^{out}}$. The value $\overline{\Delta\theta_{CLF}}$ is a function of ϵ and amplitudes $|A_s^{dr}|$, $|A_i^{dr}|$. Importantly, $\overline{\Delta\theta_{CLF}}$ grows with increase of idler-to-signal ratio (ISR) defined as $|A_i^{dr}|/|A_s^{dr}|$. In particular, ISR= 0.2 and $\epsilon = 0.6$ give strong phase noise $\overline{\Delta\theta_{CLF}} \approx 0.15\pi$ (see sec.A.1). Fig.3.21 illustrates the consequences caused by random walking of θ_{CLF2} phase. Detailed investigation of double seeding of OPO and regimes of different ISR is made in [88].

In order to mitigate the phase noise arising from fluctuations of θ_{CLF2}, we therefore have to reduce the ISR. Although it can not be precisely measured (since powers are incredibly small), the characterization of AR coating of the crystal allows to make assumption, that the ratio of back reflected to initially counter propagating fields are approximately equal for signal and idler wavelengths. Therefore, ISR is solely defined by the input powers of CLF1 and CLF2 before OPO. In practise, minimization of ISR was hard to implement: one the one hand, we are interested to reduce both CLF1 and CLF2 powers as much as we can because we do not want to contaminate the entangled modes with excessive classical noise. On the other hand, the optical power of injected locking beams should be big enough to yield decent (signal to noise ratio) quality of PDH error signal. We also need to take into consideration that auxiliary fields enter the cavity through HR mirror in presented configuration of OPO locking scheme. After searching the best configuration given technical parameters of the setup (electronics), we have chosen the input powers 1mW for the of CLF1 and 30μW for the CLF2 respectively. Hence, ISR was equal to $\sqrt{0.03} \approx 0.17$.

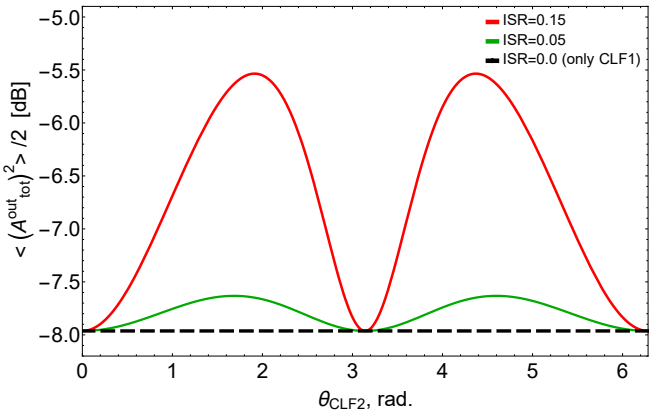

(a) Theoretical model: the random walking (scanning) of CLF2 phase θ_{CLF2} leads to increasing of quantum noise in quadratures $\hat{q}_s(\theta_{A^{out}_s}) - \hat{q}_i(\theta_{A^{out}_i})$ in comparison to the optimal phase lock $\hat{q}_s(\psi_+) - \hat{q}_i(\psi_-)$. The effect is shown for different idler-to-signal (ISR) seeds ratios, when $\epsilon = 0.6$, $\eta = 0.9$ and the absence of phase noise is assumed.

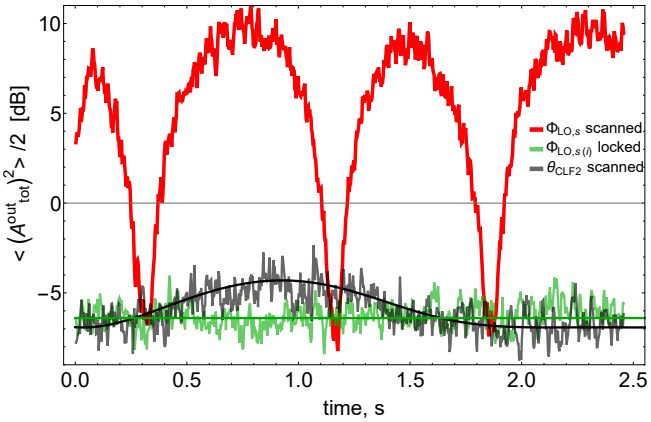

(b) Experimental data: detection of $\hat{q}_s(\theta_{A^{out}_s}) - \hat{q}_i(\theta_{A^{out}_i})$. Oscillations of cross-correlation are observed when θ_{CLF2} is slowly scanned ($\sim$ 1 Hz). The noise was recorded for zero spectral span and frequency 200KHz. It corresponds to prediction of theoretical model if $\eta = 0.85$, $\epsilon = 0.5$ and ISR$\approx$ 0.2.

Figure 3.22: Effect of double seed (CLF1 + CLF2) injection.

If interbeam correlations $S_{\hat{A}^{out}_{tot,2}, \hat{A}^{out}_{tot,2}}$ are measured on the time scale faster than characteristic velocity of θ_{CLF2} drift, we observed the fluctuation of noise level in time domain, as shown on the Fig.3.22(b). The range of these fluctuations agrees well with expected $\overline{\Delta\theta_{CLF}}$ inferred from operated pump power and ISR. The slow drift of θ_{CLF2} can be counteracted by fine adjustment of locked phase $\Phi_{lock,i}$ while fixing $\Phi_{lock,s}$ (or vice versa).

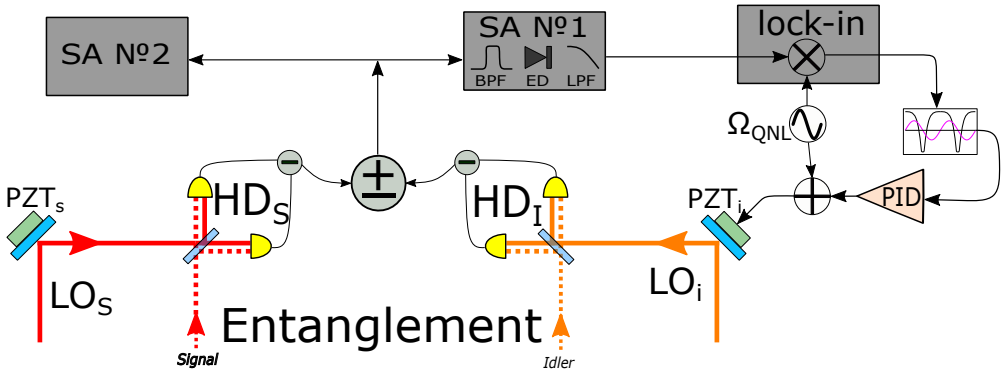

Figure 3.23: Quantum noise locking technique applied to entanglement. The error signal was obtained by combining the photocurrents from each homodyne detector, which are then filtered. The feedback signal was sent to the piezo in either of LO optical mode. See text for details. The following notations are used: SA - spectrum analyzer, PID - proportional–integral–derivative controller, PZT - piezo-electric transducer.

Shift of both signal and idler locking beams to the next FSR (see section 3.8.2) will let us exclude them from coherent phase locking scheme by proper filtering. It will enable us to inject another coherent locking beam (for example, on signal wavelength) and implement an 'ideal configuration' (referring to eq.(3.48), eq.(3.49)), where no idler seeding occurs. We also recall that the purpose of OPO locking scheme introduced in section 3.8.2 is to get rid of classical beams injection and contamination of spectral range subject to verify EPR-correlations. Therefore, we also detune the new CLF in such a way that it stays within OPO resonance but moved beyond spectral frequencies where entanglement will be demonstrated (as illustrated on Fig.3.14(b)). Given the OPO bandwidth $\approx$ 15MHz, we typically choose $|\Delta_s| \approx$5-6 MHz. In our experiment the required frequency shift might be implemented by taking the laser field and transmitting through the double AOM setup (Fig.3.14(b) and Fig.3.19). The first AOM scatters the light into $\pm$1-order while the second - into $\mp$1-order. By adjusting modulation frequencies for both

AOMs ($\Delta_1 \approx 120$MHz, $|\Delta_0| = |\Delta_s| \approx$5-6 MHz), the required frequency shift $|\Delta_s|$ is achieved. As a conclusion, locking the OPO with next-FSR frequency shifted fields performs two functions: it eliminates the classical noise from signal-idler entanglement spectral frequency, but also gets access to improved phase locking by obviating the effect of idler seeding.

3.10.4 Quantum noise locking

In this section we explore the quantum noise locking (QNL) technique [89] that can yield phase sensitive error signal in the absence of external seed, in contrast to phase locking (section 3.10.3). The experimental scheme is presented on Fig.3.23. The phase of either LO (idler on Fig.3.23) is modulated with frequency Ω_{QNL} by piezoelectric transducer. Then LOs are overlapped with entangled modes and sent onto HDs. After combining the photocurrents (for example, subtracting one from another) we observe the correlations whose level is determined by the relative phase of LOs. The electronic signal is transmitted through spectrum analyser (SA №1) that performs the function of band-pass filter (BPF) with subsequent envelope detector (ED). The lower frequency Ω_{low} of BPF is chosen to eliminate the modulation induced by PZT in LO arm: $\Omega_{low} > \Omega_{\mathsf{QNL}}$. After envelope detection signal is low-pass filtered followed by demodulation on lock-in amplifier with demodulation frequency Ω_{QNL}. As a result, we obtain QNL error signal with zero crossings corresponding to maximum correlations/anticorrelations [89], allowing us to lock them and measure the noise on the second spectrum analyser (SA №2). The original idea was developed to stabilize the phase of single-mode squeezed vacuum. However, despite the fact that in described experiment we have two phases related to each LO, the feedback signal applied to the chosen LO drives it's phase in such a way that compensates the phase drift in other arm and always maintains the (two-mode) squeezing at lowest possible level.

3.11 Results of entanglement characterization

The first measurement described in this section was done with the purpose to estimate the strength of signal-idler correlations and the performance of the phase locking. Photocurrents from both HDs were sent onto SR 780 low noise amplifier with preceded subtraction. The amplified differential photocurrent was then recorded by Agilent E4405B Spectrum Analyzer, where it's single-frequency Fourier component $\Omega = 400$ kHz was investigated. Spectra are displayed on Figure 3.24. In the beginning, the phase of one LO was running free, whereas the phase of the second LO was scanned by PZT element with frequency (∼1-5Hz). Next, the phases of two LOs were locked according to eq.(3.49) to explore the short-term stability of the scheme of the phase control. The fluctuations of the idler locking beam phase $\theta_{CLF,2}$ apparently didn't disturb the correlations on the time scale ∼0.1-1s, allowing to reach ≈ -8 dB quantum noise reduction relative to the shot noise. Increasing the measurement time, we observed the reduction of correlation strength when LO phases were locked caused by drifting of the idler phase. Finally, LO phases were locked to yield anti-squeezing.

At this step we compare the performance of phase lock with QNL technique introduced in sec.3.10.4. We chose the frequency of phase modulation $\Omega_{QNL} = 30$kHz, the Agilent E4405B spectrum analyzer with center frequency 800 kHz, RBW=300 kHz and VBW=100 kHz was used to implement BPF and ED stages (as SA №1 on the Fig.3.23). We then tuned parameters of the lock-in amplifier and adjusted the depth of phase modulation. The best shape of the error signal was reached at the following settings: LPF time constant = 100 ms, 6 dB/octave. The correlations were then recorded with the Rohde&Schwarz FPC1500 spectrum analyser (SA №2) with settings, which correspond to the previous measurement when the phase locking was engaged. Applying QNL technique, we find the maximum ≈ -6 dB of quantum noise suppression, which is not compatible to ≈ -8 dB observed using the technique detailed in section 3.10.3. We explain this modest performance of QNL technique in our case by the fact that the assymmetry between the squeezing and the antisqueezing was not high enough [89] to provide stability comparable with the phase locking. This circumstance prevails over possible benefit from the absence of the classical drive beam in the OPO. Thus, we decided to refrain from QNL technique in our experiment and rely on phase locking.

The maximum level of interbeam correlations at scanned phase of LO (trace (d) on Figure 3.24) is not limited by the drift of the phase of the idler auxiliary beam. Using this regime, we made a conclusion regarding the presence /absence of assymmetry in signal-idler total losses. We have adjusted relative signal-to-idler weight by

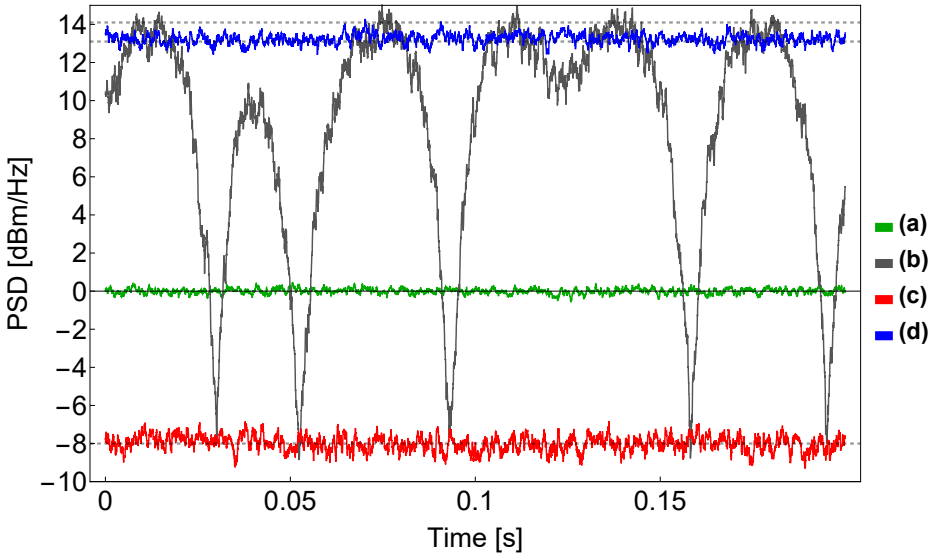

Figure 3.24: Zero-span measurement at the frequency 400 KHz, parametric gain= 3.67 ($P_P/P_{P,th} \approx 0.48$), RBW=30 kHz, VBW=300 Hz. Trace **(a)**: total (signal + idler) shot noise of local oscillators, traces (b)-(d): measurement of entangled twin-beams. Trace **(b)**: the phase of one LO was scanned showing the transition from correlations to anticorrelations. Trace **(c)**: LOs phases were set to be 0 - two-mode squeezing was recorded. Trace **(d)**: phase of one LO was flipped by 180° while the phase of other LO was maintained at 0, giving anti-squeezing.

tuning the ratio between powers of LOs. The relative difference of $P_{LO_{1064}}$ and $P_{LO_{852}}$ was found to be less than 1% to yield the strongest quantum noise suppression. Therefore we can consider the losses in two channels to be approximately equal, taking into account the reduced impact of the assymmetry at relatively low ratio $P_P/P_{P,th}$.

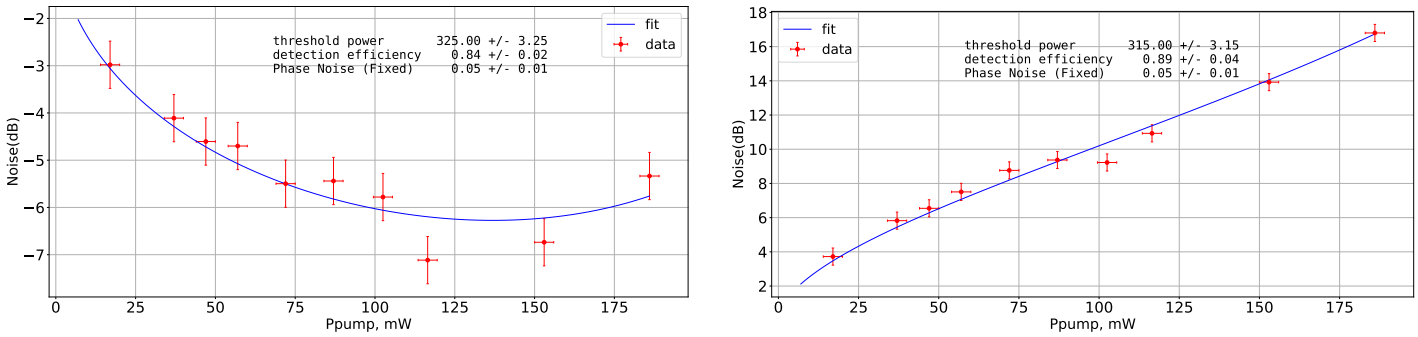

(a) Squeezing fit.

(b) Antisqueezing fit.

Figure 3.25: Fitting squeezing and antisqueezing as a function of pump power P_P.

We proceed with the characterization of the entanglement, investigating the strength of correlations as a function of pump power P_P. The dependence $S_{\hat{A}^{out}_{tot},\hat{A}^{out}_{tot}}(P_P)$ is fitted using eq.(3.26) (in the limit $\Delta \to 0$) for the case of two mode squeezing, the similar calibration is made for anti-squeezing. We extract several parameters from this fit. First of all, it is the total efficiency of homodyne detection η, that is then compared with expected value composed from all possible source of losses, which we considered and estimated independently in sections 3.10.2 and 3.9.1 (summarized in table 3.2). In a similar fashion, we verify the level of threshold pump power $P_{P,th}$ obtained in section 3.9.2. We also extract the level of the phase noise $\overline{\theta}_{\text{tot}} = \overline{\theta_s} + \overline{\theta_i}$. The data were taken in the same way as described above, but now we explore the frequency $\Omega = 200$ kHz. Here we scan the phase of LO and make a fit in order to extract the squeezing/antisqueezing levels for each value of P_P. Thus, we make sure to get values of correlations not spoiled by the drift of the phase of the idler locking beam. The best consistency with the expected η, $P_{P,\text{th}}$ values was reached when we fixed RMS quadrature fluctuation $\overline{\theta}_{\text{tot}} = 0.05$ (rad.) and then

extracted the set $\{\eta, P_{P,\text{th}}, \}$ from fits. Figure 3.25 reveals the reasonably good, although non-perfect, agreement between fits of squeezing and antisqueezing. However, relying mostly on squeezing fit, we find $P_{\text{th.}}$ =325 mW, $\eta = 0.84$. The quality of fit of the squeezing looks quite bad, the possible reason might be the phase noise that varies from one point to another. The maximum level of interbeam correlations here (≈ -6.5dB) was significantly less than on Figure 3.24. We explain it by the enhanced impact of the phase noise at lower Fourier frequencies.

η_{esc}	η_{mm}	η_{det}	η
99%	98%	90%	87%

Table 3.2: Different sources of losses in entangled modes based on previous chapters.

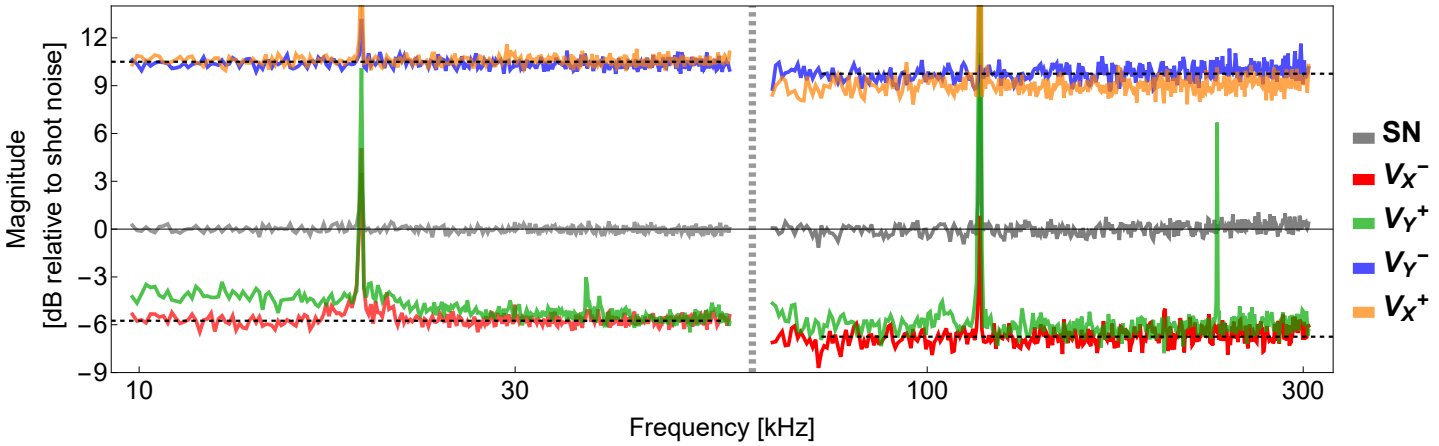

Figure 3.26: The spectra of noise in the linear combination of signal and idler modes. In particular, the difference of amplitude quadratures (red trace) and the sum of phase quadratures (green trace) display the reduction of noise compared to shot noise level (gray trace). The difference of phase quadratures and the sum of amplitude quadratures (blue and orange traces, respectively) correspond to the antisqueezing. This figure was also used in the following paper: T.B. Brasil et al, Nature Communications. 13, 4815 (2022).

At previous steps we have done the optimization of parameters of the phase locking and the stabilization of OPO cavity length. Also, the optimal value for pump power $\sigma \approx 0.6$ was found. Using these settings, we perform broadband measurement. We exploit a new configuration of data recording: the photocurrents from each HDs were first amplified by home-made amplifiers and then were directed to low-noise 16 bits analog-to-digital converter (ADC) (Spectrum M2p5913-x4). Using ADC, we implemented FFT for both sum and difference of photocurrents after digital transformation. It made possible to observe quantum noise suppression in both amplitude $\{\hat{q}_s(\phi_+), \hat{q}_i(\phi_-)\}$ and phase $\{\hat{q}_s(\phi_+ + \pi/2), \hat{q}_i(\phi_- + \pi/2)\}$ quadratures, provided $\Phi_{lock,s} = \Phi_{lock,i} = 0$ and $\pi/2$, respectively. Hence, the characterization of the entanglement (eq.(3.10), eq.(3.13)) and EPR-steering (eq.(3.11), eq.(3.12)) is performed. First, we focus on the frequency range $50 - 300$ kHz and optimize spectra of two-mode squeezing (Figure 3.26, right part). We explore quantum noise reduction in $\hat{q}_s(\phi_+) - \hat{q}_i(\phi_-)$ and $\hat{q}_s(\phi_+ + \pi/2) + \hat{q}_i(\phi_- + \pi/2)$. As a result, we obtain $V_{X_-} = -7.1$ dB ($r_{X_-} = 0.82$) for effective amplitude quadratures, and $V_{P_+} = -6.2$ dB ($r_{P_+} = 0.71$) for effective phase quadratures. We assume that $r_{X_-} \neq r_{P_+}$ was observed due to the solely technical reasons. Namely, we performed long-term measurement with big averaging (~ 1000) of FFT traces. Therefore, the drift of idler phase of locking beam influenced and limited correlations. In particular case of data on Figure 3.26 this negative impact turned out to be more detrimental for measurement $\Phi_{lock,s} = \Phi_{lock,i} = \pi/2$. However, it seems to be completely coincidental. We therefore take into account non-symmetric quantum noise reduction $r_{X_-} \neq r_{P_+}$ and obtain from eq.(3.13), eq.(3.12):

$$\Delta_D = e^{-2r_{X_-}} + e^{-2r_{P_+}} = 0.44 < 2 \tag{3.52a}$$

$$\epsilon_{\mathsf{EPR}} = \frac{1}{\cosh(2r_{X_-})} \frac{1}{\cosh(2r_{P_+})} = 0.17 < 1 \tag{3.52b}$$

Strictly speaking, we didn't directly observe inferred variances optimized for EPR-steering criterion to obtain the result given in eq.(3.52b). Instead, we measured linear combinations of quadratures with equal weights and used the feature eq.(1.29) of two-mode squeezed states. Even more impressive results Δ_D and ϵ_{EPR} are reported if correction for quantum efficiency of photodiodes is made ([90]).

As was stated earlier, the impact of the phase noise grows up with the descent of the Fourier frequency. However, we have also managed to confirm the entanglement and EPR-steering at the frequency 50 kHz and down to 10 kHz, but with moderate levels of two-mode squeezing $V_{X_-} = -6.0$ dB, $V_{P_+} = -5.2$ dB (Figure 3.26, the left part). In lower spectral range correlations are severely diminished by classical noise of injected locking beams. Replacement of the current locking scheme with the updated configuration (section 3.8.2) is ongoing work.

Chapter 4

Atomic spin oscillator at acoustic frequency range

4.1 Introduction

Room temperature spin gas of alkali atoms in an external magnetic field is a suitable choice for building light-atom interface as a crucial element of quantum communications and (distributed) quantum computation protocols [91]. Entanglement between two distant atomic spin ensembles [38, 92], light-matter teleportation [93] and teleportation of a quantum state from one spin ensemble to another [94] constitute important steps towards implementation of quantum repeater [95]. A number of experiments [96, 97] has been carried out with a purpose to explore the features of atomic quantum memory. The second application for atomic ensembles lies in the area of quantum-enhanced sensing and metrology, such as magnetometry [98, 99]. Another direction, being relevant for this thesis, is the reduction of quantum noise that limits the sensitivity of optomechanical systems [34, 35], experimentally demonstrated in [39, 40].

In order to exploit the atomic system in quantum regime, most of the experiments mentioned above were performed in MHz and sub-MHz spectral range, where one can readily reach quantum spin noise level. The latter consists of atomic shot noise (projection noise, PN), shot (imprecision) noise of probing optical field and quantum back action (QBA) noise arising due to the interaction of light with the atoms. Nevertheless, one can foresee a broad range of applications for the spin ensemble operated in lower frequency band. For example, the ability to detect magnetic fields in the acoustic spectral range is relevant for the analysis of biological signals [100, 101, 102]. As for the main subject of this thesis, the atomic ensemble in the configuration of a quantum oscillator should exhibit quantum noise limited performance at near-DC frequencies in order to be compatible with free mass motion of test mass mirrors for subsequent improvement of the sensitivity of GWDs. Exploiting the spin ensemble in a similar way, QBA evasion in the spectral domain $\Omega \lesssim 100$ kHz can be pursued for free-space levitated optomechanics, including optically trapped dielectric nano-particles [103, 104]. However, if an atomic spin oscillator is shifted down to a lower spectral range, its dynamics tends to be contaminated by ubiquitous technical noise, compromising quantum regime and precluding quantum-enhanced protocols outlined above.

In this chapter we report the atomic spin oscillator, whose quantum (back action) noise dominated motion extends from MHz spectral range down to the upper part of acoustic band. We exploit the ensemble of Cs^{133} atoms contained in a glass cell. The system is optically pumped to approach a coherent spin state (CSS). Analogous to optomechanics [105, 106], the spin ensemble induces the suppression of fluctuations of probe optical field below shot noise limit [107]. Such ponderomotive squeezing is experimentally observed and calibrated in this chapter. Although being used just as a metric for the amount of the quantum noise in the system throughout this thesis, the ponderomotive squeezing is of interest on its own, representing an alternative way to produce non-classical states of light [108]. In particular, we demonstrate that the ponderomotive squeezing is preserved down to the lower part of audioband ($\gtrsim 6$ kHz), thus confirming the strong contribution of the quantum noise to the spin motion for respective spectral range. Targeting the potential application of the atomic ensemble for quantum noise mitigation in GWDs, we investigate the feasibility to tune the spin oscillator even further towards DC-frequencies. Specifically, we show the downshift of an effective resonance frequency of the spin oscillator by *virtual rigidity* (virtual optical spring has been introduced in sec.2.3), which might be seen as the consequence of the

ponderomotive squeezing.

Jun Jia and Ryan Yde with the help from Rodrigo Adriano Thomas, Michael Zugenmaier and Luiz Couto performed initial preparations to operate the atomic ensemble in MHz and sub-MHz range. It included arranging the optical pumping scheme, testing the cells, setting the drive magnetic field together with magnetic shielding and optimization of atomic cell filling factor by the top-hat profile of the probe beam. The author of the thesis contributed to the calibration by *coherently induced Faraday rotation* (CIFAR) and *magneto optical resonance spectroscopy* (MORS). The work on the technical improvements that allowed for the transition from MHz to kHz spectral rangewas led by Tulio Brito Brazil. Those aspects are not covered here. The author participated in the final experimental run, collection of the experimental data, their processing and interpretation. In particular, the questions of the impact of the tensor alignment spin noise and the amplitude noise of the probe laser on the quantum noise limited motion of the spin oscillator in acoustic range will be discussed in this chapter.

4.2 Theory

4.2.1 Structure of atomic levels

We begin with the ground state $6S$ with orbital momentum $l = 0$ and the first excited state $6P$ ($l = 1$) of ^{133}Cs atom with single electron on external orbit (n=55). Since spin of electron is $s = 1/2$, we observe fine splitting of $6P$-state into $6P_{1/2}$ ($l \uparrow\downarrow s$) and $6P_{3/2}$ ($l \uparrow\uparrow s$), while denoting the ground state as $6S_{1/2}$. The optical transitions $6S_{1/2} \leftrightarrow 6P_{1/2}$ and $6S_{1/2} \leftrightarrow 6P_{3/2}$ correspond to $D1$-line (the wavelength 894nm) and $D2$-line (852nm) respectively. The next step is to include the hyperfine splitting of each level from $6S_{1/2}$, $6P_{1/2}$, $6P_{3/2}$ due to interaction of total electron momentum $l + s$ and nuclear spin $I = 7/2$. As a result, both $6S_{1/2}$ and $6P_{1/2}$ levels are split onto 2 sublevels each ($F = I \pm (l - s) = 7/2 \pm 1/2$: $F = 3, 4$), whereas $6P_{3/2}$ is splitted onto 4 sublebvels $F = 2, 3, 4, 5$, where F represents the total momentum of atom (electron spin + orbital momentum of electron + nuclear spin). Finally, applied external magnetic field $\boldsymbol{B}$ splits each hyperfine levels F onto $2F + 1$ (if F is integer or onto $2F$ if not) sublevels, whose energies are defined by the projection m of total momentum F onto the direction of magnetic field:

$$m = -F,\ -(F-1),\ \ldots (F-1),\ F. \tag{4.1}$$

We are interested to study the energy levels of ground level $6S_{1/2}$, whose values are given by the expression:

$$E_{F,m} = \frac{\Delta E_{HFS}}{2(2I+1)} + g_I \mu_B m B + \frac{\Delta E_{HFS}}{2}\sqrt{1 + \frac{4m}{2I+1}x + x^2}, \qquad x = \frac{(g_J - g_I)\mu_B B}{\Delta E_{HFS}}, \tag{4.2}$$

where $\Delta E_{HFS} \approx 9.2$ GHz is the hyperfine splitting of the state $6S_{1/2}$. In the first-order approximation Zeeman sublevels are equidistant and separated by *Larmor frequency* Ω_L

$$\Omega_L = \frac{g_F \mu_B B}{\hbar}. \tag{4.3}$$

If we decompose eq.(4.2) and take into account $\propto m^2$ terms, we introduce the correction for Larmor frequency determined by factor

$$\Omega_{\mathsf{QZS}} = \frac{2\Omega_L^2}{(\Delta E_{HFS}/\hbar)}. \tag{4.4}$$

This effect is known as quadratic Zeeman splitting (QZS). With QZS included, the expression for energy of Zeeman levels is given by:

$$E_{F,m} = \hbar\Omega_L m + \hbar\Omega_{\mathsf{QZS}} m^2 \tag{4.5}$$

Above we neglected the first term $\propto \Delta E_{\mathsf{HFS}}$ on the right side of eq.(4.2) since it does not depend on m and represents constant shift. In the following description we consider atoms to populate $6S_{1/2}$, $F = 4$ hyperfine level.

4.2.2 Atomic ensemble in external magnetic field

We study the behaviour of single atom and introduce the operator of orbital momentum $\hat{j}$, that can be decomposed onto operators of projections of total momentum onto OX, OY and OZ axes:

$$\hat{j}^2 = \hat{j}_x^2 + \hat{j}_y^2 + \hat{j}_z^2. \tag{4.6}$$

We can specify the commutations relations for those operators in a form:

$$\left[\hat{j}_k, \hat{j}_l\right] = i\epsilon_{kl}\hat{j}_p, \quad \left[\hat{j}^2, \hat{j}_k\right] = 0 \tag{4.7}$$

We assume the quantization axis to be OX defining the direction the magnetic field $\vec{B}$ that causes Zeeman splitting. We now introduce eigenvectors $|F, m\rangle$ of operators $\hat{j}^2$, $\hat{j}_x$:

$$\hat{j}^2 |F, m\rangle = \lambda(F) |F, m\rangle \tag{4.8a}$$

$$\hat{j}_x |F, m\rangle = m |F, m\rangle , \tag{4.8b}$$

where $\lambda(F)$ is the squared total momentum and m is defined in eq.(4.1). We specify that $m^2 \leq \lambda(j)$ from definition of $\lambda(j)$. Next, we define operators $\hat{j}_+$, $\hat{j}_-$ using projections of ensemble momentum $\left\{\hat{j}_y, \hat{j}_z\right\}$ onto axes perpendicular to quantization axis:

$$\hat{j}_\mp = \hat{j}_z \pm i\hat{j}_y, \quad \hat{j}_+ = \left(\hat{j}_-\right)^\dagger \tag{4.9}$$

which obey the following commutation relations:

$$\left[\hat{j}_x, \hat{j}_\pm\right] = \pm\hat{j}_\pm. \tag{4.10}$$

Using eq.(4.10), we can deduce the following expression:

$$\hat{j}_x \left(\hat{j}_\pm |jm\rangle\right) = \hat{j}_\pm \left(\hat{j}_x \pm 1\right) |jm\rangle = (m \pm 1) \left(\hat{j}_\pm |jm\rangle\right). \tag{4.11}$$

From eq.(4.11) we can conclude that operators $\left\{\hat{j}_+, \hat{j}_-\right\}$ are actually *ladder* operators [109] since they move down/up the atom to the next Zeeman sublevel:

$$\hat{j}_+ |F, (m-1)\rangle = \beta_{F,m,+} |F, m\rangle \tag{4.12a}$$

$$\hat{j}_- |F, m\rangle = \beta_{F,m,-} |F, (m-1)\rangle \tag{4.12b}$$

One can get the expressions for $\lambda(F)$ and $\beta_{F,m,\pm}$ using eq.(4.7), eq.(4.10). Here we just provide with the result omitting the derivation routine [109]:

$$\lambda(F) = F(F+1) \tag{4.13a}$$

$$\beta_{F,m,+} = \beta_{F,m,-} \equiv \beta_{F,m} = \sqrt{(F+m)(F-m+1)} \tag{4.13b}$$

We now make a transition from operators for single atom to operators of orbital momenta for the whole ensemble. Using eq.(4.8b), eq.(4.9), eq.(4.12) and eq.(4.13b), we introduce

$$\hat{j}_x = \sum_{m=-F}^{F} m\hat{\sigma}_{mm}, \quad \hat{J}_x = \sum_N \hat{j}_x, \tag{4.14a}$$

$$\hat{j}_y = \frac{1}{2}\sum_{m=-F}^{F} \beta_{F,m} \left(\hat{\sigma}_{m+1,m} + \hat{\sigma}_{m,m+1}\right), \quad \hat{J}_y = \sum_N \hat{j}_y, \tag{4.14b}$$

$$\hat{j}_z = \frac{1}{2i}\sum_{m=-F}^{F} \beta_{F,m} \left(\hat{\sigma}_{m+1,m} - \hat{\sigma}_{m,m+1}\right), \quad \hat{J}_z = \sum_N \hat{j}_z, \tag{4.14c}$$

$$\hat{j}_0 = \sum_{m=-F}^{F} |m|\hat{\sigma}_{mm}, \quad \hat{J}_0 = \sum_N \hat{j}_0, \tag{4.14d}$$

where $\hat{\sigma}_{kl} = |k\rangle \langle l|$ is the projection operator (meaning Zeeman sublevel for hyperfine level F: $\hat{\sigma}_{kl} \equiv |F, k\rangle \langle F, l|$) and N is the number of atoms in the ensemble. System eq.(4.14) was completed by operator $\hat{J}_0$ which represents the

total momentum, being analogous to $\hat{j}^2$. Collective operators obey commutation relations, for example $\left[\hat{J}_y, \hat{J}_z\right] = i\hat{J}_x$. The ladder operators for collective atomic motion

$$\hat{J}_+ = \hat{J}_z - i\hat{J}_y, \quad \hat{J}_- = \hat{J}_z + i\hat{J}_y \tag{4.15}$$

are mapped to the bosonic annihilation/creation operators (eq.(4.9)) corresponding to single deexcitation/excitation in the system [110]:

$$\hat{J}_+ = \sqrt{N}\sqrt{\left(\hat{1} - \hat{j}_+\hat{j}_-/N\right)}\hat{j}_-, \quad \hat{J}_- = \sqrt{N}\hat{j}_+\sqrt{\left(1 - \hat{j}_+\hat{j}_-/N\right)}. \tag{4.16}$$

Commutation relations $\left[\hat{J}_+, \hat{J}_-\right] = 2\hat{J}_x$ are fulfilled provided [111], [110]

$$\hat{J}_x = J_x - \frac{1}{2}\hat{j}_+\hat{j}_-. \tag{4.17}$$

We now consider that atomic system is prepared in such a state that projection of spin along quantization axis becomes macroscopic: $\hat{J}_x \approx J_x \approx |\langle \hat{J}_x \rangle|$. One may determine the polarization of spin ensemble $\mathcal{P}$:

$$\mathcal{P} = \frac{1}{NF}\langle \hat{J}_x \rangle = \frac{1}{NF}\sum_N \sum_{m=-F}^{F} m\langle \hat{\sigma}_{mm} \rangle \tag{4.18}$$

that represents the degree of ensemble orientation along the applied magnetic field directed along OX axis. In the limit that all atoms occupy the highest (lowest) Zeeman sublevel $m = F$ (or $m = -F$), all momenta are aligned along (opposite to) magnetic field, resulting in $\mathcal{P} = 1$ ($\mathcal{P} = -1$). Strongly polarized state of atomic ensemble allows for the approximation $\langle \hat{j}_+\hat{j}_- \rangle / \langle \hat{J}_x \rangle \ll 1$. Using that, we simplify eq.(4.16) and deduce:

$$\hat{J}_\pm \approx \hat{j}_\pm\sqrt{J_x} \tag{4.19}$$

The interaction of atomic system with applied magnetic is described by Hamiltonian $\hat{H}_B \propto \vec{B}\hat{J} = \hbar\Omega_L\hat{J}_x$, where Ω_L is given by eq.(4.3). Using eq.(4.17), we obtain the following expression $\hat{H}_B$:

$$\hat{H}_B = \hbar\Omega_L\left(J_x - \frac{\hat{J}_+\hat{J}_-}{J_x}\right) = -\hbar\Omega_S|J_x| + \frac{\Omega_S}{2}\left(\hat{x}_S^2 + \hat{p}_S^2\right) \tag{4.20}$$

where normalized projections of total momentum $\hat{x}_S$ and $\hat{p}_S$

$$\hat{x}_S = \frac{1}{\sqrt{J_x}}\hat{J}_z, \quad \hat{p}_S = \frac{-\mathsf{sign}(J_x)}{\sqrt{J_x}}\hat{J}_y \tag{4.21}$$

are defined. The mutual orientation of macroscopic angular momentum J_x and magnetic field $\vec{B}$ is encoded in the sign of effective Larmor frequency Ω_S:

$$\Omega_S = \mathsf{sign}(-J_x)\Omega_L. \tag{4.22}$$

The first term $\propto \Omega_S|\hat{J}_x|$ on the right hand side of eq(4.20) represent the offset of energy of spin system. The second term describes the precession of normalized projections of total spin ensemble perpendicular to the external magnetic field. One can see that $\hat{x}_S$ and $\hat{p}_S$ are actually canonical position and momentum in a phase space

$$\hat{x}_S = \frac{\hat{j}_- + \hat{j}_+}{\sqrt{2}}, \quad \hat{p}_S = \frac{\hat{j}_- - \hat{j}_+}{\sqrt{2}i} \tag{4.23}$$

and follow the commutation rule $[\hat{x}_S, \hat{p}_S] = i$. The behavior of collective spin as harmonic oscillator is valid in assumption of Holstein-Primakov approximation.

We can identify two different regimes of dynamics of the spin ensemble depending on the sign of projection of total momentum onto quantization axis. If $J_x < 0$ then Larmor frequency Ω_S is positive, and we observe the the 'traditional' motion of spin oscillator in phase space (rotation counterclockwise). Physically, negative sign of J_x corresponds to anti-alignment of macroscopic spin relative to magnetic field. Hence, all atoms populate the Zeeman sublevel $m = -F$ with lowest energy. In contrast,it is possible to induce the inverse population of atomic

ensemble, pushing atoms to highest Zeeman sublevel $m = F$, implying $J_x > 0$. In that case the single excitation of system will lower its total energy since atoms can only move to the states $m < F$, which is also highlighted by negative sign of atomic frequency Ω_S. At the same time, we obtain the oscillator with an effective negative mass, whose harmonic evolution in phase space is opposite to oscillator with positive Larmor frequency.

4.2.3 Interaction of atoms with light

This section has the following structure. First, we summarize the most essential steps of procedure outlined in [112] to derive the generalized Hamiltonian describing interaction between ensemble of atoms and probe light field. Next, we elaborate on the main features of Faraday interplay that is comprehensively covered in [113, 111, 114, 115] (arranged in chronological order) and forms the basement for experimental characterization provided in this chapter. Finally, we discuss the effects caused non-linear (tensor) interaction between light and ensemble beyond Faraday model, mainly inspired by analysis performed in [113].

Generalized Hamiltonian of light-atom interaction

The Hamiltonian of interaction between dipole moment of single atom and electric field is written as $\hat{H}_{int.} = \hat{\vec{d}}^{(+)}\hat{\vec{E}}^{(-)} + \hat{\vec{d}}^{(-)}\hat{\vec{E}}^{(+)}$ where superscript $(\pm)$ denotes positive/negative frequency components. We consider that the probe field is detuned from the D2-line and adiabatically eliminate the hyperfine manifold F' corresponding to excited states. The Hamiltonian is then transformed:

$$\hat{H}_{int.} = \hat{\vec{E}}^{-}\hat{\boldsymbol{\alpha}}\hat{\vec{E}}^{+}, \quad \hat{\boldsymbol{\alpha}} = \sum_{F'} \frac{\hat{\sigma}_g \boldsymbol{d} \hat{\sigma}_{F'} \boldsymbol{d} \hat{\sigma}_g}{\Delta_{F'}} \tag{4.24}$$

where $\hat{\boldsymbol{\alpha}}$ is polarizability tensor, $\hat{\sigma}_F = \sum_m |F, m\rangle \langle F, m|$, $\hat{\sigma}_g = \sum_F \hat{\sigma}_F$ $\hat{\sigma}_{F'} = \sum_{m'} |F', m'\rangle \langle F', m'|$, $\hat{\sigma}_e = \sum_{F'} \hat{\sigma}_{F'}$ and $\Delta_{F'}$ is the detuning from D2 transition. Initially prepared at $6S_{1/2}$, $F = 4$, atoms move to excited state $6P_{3/2}$ and then come back to the ground state with total momentum either $F = 4$ or $F = 3$. Here we consider the case of unchanged total spin, meaning the transition $F = 4 \leftrightarrow F = 4$. Hence, the interaction is now driven by $\hat{H}_{FF} = \hat{\sigma}_F \hat{H}_{int.} \hat{\sigma}_F$. The respective polarizability operator $\boldsymbol{\alpha}_{FF} = \hat{\sigma}_F \boldsymbol{\alpha} \hat{\sigma}_F$ can be presented in a form:

$$\hat{\boldsymbol{\alpha}}_{FF} = -\frac{d_0^2}{\Delta}\left(a_0 + i a_1 \hat{\boldsymbol{j}}\times + a_2 \hat{\boldsymbol{Q}}\right), \tag{4.25}$$

where Δ is the detuning from the resonance and d_0 is the dipole matrix element corresponding to the change of electronic angular momentum during the transition from ground to excited state. Eq.(4.25) represents the decomposition of polarizability operator onto scalar, vector and (second rank) tensor components. The vector part

$$\hat{\boldsymbol{j}}\times = \begin{bmatrix} 0 & \hat{j}_z & \hat{j}_y \\ \hat{j}_z & 0 & -\hat{j}_x \\ -\hat{j}_y & \hat{j}_x & 0 \end{bmatrix} \tag{4.26}$$

yields the contribution $\hat{H}_{FF(1)} = -(d_0^2/\Delta) i \hat{\vec{E}}^{-} \cdot \left[\hat{\boldsymbol{j}} \times \hat{\vec{E}}^{+}\right] = (d_0^2/\Delta) i \hat{\boldsymbol{j}} \cdot \left[\hat{\vec{E}}^{-} \times \hat{\vec{E}}^{+}\right]$. The tensor rank part $\hat{\boldsymbol{Q}}$ with components given by

$$\hat{Q}_{kl} = -(\hat{j}_k \hat{j}_l + \hat{j}_l \hat{j}_k) + \delta_{kl} \frac{2}{3} \hat{j}^2 \tag{4.27}$$

and scalar term form Hamiltonians $\hat{H}_{FF(2)}$ and $\hat{H}_{FF(0)}$ respectively. The coefficients $a_0(\Delta)$, $a_1(\Delta)$ and $a_2(\Delta)$ as functions of detuning are calculated in [112] for the specific case of D2-transition for ^{133}Cs prepared at ground state $F = 4$. Importantly, in the limit of large Δ the coefficient a_2 behaves as $\propto 1/\Delta \to 0$, while $a_{0,1} \to C_{0,1}$ approaching constant levels.

We exploit the encoding of probe light by Stokes vector $\hat{\vec{S}}$ which are compatible with collective variables of the atomic spin system and hence constitute a convenient tool to describe light-matter interplay [48]. The components

$\left\{\hat{S}_x, \hat{S}_y, \hat{S}_z\right\}$ represent the difference in the photon number flux operators of polarizations in different (canonical, diagonal or circular polarized) bases whereas $\hat{S}_0$ gives the total amount of photons in the system:

$$\hat{S}_x = \frac{1}{2}\left(\hat{n}_H - \hat{n}_V\right) = \frac{1}{2}\left(\hat{a}_x^\dagger \hat{a}_x - \hat{a}_y^\dagger \hat{a}_y\right) \tag{4.28a}$$

$$\hat{S}_y = \frac{1}{2}\left(\hat{n}_D - \hat{n}_A\right) = \frac{1}{2}\left(\hat{a}_x^\dagger \hat{a}_y + \hat{a}_y^\dagger \hat{a}_x\right) \tag{4.28b}$$

$$\hat{S}_z = \frac{1}{2}\left(\hat{n}_R - \hat{n}_L\right) = \frac{1}{2}\left(\hat{a}_x^\dagger \hat{a}_y - \hat{a}_y^\dagger \hat{a}_x\right) \tag{4.28c}$$

$$\hat{S}_0 = \frac{1}{2}\left(\hat{n}_H + \hat{n}_V\right) \equiv \frac{1}{2}\left(\hat{n}_D + \hat{n}_A\right) \equiv \frac{1}{2}\left(\hat{n}_R + \hat{n}_L\right) = \frac{1}{2}\left(\hat{a}_x^\dagger \hat{a}_x + \hat{a}_y^\dagger \hat{a}_y\right). \tag{4.28d}$$

The creation/annihilation operators $\hat{a}_{x,y}$ (and consequently, the operators of number of photons $\hat{n}_i$) are position-dependant and defined as

$$\hat{a}_{x,y}(z,t) = \int \frac{dk}{2\pi} \hat{a}_{x,y}(t) e^{ikz} \tag{4.29a}$$

where we assume that the probe light travels along axis OZ. Notably, in the case of linearly polarized probe field, for example, along OX-axis[1] we have $\hat{a}_x \to i\alpha$, α is the amplitude of the field[2], $|\alpha| \gg 1$. Then, Stokes operators are transformed according to:

$$S_x \approx S_0 = \frac{|\alpha|^2}{2}, \quad \hat{S}_y = \frac{i\alpha}{2}\left(\hat{a}_V^\dagger - \hat{a}_V\right), \quad \hat{S}_z = -\frac{\alpha}{2}\left(\hat{a}_V^\dagger + \hat{a}_V\right) \tag{4.30}$$

where we highlight that the operator $\hat{S}_x$ can be treated as the classical variable. One might see that $\hat{x}_{L,S}$ and $\hat{p}_{L,S}$ introduced as

$$\hat{x}_{L,S} = \frac{\hat{S}_z}{\sqrt{S_x}}, \quad \hat{p}_{L,S} = \frac{\hat{S}_y}{\sqrt{S_x}} \tag{4.31}$$

are nothing but canonical position and momentum of electromagnetic field in vertical (along OY axis) polarization. The commutation relation $\left[\hat{x}_{L,S}, \hat{p}_{L,S}\right] = i$ is fulfilled and the probe field acts as harmonic oscillator in normalized Stokes variables. Using decomposition eq.(4.24) and introduced Stokes operators eq.(4.28), we obtain explicit expressions for interaction Hamiltonian:

$$\hat{H}_{FF(0)} = a_0 \hat{S}_0, \quad \hat{H}_{FF(1)} = -a_1 \hat{S}_z \hat{j}_z, \quad \hat{H}_{FF(2)} = -a_2\left(\hat{S}_x\left[\hat{j}_x^2 - \hat{j}_y^2\right] + \hat{S}_y\left[\hat{j}_x\hat{j}_y + \hat{j}_y\hat{j}_x\right] + 2\hat{S}_0\hat{j}_z^2 - \frac{2}{3}\hat{S}_0\hat{j}^2\right) \tag{4.32}$$

In order to make a transition from interaction with single atom to *coherent* interaction, we introduce continuous spin variables:

$$\hat{j}_k(z) = \sum_{l=1}^{N} \delta(z - z^l)\hat{j}_k^l, \quad k = \overline{x,y,z} \tag{4.33}$$

where superscript l denotes the sum across the ensemble with $\hat{j}_k^l$ being the spin of individual atom. The probe optical field propagates along Z-axis, the atomic ensemble with a density ρ is confined in a volume with cross-section area A and length L. Then the Hamiltonian of interaction between the whole ensemble and light is directly obtained from eq.(4.32):

$$\hat{H}_{\mathsf{coh}} = g_{cs}\int_0^L \left[a_0\hat{S}_0 - a_1\hat{S}_z\hat{j}_z + a_2\left(\hat{S}_x\left[\hat{j}_x^2 - \hat{j}_y^2\right] + \hat{S}_y\left[\hat{j}_x\hat{j}_y + \hat{j}_y\hat{j}_x\right] - 2\hat{S}_0\hat{j}_z^2 + \frac{2}{3}\hat{S}_0\hat{j}^2\right)\right] A\rho(z)dz, \tag{4.34}$$

[1] coinciding with quantization axis and with direction of external magnetic field

[2] phase for $\hat{a}_x$ is selected without loss of generality

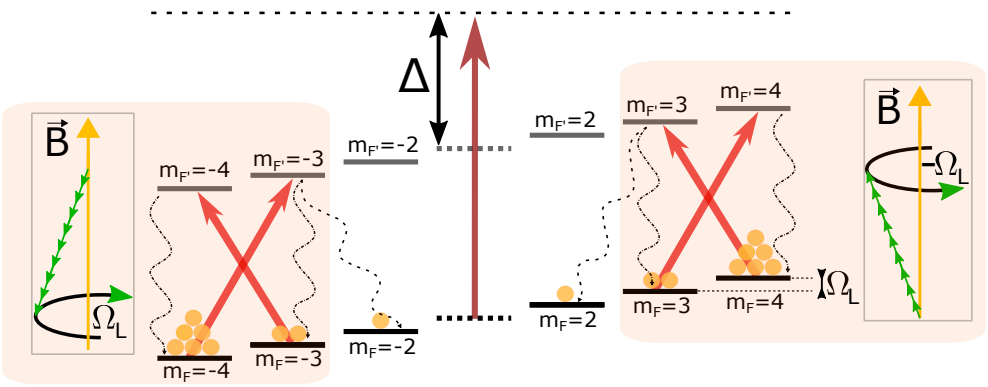

Figure 4.1: Atomic ensemble is driven by the probe light that is detuned by Δ from the transition $6S_{1/2} \leftrightarrow 6P_{3/2}$. The external magnetic field $\boldsymbol{B}$ splits both ground $F = 4$ and excited $F' = 4$ hyperfine levels. The either utmost Zeeman sublevel ($|m = -4\rangle$ or $|m = 4\rangle$) and the next Zeeman sublevel within the ground hyperfine manifold $F = 4$ constitute a two-level system that acts like harmonic oscillator. Depending on mutual orientation of $\boldsymbol{B}$ and highly polarized collective macroscopic spin ($J \approx J_x$), we observe either clockwise or counter clockwise Larmor precession of quantum orbital momentum in Y-Z plane, corresponding to either positive or negative mass oscillator. Inclusion of the third Zeeman sublevel $|m_F = 2\rangle$ or $|m_F = -2\rangle$ gives rise to dynamics of alignment operators.

where the single photon to single atom coupling rate $g_{cs} = -\hbar c \gamma_{sp} \lambda^2 / (16 A \Delta \pi)$ with spontaneous emission rate γ_{sp} describing decay from excited states. The collective spin projections in eq.(4.34) are functions of z as defined in eq.(4.33). Note that decoherence effects are not addressed so far.

The first scalar part of the Hamiltonian given by eq.(4.34) ($\hat{H}_{FF(0)} \propto \hat{S}_0$) corresponds to DC Stark shift equally moving all atomic energy levels proportional to the power of probe field. This term is not of interest for us. Next contribution comes from vector part $\hat{H}_{FF(1)} \propto \hat{S}_z \hat{j}_z$ being particular case of $\hat{\vec{S}}\hat{\vec{j}}$ that defines the mutual rotation of Stokes vector and atomic spin. The contribution of this type of interaction is extensively studied in the next subsection. The remain component $\hat{H}_{FF(2)}$ leads to dynamical Stark shift and quite complex dynamics. The role of this term in this work is predominantly negative and must be mitigated. We achieve this by tuning the adjusting the optical detuning Δ. Careful examination and calibration of impact of this contribution is provided in the last section of this chapter.

Two-level system approximation. Faraday interaction

We again assume the spin ensemble prepared in high polarized state implying that most of the atoms are in the utmost Zeeman level ($|m = -4\rangle$ or $|m = 4\rangle$). In such case, the approximation of level structure with lowest (highest) sublevel and adjacent Zeeman sublevel $|m = -3\rangle$ (or $|m = 3\rangle$) for ground hyperfine manifold (Fig.4.1) is justified [114]. We then map the atomic ensemble to an arbitrary system with total angular momentum $F = 1/2$, meaning effective spin-1/2 system. We denote $|1(2)\rangle = |F = 1/2, m = -1/2(1/2)\rangle$ and $|3(4)\rangle = |F' = 1/2, m = -1/2(1/2)\rangle$. Driving light is detuned by factor Δ from the resonance $F = 1/2 \leftrightarrow F' = 1/2$. Excluding dipole forbidden transitions $|1\rangle \leftrightarrow |3\rangle$ and $|2\rangle \leftrightarrow |4\rangle$, we can write the light-atoms interaction Hamiltonian

$$\hat{H}_{\text{l-a}} = \hat{\vec{d}}\hat{\vec{E}} = \hbar g_0 \left(\hat{\sigma}_{23} \hat{a}_L - \hat{\sigma}_{14} \hat{a}_R + \text{h.c.} \right) \tag{4.35}$$

where $\hat{a}_R(\hat{a}_L)$ are bosonic annihilation operators for right (left)-circular polarized light, g_0 is light-matter coupling strength. Assuming rotating wave approximation, neglecting populations of excited states and applying perturbation theory, one may obtain the effective master equation driven by Hamiltonian transformed from eq.(4.35) to (details are given in [116] (eq.1-3) and [114], sec.5.5):

$$\hat{H}_{\text{l-a,eff}} = g \left(\hat{\sigma}_{22} \hat{a}_L^\dagger \hat{a}_L - \hat{\sigma}_{11} \hat{a}_R^\dagger \hat{a}_R \right), \quad g = \frac{\hbar g_0^2 \Delta}{\Delta^2 + (\gamma_e/2)^2}, \tag{4.36}$$

where g is light-matter coupling rate and γ_e is excited state decay rate. The Hamiltonian eq.(4.36) causes the *AC Stark shift*, moving the energy of levels $|1\rangle$, $|2\rangle$.

Now we express ground state atomic operators $\hat{\sigma}_{kl}$ via operators of total momentum $\hat{j}_k$, $k = \overline{0,x,y,z}$ in a frame of spin-half-toy model[3], while using definitions eq.(4.28) of Stokes parameters. As a result, we write the effective Hamiltonian eq.(4.35) in a form [114]:

$$\hat{H}_{\text{l-a eff}} = g\left(\hat{S}_0\hat{j}_0 - \hat{S}_z\hat{j}_z\right) \tag{4.37}$$

The term $\hat{S}_z\hat{j}_z$ on the right side of eq.(4.37) exhibits Faraday interaction just as $\hat{H}_{FF(1)}$ from eq.(4.32). The decay from excited atomic states due to spontaneous emission is described by

$$\hat{L}_{13} = \sqrt{\frac{\gamma_e}{3}}\hat{\sigma}_{13}, \quad \hat{L}_{24} = \sqrt{\frac{\gamma_e}{3}}\hat{\sigma}_{24}, \quad \hat{L}_{23} = \sqrt{\frac{2\gamma_e}{3}}\hat{\sigma}_{23}, \quad \hat{L}_{14} = \sqrt{\frac{2\gamma_e}{3}}\hat{\sigma}_{14}. \tag{4.38}$$

In order to include the decay terms into the master equations, one has to implement the transformation similar to eq.(4.36) (for example, $\hat{L}_{14,eff} = \hat{\sigma}_{11}\hat{a}_R\sqrt{2\gamma_e/3}/\left(\Delta - i\gamma_e/2\right)$, see [116], eq.4 for details). In a result, eq.(4.37) gives the set of stochastic equations describing dynamics of Stokes components and operators of spin projections:

$$\frac{d\hat{S}_x}{dt} = -g\hat{S}_y\hat{J}_z \tag{4.39a}$$

$$\frac{d\hat{S}_y}{dt} = g\hat{S}_x\hat{J}_z \tag{4.39b}$$

$$\frac{d\hat{S}_z}{dt} = 0 \tag{4.39c}$$

$$\frac{d\hat{J}_x}{dt} = g\hat{S}_z\hat{J}_y - \gamma_{S0}\hat{S}_0\hat{J}_x - N_{Fx}\hat{F}_{st.x} \tag{4.39d}$$

$$\frac{d\hat{J}_y}{dt} = -g\hat{S}_z\hat{J}_x - \gamma_{S0}\hat{S}_0\hat{J}_y - N_{Fx}\hat{F}_{st.y} \tag{4.39e}$$

$$\frac{d\hat{J}_z}{dt} = -\gamma_{S0}\hat{S}_z\hat{J}_0 - \gamma_{S0}\hat{S}_0\hat{J}_z - N_{Fx}\hat{F}_{st.z}, \tag{4.39f}$$

Note the transition from single atom spin projection $\hat{j}_{x,y,z}$ to collective variables defined now as $\hat{J}_{x,y,z}(t) = \int_L A\rho\hat{j}_{x,y,z}(z,t)dz$ that are compatible with collective variables from eq.(4.14). Eq.(4.39a)-(4.39b) yield rotation of probe polarization in XY-plane during propagation through the atomic ensemble. Such precession is caused by quantum fluctuation of spin component $\hat{J}_z$ inducing circular birefringence. Given macroscopic value S_x, the projection of atomic momentum $\hat{J}_z$ will be imprinted onto the output Stokes component $\hat{S}_y$, as follows from eq.(4.39b). Therefore the information about spin motion can be read out. At the same time, eq.(4.39c) dictates that the component $\hat{S}_z$ remains unaffected. In turn, eq.(4.39d)-(4.39e) show that the dynamics of spin ensemble is disturbed by the probe light that might be seen as rotation around effective magnetic field created by $\hat{S}_z$. The light-matter interplay doesn't influence the Stokes variable $\hat{J}_z$ that reflects the feature of quantum non-demolition type of interaction. All 3 spin projections experience decay[4] characterized by the rate $\gamma_{S0} = \hbar g_0^2\left(\gamma_e/2\right)/\left(\Delta^2 + \left(\gamma_e/2\right)^2\right)$. Apart from that, we include the contribution from stochastic Langevin force $\hat{F}_{st.k}$ with the strength defined by factor N_{Fk}, $k = \overline{x,y,z}$ (see [116] and [112] for details).

If we exploit the definition eq.(4.21) of quadratures $\hat{x}_S$, $\hat{p}_S$ of atomic ensemble together with definition eq.(4.31) of canonical variables of optical mode $\hat{x}_{L,S}$, $\hat{p}_{L,S}$ and add harmonic motion of spin oscillator in external magnetic field (given by eq.(4.20)) to light-matter interplay eq.(4.36), we will arrive to input-output relations in a form of eq.(2.10), namely:

$$\hat{q}_{L,S,out}(\zeta_S) = \hat{q}_{L,S,in}(\zeta_S) + 2\Gamma_S\chi_S\cos\left(\zeta_S\right)\hat{x}_{L,S,in} + \sqrt{2\Gamma_S\gamma_S}\chi_S\cos\left(\zeta_S\right)\hat{f}_{th}, \tag{4.40}$$

[3]From the system eq.(4.14) applied for an arbitrary ensemble with $F = 1/2$ we obtain $\hat{\sigma}_{11} = \hat{j}_0 - \hat{j}_z$, $\hat{\sigma}_{22} = \hat{j}_0 + \hat{j}_z$, $\hat{\sigma}_{12} = \hat{j}_x - i\hat{j}_y$, $\hat{\sigma}_{21} = \hat{j}_x + i\hat{j}_y$

[4]In contrast to decoherence processes for probe optical field that are neglected here.

where $\hat{q}_{L,S,in(out)}(\zeta_S) = \hat{p}_{L,S,in(out)}\cos(\zeta_S) + \hat{x}_{L,S,out}\sin(\zeta_S)$. We introduced the *readout*[5] *(measurement) rate* $\Gamma_S = a_1 g^2 |J_x||S_x|$ for coherent interaction of atomic ensemble and probe optical field. Note the we added factor $a_1(\Delta)$ to the definition of Γ_S since an abstract $F = 1/2$ system is replaced by the specific case of ^{133}Cs atomic level structure. The *total decay rate* $\gamma_S = \gamma_{S,pb} + \gamma_{S,in}$ is split into two parts. The term $\gamma_{S,pb} = \gamma_{S0} S_0 \equiv \gamma_{S0}|\alpha|^2$ represents the *power broadening* contribution from the probe field originating from spontaneous emission eq.(4.38). The other sources of decoherence are lumped into intrinsic atomic linewidth $\gamma_{S,in}$ and will be will be briefly discussed later. The susceptibility function χ_S of the atomic oscillator is defined as in eq.(2.8). The Langevin 'thermal' force $\hat{f}_{th}$ sets the interaction with Markovian bath, being obtained by combining $\hat{F}_{st.k}$ from eq.(4.39).

4.2.4 Effect of (high-order) tensor terms

The Hamiltonian $\hat{H}_{FF(2)}$ from eq.(4.32) yields the following set of stochastic equations, describing the contribution of tensor terms to the evolution of spin operators

$$\frac{\partial \hat{j}_x}{\partial t} = -\, g_{cs} a_2 \left((\hat{S}_0 - \hat{S}_x) \left[\hat{j}_y \hat{j}_z + \hat{j}_z \hat{j}_y \right] + \hat{S}_y \left[\hat{j}_x \hat{j}_z + \hat{j}_z \hat{j}_x \right] \right), \tag{4.41a}$$

$$\frac{\partial \hat{j}_y}{\partial t} = \; g_{cs} a_2 \left((\hat{S}_0 + \hat{S}_x) \left[\hat{j}_x \hat{j}_z + \hat{j}_z \hat{j}_x \right] + \hat{S}_y \left[\hat{j}_y \hat{j}_z + \hat{j}_z \hat{j}_y \right] \right), \tag{4.41b}$$

$$\frac{\partial \hat{j}_z}{\partial t} = -\, g_{cs} a_2 \left(2\hat{S}_x \left[\hat{j}_x \hat{j}_y + \hat{j}_y \hat{j}_x \right] - 2\hat{S}_y \left[\hat{j}_x^2 - \hat{j}_y^2 \right] \right) \tag{4.41c}$$

and Stokes operators of probe light

$$\frac{\partial \hat{S}_x}{\partial z} = -\, g_{cs} a_2 \left(\hat{S}_z \left[\hat{j}_x \hat{j}_y + \hat{j}_y \hat{j}_x \right] \right), \tag{4.42a}$$

$$\frac{\partial \hat{S}_z}{\partial z} = \; g_{cs} a_2 \left(\hat{S}_z \left[\hat{j}_x^2 - \hat{j}_y^2 \right] \right), \tag{4.42b}$$

$$\frac{\partial \hat{S}_z}{\partial z} = \; g_{cs} a_2 \left(\hat{S}_x \left[\hat{j}_x \hat{j}_y + \hat{j}_y \hat{j}_x \right] - \hat{S}_y \left[\hat{j}_x^2 - \hat{j}_y^2 \right] \right) \tag{4.42c}$$

respectively. One can clearly see that the system eq.(4.39) is now perturbed by *alignment* operators $\left\{ \hat{j}_k, \hat{j}_l \right\} = \hat{j}_k \hat{j}_l + \hat{j}_l \hat{j}_k$ and $\hat{j}_k^2 - \hat{j}_l^2$, where $k, l = \overline{x, y, z}$. The presence of alignment operators is conditioned by deviation from simplified spin-1/2 model; as reflected on the Fig.4.1, the third Zeeman sublevel $|m = -2\rangle$ (or $|m = 2\rangle$) is accounted. We notice that in the approximation of highly polarized spin ensemble the following approximations for alignment operators are valid [115]:

$$\hat{j}_x^2 - \hat{j}_y^2 \approx F(F - 1/2) \tag{4.43a}$$

$$\hat{j}_x \hat{j}_y + \hat{j}_y \hat{j}_x \approx \pm(2F - 1)\hat{j}_y \tag{4.43b}$$

Tensor Stark shift

One of the consequences of tensor interaction is *dynamical shift of the spin resonance frequency*. We exploit approximation eq.(4.43) for alignment operators and select the following terms from eq.(4.41b)-(4.41c):

$$\frac{\partial \hat{j}_y}{\partial t} = \; g_{cs} a_2 (2F - 1) \left(\hat{S}_0 + \hat{S}_x \right) \hat{j}_z \tag{4.44a}$$

$$\frac{\partial \hat{j}_z}{\partial t} = -\, g_{cs} a_2 (2F - 1) 2 \hat{S}_x \hat{j}_y. \tag{4.44b}$$

[5] factor of 2 in front of the readout rate in eq.(4.40) is the matter of selected convention

The construction of the system eq.(4.44) resembles rotation of spin projections in YZ-plane around X-axis, thus giving the amendment $\delta\Omega_S^{(2)}$ to oscillation frequency Ω_S defined by the strength of applied magnetic field. Using the following features of alignment operators

$$\langle m|\,\hat{j}_x^2\,|m\rangle = m^2, \tag{4.45a}$$

$$\langle m|\,\hat{j}_{y(z)}^2\,|m\rangle = \frac{F(F+1)-m^2}{2}, \tag{4.45b}$$

$$\langle m|\,\hat{j}_x\hat{j}_y+\hat{j}_y\hat{j}_x\,|m\rangle = 0, \tag{4.45c}$$

one may calculate the shift $\delta\Omega_S^{(2)} = \delta E_{F,m}^{(2)}/\hbar$, where

$$\delta E_{F,m}^{(2)} = E_{F,m}^{(2)} - E_{F,m-1}^{(2)} = 2g_{cs}a_2S_0\left[2m+1\right]. \tag{4.46}$$

and $E_{F,m}^{(2)} = \langle F,m|\,\hat{H}_{FF(2)}\,|F,m\rangle = -g_{cs}a_2S_0\left[F(F+1)-2m^2\right]$. The overall resonance frequency $\delta E_{F,m} = E_{F,m} - E_{F,m-1}$ corresponding to transition between two adjacent Zeeman sublevels now depends on projection of total spin m. The formula eq.(4.46) is given for particular case of linear polarization of probe light that coincides with quantization axis OX (making the approximation $\hat{S}_x \approx S_x \approx S_0$ justified). In contrast, one can select the arbitrary angle β between direction of magnetic field and probe polarization. We then change the basis of Stokes operators from $\left\{\hat{S}_x,\hat{S}_y,\hat{S}_z\right\}$ to $\left\{\hat{S}_{||},\hat{S}_{\perp},\hat{S}_z\right\}$, where $\left[\hat{S}_{||},\hat{S}_{\perp}\right] = \boldsymbol{R(2\beta)}\left[\hat{S}_x,\hat{S}_y\right]$, and $\boldsymbol{R(2\beta)}$ is the rotation matrix. The component $\hat{S}_{||} \approx S_0 = |\alpha|^2/2$ becomes classical, whereas $\hat{S}_{\perp}$ and $\hat{S}_z$ are quantum operator with zero mean. Change of the basis converts eq.(4.46) to:

$$\delta E_{F,m}^{(2)} = g_{cs}a_2S_0\left(\frac{1+3\cos\left(2\beta\right)}{2}\right)\left[2m+1\right]. \tag{4.47}$$

Specifically, the selection $\beta = -(1/2)\arccos\left(1/3\right) \approx 55^\circ$ cancels the tensor Stark shift. Alternatively, we can adjust the polarization angle to counteract quadratic Zeeman splitting expressed in eq.(4.5).

Coupling of intensity noise

As follows from eq.(4.45a)-(4.45b), the alignment operator $\hat{j}_x^2 - \hat{j}_y^2$ has the strong spectral component at $\Omega = 0$, induced by transition to excited hyperfine level and subsequent decay back without changing the projection of total momentum m. This operator couples to $\hat{S}_y$ and shapes the response of spin projection $\hat{j}_z$, see eq.(4.41c). Since the Stokes component $\hat{S}_y$ contains the quantum back action noise centered at $\Omega = \Omega_S$ (from Faraday interaction model), the spin operator $\hat{j}_x^2 - \hat{j}_y^2$ also contributes to the noise budget in the spectral range $\Omega = \Omega_S$. Importantly, $\hat{j}_z$ spin quadrature is contaminated by intensity fluctuations (if any) of probe optical field contained in $\hat{S}_{||}$ Stokes quadrature representing total photon flux. The amount of added noise is defined by polarization angle β; the ratio between projected intensity noise of probe and back-action noise ('desired' noise source) from Faraday model is $4\left(2F-1\right)^2\left(a_2/a_1\right)^2\left(1+\sin^2\left(2\beta\right)Z\right)$ [113], where Z is the added (on top of shot noise) amplitude noise of probe laser in shot noise units. Notably, the impact of probe power fluctuation is maximized at $\beta = \pi/4$ and minimized at $\beta = 0, \pi/2$, when only shot noise of laser is projected.

P-P interaction

The other alignment spin operator $\hat{j}_x\hat{j}_y + \hat{j}_y\hat{j}_x$ has non-zero matrix element $\langle m'|\,\hat{j}_x\hat{j}_y+\hat{j}_y\hat{j}_x\,|m\rangle$ if $|m'-m| = 1$ leading to spectral response at $\Omega = \Omega_S$ that competes to Faraday interplay. Combining eq.(4.43b) and $\hat{H}_{FF(1)}$, we study the following interaction Hamiltonian

$$\hat{H}_{l-a,eff}^{(pp)} = a_1g_{cs}\left(\hat{S}_z\hat{j}_z + \mathcal{E}_S\hat{S}_{\perp}\hat{j}_y\right), \quad \mathcal{E}_S = -14\frac{a_2}{a_1}\cos\left(2\beta\right). \tag{4.48}$$

Written in canonical variables[6], this Hamiltonian takes the form $\hat{H}^{(pp)}_{l-a,eff} = \sqrt{\Gamma_S}\left(\hat{x}_{L,S}\hat{x}_S + \mathcal{E}_S\hat{p}_{L,S}\hat{p}_S\right)$ and results in the stochastic equations of motion (decoherence effects are added) given by [115]

$$\frac{\partial\hat{x}_S}{dt} = \Omega_S\hat{p}_S + (\gamma_S + 2\mathcal{E}_S\Gamma_S)\,\hat{x}_S + \sqrt{\gamma_S}\hat{f}_{st,x} - \mathcal{E}_S\sqrt{\Gamma_S}\hat{p}_{L,S,in}, \tag{4.49a}$$

$$\frac{\partial\hat{p}_S}{dt} = -\Omega_S\hat{x}_S + (\gamma_S + 2\mathcal{E}_S\Gamma_S)\,\hat{p}_S + \sqrt{\gamma_S}\hat{f}_{st,P} - \sqrt{\Gamma_S}\hat{x}_{L,S,in}, \tag{4.49b}$$

$$\frac{\partial\hat{x}_{L,S}}{dt} = \sqrt{\Gamma_S}\mathcal{E}_S\hat{p}_S, \tag{4.49c}$$

$$\frac{\partial\hat{p}_{L,S}}{dt} = -\sqrt{\Gamma_S}\hat{x}_S. \tag{4.49d}$$

In general, the light-matter interaction is no longer QND, since atomic motion is now directly recorded on both optical phase quadrature $\hat{p}_{L,S,out}$ and amplitude quadrature $\hat{x}_{L,S,out}$. Similarly, the probe light perturbs the spin ensemble dynamics, getting coupled to both canonical position $\hat{x}_S$ and momentum $\hat{p}_S$. Secondly, the linewidth of atomic oscillator is modified, resulting in $\gamma_{S,ten} = \gamma_S + 2\mathcal{E}_S\Gamma_S$. This effect will be referred to as *tensor broadening*.

In order to cancel the effect of tensor broadening and deviation from QND-type interaction, one has to nullify $\mathcal{E}_S$ and set polarization angle $\beta = \pi/4$. Clearly, such a choice will boost the projection of amplitude noise of probe field onto atomic motion and establish non-zero tensor Stark shift of resonance frequency. Nevertheless, in described experiment the configuration $\mathcal{E}_S = 0$ is mostly preferred, since we want to simplify input-output relations for characterization of atomic ensemble. Therefore, we will fix $\beta = \pi/4$ throughout the rest of this chapter and deviate only for calibration of input probe polarization (will be clearly specified and described later).

One can present Hamiltonian $\hat{H}^{(pp)}_{l-a,eff}$ from eq.(4.48) in the form

$$\hat{H}^{(pp)}_{l-a,eff} = \left(\sqrt{\Gamma_S}/2\right)\left[(1+\mathcal{E}_S)\,\hat{H}_{BS} + (1-\mathcal{E}_S)\,\hat{H}_{TMSq}\right], \tag{4.50}$$

where $\hat{H}_{BS} = \hat{a}_{L,S}\hat{b}^\dagger_S + \hat{a}^\dagger_{L,S}\hat{b}_S$ expresses swapping between photon and atomic excitation (beam-splitter type interaction) while $\hat{H}_{TMSq} = \hat{a}_{L,S}\hat{b}_S + \hat{a}^\dagger_{L,S}\hat{b}^\dagger_S$ induces the entanglement between light and spin ensemble (two mode squeezing type interaction)[7]. Being determined by factor $\mathcal{E}_S$, the relative weights of $\hat{H}_{BS}$ and $\hat{H}_{TMSq}$ are equal if $\mathcal{E}_S = 0$, yielding QND Hamiltonian $\propto \hat{x}_{L,S}\hat{x}_S$.

4.3 Experimental realization and preliminary characterization

4.3.1 Atomic ensemble in a cell

The spin ensemble consisting of $\sim 10^{10}$ cesium-133 atoms is placed in the square $d_c \times d_c \times L_c$ channel of encapsulated glass vapour cell. The detailed description of cell construction and some aspects of their fabrication can be found in [114, 115]. The dimensions of the channel have been selected such that the transverse cross section is 2mm×2mm whereas the length is $L_c = 80$ mm. The choice of cell geometry is motivated by the application of quantum noise reduction in GWDs. First, large (in comparison to [39, 40]) transverse dimensions mitigate the negative impact of collisions between atoms and the walls of the cell. The reduction of this collision rate, as well as anti-relaxation coating for the cell walls, decreases the respective contribution (designated as $\gamma_{S,walls}$) to the total (intrinsic) spin damping rate $\gamma_{S,in}$. In turn, big cell length L_c facilitates achieving large optical depth and hence, large spin quantum cooperativity (atomic readout rate). Moreover, we explore the possibility to convert the probe optical field into top-hat configuration (will be mentioned in sec.4.3.4). Maintaining a good quality of top-hat beam within such a long cell becomes more feasible for increased size of cross-section area (in particular, $d_c = 2$mm turns out to be sufficient for $L_c = 8$cm). In general, the increase of cell size is accompanied by the number of drawbacks, such as stronger coupling to the classical noise and slower motional averaging.

[6] In contrast to eq.(4.31), we need to re-define quadratures for optical field: $\hat{x}_{L,S} = \hat{S}_z/\sqrt{S_{||}}$, $\hat{p}_{L,S} = \hat{S}_\perp/\sqrt{S_{||}}$

[7] Annihilation/creation operators for Stokes quadrature are annihilation/creation operators in for the optical mode denote by polarization perpendicular to linear polarization of probe field ($\hat{a}_{L,S} \equiv \hat{a}_\perp$), see eq.(4.30) and account for rotation of Stokes operator basis $\left[\hat{S}_{||}, \hat{S}_\perp\right] = \boldsymbol{R(2\beta)}\left[\hat{S}_x, \hat{S}_y\right]$. The annihilation/creation operators for atomic ensemble are ladder operators ($\hat{b}_S = \hat{j}_-$, $\hat{b}^\dagger_S = \hat{j}_+$) introduced in eq.(4.9)

Polarized spin ensemble precesses around external bias magnetic field, created by the system of coils. The spatial inhomogeneity of bias field leads to an increase of atomic linewidth (the respective contribution is denoted as $\gamma_{S,inh}$). To prevent the perturbation of spin dynamics caused by stray magnetic fields coming from environment, the cell and coils are placed in multi-layer magnetic shielding. Clean current sources are necessary to avoid undesired technical spin noise due to unstable bias field.

The preliminary characterization of the cell filled with atoms includes the measurement of cell transmission, T2-coherence time and calibration of vapour density. The procedures are outlined in [117, 115]. The results of characterization of the cell used for measurements reported in this chapter will be summarized in Jun Jia upcoming thesis.

The probe optical field used for calibration of the spin oscillator in this chapter was generated by DL Pro laser (Littman Metcalf configuration). However, it is the local oscillator (LO, coming from M-Squared Ti:Sapphire laser) for homodyne detection of idler mode of entanglement (in chapter 3) that should be ultimately used as the probe beam for the atomic ensemble. The amplitude noise of TiSapph laser, being significantly higher in comparison to the DL Pro diode laser, will allegedly counteract quantum noise limited dynamics of the spin oscillator. Therefore, the intensity stabilization loop will be needed on the next steps of the experiment.

To conclude this section, we list the contributions to the total spin decay rate γ_S. Apart from spin-wall collisions ($\propto \gamma_{S,walls}$) and broadening due to inhomogeneous magnetic field ($\propto \gamma_{S,inh}$), one needs to account for spin-exchange collisions ($\propto \gamma_{S,exc}$). Their impact is reduced by increasing the polarization of the spin ensemble. Similarly to probe light induced broadening ($\gamma_{S,pb}$), there is a broadening arising from pumping optical fields.

4.3.2 Initialization and characterization of spin state

Atomic thermal noise

Finite polarization $\mathcal{P}$ of spin ensemble given by eq(4.18) increases the noise of spin quadratures arising from the coupling with environment. We assume that occupations of Zeeman sublevels follow $\langle\hat{\sigma}_{mm}\rangle \sim \mathrm{e}^{r_S m}$, where $r_S = 1/T_S$ is the parameter related to the spin temperature T_S. The spectrum of stochastic thermal force $\hat{F}_{st.y(z)}$ introduced in eq.(4.39) is given by the expression [114]:

$$\langle\hat{F}^{\dagger}_{st.y}\hat{F}_{st.y}\rangle = \frac{N}{2Z_S}\sum_{m=-F}^{F}\exp\left(r_S m\right)\left[F(F+1)-m^2\right], \quad Z_S = \sum_{m=-F}^{F}\exp\left(r_S m\right). \tag{4.51}$$

In a framework of Holstein-Primakov approximation one calculates the environmental noise σ_{Th} perceived by canonical spin variables $\hat{x}_S$, $\hat{p}_S$ by introducing thermal occupation n_S

$$\sigma_{Th} = \langle\hat{f}^{\dagger}_{th}\hat{f}_{th}\rangle = (n_S + 1/2), \tag{4.52}$$

where $\hat{f}_{th}$ is the normalized stochastic thermal force from eq.(4.40). Thus n_S is determined by the degree of spin orientation. In particular, $\mathcal{P} = 1$ corresponds to $n_S = 0$ and bottom limit of thermal noise $S_{\hat{f}_{th}} = 1/2$ which can be treated as shot noise of atoms (projection noise). In the more relevant for us regime $\mathcal{P} \approx 0.9$ we obtain $n_S \approx 0.5$ and roughly twice more thermal noise compared to perfectly polarized ensemble.

Optical pumping

In order to approach coherent spin state with minimal possible thermal noise, we exploit the scheme of optical pumping with two optical fields involved. The idea is presented on Fig.4.2. The first field, named as optical pump, is circularly polarized and adjusted to the transition $|F=4\rangle \leftrightarrow |F'=4\rangle$ of D1-line ($6S_{1/2} \leftrightarrow 6P_{1/2}$). Depending on the choice between σ_+ and σ_--polarization, the field pushes atoms to the excited hyperfine level, increasing (decreasing) projection of total spin by $|\Delta m| = 1$. Coming back to the ground level due to spontaneous decay, atoms eventually move towards utmost Zeeman sublevel $|F=4, m_F=4\rangle$ (or $|F=4, m_F=-4\rangle$) that is a dark state. We also note, that pump induces power broadening due to the coherence between $|F=4, m_F=4\rangle$ (or $|F=4, m_F=-4\rangle$) and $|F=4, m_F=3\rangle$ (or $|F=4, m_F=-3\rangle$) since the last is affected by pump and hence, not dark.

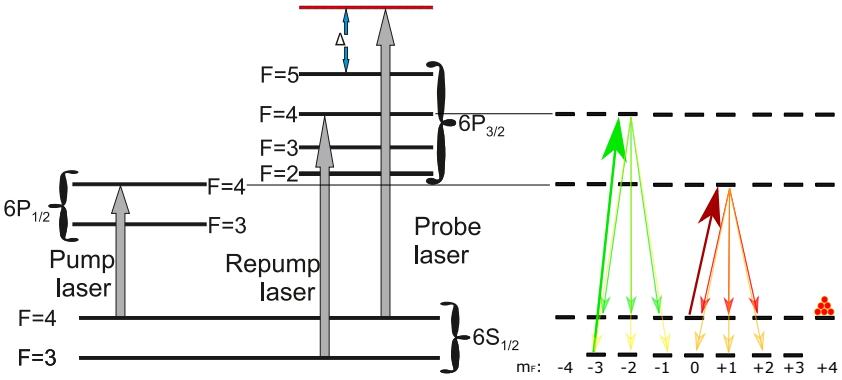

Figure 4.2: The scheme of energy levels of atomic spin ensemble. Pump and repump lasers are needed to prepare the spin state with optimized spin polarization (see text for details). Probe optical field reading out the spin motion is also shown on the figure.

Being transferred to $F' = 4$ by pump, atoms can decay to $F = 4$ but also to $F = 3$ hyperfine level which is undesirable event in the sense of optical pumping scheme performance. The role of the second optical field, referred to as repump, is to eject atoms from hyperfine level $F = 3$, thus forcing them to move to $F = 4$. Affected by circularly polarized repump, spins tend to increase their quantum number m on the level $F = 4$. Therefore, the repump itself may act similar to pump, enhancing its effectiveness. Different choices of frequencies for repump are possible. We typically select the transition $F = 3 \rightarrow F' = 4$, as illustrated on Fig.4.2.

Pump and repump are produced by DFB (distributed feedback) laser and DL Pro laser (Littman Metcalf configuration) respectively, generating radiation at 894 nm and 852 nm. Two fields are overlapped at some point and then propagate together. We use the scattering on AOM into the 1st order to control the optical power. Pump and repump finally enter the cell orthogonal to probe and parallel to magnetic field. Special care has to be taken in order to properly illuminate the cell, covering the whole longitudinal section.

Characterization: MORS

The foundation to calibrate the spin polarization is the method presented in [118]. One refers to this technique as Magneto-Optical Resonance Spectroscopy (MORS). The method gives the opportunity to recover the distribution of populations on Zeeman sublevels. Dependence of frequency of Zeeman transition $E_{F,m+1} \leftrightarrow E_{F,m}$ on number m due to quadratic Zeeman splitting (see eq.(4.5)) is a crucial factor in MORS. In order to implement the calibration, the static magnetic field causing splitting of hyperfine level and yielding Larmor precession is combined with an orthogonal and weak alternating magnetic field. Its frequency is swept across the range of Zeeman manifold, sequentally exciting the transitions between neighboring sublevels. Following eq.(4.39b), the resulting atomic motion is recorded onto probe light that is measured by means of polarization homodyne detection.

If hyperfine multiplet $F = 4$ is investigated, the spectrum of extracted MORS signal in general contains 8 peaks[8]. The peaks are spaced according to eq.(4.3), the linewidth of each peak is defined by coherence time of sublevels, and the amplitudes depend on population difference between corresponding adjacent sublevels. The last circumstance is the key to recovering the distribution of spin populations.

While performing the fit of the signal, we make several assumptions. Mainly, the population distribution should obey thermal distribution as outlined earlier. If the spin temperature T_S is extracted from MORS fit, one can directly calculate spin polarization using $\mathcal{P} = (1/Z_S F) \sum_{m=-F}^{F} m \exp(r_S m)$. In addition, we assign equal Zeeman coherence to all transitions and hence, equal linewidth for all peaks. Details can be found in [115].

To characterize the cells in this thesis, two different fashions of MORS calibration were carried out. If all optical fields (pump/repump/probe) as well as RF modulation of magnetic field are permanently on, we name this configuration as 'continuous' MORS. In this case the probe optical field causes additional broadening of atomic lines because of the light absorption. Together with the pump broadening, it prevents observation of

[8] $(2F + 1) - 1$, where $2F + 1$ is the number of Zeeman sublevels

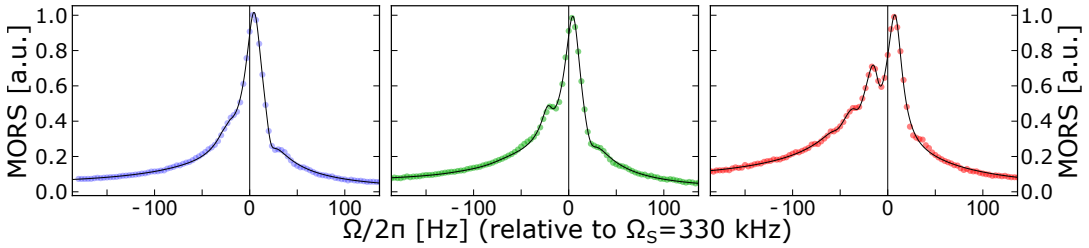

Figure 4.3: Pulsed MORS. From left to right we reduce the pump power from 40μW to 18μW and then to 3μW and observe the reduction of spin polarization from $\mathcal{P} = 0.98$ (left panel) to $\mathcal{P} = 0.95$ (middle) and finally to $\mathcal{P} = 0.92$ (right).

resolved MORS signal. One way to circumvent this obstacle is to increase the line separation by tuning the polarization angle β of input probe and exploiting tensor Stark shift given by eq.(4.47).

Alternatively, the issue of broadening is addressed in pulsed scheme. There are several possible variations of calibration by MORS in pulsed regime [117], [40], [118]. We exploit the following cycle: first, pump and repump are sent in pulse and prepare the state close to coherent spin state ($|F = 4, m_F = 4\rangle$). The pumping fields are then switched off and immediately after that, the RF magnetic field at Larmor frequency is produced. The duration of pulse controlling alternating magnetic field is of the order of $t_{B,rf} = 20\mu$s such that $\Omega_{QZS} \ll 1/t_{B,rf}$ is fulfilled. As a result, all transitions between adjacent Zeeman sublevels are excited. So far the probe field is on with the power $P_p \approx 1$ mW. This value is selected because we want to reproduce the experimental conditions in the next section. In particular, we need to take into consideration the effect of depolarizing the ensemble due to the probe field. Finally, the RF magnetic field is shut off and at the same time the power of probe beam is reduced down to the level $\sim 10\mu$W. This is the stage where the spin state is measured. The power of probe is controlled by the efficiency of scattering onto the 1st order on AOM, in the same way as for pump/repump.

The scheme presented above, although minimizing the impact of power broadening, leads to the following possible issue. The perturbation of spin dynamics by back-action due to the probe light (expressed in a term $d\hat{J}_y/dt \propto \hat{S}_z\hat{J}_x$) is considered as insignificant in contrast to impact by RF magnetic field. It is not entirely clear whether the model given in [117] and [115] is perfectly valid under the circumstance of strong probe power $P_p \approx 1$ mW during initialization stage.

Examples of pulsed MORS signal with imposed fit are demonstrated on Fig.4.3. We pump atoms towards Zeeman state with the highest energy $|m_F = 4\rangle$ and achieve relatively strong orientation of the ensemble. Therefore, we don't witness all 8 peaks, but only 2 (3 on the most right subplot) and identify them as $|m_F\rangle \leftrightarrow |m_F - 1\rangle$ where $m_F = 4, 3$ (also $m_F = 2$) respectively, if counting from right to left[9]. The height of $|m_F = 4\rangle \leftrightarrow |m_F = 3\rangle$ is the biggest, signifying inverted spin population as expected. We then make another simplification of the model and reduce the number of transitions down to 3, considering the levels $|F = 4, m\rangle$, $m \leq 1$ completely unpopulated. Optimization of optical pumping yields the largest spin polarization $\mathcal{P} = 0.98$ extracted from the fitting. As shown on the Fig.4.3, the polarization reduces with the decline of pump power. The linewidth of peaks γ_{MORS} gives the T_2 coherence time, limited by spin-spin, spin-wall collisions and inhomogeneity of static magnetic field. Presented on the Fig.4.3 data exhibit $\gamma_{MORS} \approx 20$ Hz for the cell with cross section 5mm×5mm (given for illustrative purposes). For the cell tested in this chapter (2mm×2mm) we obtain $\gamma_{MORS} \approx 90$ Hz (not shown here) for the peak linewidth in pulsed experiment. Looking at the Fig.4.3, one may note the presence of a bump on the right with respect to resolved Zeeman transitions. This spectral component looks significantly lower and broader than the other lines of MORS signal. Therefore the bump isn't considered directly in the estimation of spin temperature. Instead, we account for it in the model as a background shaped by Gaussian function. We also attempt to analyze its origin in the following section, although without reaching clear understanding.

The estimated polarization drops down to $\mathcal{P} = 0.89 - 0.91$ in the continuous regime. We will see in the next section that results of the fit with spin noise model better match polarization obtained in continuous MORS in comparison to the pulsed configuration, where the polarization seems to be overestimated.

[9] the spacing between adjacent Zeeman sublevels grows up as m increases according to eq.(4.5)

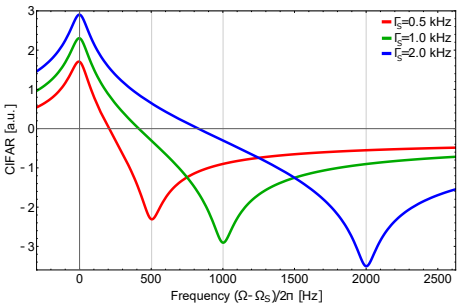

(a) Scaling of signal with changing of readout rate Γ_S is demonstrated. $\Omega_S = 40.8$ kHz, $\gamma_S = 100$ Hz, $\mathcal{E}_S = 0$, $\zeta_S = 0$, $\phi_S = -\pi/4$

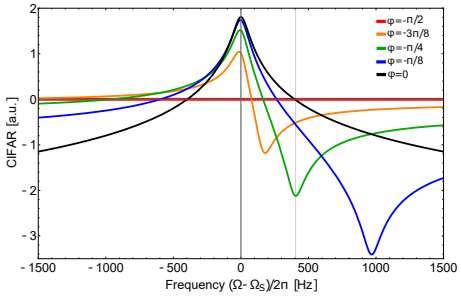

(b) The effect of varying the drive phase ϕ_S is presented. Green curve ($\phi = -\pi/4$) allows to extract the real readout rate $\Gamma_s = 400$ Hz. $\Omega_S = 40.8$ kHz, $\gamma_S = 100$ Hz, $\mathcal{E}_S = 0$, $\zeta_S = 0$

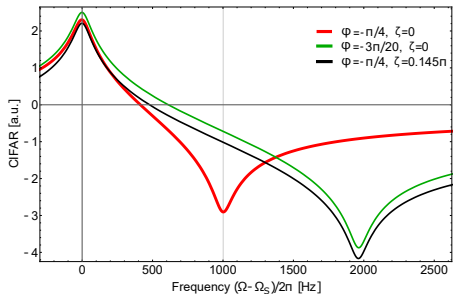

(c) The deviation of detection angle from $\zeta_S = 0$ leads to effective changing of fitted readout rate Γ_s as well as the choice $\phi_S \neq -\pi/4$ for the modulation phase. The rest parameters are $\Omega_S = 40.8$ kHz, $\gamma_S = 100$ Hz, $\mathcal{E}_S = 0$, $\Gamma_s = 1000$ Hz.

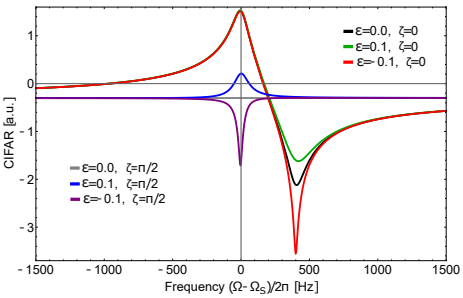

(d) The impact on tensor effects ($\mathcal{E}_S \neq 0$) is shown for cases $\zeta_S = 0$ and $\zeta_S = \pi/2$. In the fist case the tensor term changes the shape of dispersive signal, while on the second case it adds the Lorenz peak on top of the flat response. $\Omega_S = 40.8$ kHz, $\gamma_S = 100$ Hz, $\Gamma_s = 1000$ Hz, $\phi_S = -\pi/4$

Figure 4.4: CIFAR signal: theoretical curves

4.3.3 Calibration of readout rate

We extract the spin measurement rate Γ_S, investigating the atomic response to strong modulation of probe light polarization. The outlined technique is referred to as Coherently induced Faraday rotation (CIFAR) [44]. The advantage of presented below scheme is that calibration signal doesn't depend on detection efficiency. At the same time, full susceptibility function (resonanse frequency Ω_s and the linewidth γ_S) can be reconstructed exploiting this method.

Instead of vacuum noise in the input, the spin ensemble is now driven by light state $\hat{x}_{L,S,in} \to G\sin(\phi_S)$, $\hat{p}_{L,S,in} \to G\cos(\phi_S)$[10]. The modulation phase ϕ is directly related to the carrier phase, as introduced in the section2.3. The input-output relations eq.(2.10) are then written in matrix form

$$\begin{bmatrix} q_{L,S,out}(\zeta_S) \\ q_{L,S,out}(\zeta_{S\perp}) \end{bmatrix} = \begin{bmatrix} \sin(\zeta_S) & -\cos(\zeta_S) \\ \cos(\zeta_S) & \sin(\zeta_S) \end{bmatrix} \begin{bmatrix} 1 & 0 \\ 2\Gamma_S\chi_S & 1 \end{bmatrix} \begin{bmatrix} \sin(\phi_S) \\ \cos(\phi_S) \end{bmatrix} G. \tag{4.53}$$

We consider the absence of tensor effects here and the arbitrary homodyne detection angle ζ_S. Also, thermal force $\hat{f}_T$ is negligibly small compared to back action noise and imprecision noise caused by strongly modulated input light quadrature. Measuring the spectrum of $\hat{q}_{L,S,out}(\zeta_S)$, we obtain

$$S_{\text{CIFAR}} = S_{q_{L,S,out}(\zeta)} = |\sin(\phi_S + \zeta_S) + \gamma_S\Gamma_S\cos(\zeta_S)\cos(\phi_S)|^2|G|^2 \tag{4.54}$$

The induced interference between amplitude and phase quadratures of light generates a characteristic dispersive signal, demonstrated on Fig.4.4. In particular, selecting the phase detected output quadrature ($\zeta_S = 0$) and equal modulation of input amplitude and phase quadratures ($\phi_S = \pi/4$) formula eq.(4.54), one may estimate Γ_S just

[10] implying their spectral components on some specific frequency Ω

measuring the distance between maximum and minimum of the curve (shown on Fig.4.4(a)), in approximation of small spin linewidth $\gamma_S \ll \Gamma_S$. Modulation phase ϕ_S different from $\pi/4$ as well as homodyne angle $\zeta_S \neq 0$ alter the extrema spacing, see figure4.4(b)-(c). Inclusion of tensor effects ($\mathcal{E} \neq 0$) changes[11] the expression for calibration signal[44]:

$$S_{\text{CIFAR}} = \left|\left(1 - 2\Gamma_S \mathcal{E} \chi_S \left[\frac{\gamma_S}{2} - i\Omega\right]\right) \sin\left(\phi_S + \zeta_S\right) + \gamma_S \Gamma_S \left[(1-\mathcal{E})\cos\left(\phi_S + \zeta_S\right) + (1+\mathcal{E})\cos\left(\phi_S - \zeta_S\right)\right]\right|^2 |G|^2 \tag{4.55}$$

Impact of tensor interaction is demonstrated on Fig.4.4(d). When observing pure amplitude quadrature $x_{L,S,out}$, Lorentzian shape is arising on top of the flat constant background. The amplitude of Lorenzian is determined by amplitude and sign of $\mathcal{E}_S$. In generic case $\zeta_S \neq -\phi_S \neq \pm\pi/2$ the tensor interaction adjusts the shape of dispersive curve as well as the distance between minimum and maximum that is now $\approx \Gamma_S\left(1 + \mathcal{E}_S^2\right)$ in the limit of low atomic losses.

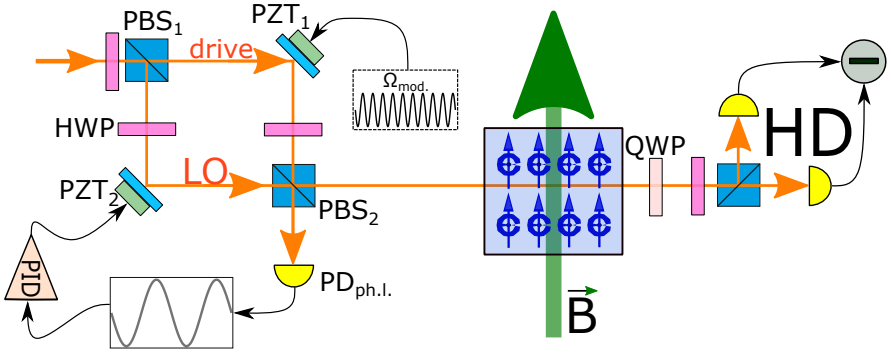

Figure 4.5: Sketch of experimental setup to calibrate readout rate. The laser field after passing polarizing beam splitter PBS_1 is separated onto strong local oscillator LO ($P_{LO} \approx 1\text{mW}$) and weak drive ($P_{dr.} \approx 20\mu\text{W}$) fields. LO and drive are then recombined on the second polarizing beam splitter PBS_2. One output of PBS_2 is sent to photodetector $PD_{ph.l.}$ to generate error signal for phase lock while the other output mode is transmitted through atomic cell and detected on homodyne detector HD.

Experimental setup is shown on Fig.4.5. The linearly polarized optical field denoted as 'drive' is phase-modulated with modulation strength G at frequency $\Omega_{mod.}$ using piezo-electric transducer PZT_1 and subsequently overlapped with orthogonal polarized Local Oscillator LO on polarizing beam-splitter PBS_2. As a result, one of the output modes of PBS_2 contains the state $q_{mod.}(\phi) \sim \left(\hat{x}_{L,S,vac} \sin\phi_S + \hat{p}_{L,S,vac}\cos\phi_S\right)|G|\sin\left(\Omega_{mod.}t\right)$ with arbitrary modulated polarization quadrature (see [44] for details). The phase angle ϕ_S is set by phase lock loop between LO and drive fields. For that purpose, the second output of polarization-sensitive interferometer is used to generate the interference fringes as error signal. The feedback signal is then applied to the piezo element PZT_2 in one of the interferometer arms. The optical mode in desired polarization state $q_{mod.}(\phi_S)$ probes the atomic oscillator and the output filed is detected on the 'self-homodyning' detection setup with subsequent spectral analysis. To obtain the signal as on Fig.4.4, one needs to scan the modulation frequency $\Omega_{mod.}$ around preset Larmor frequency. We have chosen $\Omega_S \approx 40$ kHz since our phase modulator (the piezo element) itself demonstrates reasonably clean and flat spectral response to the applied voltage in this frequency range. Another important technical detail is the selection of the operating point for phase modulation depth defined by G. Excessively strong drive voltage might cause distortion of observed spectral signal since the optical field cannot be described by harmonic oscillator model any longer and the simplified model eq.(4.36) of light-matter interaction isn't valid [44]. Hence, the fit will be compromised, yielding unreliable values for extracted parameters. From the other side, the modulation should be strong enough to provide decent amplitude of spectral signal for fit. After careful search we have chosen the amplitude of drive voltage ≈ 250mV. Out of the same considerations we selected low ratio between optical powers of drive and local oscillator $P_{dr.}/P_{LO} \approx 20\mu\text{W}/1\text{mW} = 0.02$.

Fig.4.4(b,c) reveal the enhanced sensitivity of horizontal scaling of S_{CIFAR} to ϕ_S and ζ_S. Consequently, the trustworthiness of fit strongly depends on the correct knowledge of detection and modulation phases. In order

[11] only amendment due to 'P-P' interaction is accounted

to calibrate ϕ_S and ζ_S, the following procedure was exploited. Initially we make sure the input polarization of light is set to QND configuration, remove QWP from the detection stage, scan modulation phase and search for flat response of S_{CIFAR}. Thus, the angle $\phi_{S,0} = \pi/2$ is found as dictated by eq.(4.54). Secondly, ϕ_S is scanned again (shown on Fig.4.6, top panel) until S_{CIFAR} becomes perfectly symmetric Lorenz peak. In described case it happens at $\phi_{S,1} = \phi_{S,0} - 84°$. At this stage we note that expected $\phi_{S,1}$ should be shifted precisely by $\pi/2$ from $\phi_{S,0}$ since HWP alone in the detection setup should match to the pure phase quadrature $\hat{p}_{L,S}$ ($\zeta_S \equiv 0$). We then conclude that HWP used in the experiment is non-ideal and adds some circularity to the polarization giving detection phase $\zeta_S = -6°$[12].

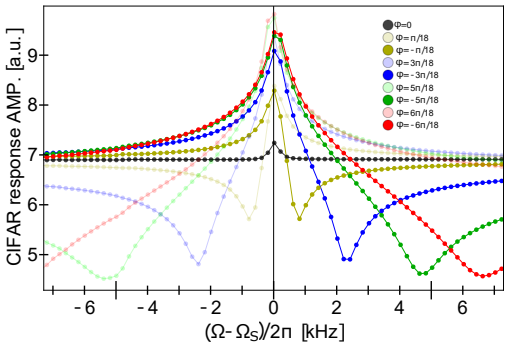

(a) Amplitude response: calibration of modulation angle ϕ

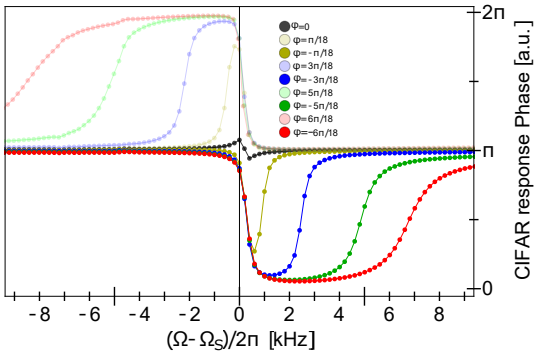

(b) phase response: calibration of modulation angle ϕ

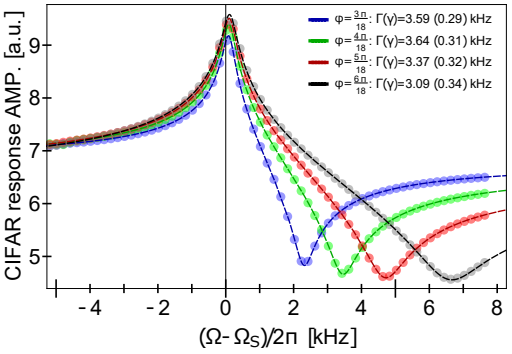

(c) Amplitude response: fit of several traces

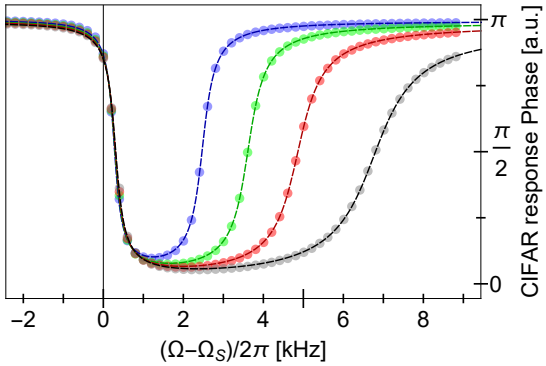

(d) Phase response: fit of several traces

Figure 4.6: CIFAR: experimental data. Temperature is set $T = 38°$, probe power $P_{LO} \approx 1$mW.

Having both detection and modulation angles calibrated, we select several points for ϕ_S and perform a fit of each dataset with the model of amplitude and phase CIFAR response. As seen from the Fig.4.6, bottom panel, the different $\phi_{S,i}$ yield different values for extracted readout rate Γ_S and damping rate γ_S. The uncertainty $\approx 15\%$ on both parameters is mainly attributed to imperfect calibration of ϕ_S, which is limited by the software of a FPGA board in the phase lock loop. Nevertheless, obtained values for Γ_S and γ_S will serve as a reasonable reference for further examination of atomic ensemble (performed in sec.4.4.2). Directly from the CIFAR we evaluate the ratio $\Gamma_S/\gamma_S \gtrsim 10$, a prerequisite for high cooperativity.

Finally, we apply CIFAR to explore the dependence of spin parameters on probe power P_{LO} and pump intensity P_{pump}. The quality of fit is impaired with increase of P_{LO}, but we are able to identify that the damping rate γ_S is dominated by intrinsic linewidth, giving the room for improvement of cooperativity. From the other side, the growth of P_{pump} irrevocably reduces the ratio Γ_S/γ_S (Fig.4.7). Thus, we choose the value $P_{pump} \approx 40\mu$W for the experiment, big enough to provide strong spin polarization and yielding relatively high Γ_S/γ_S ratio at the same time.

[12]such statement comes from the simple feature of eq.(4.54) producing symmetric Larmor peak whenever $\zeta_S + \phi_{S,1} = 0$.

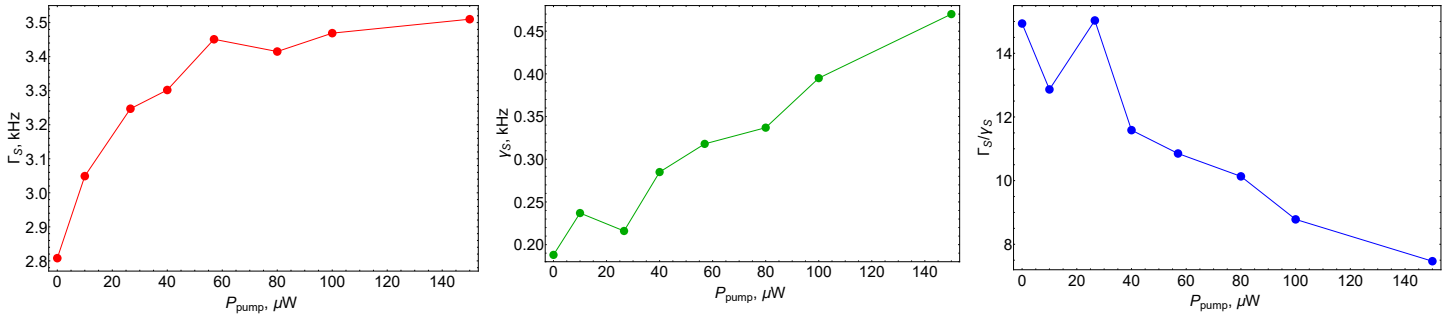

(a) (b) (c)

Figure 4.7: The extracted readout rate Γ_S and atomic linewidth γ_S when the pump power is varied.

4.3.4 Broadband noise

Motional effects (or external spin degrees of freedom) have to be taken into account while studying the dynamics of the atomic ensemble interacting with an optical field. For that purpose, a theoretical approach presented in [119] utilizes the Bloch-Heizenberg-Langevin formalism and incorporates boundary conditions as atoms interact with the cell walls. The solution is obtained by introducing the basis of atomic diffusion modes [120], that might be understood as writing ladder operator eq.(4.9) in a form $\hat{j}_{\mp} = \sum_k \hat{j}_{\mp,k} u_k(\boldsymbol{r})$. Each atomic mode $\hat{j}_{\mp,k}$ is assigned to its own damping rate $\gamma_{dS,k}$[13] and coupling strength defined by its overlapping I_k with the optical mode of the probe field. The characteristic shape of the experimentally observed spin spectrum is illustrated on Fig.4.8 that reflects the presence of multiple atomic modes. One may identify narrowband structure (Fig.4.8, right inset) centered around $\Omega \approx 1.017$ MHz and linewidth $\lesssim 0.5$ kHz. It corresponds to the contribution to γ_S from spin-spin and spin-wall collisions arising from uniform (homogeneous) mode $k = 0$. At the same time, non-zero overlapping I_k with higher modes ($k > 0$) forms a structure, that resembles a broad pedestal (Fig.4.8, left inset). While the broad peak has the same central frequency as narrow peak on the top, the linewidth of composite response from $\sum_{k=1} \hat{j}_{\mp,k}$ is of the order of transient time of an atom crossing the cell[14] in directions orthogonal to propagating probe field. The utilization of an anti-relaxation coating for the cell leads to strong reduction of the damping rate $\gamma_{dS,0}$ in comparison to $\gamma_{dS,k}$, $k > 0$ making long-lived mode clearly distinguishable [119].

Alternatively, one can regard the cumulative response of atomic diffusion modes $k \neq 0$ as a single mode described by canonical variables $\{\hat{x}_{S,bb}, \hat{p}_{S,bb}\}$ complementary to $\{\hat{x}_S, \hat{p}_S\}$. The mode $\{\hat{x}_{S,bb}, \hat{p}_{S,bb}\}$ originates from time-dependent coupling $g_{cs}(t)$ between single atoms and optical field due to non-homogeneous intensity distribution of the probe [121], [115]. The dynamics of mode $\{\hat{x}_{S,bb}, \hat{p}_{S,bb}\}$ is driven by the Hamiltonian with the same structure as for $\{\hat{x}_S, \hat{p}_S\}$, meaning Larmor precession disturbed by Faraday rotation. Consequently, we introduce the readout rate $\Gamma_{S,bb}$, damping rate $\gamma_{S,bb}$ and susceptibility function

$$\chi_{S,bb} = \Omega_S / \left(\Omega_S^2 - \omega^2 - i\gamma_{S,bb}\omega + \left(\gamma_{S,bb}/2\right)^2\right). \tag{4.56}$$

We hence consider that the mode $\{\hat{x}_{S,bb}, \hat{p}_{S,bb}\}$ gives rise to Lorenz peak, but more correct way to treat it would be to define Gaussian peak instead since the superposition of big amount of Lorenz modes should be approximated by Gaussian distribution. We will refer to the respective contribution to the spin noise spectrum as *broadband noise*.

The influence of the size of the probe Gaussian beam on the features the of broadband response is carefully examined in [115]. The linewidth of broad peak declines with the growth of beam diameter w_{pG}. Such observation looks consistent with the argument presented in [119]: the overlapping I_k with high-order atomic modes scales down faster for larger k (those have bigger decay rate). The strength of the broadband noise coupling $\Gamma_{S,bb}$ is also reduced for increased w_{pG}. This is an expected result as well since intensity distribution within cell becomes more homogeneous in such case. Enlarging the size of the probe beam and aiming to mitigate the undesired broad pedestal in the spin spectrum, one needs to consider the problem of optical losses: the edges of the optical mode are truncated by the cell channel at certain moment and the transmission is degraded. This obstacle might

[13] 'd' in subscript means 'diffusion'

[14] Considering the filling of the cell with the probe beam approaches unity

be tackled by substituting Gaussian beam with *top-hat* profile. To produce top-hat beam, the initial Gaussian beam was converted exploiting aspherical beam shaping lens. After such transformation the mode is transmitted through the system of spherical lenses in order to match the geometry of the cell [122]. The efforts in producing the most suitable top-hat beam culminated in a converging configuration with the size $w_{pth,1} \approx 1.9$ mm on the input of the cell and $w_{pth,1} \approx 1.6$ mm on the output yielding a filling factor FF

$$FF = \frac{1}{Ld_c^2}\int_{z=0}^{L_c} w_{pth}^2(z)dz \approx 0.7 \tag{4.57}$$

In order to characterize the amount of broadband noise in the spin system, we extend the input-output relations eq.(4.40). Interaction of the probe field with the atomic mode $\{\hat{x}_{S,bb}, \hat{p}_{S,bb}\}$ together with perturbation by stochastic thermal force will be recorded according to

$$\hat{p}_{L,S,bb} = 2\Gamma_{S.bb}\chi_{S,bb}\hat{x}_{L,S,in} + \sqrt{2\Gamma_{S,bb}\gamma_{S,bb}}\chi_{S,bb}\hat{f}_{th,bb}. \tag{4.58}$$

Therefore, the measured optical phase quadrature in described here experiment will be $\hat{p}_{L,out} = \hat{p}_{L,S,bb} + \hat{p}_{L,S,out}$, where $\hat{p}_{L,S,out} \equiv \hat{q}_{L,S,out}|_{\zeta_S=0}$ is taken from eq.(4.40). Notably, the Langevin force $\hat{f}_{th,bb}$ in general might be different from the stochastic force $\hat{f}_{th}$ acting on long-lived atomic mode. The PSD of $\hat{p}_{L,out}$ normalized by shot noise (SN) is given by

$$S_{L,out} = \langle \hat{p}^{\dagger}_{L,out}\hat{p}_{L,out}\rangle = 1 + A_{nb}^2/((\Omega_S-\omega)^2 + (\gamma_S/2)^2) + A_{bb}^2/((\Omega_S-\omega)^2 + (\gamma_{S,bb}/2)^2). \tag{4.59}$$

The terms on right side are flat spectrum of SN, contributions from $\{\hat{x}_S, \hat{p}_S\}$ and $\{\hat{x}_{S,bb}, \hat{p}_{S,bb}\}$. We don't care about separating back action term from thermal noise for both atomic modes at the moment. Therefore, we introduce constants A_{nb} and A_{bb}[15] for $\hat{x}_S, \hat{p}_S$ and $\hat{x}_{S,bb}, \hat{p}_{S,bb}$ respectively representing the strength of combined back action noise and thermal noise. The approximation $\chi_S \approx 0.5/(\Omega_S - \omega - i\gamma_S)$ for the narrowband susceptibility function is assumed in eq.(4.59) provided $\Omega_S \approx \omega \gg \gamma_S$ and same for $\chi_{S,bb}$. The fit of spectrum on Fig.4.8 using eq.(4.59) yields $\gamma_{S,bb} \sim 75$ kHz. Indeed, this value is in a reasonable agreement with transient time $\tau_{tr} \sim 2r_{hat}/\mathcal{V}_S$, where $\mathcal{V}_S \sim 100$ m/s is the thermal velocity at temperature $T = 30 - 40°$. The height of broadband noise h_{bb} is 0.3 in SN units which is the substantial improvement compared with probing the ensemble using Gaussian beam [115]. The ratio between heights of narrow and broadband peaks (h_n and h_{bb}) can serve as the most straightforward metric of suppression of high order atomic modes ($k > 0$). The response of $\{\hat{x}_S, \hat{p}_S\}$ is distributed between several peaks in the spin noise spectrum presented on Fig.4.8 owing to spin polarization $\mathcal{P} < 1$ and the strength of magnetic field big enough to resolve Zeeman multiplets. Hence, we reconstruct the Lorenz peak with the linewidth $\gamma_S \approx 300$ Hz extracted from CIFAR and integrated area as for split configuration calculated by fitting[16] experimental data. Doing so, we obtain the effective height $h_{n,eff}$ of peak produced by the mode $k = 0$ and find the ratio $h_{n,eff}/h_{bb} \sim 800$.

4.4 Quantum noise limited spin oscillator

4.4.1 Noise budget in a framework of Faraday interaction model

We can calculate the spectrum of the atomic noise using eq.(4.40) with added broadband noise as

$$S_S(\Omega)|_{\hat{q}_L(\zeta_S)} = 1 + 4\eta S_{QBA}\cos^2(\zeta_S) + 2\eta S_{corr}\sin(2\zeta_S) + 4\eta S_{Th}\cos^2(\zeta_S) + \eta S_{bb}\cos^2(\zeta_S). \tag{4.60}$$

where the total noise is normalized to the shot noise of the probe light. The right-hand side of eq.(4.60) consists of the following terms: the unity represents the imprecision noise, $S_{QBA} = \Gamma_S^2\,|\chi_S(\Omega)|^2$ is back-action noise, $S_{corr} = \Gamma_S \mathrm{Re}\,[\chi_S(\Omega)]$ are cross correlations between SN and QBAN, $S_{Th} \approx 2\gamma_S\Gamma_S\,|\chi_S(\Omega)|^2\,\sigma_{Th}$ is thermal noise with σ_{Th} given by eq.(4.52), S_{bb} represents the broadband noise. Since we use the spectral range $|\Omega - \Omega_S| \sim \gamma_S \ll \gamma_{S,bb}$ to calibrate the spin oscillator, the broadband noise is seen as an offset added to the shot noise rather than the

[15] $A_{nb}^2 = \Gamma_S^2 + \Gamma_S\gamma_S(2n_S+1)$ and similarly for A_{bb}

[16] In order to fit the narrowband part of the spectrum, the model eq.(4.59) has to be modified: $A_{nb}^2/((\Omega_S-\omega)^2 + (\gamma_S/2)^2)$ is replaced by a superposition of Lorenz functions. This circumstance will be of crucial importance in the section 4.4.2.

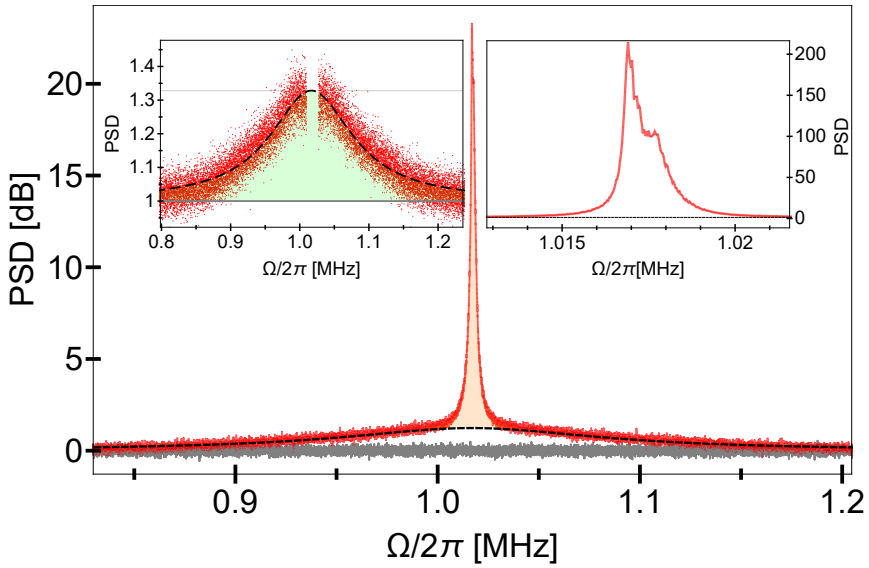

Figure 4.8: Main plot: the (composite) spin noise spectrum measured at the strength of external magnetic field corresponding to $\Omega_S \approx 1.017$ MHz. The left subplot shows the broadband noise formed by high-order diffusion modes $\sum_{k=1} \hat{j}_{\mp,k}$ according to [119]. The right subplot demonstrates the narrow line of long-lived atomic mode with decay rate defined by spin-spin and spin-wall damping mechanisms. This line is split because of quadratic Zeeman effect and non-perfect spin polarization. See text for details.

component shaped by the Lorenz function $\chi_{S,bb}$ (see eq.(4.58)). The detection efficiency η is introduced to account for optical losses on the cell and in the optical path towards the homodyne detection.

Each noise source was initially estimated independently. Specifically, the readout rates and the susceptibility function were reconstructed by CIFAR, giving the information about QBAN and cross-correlation terms. The thermal occupation $n_S \propto S_{Th}$ was obtained from MORS, the broadband noise was calibrated in the section 4.3.4. The detection efficiency $\eta = 0.92$ is obtained by measuring the transmission of the cell and characterizing each optical element after the ensemble, including the quantum efficiency of photodiodes.

In the following section, we will fit the spectra of spin noise at different detection angles ζ_S and evaluate the amount of QBAN in the atomic oscillator compared to all other noise sources. The fit with the spin model can be used to independently validate the models for CIFAR and MORS. However, we mainly rely on spin noise fit.

We will see that the model given by eq.(4.60) appears as incomplete because of two reasons. First, the probe laser is not shot noise limited, and the extra intensity fluctuations are perceived by the atomic ensemble. Secondly, the light-matter interaction is restricted by the Faraday model meaning the QND regime. However, as we have seen in section 4.2.4, the tensor interaction plays a significant role and can't be ignored.

Provided relatively low level of the thermal noise (meaning small n_S), properly adjusted detection angle ζ_S yields the drop of noise level below the shot noise, manifesting *ponderomotive squeezing*. In the limit $\chi_S \approx \mathrm{Re}\{[\chi_S]\}$ the maximal value of the squeezing induced by spin ensemble is achieved for the optimal detection phase $\zeta_{S,opt}$ and in a narrow spectral range around Ω_{opt}, expressed by

$$S_S(\Omega_{opt})|_{\hat{q}_{L,out}(\zeta_{S,opt})} \approx 1 - \eta \frac{C_q}{C_q + 1}, \tag{4.61}$$

where C_q is the *atomic quantum cooperativity* defined as the ratio between QBAN and thermal noise:

$$C_q = \frac{S_{QBA}}{S_{Th}} = \frac{\Gamma_S}{\gamma_S (1 + 2n_S)}. \tag{4.62}$$

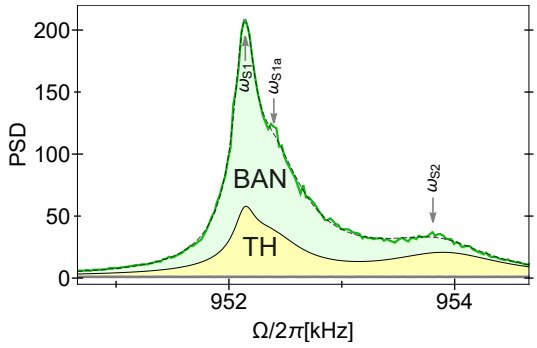

(a) 'Positive-mass' ($\Omega_S > 0$) spin ensemble, phase quadrature is detected

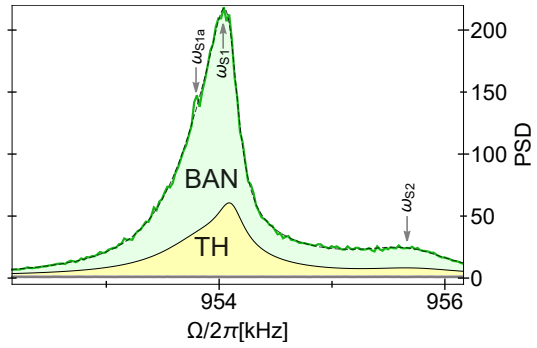

(b) 'Negative-mass' ($\Omega_S < 0$) spin ensemble, phase quadrature is detected

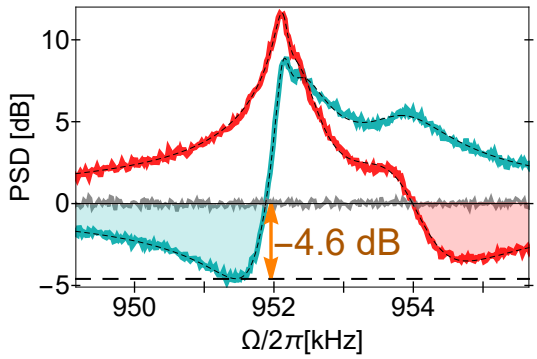

(c) 'Positive-mass' ($\Omega_S > 0$) spin ensemble, ponderomotive squeezing is detected

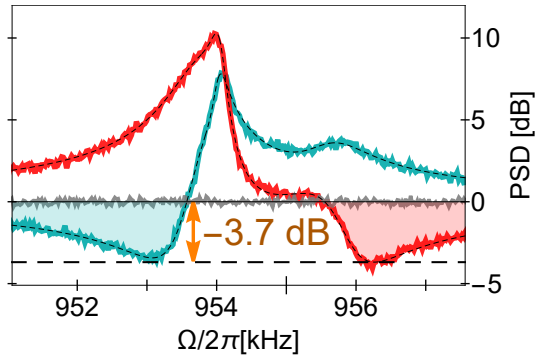

(d) 'Negative-mass' ($\Omega_S < 0$) spin ensemble, ponderomotive squeezing is detected

Figure 4.9: The spectra of the optical field after probing the atomic spin oscillator with $|\Omega_S|/(2\pi) = 0.96$ MHz. **Top panel**: the phase quadrature ($\zeta_S = 0$) is detected. We distinguish the positive (a) and negative (b) mass configurations, comparing the frequency of the strongest transition ω_{S1} to the other transitions from the $F = 4$ multiplet (only ω_{S1a} can be identified). In addition, we observe the spectral component at frequency ω_{S2} that is always bigger than ω_{S1} and ω_{S1a}, regardless of the sign of the mass of the oscillator at $F = 4$. This line presumably appears because of inhomogeneous magnetic field across the cell. We include it as a third oscillator into the model. **Bottom panel**: Adjustment of the homodyne detection phase $\zeta = \zeta_{opt}$ allows for the observation of the ponderomotive squeezing.

4.4.2 Calibration of quantum back action noise

Atomic oscillator in MHz spectral range. Multi-oscillator model

We initially select the frequency detuning $\Delta = 1.6$ GHz[17] of the optical field from the transition $6S_{1/2}, F = 4 \leftrightarrow 6P_{3/2}, F' = 5$ and the optical power of the probe field $P_{probe} \approx 1$ mW. We then start with the measurement of spin noise, setting magnetic field to the level, which corresponds to the resonance frequency $\Omega_L = 0.96$ MHz according to eq.(4.3). By controlling the polarization of the optical pumping fields, we can initialize the atomic state with the macroscopic spin oriented along or opposite to the external magnetic field. Thus, we switch between the regimes of the ensemble with positive and negative mass [39]. The respective spin noise spectra are shown on Fig.4.9a-4.9b in which the phase quadrature is detected. Analogous to Fig.4.3, one can resolve at least two lines from $F = 4$ hyperfine manifold due to the quadratic Zeeman splitting and finite spin polarization. With regard to the model given by eq.(4.60), we obtain two two-level systems, hence, two oscillators. When the macroscopic spin is counter-oriented to the static magnetic field (Fig.4.9a), the first oscillator is formed by $|F = 4, m_F = -4\rangle$ and $|F = 4, m_F = -3\rangle$ levels, the second corresponds to $|F = 4, m_F = -3\rangle \leftrightarrow |F = 4, m_F = -2\rangle$ transition. In the case of spin polarization along magnetic field (Fig.4.9b) we identify $|F = 4, m_F = 4\rangle \leftrightarrow |F = 4, m_F = 3\rangle$ and $|F = 4, m_F = 3\rangle \leftrightarrow |F = 4, m_F = 2\rangle$ transitions with the two observed peaks, respectively. In the positive-mass

[17] the adjustment of Δ later will be of critical importance

(negative-mass) regime the 'desired' $|F=4, m_F=-4\rangle \leftrightarrow |F=4, m_F=-3\rangle$ ($|F=4, m_F=4\rangle \leftrightarrow |F=4, m_F=3\rangle$) oscillator prevails, confirming that the atomic ensemble was prepared in the correct state with polarization $\mathcal{P}$ approaching unity. At the time of data processing, the low broad spectral component to the right of $F=4$ multiplet (it is named 'bump' in the section 4.3.2) in both spectra was recognized as unresolved $F=3$ manifold, rising due to the limited performance of the repump. Considering relatively high degree of orientation on $F=3$, we decided to account for it by adding the third oscillator into the model. Having done tests afterwards, we realized that the spectral spacing between *alleged* $F=3$ and $F=4$ structures doesn't follow eq.(4.2) while changing the strength of the applied magnetic field. Moreover, reducing the repump power, we managed to find the real (resolved) $F=3$ manifold. Our current understanding (not reinforced by profound investigations) is that the component at ω_{S2} still belongs to $F=4$ level, which is however split due to the inhomogeneity of the magnetic field through the cell. Therefore, the atoms perceive different field and experience different energy shift at specific parts of the cell (for example, the center versus edges). In such case scenario, complementing the model by another single oscillator[18] also seems justified.

Based on the discussion above, the model eq.(4.60) should be extended to the case of three oscillators. To implement that, we replace the contribution of QBAN S_{QBA} by the term

$$S_{QBA,\sum} = |\sum_{i}^{n=3} e^{i\psi_{S,i}} \Gamma_{S,i} \chi_{S,i}(\Omega_{S,i}, \gamma_{S,i}, \Omega)|^2. \tag{4.63}$$

Such a modification reflects that each oscillator is assigned a specific readout rate $\Gamma_{S,i}$, a damping rate $\gamma_{S,i}$ and a resonance frequency $\Omega_{S,i}$. Secondly, introducing phases $\psi_{S,i}$, we emphasize that quantum back action noise can interfere between different oscillators. The last circumstance isn't valid for thermal noise that is now calculated as $S_{Th,\sum} = \sum_i^{n=3} S_{Th,i}$ where $S_{Th,i}$ is defined as in eq.(4.60). It means that the interaction of each oscillator with the environment is determined by the individual thermal occupations $n_{S,i}$.

The utilization of the multi-oscillator model apparently questions the trustworthiness of extracted parameters assigned to an individual oscillator. Instead, we rely on total quantum back action noise and thermal noise calculated as integrated areas of spectrum based on the performed fit. In particular, we estimate their ratio and find cooperativity $C_q = 2.7$ for the positive-mass system that agrees well with the measured ponderomotive squeezing $S_S = -4.6$ dB, shown on Fig.4.9c. Upon inverting the spin population, we witness the drop of the squeezing down to $S_S = -3.7$ dB, see Fig.4.9d. Since we flip the orientation of $\boldsymbol{B}$ in this particular experiment instead of switching the polarization of pumping fields, the small reduction of the ponderomotive squeezing may be related to sub-optimal current ratio between coils controlling magnetic field. Therefore, an extra broadening is added to the spin decay rate. However, regardless the sign of the effective mass, the motion of the spin ensemble is predominantly driven by quantum noise in MHz spectral range.

The correctness of extracted QBAN and thermal noise is further confirmed by studying their behaviour as a function of the probe detuning Δ. The expressions for the integrated areas are $\int_\Omega S_{QBA} d\Omega \propto \Gamma_S^2 \int_\Omega |\chi_S(\Omega)|^2 d\Omega = \Gamma_S^2/\gamma_S \propto A^2/\left[\Delta^2\left(\gamma_{S,in}\Delta^2 + C\right)\right]$ and $\int_\Omega S_{Th} d\Omega \propto \gamma_S \Gamma_S \int_\Omega |\chi_S(\Omega)|^2 d\Omega = \Gamma_S \propto A/\Delta^2$ respectively[19]. Here $\Gamma_S = A/\Delta^2$, $\gamma_S = \gamma_{S,in} + C/\Delta^2$, where A, C and $\gamma_{S,in}$ are constants that don't depend on Δ. We validate the expected behavior both for $\int_\Omega S_{QBA}$ and $\int_\Omega S_{Th}$ while varying Δ, as shown in Fig.4.10. Only two oscillators from resolved $F=4$ manifold are taken into account when fitting $\int_\Omega S_{QBA}(\Delta)$ and $\int_\Omega S_{Th.}(\Delta)$, whereas the last oscillator ('spurious $F=4$') is discarded.

Spin oscillator when resonance frequency is reduced from 130 kHz down to 10 kHz at fixed (1.6 GHz) detuning Δ. Growth of n_S

We stick to the positive-mass configuration and reduce Ω_S to 130 kHz. The quadratic Zeeman splitting between $|m_F=4\rangle \leftrightarrow |m_F=3\rangle$ and $|m_F=3\rangle \leftrightarrow |m_F=2\rangle$ now becomes negligible, and those two oscillators effectively merged into one. We now have to choose between the single oscillator model and its extension up to two oscillators in total, since the 'spurious $F=4$' oscillator is still pronounced. We compare two models when fitting the spectrum of the phase quadrature $\hat{p}_{L,out}$ and the quadrature $\hat{q}_{L,out}(\zeta_{S,opt})$, which yields the strongest

[18] We will refer to it as 'spurious $F=4$' oscillator

[19] The coefficient a_1 is considered to be independent on the detuning Δ here, such approximation works well withing the range of Δ investigated in this experiment

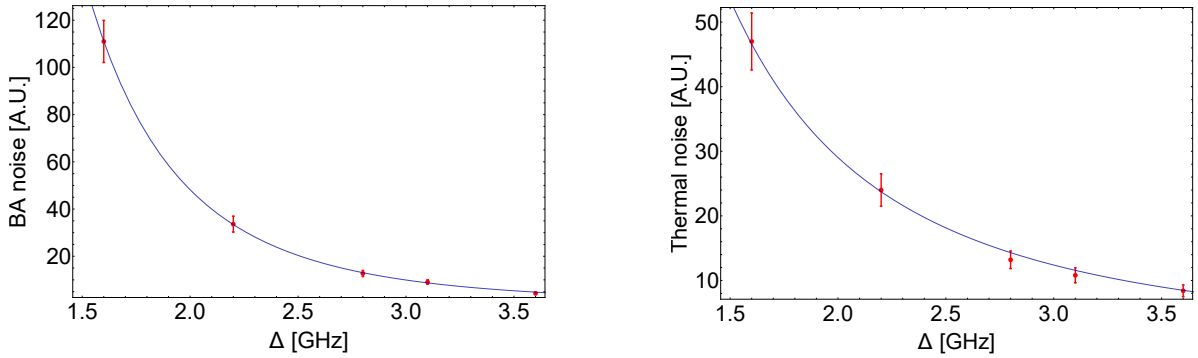

Figure 4.10: Quantum back action noise (left) and thermal noise (right) at varied dutuning Δ. Red points are experimental data, obtained from integrated area of the respective noise. Blue lines are imposed fits: $N_{QBA}/\left[\Delta^2\left(\gamma_{S,in}\Delta^2+C\right)\right]$ for QBA noise and N_{th}/Δ^2 for thermal noise respectively, see text for details. The normalization constants N_{QBA} and N_{th} are not parameters of importance for us here. The coefficients $\gamma_{S,in}$ and C define contributions of intrinsic linewidth and power broadening to the total decay rate and thus should be fixed according to the earlier stages of calibration (CIFAR and MORS).

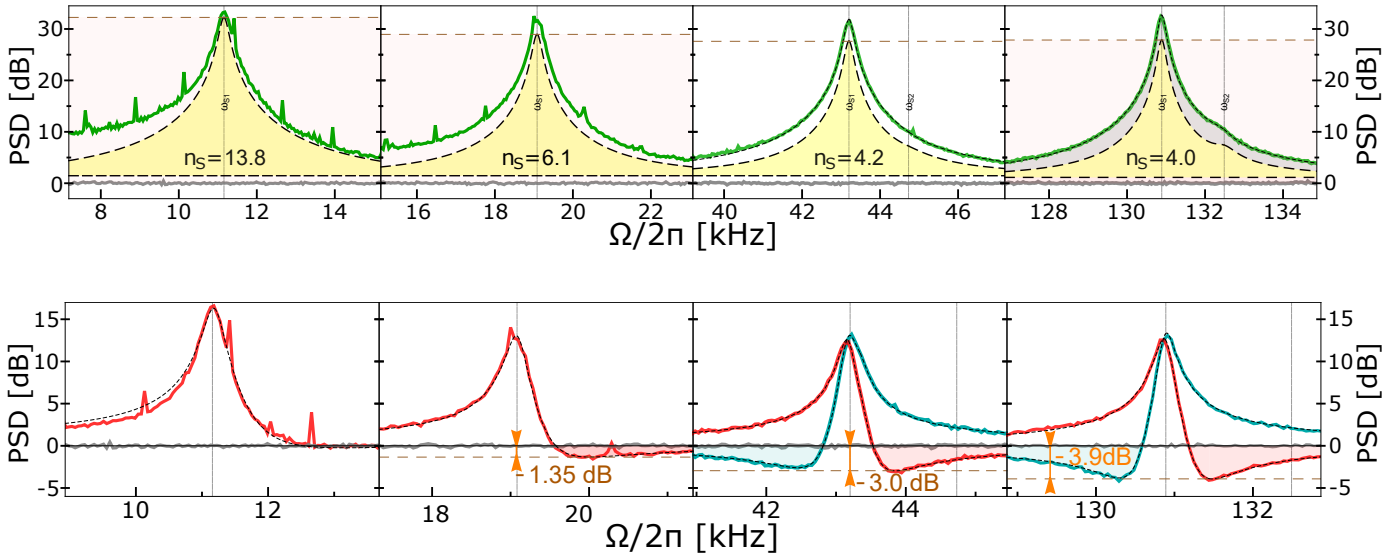

Figure 4.11: Spin noise spectra at the resonance frequency scanned from $\Omega_S = 130$ kHz down to 11 kHz when the detection angle ζ_S is set to observe the phase quadrature (top panel) and the largest ponderomotive squeezing (bottom panel). The optical detuning Δ is set to 1.6 GHz.

ponderomotive squeezing. It was found that the readout rate for the 'desired' oscillator is equal to $\Gamma_{S,1} = 3.8$ kHz in both cases, whereas the remaining oscillator exhibits $\Gamma_{S,2} = 0.15$ kHz $\ll \Gamma_{S,1}$. We then decided to proceed with the single oscillator model from this point and extracted all essential parameters of the atomic spin ensemble. The measurement rate Γ_S (index '1' is omitted) and the linewidth $\gamma_S = 0.22$ kHz are in reasonable agreement with the results of the CIFAR calibration, whereas the amount of thermal noise, encoded in the thermal occupation $n_S = 3.7$, is bigger than the value $n_S = 0.6$ estimated from MORS. Finally, we get the cooperativity $C_q = 1.9$ and the level of ponderomotive squeezing $S_S = -4.0$ dB, which matches well to the experimentally observed value and thus supports the validity of the model.

We proceed by shifting the Larmor frequency down towards the acoustic range (see Fig.4.11). As follows from the fit, the reduction of Ω_S is accompanied by a gradual rise of the atomic linewidth and a drastic enlargement of the thermal occupation n_S while the readout rate remains at the same level as well as the broadband noise S_{bb}. The growth of the spin damping rate might be again attributed to sub-optimal ratio between coils. At the

same time, we don't expect the decline of the spin polarization when the frequency is reduced. As will be shown below, the observed increase in n_S effectively accounts for the noise sources driving the spins that have not been explicitly included in the model eq.(4.60). Big values of n_S explain the degradation of the cooperativity in the lower spectral range. As a result, the ponderomotive squeezing entirely disappears at $\Omega_S \approx 10$ kHz.

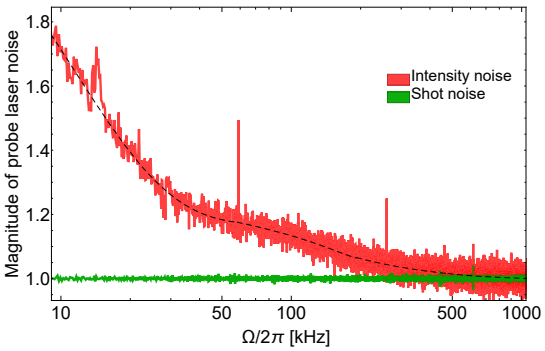

(a) Spectra of the probe laser amplitude (red) and shot (green) noise.

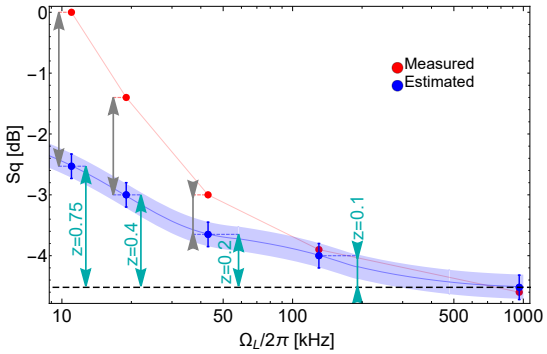

(b) The ponderomotive squeezing as a function of the Larmor frequency

Figure 4.12: The reduction of the ponderomotive squeezing with lowering the Larmor frequency Ω_S is attributed to the enhancement of the laser intensity noise (**left subplot**, red trace). **Right subplot:** blue dots/blue curve (with shaded blue area as confidence interval) predict the decline of quantum noise suppression using formula eq.(4.64). The discrepancy between model and experimentally observed ponderomotive squeezing (red data) is increased towards the acoustic frequency range and presumably originates from the impact of 'DC'-noise.

How laser intensity noise compromises quantum-noise-limited behaviour of the spin oscillator in the framework of the Faraday interaction model

One can relate the reduction of the ponderomotive squeezing to the rise of the colored intensity noise of the probe laser upon lowering the resonance frequency Ω_S. In order to interrogate the atomic ensemble, we use a DL Pro laser (Littman Metcalf configuration, the same as for the repump in MORS experiment). The spectrum of its amplitude noise is shown on Fig.4.12a, when the optical power is set to the operating point of 1mW. In the previous subsection we included the intensity fluctuations (among other effects) into the effective thermal occupation. Now we make an attempt to quantitatively evaluate the contribution of the probe laser noise to the spin noise budget using the link eq.(4.61) between the cooperativity and the level of the ponderomotive squeezing. To do that, we modify the expression eq.(4.62) for C_q and arrive to $C_q = S_{QBA}/\left(S_{Th} + S_{int}\right)$, where the term S_{int} represents initial intensity fluctuations perceived by atoms and printed back onto the output light quadrature. Here we follow the logic that any extra noise (the intensity noise of probe laser in our case) uncorrelated with QBAN should be added in the same manner as we account for thermal noise. In order to calculate the term S_{int}, we first consider the coupling of probe power fluctuations to the spin noise at frequencies close to Ω_S by means of tensor interaction in the way outlined in the subsection 4.2.4. However, the magnification of probe intensity noise down to 10 kHz isn't significant enough to explain the drop of quantum noise reduction that was observed in experiment (Fig.4.11). Our next assumption is that the atomic ensemble senses the power fluctuations of probe via Faraday interaction model[20]. Namely, an extra laser noise is coupled through the same readout rate Γ_S as quantum noise limited light. Therefore, we define the 'classical back action noise' $S_{cl.BA}$ as the response of atomic system on the intensity laser noise. The expression eq.(4.62) for cooperativity is now converted to:

$$C_q = \frac{S_{QBA}}{S_{Th} + S_{cl.BA}} = \frac{S_{QBA}}{S_{Th} + Z S_{QBA}}, \tag{4.64}$$

where Z is the amount of laser intensity noise on top of SN in SN units. Eq.(4.64) readily explains the drop of ponderomotive squeezing from $\Omega_S \approx 1$ MHz to $\Omega_S \approx 100$ kHz. However, the discrepancy between the prediction by the model and the data grows when audioband is approached, as shown on Fig.4.12b.

[20]It directly contradicts to [113] though

Spin noise formed by tensor interaction

We continue extending the model given by eq.(4.60) and now focus on the Hamiltonian $\hat{H}_{FF(2)}$ from eq.(4.32). It is responsible for the tensor dynamics beyond Faraday interplay $\propto a_1 \hat{S}_z \hat{j}_z$. We start with the term $\hat{j}_x\hat{j}_y + \hat{j}_y\hat{j}_x$ and explore its impact on the spin noise spectra, varying the angle β of the probe polarization before entering the atomic cell. The experimental results are demonstrated on the Fig.4.13. In accordance with section 4.2.4, we see that a deviation from $\beta = \pi/4$ is accompanied by the disturbed amplitude quadrature of light $\hat{x}_{L,S,out}$. It is manifested in the characteristic dip/peak in the spectrum (presented on Fig.4.13a), which should be flat around Larmor frequency Ω_S in the framework of the Faraday rotation model. Next, we set the homodyne phase to detect the phase quadrature and also see different spectra depending on β, shown on the Fig.4.13b. This effect might be seen as an alteration of the readout rate Γ_S and the damping rate γ_S[21]. The last circumstance in turn changes the level of ponderomotive squeezing, see Fig.4.13c. Eventually, we get rid of the term $\hat{j}_x\hat{j}_y + \hat{j}_y\hat{j}_x$, setting β such that the output light quadrature $\hat{x}_{L,S,out}$ is unperturbed after passing the spin ensemble. Hence, the corresponding alignment operator doesn't contribute to the spin noise budget.

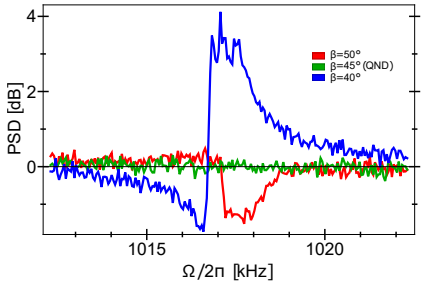

(a) The observation of the amplitude quadrature.

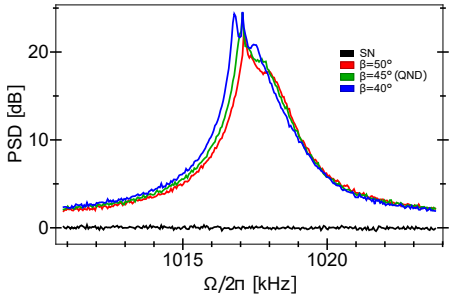

(b) The observation of the phase quadrature.

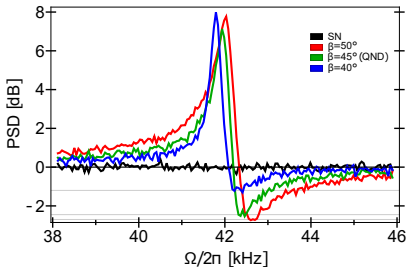

(c) The observation of the maximized ponderomotive squeezing.

Figure 4.13: Effect of the term $\hat{j}_x\hat{j}_y + \hat{j}_y\hat{j}_x$ and its compensation by the adjustment of the polarization angle β of the input light.

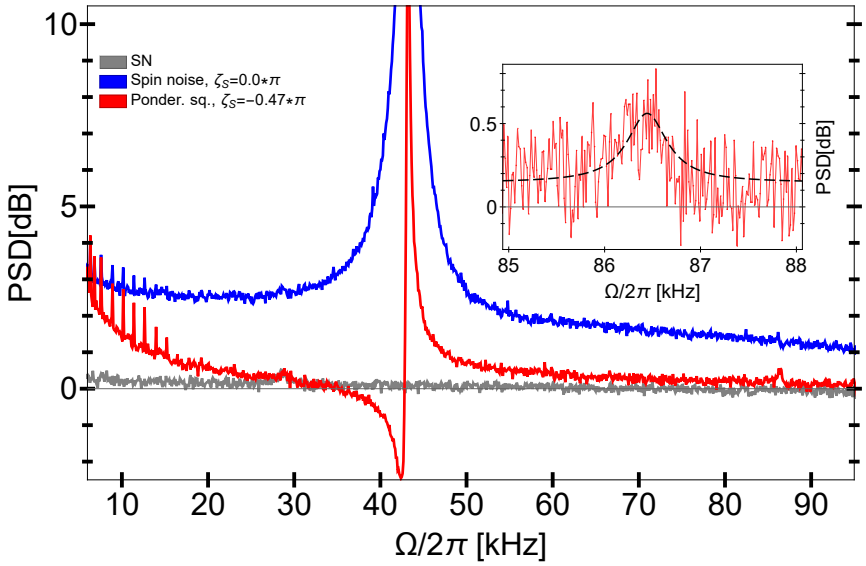

Figure 4.14: Spin noise spectra measured at the magnetic field corresponding to $\Omega_S \approx 43$ kHz. One can identify the spin response centered around Larmor frequency, but also two peaks located at $\Omega \approx 2\Omega_S$ (shown on subplot) and $\Omega \approx 0$ (the enhancement of the noise below $\Omega \lesssim 20$ kHz for the red curve). The last two are presumably attributed to the tensor operator $\hat{j}_x^2 - \hat{j}_y^2$.

[21] If the atomic linewidth is enlarged, then we have *tensor broadening*, as mentioned in the section 4.2.4

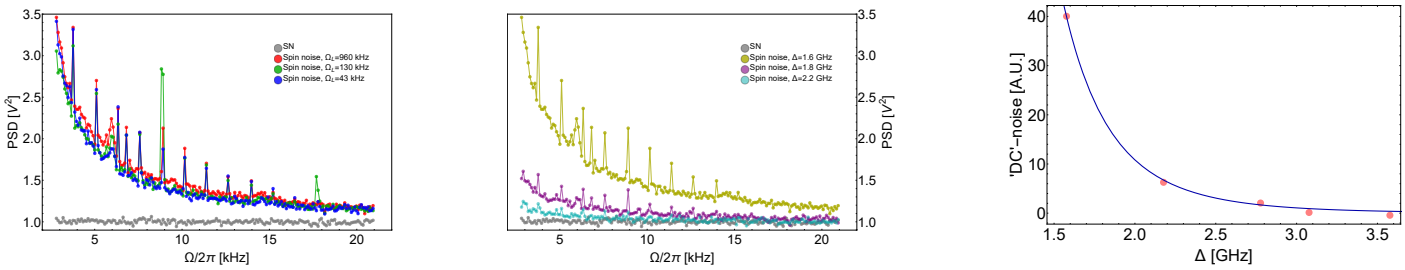

Figure 4.15: **Left plot**: 'DC'-noise at different frequencies Ω_L while the detuning $\Delta = 1.6$ GHz is fixed. One can make a conclusion that the bandwidth and the center frequency (assumed to be 0) doesn't change with the strength of the magnetic field. **Middle plot**: Spectra of 'DC'-noise at different Δ while the Larmor frequency $\Omega_L = 960$ kHz is fixed. The amplitude of the noise is clearly reduced with increase of the detuning. **Right plot**: Red dots: the integrated areas of DC-noise, recovered from spin noise spectra and measured at different detunings. Blue curve: imposed fit using the function $N_{DC}/\left[\Delta^4\left(\gamma_{S,in}\Delta^2 + C\right)\right]$. The parameters $\gamma_{S,in}$ and C are set to match the results of the fit of $S_{QBA}(\Delta)$ (presented on Fig.4.10), although it might seem to be unnecessary requirement. See text for the details.

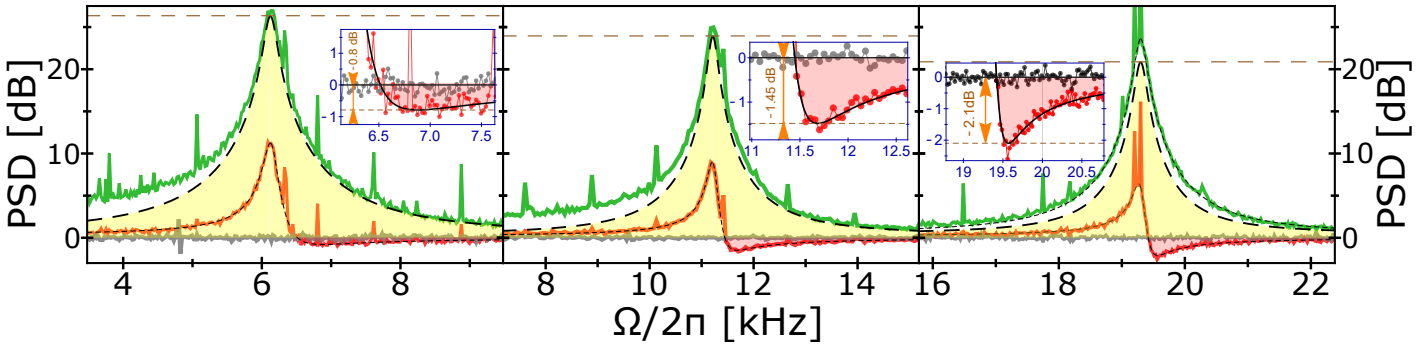

Figure 4.16: Spin noise spectra at the resonance frequency varied within the acoustic spectral range ($\Omega_S = 6$, 11, 19 kHz from left to right) and the detuning $\Delta = 3.1$ GHz. Main plots demonstrate the measurements of the phase optical quadrature, whereas the insets show the optimized ponderomotive squeezing for a specific Ω_S. One can clearly see the improvement compared to the case of $\Delta = 1.6$ GHz, outlined on Fig.4.11.

Apart from the atomic response recorded onto the probe optical field and manifesting in the frequencies near Ω_S, we notice other spectral components. An example is shown on Fig.4.14, where the magnetic field is tuned to $\Omega_S \approx 43$ kHz. One can see two components that are clearly separated from the Fano resonance curve corresponding to the ponderomotive squeezing. The first feature is a tiny peak at $\Omega \approx 86$ kHz, whereas the second is represented by the abrupt rise of the noise towards DC-frequencies. The latter presumably constitutes the peak centered at $\Omega = 0$, although we didn't manage to characterize the spectra below 1 kHz due to the limited performance of our homodyne detection. We suppose that the spin responses at $\Omega = 0$ and $\Omega = 2\Omega_S$ originate from the second spin alignment operator $\hat{j}_x^2 - \hat{j}_y^2$. The main argument in favour of this is the fact that the matrix elements $\langle m'|\,\hat{j}_x^2 - \hat{j}_y^2\,|m\rangle \neq 0$ if $|m' - m| = 0$ (according to eq.(4.45a)- (4.45b)) or $|m' - m| = 2$. However, the reasoning outlined above contains the following flaw. The alignment operator $\hat{j}_x^2 - \hat{j}_y^2$ couples to the orientation spin operator $\hat{j}_z$ through the Stokes component $\hat{S}_y$ (see eq.(4.41c)) that produces the response at spectral frequency $\Omega = \Omega_S$. Therefore, spin components $\hat{j}_{y(z)}$ should not be affected at $\Omega = 0$ and $\Omega = 2\Omega_S$ even despite the fact that the alignment operator $\hat{j}_x^2 - \hat{j}_y^2$ itself exhibits the dynamics at these frequencies. It apparently means that the rise of the DC-component and the component at twice Larmor frequency in the spectrum of light field $\hat{q}_{L,S,out}$ probing the atomic ensemble is not predicted by eq.(4.41)-(4.42), if they are analyzed using a simplified 'perturbation theory' approach. In the absence of the precise analytical solution and/or numerical simulations of the light-spin coupling by means of the tensor interaction, we don't attempt to resolve this question here. At the same time, an experimental observation of DC and double Larmor peaks is reported in [123] with rationale given by [124].

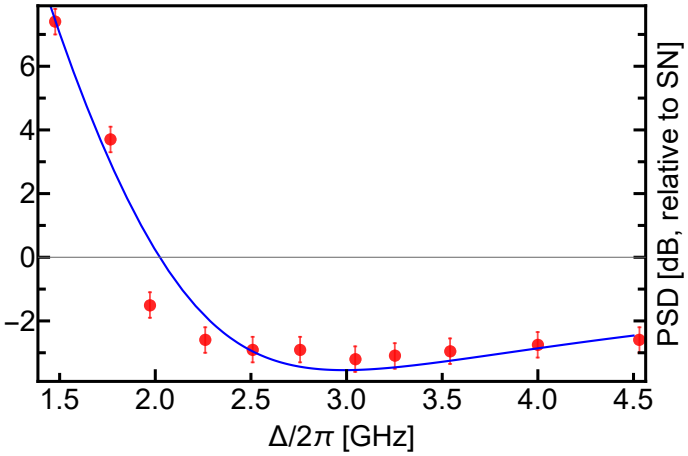

Figure 4.17: The influence of the detuning Δ on the value of the ponderomotive squeezing, the Larmor frequency Ω_S is within the spectral range where the 'DC-noise' is significant. The obtained results can be interpreted as an evidence that there is an optimal $\Delta|_{opt}$ ($= 3.0 - 3.5$ GHz in considered case), at which the ratio between QBAN and other noise sources (including "DC-noise") is maximized. It agrees with eq.(4.65).

We now focus on the DC-component (we will refer to it as 'DC'-noise) that covers the spectral range $\Omega \lesssim 20$ kHz and isn't changed when the Larmor frequency is varied (see Fig.4.15). Consequently, the 'DC'-noise has a tangible overlap with the Larmor peak when the spin oscillator is shifted down to the audioband. In order to account for the 'DC'-noise in the spin model, we introduce the term S_{DC} that has to be added to eq.(4.60). The presence of S_{DC} allows to explain the mismatch between the experimentally observed ponderomotive squeezing in the acoustic band and the value predicted by Eq.(4.64).

One possible way to understand the origin of the 'DC'-noise is to explore its integrated area as a function of the detuning Δ in a manner that it was done for QBAN and thermal noise. Having in mind the tensor interaction, we expect $S_{DC} \propto (a_2/a_1)^2 (\Gamma_S)^2 |\chi_{S,DC}(\Omega)|^2$, where $\chi_{S,DC}(\Omega)$ is the susceptibility function that defines the spectral shape of the 'DC'-noise. In the absence of any analytical or numerical solution, we can't directly introduce $\chi_{S,DC}(\Omega)$. However, we anticipate somewhat similar to the Lorenz peak with center frequency located at $\Omega = 0$. Consequently, one may surmise $\int_\Omega |\chi_{S,DC}(\Omega)|^2 d\Omega \propto \int_\Omega |\chi_S(\Omega)|^2 d\Omega$ if the mechanisms forming decay rate γ_S are still valid for S_{DC}. Finally, we obtain the expression $\int_\Omega S_{DC} \propto (a_2/a_1)^2 \int_\Omega S_{QBA} \propto 1/\left[\Delta^4 \left(\gamma_{S,in}\Delta^2 + C\right)\right]$ for the integrated area of the DC-noise, using the approximations $a_2 \propto 1/\Delta$ and $a_1 \approx 1$. This dependence on the detuning is validated on Fig.4.15 for the experimental data, when Ω_S is moved up to the MHz range to avoid an overlapping with the 'DC'-noise. The less assumption-dependent but also less specific conclusion is that $\int_\Omega S_{DC} d\Omega$ scales down faster than $1/\Delta^4$ as Δ is increased. It is already sufficient to claim that the 'DC'-noise doesn't come from the Faraday interaction model.

The fast reduction of S_{DC} upon increasing the probe detuning, being presumably explained by the term a_2, opens the possibility to optimize the cooperativity and the ponderomotive squeezing in audio frequency range. However, one needs to compare the 'DC'-noise with S_{QBA} and S_{Th} ($S_{cl.BA}$) since the latter three terms also depend on the detuning. We express the cooperativity as a function of the detuning, using $\left[\int_\Omega S_{QBA} d\Omega\right](\Delta)$, $\left[\int_\Omega S_{Th} d\Omega\right](\Delta)$, $\left[\int_\Omega S_{cl.BA} d\Omega\right](\Delta)$ obtained earlier, and then apply the approximation eq.(4.61) with added S_{DC} term. We finally arrive to the formula:

$$S_S \approx 1 - \eta \frac{C_q(\Delta)}{C_q(\Delta) + 1} + \frac{D}{\Delta^r}, \tag{4.65}$$

where $C_q(\Delta) \propto 1/(1 + B\Delta^2)$ (the coefficient B might be expressed using A, C, $\gamma_{S,in}$ and Z defined above) and $S_{DC} = D/\Delta^r$ ($r \in [4, 6]$) is the simplified expression for 'DC-noise'. Eq.(4.65) predicts the existence of a minimum of S_S that is achieved at some optimized Δ_{opt}. It turned out that set of parameters chosen for outlined experiments gives $\Delta_{opt} \in 3 - 3.5$ GHz, which is higher in comparison to the initial value $\Delta_{in} = 1.6$ GHz. Thus, increasing the detuning, we managed to improve the performance of the spin oscillator in audio frequency range, as shown on Fig.4.16. In particular, we observed $S_S = -1.4$ dB and $S_S = -0.85$ dB of the ponderomotive squeezing at

$\Omega_S = 11$ kHz and $\Omega_S = 6$ kHz respectively at $\Delta = 3.1$ GHz. The validity of the expression eq.(4.65) is confirmed as shown on Fig.4.17. Exceeding the value Δ_{opt} leads to the situation where the reduction of the 'DC-noise' cannot compensate the decline of S_{QBA}/S_{Th} due to the significance of the intrinsic spin linewidth. Notably, if the system is operated in the 'power-broadening' limited regime ($\gamma_{S,in} \ll \gamma_S \approx \gamma_{S,pb} = C/\Delta^2$), then it will be possible to keep boosting Δ until the 'DC'-noise is completely eliminated. However, the strong intensity noise of the probe laser precluded us to reach the configuration where the contribution of the power broadening to the linewidth dominates for the spin oscillator in acoustic range.

4.4.3 'Virtual rigidity' interpretation

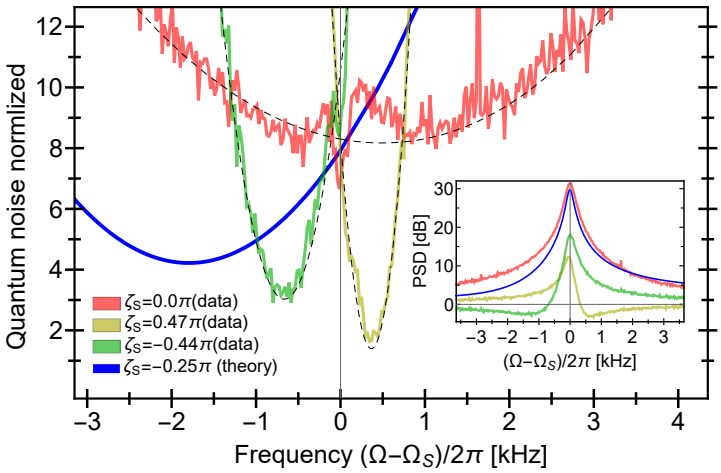

Figure 4.18: **Main plot**: Force-normalized quantum noise of light (SN and QBAN) exhibiting the tuning of effective resonance frequency Ω_S, corresponding to the position of the minimum for each curve. The shift depends on the homodyne detection phase ζ_S, see eq.(2.22). In addition, the effective readout rate $\tilde{\Gamma}_S = \Gamma_S \cos^2\phi$ is reduced, leading to a reduction of the parabola's vertical offset and an increase of its steepness. **Inset (right bottom subplot)**: The corresponding unnormalized spectra showing the ponderomotive squeezing.

We demonstrate that the ponderomotive squeezing in spin noise spectra is directly linked to the *virtual rigidity* defined in section 2.3. Considering the lossless detection $\eta = 1$ and the absence of the broadband noise, we present eq.(4.60) in a form:

$$S_S = N_{S,th}\left(\sigma_{Th} + \sigma_{LN}\right) \tag{4.66}$$

where $N_{S,th} = 8\Gamma_S\gamma_S\left|\chi_S\right|^2\cos^2\left(\zeta_S\right)$ is the normalization factor, the physical meaning of which is the response of the oscillator to the thermal force (being a particular case of the external force driving the motion of the oscillator). In turn,

$$\sigma_{L.N.} = \frac{1}{2}\frac{\Gamma_S}{\gamma_S} + \frac{1}{4}\frac{\sin\left(2\zeta_S\right)}{\cos^2\left(\zeta_S\right)}\frac{\mathrm{Re}[\chi_S]}{\gamma_S\left|\chi_S\right|^2} + \frac{1}{8\Gamma_S\gamma_S\left|\chi_S\right|^2\cos^2\left(\zeta_S\right)} \tag{4.67}$$

is the spectrum of the force, which represents the quantum noise of light normalized by the tranfer function $N_{S,th}$. If the phase quadrature $\hat{p}_{L,S,out}$ is detected, then eq.(4.67) becomes $\sigma_{L.N.}(\zeta_S)|_{\zeta_S=0} = \Gamma_S/\left(2\gamma_S\right) + 1/\left(8\Gamma_S\gamma_S\left|\chi_S\right|^2\right)$. On the other hand, the general form of eq.(4.67) might be written as $\sigma_{L.N.}(\zeta_S) = \Gamma_{S,eff}/\left(2\gamma_S\right) + 1/\left(8\Gamma_{S,eff}\gamma_S|\chi_{S,eff}|^2\right)$, where $\Gamma_{S,eff} = \Gamma_S\cos^2\left(\zeta_S\right)$ is the effective readout rate, $\chi_{S,eff} = \Omega_{S,eff}/\left(\Omega_{S,eff}^2 - \Omega^2 - i\gamma_S\Omega + \left(\gamma_S/2\right)^2\right) \approx 0.5/\left(\Omega_{S,eff} - \Omega - i\gamma_S\right)$ is the effective susceptibility function with the modified resonance frequency $\Omega_{S,eff}$ according to eq.(2.22). We retrieve σ_{LN} from spin noise spectra, collected in the experiment ($\Omega_S \approx 40$ kHz) and measured at different homodyne angles ζ_S. As shown on Fig.4.18, we observe the effective downshift of the Larmor frequency by $\Delta\Omega_{S,eff} = -0.8$ kHz and expect to get $\Delta\Omega_{S,eff} \approx -2$ kHz at selected parameters of the

spin ensemble - it would be just a matter of setting the detection angle to $\pi/4$[22]. Combining this result with the ponderomotive squeezing at $\Omega = 6$ kHz, we would obtain the quantum-noise-dominated motion of the spin oscillator with the effective resonance frequency $\Omega_{S,eff} \approx 4$ kHz, thus approaching the lower part of audioband at experimental conditions demonstrated here.

[22]However, we were not interested in such a choice of ζ_S, since our purpose was to maximize the level of ponderomotive squeezing that happens at detection phase near $\pi/2$

Chapter 5

Conclusions and future directions

5.1 Combining entanglement and atoms: frequency-dependent conditional squeezing

We have outlined the preparation and characterization of the entangled state of light and the atomic spin ensemble in quantum regime, as reported in chapters 3 and 4, respectively. Each system has a potential to become a crucial element of diverse quantum enhanced protocols, such as quantum metrology or quantum networks. In this thesis, we focus on the specific application that is the quantum noise reduction in laser interferometer-type GWDs, exploring the approach [42] detailed in the chapter 2. This scheme is expected to provide a sensitivity enhancement for the next generations of interferometric GWDs in the frequency band, where the *quantum radiation pressure noise* together with the *imprecision noise* will dominate. Therefore, the ultimate goal is to address the spectral range $\Omega \lesssim 100$ Hz, which is unreachable for either of two independently prepared systems at the time of writing this thesis. Specifically, the entanglement between optical modes is preserved down to $\Omega \approx 10$ kHz, but severely contaminated by technical noise at lower frequencies. In turn, an environmental noise, particularly acting on the atomic ensemble through the tensor alignment dynamics, prevails over the *quantum back action noise* of the spin oscillator at $\Omega \lesssim 10$ kHz. It is manifested in the deterioration of the *ponderomotive squeezing* produced by the atomic ensemble, when its resonant frequency is decreased. Applying the advanced locking scheme for OPO (sec. 3.8.2), we predict the extension of operational range of entanglement down to 1 kHz. We also see the detrimental impact of amplitude noise of probe optical field for the spin oscillator as substantial. Using the intensity stabilization loop, we hope to provide a quantum regime for the atomic ensemble approaching spectral frequencies $\Omega \approx 1$ kHz.

After modifications considered above are implemented, one can perform the tests of a hybrid quantum system, implying that the entangled light and the atomic ensemble are coupled and the spectral range 1-20 kHz is covered. Without having any prototype of quantum mechanical oscillator mimicking the dynamics of the test mass mirror in the GWD interferometer, we intend to prove the experimental feasibility of quantum noise reduction scheme [42] by presenting a *two-mode conditional squeezed state of light* where the phase of one optical mode experiences the *frequency dependent rotation* induced by the interaction with the spin oscillator. The latter thus replaces a filter cavity, which compensates the rotation of the signal quadrature caused by the quantum radiation pressure noise in the GWD. The rest of this chapter is devoted to the proposal and modelling of the experiment that can be seen as alternative to techniques studied in [29, 30].

The planned experiment starts with entangling two optical modes, encoded in quadrature bases $\hat{x}_{L,I}, \hat{p}_{L,I}$ and $\hat{x}_{L,S}, \hat{p}_{L,S}$ respectively. Having been prepared by means of spontaneous parametric down conversion (SPDC) process (see sec.1.3.1), such two-mode squeezed vacuum (TMSV) state is characterized by coefficient r determining the strength of interbeam correlations (eq.(1.17)). The first optical mode $\hat{q}_{L,I}(\zeta_I) = \cos(\zeta_I)\hat{p}_{L,I} + \sin(\zeta_I)\hat{x}_{L,I}$, being referred to as signal, is directed to homodyne detection, the homodyne phase ζ_I is adjusted. The other mode $\hat{x}_{L,S}, \hat{p}_{L,S}$, named 'idler', initially probes the atomic ensemble. It leads to the transformation according to input-output relations eq.(4.40). Consequently, one can use the following expression to present the phase quadrature $\hat{p}_{L,S,out}$ of the idler mode that passed through the spin oscillator:

$$\hat{p}_{L,S,out} = N_{LNS}\left[\cos(\theta_{S,eff})\hat{p}_{L,S} + \sin(\theta_{S,eff})\hat{x}_{L,S} + U_{th}\hat{f}_{th}\right], \tag{5.1}$$

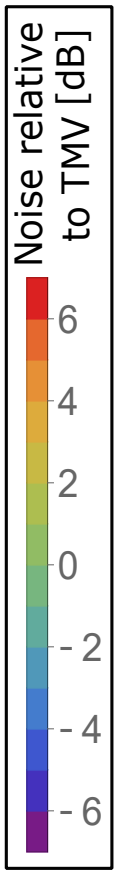

Figure 5.1: The **simulated** spectra of entangled two mode squeezed vacuum (TMSV) state of light (the squeezing factor $r = 0.75$ corresponding to ≈ -6.5 dB quantum noise reduction with respect to the shot noise of two modes), whose idler mode interacts with the atomic spin ensemble. Both modes are measured by means of homodyne detection, the idler quadrature is renormalized by total quantum light noise (SN+QBAN), see text for details. The idler homodyne phase ζ_S is set to record the phase quadrature, while the signal detection angle ζ_I is varied. The resulting noise follows eq.(5.2) that is normalized by the noise of vacuum states in each mode (TMV). For all subplots the atomic coupling rate $\Omega_{qS} = \sqrt{\Gamma_S \Omega_S}$ and full spin damping rate γ_S are set to 4 kHz (marked with black dashed vertical lines) and 0.4 kHz respectively. The resonance spin frequency Ω_S is always *positive* here. Equal relative weights for signal and idler quadratures are selected ($g = \sqrt{0.5}$), unless otherwise specified. **Top left panel**: $\Gamma_S = 16$ kHz, $\Omega_S = 1$ kHz, thermal noise and projected noise are ignored (the last term on the right side of eq.(5.1) is manually zeroed), optical losses in both signal ad idler modes are absent. **Top right panel**: $\Gamma_S = 6$ kHz, $\Omega_S = 2.7$ kHz, spin projection noise is added while n_S=0, optical losses are absent. **Bottom left panel**: $\Gamma_S = 6$ kHz, $\Omega_S = 2.7$ kHz, thermal noise is included (n_S=2.5), optical losses are absent. **Bottom right panel** (most realistic case for the experimental setup discussed in this thesis): $\Gamma_S = 6$ kHz, $\Omega_S = 2.7$ kHz, n_S=2.5, optical losses are 20% for each mode. **Insets** on right top corner for bottom and top right panels: $S_{SqC}(\Omega, \zeta_I(\Omega)|_{opt})$ is compared to two mode squeezing $S_{TMSV} = \exp(-2r)$ (see eq.(1.31)) before idler mode interacts with atomic ensemble. White dashed curves show the contour $\zeta_I(\Omega)|_{opt} = -\text{ArcTan}\left[2\Gamma_S \chi_S(\Omega)\right]$ that determines the optimal detection phase ζ_I for specific spectral frequency Ω to minimize the noise S_{SqC} in two optical modes.

where $N_{LNS} = \sqrt{1 + 4\Gamma_S^2|\chi_S|^2}$, $\theta_{S,eff} = \mathrm{ArcTan}\,(2\chi_S\Gamma_S)$. If $\hat{p}_{L,S,out}$ is measured by means of homodyne detection and renormalized dividing by N_{LNS}, then one can see (looking at the first 2 terms on the right side of eq.(5.1)) the interaction of idler mode with spin ensemble as the effective rotation of the quadrature $\hat{q}_{L,S} \equiv \hat{q}_{L,S}(\theta_{S,eff}) = \hat{p}_{L,S,out}/N_{LNS}$ defined by effective phase angle $\theta_{S,eff}$. In fact, it is caused by change of the ratio between QBAN ($\propto \hat{x}_{L,S}$) and imprecision noise ($\propto \hat{p}_{L,S}$) with the Fourier frequency Ω. The factor $U_{th} = (2\sqrt{2\Gamma_S\gamma_S})\chi_S/N_{LNS}$ in eq.(5.1) represents the rescaling of thermal force acting on the ensemble, and the broadband noise is neglected. The expression

$$S_{SqC} = \left\langle \Delta \left(g\hat{q}_{L,I}(\zeta_I) + \left(\sqrt{1-g^2}\right) \hat{q}_{L,S}(\theta_{S,eff}) \right)^2 \right\rangle \tag{5.2}$$

determines the noise obtained by combined measurement of signal and idler quadratures with arbitrary relative weight (defined by factor g), normalized by noise in both modes containing vacuum state (representing two-mode SN or two-mode vacuum (TMV)). In order to maintain the strongest interbeam correlations across the wide spectral range[1], one will need to align the signal homodyne angle

$$\zeta_I(\Omega)|_{opt} = -\theta_{S,eff} = -\mathrm{ArcTan}\,(2\chi_S\Gamma_S) \tag{5.3}$$

as function of the frequency Ω. If the spin oscillator can be approximated by the motion of a free mass object, then the functional dependence given by eq.(5.3) is exactly opposite to the rotation of the signal phase accumulated while passing the GWD interferometer, provided the correct choice of the atomic coupling rate Ω_{qS}. The role of *the negative mass (the negative resonance frequency[2])* of the spin oscillator becomes clear at this point: if the positive mass is used instead, then the atomic ensemble turns the idler quadrature in the phase space in such a way, that the undesired rotation of the signal quadrature is enhanced rather than being cancelled.

Aiming at proof-of-principle demonstration, we set the task for creating such a frequency dependent two mode squeezed state of light that would be relevant for broadband quantum noise reduction in a *fictitious* GWD interferometer with coupling rate $\Omega_{qM} = \sqrt{K_I'} = 4$ kHz (which is in fact two orders higher than in contemporary versions). Different configurations of parameters, describing the spin oscillator with coupling rate $\Omega_{qS} = \sqrt{\Gamma_S\Omega_S} = 4$ kHz, are explored and shown on Fig.5.1. The spectrum of the entanglement source is assumed to be flat and spanned down to DC-frequencies with squeezing factor $r = 0.75$ roughly matching the experimental results presented in chapter 3. The upper left subplot demonstrates the most optimal configuration. Specifically, the inequality $\Omega_S, \gamma_S \ll \Omega_{qS}$ is fulfilled, making the approximation of free mass motion justified. In a result, the 'desired' rotation of the idler quadrature is obtained, starting from $\hat{p}_{L,S}$ well above Ω_{qS} to $\hat{x}_{L,S}$ at frequencies approaching DC. The situation changes if the Larmor frequency Ω_S is increased and becomes comparable to Ω_{qS}, as shown on the top right subfigure of Fig.5.1. In contrast to the previous case, the effective idler phase $\theta_{S,eff}$ now reaches $\pi/2$ at spectral range significantly higher than $\Omega = 0$. It can also be seen as a displacement of 'effective' atomic coupling rate that may be defined as characteristic spectral frequency Ω giving some specific ratio between QBAN and SN (for example, unity). In addition, the impact of finite atomic damping rate and projection noise is manifested in degradation of interbeam correlations which is mostly pronounced near transient spectral frequencies around Ω_{qS}. Further increase of Ω_S will shrink the range of idler phase rotation, similarly to the impact or big atomic linewidth γ_S (both cases aren't covered here). The bottom left subplot of Fig.5.1 exhibits the detrimental influence of finite atomic thermal noise. The presence of thermal and projection noise may be considered as one of the most critical drawbacks of atomic spin ensemble in comparison to filter cavities. Finally, optical losses are included into the model on the bottom right subplot.

Overall, the bottom right subfigure of Fig.5.1 shows the realistic configuration, based on the characterization of the spin oscillator performed in chapter 4 and envisioning upcoming upgrades. In particular, we emulate the composite effect of thermal noise, environmental noise and tensor alignment spin noise using thermal occupation $n_S = 2.5$. Indeed, doing optimization of ponderomotive squeezing for the case $\Omega_S \approx 10$ kHz, we managed to reduce n_S down to 2.5-3 appearing from the fit of total spin noise. The total homodyne detection efficiency is estimated to exceed 85% for either of optical mode. In turn, optical losses related to the entanglement source as well as phase noise are accounted by the initial value of two mode squeezing. We thus expect that the theoretical prediction is in general reproducible using the experimental setup reported in this thesis, provided technical improvements outlined earlier.

[1] Meaning the range where QBAN competes with SN

[2] The sign of the resonance frequency Ω_S defines the sign of the susceptibility function $\chi_S(\Omega)$

Bibliography

[1] Einstein, A. Die grundlage der allgemeinen relativitätstheorie. *Annalen der Physik* **49**, 769–822 (1916). URL https://doi.org/10.1002/andp.19163540702.

[2] Barish, B. & Weiss, R. Ligo and the detection of gravitational waves. *Physics Today* **52**, 44–50 (1999).

[3] Aasi, J. *et al.* Advanced ligo. *Classical and Quantum Gravity* **32**, 074001 (2015). URL https://iopscience.iop.org/article/10.1088/0264-9381/32/7/074001.

[4] Abramovici, A. *et al.* Ligo: The laser interferometer gravitational-wave observatory. *Science (New York, N.Y.)* **256**, 325–33 (1992).

[5] Weber, J. Evidence for discovery of gravitational radiation. *Phys. Rev. Lett.* **22**, 1320–1324 (1969). URL https://link.aps.org/doi/10.1103/PhysRevLett.22.1320.

[6] Danilishin, S. & Khalili, F. Quantum measurement theory in gravitational-wave detectors. *Living Reviews in Relativity* **15** (2012). URL http://aop.osa.org/abstract.cfm?URI=aop-12-4-1012.

[7] Wade, A. *Quantum limited measurements in gravitational wave detectors - PhD thesis.* Ph.D. thesis (2016). URL http://hdl.handle.net/1885/110016.

[8] Abbott, R. *et al.* Gwtc-3: Compact binary coalescences observed by ligo and virgo during the second part of the third observing run (2021). 2111.03606.

[9] Yap, M. J. *Quantum noise reduction for gravitational-wave interferometers with non-classical states - PhD thesis.* Ph.D. thesis (2020). URL http://hdl.handle.net/1885/205760.

[10] Abbott, B. P. *et al.* Observation of gravitational waves from a binary black hole merger. *Phys. Rev. Lett.* **116**, 061102 (2016). URL https://link.aps.org/doi/10.1103/PhysRevLett.116.061102.

[11] Abbott, B. P. *et al.* Gw170817: Observation of gravitational waves from a binary neutron star inspiral. *Phys. Rev. Lett.* **119**, 161101 (2017). URL https://link.aps.org/doi/10.1103/PhysRevLett.119.161101.

[12] Caves, C. M. Quantum-mechanical radiation-pressure fluctuations in an interferometer. *Physical Review Letters* **45**, 75–79 (1980). URL https://journals.aps.org/prl/abstract/10.1103/PhysRevLett.45.75.

[13] Walls, D. F. & Milburn, G. J. *Quantum optics: 2nd edition* (Springer, 2008). URL https://link.springer.com/book/10.1007/978-3-540-28574-8.

[14] Caves, C. M. & Schumaker, B. L. New formalism for two-photon quantum optics. i. quadrature phases and squeezed states. *Phys. Rev. A* **31**, 3068–3092 (1985). URL https://link.aps.org/doi/10.1103/PhysRevA.31.3068.

[15] Lvovsky, A. *Squeezed Light* (Photonics, 2015). URL https://doi.org/10.1002/9781119009719.ch5.

[16] Kimble, H. J., Levin, Y., Matsko, A. B., Thorne, K. S. & Vyatchanin, S. P. Conversion of conventional gravitational-wave interferometers into quantum nondemolition interferometers by modifying their input and/or output optics. *Phys. Rev. D* **65**, 022002 (2001). URL https://link.aps.org/doi/10.1103/PhysRevD.65.022002.

[17] Vyatchanin, S. P. & Matsko, A. B. Quantum limit of force measurement. *Zhurnal Eksperimentalnoi i Teoreticheskoi Fiziki* **104**, 2668–2675 (1993).

[18] Acernese, F. *et al.* Quantum backaction on kg-scale mirrors: Observation of radiation pressure noise in the advanced virgo detector. *Phys. Rev. Lett.* **125**, 131101 (2020). URL https://link.aps.org/doi/10.1103/PhysRevLett.125.131101.

[19] Abadie, J. *et al.* A gravitational wave observatory operating beyond the quantum shot-noise limit. *Nature Physics* **7**, 962–965 (2011). URL https://www.nature.com/articles/nphys2083.

[20] Tse, M. *et al.* Quantum-enhanced advanced ligo detectors in the era of gravitational-wave astronomy. *Phys. Rev. Lett.* **123**, 231107 (2019). URL https://link.aps.org/doi/10.1103/PhysRevLett.123.231107.

[21] Acernese, F. *et al.* Increasing the astrophysical reach of the advanced virgo detector via the application of squeezed vacuum states of light. *Phys. Rev. Lett.* **123**, 231108 (2019). URL https://link.aps.org/doi/10.1103/PhysRevLett.123.231108.

[22] Cripe, J. *et al.* Measurement of quantum back action in the audio band at room temperature. *Nature* **568**, 1–4 (2019). URL https://www.nature.com/articles/s41586-019-1051-4.

[23] Clark, J. B., Lecocq, F., Simmonds, R. W., Aumentado, J. & Teufel, J. D. Observation of strong radiation pressure forces from squeezed light on a mechanical oscillator. *Nature Physics* **14**, 683–687 (2016). URL https://www.nature.com/articles/nphys3701.

[24] Yap, M. *et al.* Broadband reduction of quantum radiation pressure noise via squeezed light injection. *Nature Photonics* **14**, 1–5 (2020). URL https://www.nature.com/articles/s41566-019-0527-y.

[25] Oelker, E. *et al.* Audio-band frequency-dependent squeezing for gravitational-wave detectors. *Phys. Rev. Lett.* **116**, 041102 (2016). URL https://link.aps.org/doi/10.1103/PhysRevLett.116.041102.

[26] Zhao, Y. *et al.* Frequency-dependent squeezed vacuum source for broadband quantum noise reduction in advanced gravitational-wave detectors. *Phys. Rev. Lett.* **124**, 171101 (2020). URL https://link.aps.org/doi/10.1103/PhysRevLett.124.171101.

[27] Barsotti, L., Harms, J. & Schnabel, R. Squeezed vacuum states of light for gravitational wave detectors. *Reports on Progress in Physics* **82** (2018). URL https://iopscience.iop.org/article/10.1088/1361-6633/aab906/meta.

[28] Ma, Y. *et al.* Proposal for gravitational-wave detection beyond the standard quantum limit via epr entanglement. *Nature Physics* **13** (2016). URL https://www.nature.com/articles/nphys4118.

[29] Yap, M. J. *et al.* Generation and control of frequency-dependent squeezing via einstein–podolsky–rosen entanglement. *Nature Photonics* **14**, 1–4 (2020). URL https://www.nature.com/articles/s41566-019-0582-4.

[30] Südbeck, J., Steinlechner, S., Korobko, M. & Schnabel, R. Demonstration of interferometer enhancement through einstein–podolsky–rosen entanglement. *Nature Photonics* **14** (2020). URL https://www.nature.com/articles/s41566-019-0583-3.

[31] Wade, A. *et al.* Polarization speed meter for gravitational-wave detection. *Phys. Rev. D* **86** (2012). URL https://journals.aps.org/prd/abstract/10.1103/PhysRevD.86.062001.

[32] Sun, K.-X., Fejer, M., Gustafson, E. & Byer, R. Sagnac interferometer for gravitational-wave detection. *Physical review letters* **76**, 3053–3056 (1996). URL https://journals.aps.org/prl/abstract/10.1103/PhysRevLett.76.3053.

[33] Chen, Y. Sagnac interferometer as a speed-meter-type, quantum-nondemolition gravitational-wave detector. *Phys. Rev. D* **67**, 122004 (2003). URL https://link.aps.org/doi/10.1103/PhysRevD.67.122004.

[34] Polzik, E. S. & Hammerer, K. Trajectories without quantum uncertainties. *Annalen der Physik* **527** (2015). URL https://onlinelibrary.wiley.com/doi/10.1002/andp.201400099.

[35] Tsang, M. & Caves, C. M. Evading quantum mechanics: Engineering a classical subsystem within a quantum environment. *Phys. Rev. X* **2**, 031016 (2012). URL https://link.aps.org/doi/10.1103/PhysRevX.2.031016.

[36] Hammerer, K., Aspelmeyer, M., Polzik, E. & Zoller, P. Establishing einstein-poldosky-rosen channels between nanomechanics and atomic ensembles. *Physical review letters* **102**, 020501 (2009). URL https://journals.aps.org/prl/abstract/10.1103/PhysRevLett.102.020501.

[37] Duan, L.-M., Giedke, G., Cirac, J. I. & Zoller, P. Inseparability criterion for continuous variable systems. *Phys. Rev. Lett.* **84**, 2722–2725 (2000). URL https://link.aps.org/doi/10.1103/PhysRevLett.84.2722.

[38] Julsgaard, B., Kozhekin, A. & Polzik, E. Experimental long-lived entanglement of two macroscopic objects. *Nature* **413**, 400–3 (2001). URL https://www.nature.com/articles/35096524.

[39] Møller, C. *et al.* Back action evading quantum measurement of motion in a negative mass reference frame. *Nature* **547** (2016). URL https://www.nature.com/articles/nature22980?proof=thttps%3A%2F%2Fwww.nature.com%2Farticles%2Fsj.bdj.2014.353%3Fproof%3Dt.

[40] Thomas, R. *et al.* Entanglement between distant macroscopic mechanical and spin systems. *Nature Physics* **17**, 1–6 (2021). URL https://www.nature.com/articles/s41567-020-1031-5.

[41] Danilishin, S., Khalili, F. & Miao, H. Advanced quantum techniques for future gravitational-wave detectors. *Living Reviews in Relativity* **22** (2019). URL https://link.springer.com/article/10.1007/s41114-019-0018-y.

[42] Khalili, F. Y. & Polzik, E. S. Overcoming the standard quantum limit in gravitational wave detectors using spin systems with a negative effective mass. *Phys. Rev. Lett.* **121**, 031101 (2018). URL https://link.aps.org/doi/10.1103/PhysRevLett.121.031101.

[43] Zeuthen, E., Polzik, E. & Khalili, F. Y. Gravitational wave detection beyond the standard quantum limit using a negative-mass spin system and virtual rigidity. *Phys. Rev. D* **100**, 062004 (2019). URL https://link.aps.org/doi/10.1103/PhysRevD.100.062004.

[44] Thomas, R., Ostfeldt, C., Baerentsen, C., Parniak, M. & Polzik, E. Calibration of spin-light coupling by coherently induced faraday rotation. *Optics Express* **29** (2021). URL https://opg.optica.org/oe/fulltext.cfm?uri=oe-29-15-23637&id=453210.

[45] Kimble, H. The quantum internet. *Nature* **453**, 1023–30 (2008). URL https://www.nature.com/articles/nature07127.

[46] Knill, E., Laflamme, R. & Milburn, G. A scheme for efficient quantum computation with linear optics. *Nature* **409**, 46–52 (2001). URL https://www.nature.com/articles/35051009.

[47] Kurizki, G. *et al.* Quantum technologies with hybrid systems. *Proceedings of the National Academy of Sciences* **112**, 3866 (2015).

[48] Braunstein, S. L. & van Loock, P. Quantum information with continuous variables. *Rev. Mod. Phys.* **77**, 513–577 (2005). URL https://link.aps.org/doi/10.1103/RevModPhys.77.513.

[49] Bennett, C. H. *et al.* Teleporting an unknown quantum state via dual classical and einstein-podolsky-rosen channels. *Phys. Rev. Lett.* **70**, 1895–1899 (1993). URL https://link.aps.org/doi/10.1103/PhysRevLett.70.1895.

[50] Braunstein, S. L. & Kimble, H. J. Teleportation of continuous quantum variables. *Phys. Rev. Lett.* **80**, 869–872 (1998). URL https://link.aps.org/doi/10.1103/PhysRevLett.80.869.

[51] Vaidman, L. Teleportation of quantum states. *Phys. Rev. A* **49**, 1473–1476 (1994). URL https://link.aps.org/doi/10.1103/PhysRevA.49.1473.

[52] Radnaev, A. *et al.* A quantum memory with telecom-wavelength conversion. *Nature Physics* **6(11)** (2010). URL https://www.nature.com/articles/nphys1773.

[53] Rakonjac, J. V. *et al.* Entanglement between a telecom photon and an on-demand multimode solid-state quantum memory. *Phys. Rev. Lett.* **127**, 210502 (2021). URL https://link.aps.org/doi/10.1103/PhysRevLett.127.210502.

[54] Mannami, K. *et al.* Coupling of a quantum memory and telecommunication wavelength photons for high-rate entanglement distribution in quantum repeaters. *Optics Express* **29** (2021). URL https://opg.optica.org/oe/fulltext.cfm?uri=oe-29-25-41522&id=465522.

[55] Yadin, B., Fadel, M. & Gessner, M. Metrological complementarity reveals the einstein-podolsky-rosen paradox. *Nature Communications* **12** (2021). URL https://www.nature.com/articles/s41467-021-22353-3.

[56] Schrodinger, E. Discussion of probability relation between separated systems. *Mathematical Proceedings of the Cambridge Philosophical Society* **31**, 555–563 (1935). URL http://dx.doi.org/10.1017/S0305004100013554.

[57] Einstein, A., Podolsky, B. & Rosen, N. Can quantum-mechanical description of physical reality be considered complete? *Phys. Rev.* **47**, 777–780 (1935). URL https://link.aps.org/doi/10.1103/PhysRev.47.777.

[58] Bell, J. S. On the einstein podolsky rosen paradox. *Physics Physique Fizika* **1**, 195–200 (1964). URL https://link.aps.org/doi/10.1103/PhysicsPhysiqueFizika.1.195.

[59] Clauser, J. F., Horne, M. A., Shimony, A. & Holt, R. A. Proposed experiment to test local hidden-variable theories. *Phys. Rev. Lett.* **23**, 880–884 (1969). URL https://link.aps.org/doi/10.1103/PhysRevLett.23.880.

[60] Bohm, D. *Quantum theory* (1951).

[61] Reid, M. D. *et al.* Colloquium: The einstein-podolsky-rosen paradox: From concepts to applications. *Rev. Mod. Phys.* **81**, 1727–1751 (2009). URL https://link.aps.org/doi/10.1103/RevModPhys.81.1727.

[62] Reid, M. D. Demonstration of the einstein-podolsky-rosen paradox using nondegenerate parametric amplification. *Phys. Rev. A* **40**, 913–923 (1989). URL https://link.aps.org/doi/10.1103/PhysRevA.40.913.

[63] Wiseman, H. M., Jones, S. J. & Doherty, A. C. Steering, entanglement, nonlocality, and the einstein-podolsky-rosen paradox. *Phys. Rev. Lett.* **98**, 140402 (2007). URL https://link.aps.org/doi/10.1103/PhysRevLett.98.140402.

[64] Peres, A. Separability criterion for density matrices. *Phys. Rev. Lett.* **77**, 1413–1415 (1996). URL https://link.aps.org/doi/10.1103/PhysRevLett.77.1413.

[65] Ou, Z. Y., Pereira, S. F., Kimble, H. J. & Peng, K. C. Realization of the einstein-podolsky-rosen paradox for continuous variables. *Phys. Rev. Lett.* **68**, 3663–3666 (1992). URL https://link.aps.org/doi/10.1103/PhysRevLett.68.3663.

[66] Steinlechner, S., Bauchrowitz, J., Eberle, T. & Schnabel, R. Strong einstein-podolsky-rosen steering with unconditional entangled states. *Phys. Rev. A* **87**, 022104 (2013). URL https://link.aps.org/doi/10.1103/PhysRevA.87.022104.

[67] Schori, C., Sorensen, J. L. & Polzik, E. S. Narrow-band frequency tunable light source of continuous quadrature entanglement. *Phys. Rev. A* **66**, 033802 (2002). URL https://link.aps.org/doi/10.1103/PhysRevA.66.033802.

[68] Villar, A. S., Cruz, L. S., Cassemiro, K. N., Martinelli, M. & Nussenzveig, P. Generation of bright two-color continuous variable entanglement. *Phys. Rev. Lett.* **95**, 243603 (2005). URL https://link.aps.org/doi/10.1103/PhysRevLett.95.243603.

[69] Li, Y., Guo, X., Wang, X. & Zhang, K. Observation of two-color continuous variable quantum correlation at 0.8 and 1.5 micrometer. *JOSA B* **27**, 842–843 (2010). URL https://aip.scitation.org/doi/full/10.1063/1.3467045.

[70] Coutinho dos Santos, B., Dechoum, K., Khoury, A. Z., da Silva, L. F. & Olsen, M. K. Quantum analysis of the nondegenerate optical parametric oscillator with injected signal. *Phys. Rev. A* **72**, 033820 (2005). URL https://link.aps.org/doi/10.1103/PhysRevA.72.033820.

[71] Guo, X., Xie, C. & Li, Y. Generation and homodyne detection of continuous-variable entangled optical beams with a large wavelength difference. *Phys. Rev. A* **84**, 020301 (2011). URL https://link.aps.org/doi/10.1103/PhysRevA.84.020301.

[72] Guo, X., Zhao, J. & Li, Y. Robust generation of bright two-color entangled optical beams from a phase-insensitive optical parametric amplifier. *Applied Physics Letters* **100**, 091112 (2012). URL https://doi.org/10.1063/1.3690876. https://doi.org/10.1063/1.3690876.

[73] Wang, N., Du, S. & Li, Y. Compact 6 dB two-color continuous variable entangled source based on a single ring optical resonator. *Applied Sciences* **8**, 330 (2018). URL https://www.mdpi.com/2076-3417/8/3/330.

[74] Brasil, T. B. *Multicolor entanglement to link quantum systems*. Ph.D. thesis (2021). URL https://www.teses.usp.br/teses/disponiveis/43/43134/tde-10062021-094717/es.php.

[75] Stefszky, M. S. *Generation and detection of low-frequency squeezing for gravitational-wave detection - PhD thesis*. Ph.D. thesis (2012). URL http://hdl.handle.net/1885/156058.

[76] Mansell, G. *Squeezed light sources for current and future interferometric gravitational-wave detectors*. Ph.D. thesis (2018). URL http://hdl.handle.net/1885/154249.

[77] Pasiskevicius, V., Wang, S., Tellefse, J., Laurell, F. & Karlsson, H. Efficient nd:yag laser frequency doubling with periodically poled ktp. *Applied optics* **37**, 7116–9 (1998). URL https://opg.optica.org/ao/abstract.cfm?uri=ao-37-30-7116.

[78] Mabuchi, H., Polzik, E. & Kimble, H. Blue-light induced infrared absorption in knbo3. *Journal of the Optical Society of America B* **11** (1994). URL https://opg.optica.org/josab/abstract.cfm?uri=josab-11-10-2023.

[79] Blachman, R., Bordui, P. & Fejer, M. Laser-induced photochromic damage in potassium titanyl phosphate. *Applied Physics Letters* **64**, 1318 – 1320 (1994). URL https://aip.scitation.org/doi/10.1063/1.111920.

[80] Boyd, G. & Kleinman, D. Parametric interaction of focused gaussian light beams. *Journal of Applied Physics* **39**, 3597 – 3639 (1968). URL https://aip.scitation.org/doi/10.1063/1.1656831.

[81] Kerdoncuff, H. *et al.* Cavity-enhanced sum-frequency generation of blue light with near-unity conversion efficiency. *Optics Express* **28** (2020). URL https://opg.optica.org/oe/fulltext.cfm?uri=oe-28-3-3975&id=426405.

[82] Rambach, M. *Narrowband Single Photons for Light-Matter Interfaces*. Ph.D. thesis (2017).

[83] Kaddour, Z., Taleb, A., Aït-Ameur, K. & Martel, G. Revisiting gouy phase. *Optics Communications* **280**, 256–263 (2007). URL https://www.sciencedirect.com/science/article/pii/S0030401807008590?via%3Dihub.

[84] Black, E. An introduction to pound drever hall laser frequency stabilization. *American Journal of Physics* **69**, 79–87 (2001). URL https://aapt.scitation.org/doi/10.1119/1.1286663.

[85] Patrick, K. *Laser Characterization and Stabilization for Precision Interferometry.* Ph.D. thesis, Hannover U (2010).

[86] Tricot, F., Phung, D. H., Lours, M., Guerandel, S. & De Clercq, E. Power stabilization of a diode laser with an acousto-optic modulator. *Review of Scientific Instruments* **89**, 113112 (2018). URL https://hal.sorbonne-universite.fr/hal-01981700.

[87] Vahlbruch, H. *et al.* Coherent control of vacuum squeezing in the gravitational-wave detection band. *Phys. Rev. Lett.* **97**, 011101 (2006). URL https://link.aps.org/doi/10.1103/PhysRevLett.97.011101.

[88] Ning, W. & Yongmin, L. Quantum analysis and experimental investigation of the nondegenerate optical parametric oscillator with unequally injected signal and idler. *Phys. Rev. A* **93**, 013831 (2016). URL https://link.aps.org/doi/10.1103/PhysRevA.93.013831.

[89] McKenzie, K. *et al.* Quantum noise locking. *Journal of Optics B: Quantum and Semiclassical Optics* **7** (2005). URL https://iopscience.iop.org/article/10.1088/1464-4266/7/10/032.

[90] Brasil, T. B., Novikov, V., Kerdoncuff, H., Lassen, M. & Polzik, E. Two-colour high-purity einstein-podolsky-rosen photonic state. *arXiv:2110.00066* (2021). URL https://arxiv.org/abs/2110.00066.

[91] Hammerer, K., Soerensen, A. S. & Polzik, E. S. Quantum interface between light and atomic ensembles. *Rev. Mod. Phys.* **82**, 1041–1093 (2010). URL https://link.aps.org/doi/10.1103/RevModPhys.82.1041.

[92] Krauter, H. *et al.* Entanglement generated by dissipation and steady state entanglement of two macroscopic objects. *Phys. Rev. Lett.* **107**, 080503 (2011). URL https://link.aps.org/doi/10.1103/PhysRevLett.107.080503.

[93] Sherson, J. *et al.* Quantum teleportation between light and matter. *Nature* **443**, 557–560 (2006). URL https://www.nature.com/articles/nature05136.

[94] Krauter, H. *et al.* Deterministic quantum teleportation between distant atomic objects. *Nature Physics* **9**, 400 (2012). URL https://www.nature.com/articles/nphys2631.

[95] Briegel, H.-J., Dür, W., Cirac, J. I. & Zoller, P. Quantum repeaters: The role of imperfect local operations in quantum communication. *Phys. Rev. Lett.* **81**, 5932–5935 (1998). URL https://link.aps.org/doi/10.1103/PhysRevLett.81.5932.

[96] Julsgaard, B., Sherson, J., Cirac, J., Fiurásek, J. & Polzik, E. Experimental demonstration of quantum memory for light. *Nature* **432**, 482–6 (2004). URL https://www.nature.com/articles/nature03064.

[97] Jensen, K. *et al.* Quantum memory for entangled two-mode squeezed states. *Nature Physics* **7**, 13 (2010). URL https://www.nature.com/articles/nphys1819.

[98] Wasilewski, W. *et al.* Quantum noise limited and entanglement-assisted magnetometry. *Phys. Rev. Lett.* **104**, 133601 (2010). URL https://link.aps.org/doi/10.1103/PhysRevLett.104.133601.

[99] Mitchell, M. W. & Palacios Alvarez, S. Colloquium: Quantum limits to the energy resolution of magnetic field sensors. *Rev. Mod. Phys.* **92**, 021001 (2020). URL https://link.aps.org/doi/10.1103/RevModPhys.92.021001.

[100] Jensen, K. *et al.* Non-invasive detection of animal nerve impulses with an atomic magnetometer operating near quantum limited sensitivity. *Scientific Reports* **6** (2016).

[101] Jensen, K. *et al.* Magnetocardiography on an isolated animal heart with a room-temperature optically pumped magnetometer. *Scientific Reports* **8**, 16218 (2018). URL https://doi.org/10.1038/s41598-018-34535-z.

[102] Aslam, N. *et al.* Quantum sensors for biomedical applications. *Nature Reviews Physics* **5**, 157–169 (2023).

[103] Tebbenjohanns, F., Mattana, M. L., Rossi, M., Frimmer, M. & Novotny, L. Quantum control of a nanoparticle optically levitated in cryogenic free space. *Nature* **595**, 378 (2021). URL https://doi.org/10.1038/s41586-021-03617-w.

[104] Militaru, A. *et al.* Ponderomotive squeezing of light by a levitated nanoparticle in free space. *Phys. Rev. Lett.* **129**, 053602 (2022). URL https://link.aps.org/doi/10.1103/PhysRevLett.129.053602.

[105] Nielsen, W., Tsaturyan, Y., Møller, C., Polzik, E. & Schliesser, A. Multimode optomechanical system in the quantum regime. *Proceedings of the National Academy of Sciences* **114** (2016). URL https://www.pnas.org/doi/10.1073/pnas.1608412114.

[106] Mason, D., Chen, J., Rossi, M., Tsaturyan, Y. & Schliesser, A. Continuous force and displacement measurement below the standard quantum limit. *Nature Physics* **15** (2019). URL https://www.nature.com/articles/s41567-019-0533-5.

[107] Brooks, D. *et al.* Non-classical light generated by quantum-noise-driven cavity optomechanics. *Nature* **488**, 476–80 (2012). URL https://www.nature.com/articles/nature11325.

[108] Schnabel, R. Squeezed states of light and their applications in laser interferometers. *Physics Reports* **684** (2016). URL https://www.sciencedirect.com/science/article/pii/S0370157317300595.

[109] Barabanov, A. L. *Lectures on quantum mechanics* (Moscow Institute of Physics and Technologies, 2005). URL https://mipt.ru/education/chair/theoretical_physics/biblio/qm-barabanov.php.

[110] Hammerer, K. *Quantum Information Processing with Atomic Ensembles and Light.* Ph.D. thesis (2006). URL https://mediatum.ub.tum.de/doc/603134/603134.pdf.

[111] Zhao, H. *Spin squeezing and entanglement with room temperature atoms for quantum sensing and communication.* Ph.D. thesis (2014). URL https://nbi.ku.dk/english/theses/phd-theses/heng-shen.

[112] Vasilyev, D., Hammerer, K., Korolev, N. & Sørensen, A. Quantum noise for faraday light matter interfaces. *Journal of Physics B-atomic Molecular and Optical Physics - J PHYS-B-AT MOL OPT PHYS* **45** (2012). URL https://iopscience.iop.org/article/10.1088/0953-4075/45/12/124007.

[113] Julsgaard, B. *Entanglement and Quantum Interactions with Macroscopic Gas Samples.* Ph.D. thesis (2003).

[114] Moller, C. *Quantum back-action evasion in hybrid spin-optomechanical system.* Ph.D. thesis (2018). URL https://nbi.ku.dk/english/theses/phd-theses/christoffer-bo-moeller/.

[115] Thomas, R. A. *Optical spin-mechanics quantum interface: entanglement and back-action evasion.* Ph.D. thesis (2021). URL https://nbi.ku.dk/english/theses/phd-theses/rodrigo-a-thomas/Rodrigo-A-Thomas.pdf.pdf.

[116] Reiter, F. & Sorensen, A. S. Effective operator formalism for open quantum systems. *Phys. Rev. A* **85**, 032111 (2012). URL https://link.aps.org/doi/10.1103/PhysRevA.85.032111.

[117] Zugenmaier, M. *Towards a room temperature single photon source based on atomic vapour.* Ph.D. thesis (2018). URL https://nbi.ku.dk/english/theses/phd-theses/phd_theses_2018/michael_zugenmaier/.

[118] Julsgaard, B., Sherson, J., Sorensen, J. & Polzik, E. Characterizing the spin state of an atomic ensemble using the magneto-optical resonance method. *Journal of Optics B Quantum and Semiclassical Optics* **6** (2003). URL https://iopscience.iop.org/article/10.1088/1464-4266/6/1/002.

[119] Shaham, R., Katz, O. & Firstenberg, O. Quantum dynamics of collective spin states in a thermal gas. *Phys. Rev. A* **102**, 012822 (2020). URL https://link.aps.org/doi/10.1103/PhysRevA.102.012822.

[120] Tang, Y., Wen, Y., Cai, L. & Zhao, K. Spin-noise spectrum of hot vapor atoms in an anti-relaxation-coated cell. *Phys. Rev. A* **101**, 013821 (2020). URL https://link.aps.org/doi/10.1103/PhysRevA.101.013821.

[121] Baerentsen, C. *et al.* Squeezed light from an oscillator measured at the rate of oscillation. *Arxiv* (2023). URL https://arxiv.org/abs/2302.13633.

[122] Baerentsen, C. *Generation of non-classical states in a hybrid spin-optomechanical system.* Ph.D. thesis (2023). URL https://nbi.ku.dk/english/theses/phd-theses/christian-folkersen-baerentsen.

[123] Fomin, A. A. *et al.* Spin-alignment noise in atomic vapor. *Phys. Rev. Research* **2**, 012008 (2020). URL https://link.aps.org/doi/10.1103/PhysRevResearch.2.012008.

[124] Kozlov, G., Fomin, A., Petrov, M., Ryzhov, I. & Zapasskii, V. Raman scattering model of the spin noise. *Optics Express* **29** (2021). URL https://opg.optica.org/oe/fulltext.cfm?uri=oe-29-4-4770&id=447068.

Appendices

Appendix A

Chapter 3: entanglement source

A.1 Phase noise associated with double seeding of OPO

$\Delta\theta_{CLF} = \theta_{A_s^{out}} + \theta_{A_i^{out}}$ defines the deviation from antisymmetric phases of signal and idler drive fields exiting the OPO (which are, in turn, directly linked to homodyne phases). The phases $\theta_{A_{s(i)}^{out}}$ can be obtained from the phasor diagram depicted on the Fig.3.21 or using eq.(3.50):

$$\tan\left(\theta_{A_{s(i)}^{out}}\right) = \frac{\epsilon|A_{i(s)}^{dr}|\sin\left(\theta_P - \theta_{CLF,2(1)}\right) + |A_{s(i)}^{dr}|\sin\left(\theta_{CLF,1(2)}\right)}{\epsilon|A_{i(s)}^{dr}|\cos\left(\theta_P - \theta_{CLF,2(1)}\right) + |A_{s(i)}^{dr}|\cos\left(\theta_{CLF,1(2)}\right)}. \tag{A.1}$$

The root mean square $\overline{\Delta\theta_{CLF}}$ corresponding to the amount of phase noise can be obtained by fixing the $\theta_{CLF,1}$ (for example, equal to zero) and performing the integration of $\Delta\theta_{CLF}$ on $\theta_{CLF,2}$ over 2π range, since the fluctuation of phase of idler coherent filed relative to signal phase is relevant.